

# Electron Spin Resonance detectors from 400 MHz to 360 GHz

Thèse N° 9356

Présentée le 8 mars 2019

à la Faculté des sciences et techniques de l'ingénieur  
Laboratoire de microsystemes 1  
Programme doctoral en microsystemes et microélectronique

pour l'obtention du grade de Docteur ès Sciences

par

**Alessandro Valentino MATHEOUD**

Acceptée sur proposition du jury

Prof. Ph. Renaud, président du jury  
Dr G. Boero, directeur de thèse  
Prof. J. Anders, rapporteur  
Dr L. Sirigu, rapporteur  
Prof. C. Dehollain, rapporteuse

2019



*A Lidia, Eligio, Antonio e Agnese...*



# Abstract

Methods based on the electron spin resonance (ESR) phenomenon are non-invasive tools adopted to investigate paramagnetic systems at temperatures ranging from above 1000 K to below 1 K. At room temperature, commercially available spectrometers achieve spin sensitivities in the order of  $10^{10}$  spins/Hz<sup>1/2</sup> on samples with volumes of a few  $\mu\text{L}$ . Since 2008, the group of Dr. G. Boero has been working on a novel detection technique based on the integration of ESR sensors on single silicon (Si) chips. The proposed methodology allowed to study samples in the nL scale and reach a spin sensitivity at least two orders of magnitude better than the best commercially available spectrometers, comparable to the performance of microresonators. The detection principle is based on an inductive approach and can be summarized as follows. An ESR sensitive sample is placed in close proximity to the planar inductor (coil) of an LC oscillator operating at microwave frequency. In presence of a suitable static magnetic field, whose direction and magnitude respectively depend on the orientation of the inductor and the working frequency of the oscillator, the ESR phenomenon takes place. It causes a variation in the sample magnetization which translates to a variation of the inductance, leading to both a frequency shift of the LC oscillator (frequency detection) and a variation of the oscillation amplitude (amplitude detection). Consequently, the ESR phenomenon may be detected by tracking the operating point of the oscillator.

In order to maximize the spin sensitivity, it is necessary to maximize the ESR signal generated by the sample under inspection and minimize the intrinsic noise of the oscillator. The former objective is achieved by (1) maximizing the operating frequency, (2) matching the coil size to the expected sensitive volume, and (3) cooling down the system to cryogenic temperatures (if possible) so as to benefit from the larger magnetization of paramagnetic samples. The latter strictly depends on (1) the nature of the noise (thermal noise or  $1/f$  noise), (2) the working frequency, (3) the detection method (either amplitude or frequency detection), (4) the bias point of the oscillator, (5) the ambient temperature, and (6) the design methodology (e.g., transistors, topology, quality factor, layout, parasitics, electrical coupling with other subsystems, etc.). Moreover, also the microwave magnetic field generated by the LC oscillator contributes to maximizing the spin sensitivity. For the frequency detection, it must be as low as possible in order not to degrade the spectral purity of the ESR signal (saturation). Conversely, for the amplitude detection, it must be tunable since its optimal magnitude is greater than zero and depends on the nature of the paramagnetic target. In general, the microwave magnetic field strictly depends on both the amplitude of the AC current circulating in the coil and on its geometrical size, leading to further constraints at design level.

---

In this thesis, we investigate the application of the aforementioned ESR detection principle in the frequency range from 400 MHz to 360 GHz. Firstly, a semi-integrated solution operating from 400 MHz to 610 MHz is developed for an industrial application supported by the Swiss Commission for Technology and Innovation (CTI project). In such context, the originality of the work stands in the implementation of a completely standing alone portable scanner for contactless inspection over a large volume (i.e., ESR targets as large as  $4 \times 4 \text{ mm}^2$  located up to 3 mm above the sensing coil). Here, a frequency noise spectral density of  $0.15 \text{ Hz/Hz}^{1/2}$  is achieved. Additionally, ferromagnetic related applications and zero-field measurements are also investigated with the proposed architecture.

Secondly, a set of single-chip ESR detectors working from 10 GHz to 146 GHz and based on complementary metal-oxide semiconductor (CMOS) technologies are characterized from 300 K down to 4 K (i.e., the minimum temperature achievable with the available cooling power). Here, (1) the best spin sensitivity on samples of  $\alpha, \gamma$ -bis(diphenylene)- $\beta$ -phenylallyl (BDPA)/benzene complex at room temperature is achieved with the 146 GHz detector (approximately  $10^7 \text{ spins/Hz}^{1/2}$ ), (2) it improves by almost two orders of magnitude at cryogenic temperature with the 20 GHz oscillator, (3) the saturation issue caused by the microwave magnetic field heavily affects all the reported spectral resolutions, (4) an ESR experiment at a frequency as high as 360 GHz can be performed thanks to the fourth harmonic signal generated by the 90 GHz detector, and (5) the best noise performance normalized to the working frequency are obtained with the 10 GHz detector (noise floor of  $2 \text{ Hz/Hz}^{1/2}$  @ 10 kHz offset from the carrier). The latter results the best device for ferromagnetic resonance applications (FMR) and it also allows to achieve the record distance resolution of  $0.3 \text{ pm/Hz}^{1/2}$  when used as a proximity sensor.

After that, the possibility of using integrated technologies based on high electron mobility transistors (HEMT) is investigated so as to overcome the main limitations of the CMOS based detectors: (1) the relatively high power consumption which denies their use at temperatures below 4 K and (2) the high saturation issue of the ESR spectra due to the amplitude of the intrinsic microwave magnetic field produced by the LC oscillators. In this context, two HEMT LC oscillators respectively working at 11 GHz and 25 GHz are realized. In particular, the former achieves the record minimum power consumption ( $90 \text{ }\mu\text{W}$  at 300 K and  $4 \text{ }\mu\text{W}$  below 30 K) currently reported in the literature for low power LC oscillators working in the same frequency range. Also, the proposed sensor achieves a minimum microwave magnetic field of less than  $1 \text{ }\mu\text{T}$  at 300 K and less than  $0.1 \text{ }\mu\text{T}$  below 30 K, which are orders of magnitude below the values achieved by the previously reported CMOS detectors. It is worthy to note that the realized topology is versatile since it allows to perform in parallel both the amplitude and the frequency detection. Furthermore, an analytical model is developed in order to estimate the minimum achievable power consumption for an LC single-ended Colpitts oscillator based on a single field-effect-transistor (FET). In the proposed modeling, both the Level 1 and the EKV approaches are taken into account.

Lastly, the DC characterization of a standing alone HEMT transistor is provided from 300 K down to 1.4 K, ranging from the standard  $I_{DS}-V_{DS}$  curves to the extraction of both the number of carriers ( $3.5 \times 10^{16} \text{ m}^{-2}$ ) and their effective mobility ( $0.65 \text{ m}^2/\text{Vs}$  at 300 K,  $1.2 \text{ m}^2/\text{Vs}$  below

---

30 K). The former comes from the analysis of the Shubnikov-de-Haas oscillations whereas the latter is calculated by means of Hall-effect based experiments. Also, the possibility to work in deep cryogenic conditions with the 11 GHz HEMT LC oscillator allows to investigate the presence of frequency jumps in the operating frequency when sweeping the bias voltage.

Keywords: Electron spin resonance, ESR, ESR spectroscopy, LC oscillator, CMOS, HEMT, microwave, cryogenic, low power, low noise, proximity sensor.





## Résumé

Les méthodes basées sur le phénomène de résonance de spin électronique (ESR) forment un ensemble de techniques non invasives pour l'étude de systèmes paramagnétiques à des températures comprises entre plus de 1000 K et moins de 1 K. À température ambiante, les spectromètres disponibles commercialement atteignent la sensibilité de l'ordre de  $10^{10}$  spins/Hz<sup>1/2</sup> sur des volumes de  $\mu\text{L}$ . Depuis 2008, le groupe dirigé par Dr. G. Boero travaille sur de nouvelles techniques de détection basées sur l'intégration de capteurs ESR sur des puces individuelles en silicium. La méthodologie proposée a permis d'étudier des échantillons à l'échelle du nL et à des niveaux de sensibilité supérieurs d'environ deux ordres de grandeur par rapport aux spectromètres commerciaux, avec des performances similaires à celles des microrésonateurs.

Le principe de détection du signal est fondé sur une approche inductive qui peut être résumée comme suit. Un échantillon paramagnétique est placé près de l'inducteur planaire (bobine) d'un oscillateur LC micro-ondes. En présence d'un champ magnétique statique donné, dont la direction et le module dépendent de l'orientation de l'inducteur et de la fréquence de travail, la résonance électronique de spin a lieu. Cela entraîne une modification de la magnétisation de l'échantillon, ce qui se traduit par une variation d'inductance qui entraîne à la fois une modification de la fréquence de travail de l'oscillateur (détection en fréquence) et une variation de l'amplitude d'oscillation (détection en amplitude). En conséquence, le phénomène ESR peut être détecté en traçant le point de fonctionnement de l'oscillateur.

Pour maximiser la sensibilité du système, il est nécessaire de maximiser le signal ESR induit par l'échantillon analysé et, en même temps, de minimiser le bruit intrinsèque de l'oscillateur. Le premier objectif est atteint (1) en maximisant la fréquence de fonctionnement, (2) en adaptant la taille de la bobine au volume sensible désiré, et (3) en refroidissant le système à des températures cryogéniques (si possible) pour bénéficier de la plus grande magnétisation associé aux échantillons paramagnétiques. Le deuxième objectif dépend strictement de (1) la nature du bruit (bruit thermique ou bruit  $1/f$ ), (2) de la fréquence de travail, (3) du type de détection (en amplitude ou en fréquence), (4) de l'alimentation de l'oscillateur, (5) de la température et (6) de la méthodologie de projet suivie (par exemple, le type de transistor, ses dimensions, la topologie du circuit, le facteur de qualité, la disposition physique des composants intégrés et leur connexions, la présence de résistances parasites, d'un couplage électrique avec les autres systèmes, etc.). De plus, le champ magnétique micro-ondes généré par l'oscillateur LC contribue également à maximiser la sensibilité du système. En ce qui concerne la détection en fréquence, l'amplitude de ce champ doit être la plus faible possible

---

pour ne pas dégrader la pureté spectrale du signal ESR (saturation). Au contraire, dans le cas d'une détection d'amplitude, il faut la faire varier car sa valeur optimale est supérieure à zéro et dépend de la nature de l'échantillon paramagnétique. En général, le champ magnétique micro-ondes dépend strictement de l'amplitude du courant alternatif qui circule dans la bobine et de ses dimensions géométriques, ce qui entraîne d'autres contraintes au niveau du design.

Dans cette thèse, on a appliqué la méthode de détection ESR susmentionnée dans la gamme de fréquences comprise entre 400 MHz et 360 GHz. Premièrement, une solution industrielle supervisée par la Commission suisse pour la Technologie et l'Innovation (projet CTI) a été développée entre 400 MHz et 610 MHz. Dans ce contexte, l'originalité du travail réside dans la mise en place d'un scanner portable sur des volumes de détection à des distances relativement importantes (les échantillons ESR peuvent avoir une surface large jusqu'à  $4 \times 4 \text{ mm}^2$  et peuvent être déplacés jusqu'à 3 mm au-dessus de la bobine du capteur). En particulier, la densité spectrale du bruit de fréquence atteinte est de  $0,15 \text{ Hz/Hz}^{1/2}$ . En outre, l'appareil est aussi utilisé pour étudier des applications ferromagnétiques et pour des mesures à champ nul.

D'autre part, un ensemble de détecteurs ESR intégrés sur puce, fonctionnant entre 10 GHz et 146 GHz et basé sur technologie CMOS, est caractérisé de 300 K à 4 K (i.e., à la température minimale atteinte avec la puissance de refroidissement disponible). Dans ce contexte, (1) la meilleure sensibilité sur des échantillons de  $\alpha, \gamma$ -bis(diphénylène)- $\beta$ -phénylallyl (BDPA)/benzène complexe à température ambiante est atteinte avec le capteur à 146 GHz (environ  $10^7 \text{ spins/Hz}^{1/2}$ ), (2) elle s'améliore d'environ deux ordres de grandeur avec l'oscillateur à 20 GHz à des températures cryogéniques, (3) les problèmes de saturation causés par le champ magnétique micro-ondes affectent défavorablement toutes les résolutions spectrales observées, (4) une mesure ESR au maximum de fréquence de 360 GHz a été réalisée grâce à la quatrième harmonique générée par le capteur à 90 GHz et (5) les meilleures performances de bruit, normalisées par rapport à la fréquence de travail, sont obtenues avec le capteur à 10 GHz (avec une base de bruit égale à  $2 \text{ Hz/Hz}^{1/2}$  à 10 kHz de la porteuse). Le dernier dispositif se révèle être le meilleur pour des applications de résonance ferromagnétique (FMR) et permet également d'atteindre la résolution record de  $0,3 \text{ pm/Hz}^{1/2}$  lorsqu'il est utilisé comme capteur de proximité.

Par la suite, la possibilité d'utiliser des technologies intégrées basées sur des transistors à haute mobilité (HEMT) est également examinée afin de surmonter les principales limitations apparues avec les capteurs CMOS: (1) la consommation élevée (qui empêche leur utilisation à des températures plus basses de 4 K) et (2) le problème de la saturation élevée des spectres ESR due à l'amplitude des champs magnétiques micro-ondes produits par les oscillateurs LC. Dans ce contexte, deux oscillateurs HEMT LC fonctionnant à 11 GHz et 25 GHz ont été réalisés. En particulier, le système à 11 GHz atteignant le record de puissance minimale consommée ( $90 \text{ }\mu\text{W}$  à 300 K et  $4 \text{ }\mu\text{W}$  en dessous de 30 K) parmi tous les oscillateurs fonctionnant à des fréquences similaires rapportés dans la littérature. De plus, le capteur proposé atteint un champ magnétique micro-ondes minimal inférieure à  $1 \text{ }\mu\text{T}$  à 300 K et inférieure à  $0,1 \text{ }\mu\text{T}$  en dessous de 30 K, valeurs qui sont plusieurs ordres de grandeur inférieures à celles rapportées avec les capteurs CMOS. Il convient de noter que la topologie construite est aussi polyvalente

---

dans le sens où elle permet d'effectuer simultanément la détection des signaux en amplitude et en fréquence. En outre, un modèle analytique a été mis au point pour estimer la consommation électrique minimale pouvant être atteinte avec un oscillateur Colpitts LC non différentiel basé sur un unique transistor à effet de champ (FET). Dans le modèle proposé, soit l'approche Niveau 1 ou l'approche EKV sont prises en compte.

Enfin, la caractérisation en courant continu d'un seul transistor entre 300 K et 1,4 K est effectuée, incluant entre autres les courbes  $I_{DS}-V_{DS}$  ainsi que l'extraction du nombre de porteurs de charge ( $3,5 \times 10^{16} \text{ m}^{-2}$ ) combiné avec leur mobilité efficace ( $0,65 \text{ m}^2/\text{Vs}$  à 300 K,  $1,2 \text{ m}^2/\text{Vs}$  en dessous de 30 K). Le premier est calculé à partir de l'analyse des oscillations de Shubnikov-de-Haas, tandis que le second est extrait d'une série de mesures à effet Hall. De plus, la possibilité de travailler à des températures cryogéniques extrêmes avec l'oscillateur LC de type HEMT permet d'étudier la présence de sauts de fréquence de travail lorsque la tension d'alimentation varie.

Mots clés: résonance de spin électronique, ESR, spectroscopie ESR, oscillateur LC, CMOS, HEMT, micro-ondes, températures cryogéniques, faible consommation de puissance, capteur de proximité à faible bruit.



## Riassunto

I metodi basati sul fenomeno di risonanza di spin elettronico (ESR) formano un insieme di tecniche non invasive per lo studio di sistemi paramagnetici a temperature comprese tra oltre 1000 K e meno di 1 K. A temperatura ambiente, gli spettrometri disponibili in commercio raggiungono sensibilità dell'ordine di  $10^{10}$  spins/Hz<sup>1/2</sup> su volumi di alcuni  $\mu$ L. A partire dal 2008, il gruppo guidato dal Dr. G. Boero lavora su nuove tecniche di rivelazione basate sull'integrazione di sensori ESR su singoli microchip in silicio. La metodologia proposta ha permesso lo studio di campioni sulla scala dei nL e a livelli di sensibilità maggiori di circa due ordini di grandezza rispetto agli spettrometri commerciali, con performance simili a quelle dei microrisonatori.

Il principio di rivelazione del segnale si fonda su un approccio induttivo che può essere riassunto come di seguito. Un campione paramagnetico viene piazzato in prossimità dell'induttore planare (bobina) di un oscillatore LC a microonde. In presenza di un determinato campo magnetico statico, la cui direzione e il cui modulo dipendono dall'orientazione dell'induttore e dalla frequenza di lavoro, la risonanza di spin elettronico ha luogo. Essa causa una variazione della magnetizzazione del campione, la quale si traduce in una variazione di induttanza che, a sua volta, conduce sia ad un cambiamento della frequenza di lavoro dell'oscillatore (rivelazione in frequenza) che ad una variazione dell'ampiezza di oscillazione (rivelazione in ampiezza). Di conseguenza, il fenomeno ESR può essere rivelato tracciando il punto di lavoro dell'oscillatore.

Per massimizzare la sensibilità del sistema, è necessario massimizzare il segnale ESR indotto dal campione in analisi e, al contempo, minimizzare il rumore intrinseco dell'oscillatore. Il primo obiettivo è raggiunto (1) massimizzando la frequenza di lavoro, (2) adattando la dimensione della bobina al volume sensibile atteso e (3) raffreddando il sistema a temperature criogeniche (se possibile) in modo da beneficiare di una più grande magnetizzazione associata ai campioni paramagnetici. Il secondo obiettivo dipende strettamente (1) dalla natura del rumore (rumore termico o rumore  $1/f$ ), (2) dalla frequenza di lavoro, (3) dal metodo di rivelazione (in ampiezza o in frequenza), (4) dall'alimentazione dell'oscillatore, (5) dalla temperatura e (6) dalla metodologia di progetto (e.g., tipo di transistor, dimensioni, topologia, fattore di qualità, disposizione fisica dei componenti integrati e delle connessioni, resistenze parassite, accoppiamento elettrico con altri sistemi, etc.). Inoltre, anche il campo magnetico a microonde generato dall'oscillatore LC contribuisce a massimizzare la sensibilità del sistema. Per quanto riguarda la rivelazione in frequenza, l'ampiezza di tale campo deve essere il più bassa possibile in modo da non degradare la purezza spettrale del segnale ESR (saturazione).

---

Al contrario, nel caso della rivelazione in ampiezza, essa deve poter essere variata in quanto il suo valore ottimale è maggiore di zero e dipende dalla natura del campione paramagnetico. In generale, il campo magnetico a microonde dipende strettamente sia dall'ampiezza della corrente AC che circola nella bobine che dalle sue dimensioni geometriche, portando ad ulteriori vincoli a livello di progetto.

In questa tesi, viene studiata l'applicazione del metodo di rivelazione succitato nell'intervallo di frequenze compreso tra 400 MHz e 360 GHz. In primo luogo, è stata sviluppata una soluzione industriale operante tra 400 MHz e 610 MHz e supervisionata dalla Commissione svizzera per la Tecnologia e l'Innovazione (progetto CTI). In tal contesto, l'originalità del lavoro risiede nell'implementazione di uno scanner portatile per rivelazione a distanza su volumi relativamente grandi (i.e., i campioni ESR possono avere una superficie larga fino a  $4 \times 4 \text{ mm}^2$  e possono essere collocati fino a 3 mm al di sopra della bobina del sensore). In particolare, la densità spettrale di rumore in frequenza raggiunta è di  $0,15 \text{ Hz/Hz}^{1/2}$ . In aggiunta, l'apparato è utilizzato per studiare delle applicazioni ferromagnetiche e misure a campo zero.

In secondo luogo, un insieme di rivelatori ESR integrati su microchip, operanti da 10 GHz a 146 GHz e basati su tecnologie CMOS, sono caratterizzati da 300 K a 4 K (i.e., la minima temperatura raggiungibile con la potenza di raffreddamento disponibile). In tal contesto, (1) la miglior sensibilità su campioni di  $\alpha, \gamma$ -bis(difenilene)- $\beta$ -phenylallyl (BDPA)/benzene complex a temperatura ambiente è raggiunta con il sensore a 146 GHz (circa  $10^7 \text{ spins/Hz}^{1/2}$ ), (2) essa migliora di circa due ordini di grandezza a temperature criogeniche con l'oscillatore a 20 GHz, (3) i problemi di saturazione causati dal campo magnetico a microonde influenzano negativamente le risoluzioni spettrali riportate, (4) un esperimento ESR alla massima frequenza di 360 GHz è stato eseguito grazie alla quarta armonica generata dal sensore a 90 GHz e (5) le migliori prestazioni di rumore, normalizzate alla frequenza di lavoro, sono ottenute con il sensore a 10 GHz (base di rumore pari a  $2 \text{ Hz/Hz}^{1/2}$  a 10 kHz offset dalla portante). Quest'ultimo dispositivo risulta essere il migliore per applicazioni di risonanza ferromagnetica (FMR) e permette, inoltre, di raggiungere la risoluzione record di  $0,3 \text{ pm/Hz}^{1/2}$  quando viene impiegato come sensore di prossimità.

Successivamente viene vagliata la possibilità di usare tecnologie integrate basate su transistor ad alta mobilità (HEMT) in modo da superare le limitazioni principali emerse coi sensori CMOS: (1) l'elevato consumo di potenza (che impedisce il loro uso a temperature inferiori a 4 K) e (2) il problema di un'elevata saturazione degli spettri ESR a causa dell'ampiezza del campo magnetico a microonde prodotto dall'oscillatore LC. In questo contesto, si sono realizzati due oscillatori LC di tipo HEMT operanti a 11 GHz e 25 GHz. In particolare, il sistema a 11 GHz raggiunge il record di minima potenza consumata ( $90 \text{ }\mu\text{W}$  a 300 K e  $4 \text{ }\mu\text{W}$  al di sotto di 30 K) tra tutti gli oscillatori riportati in letteratura operanti a frequenze simili. Inoltre, il sensore proposto raggiunge un campo magnetico a microonde minimo inferiore a  $1 \text{ }\mu\text{T}$  a 300 K e inferiore a  $0,1 \text{ }\mu\text{T}$  al di sotto di 30 K, valori che sono ordini di grandezza al di sotto di quelli riportati coi sensori CMOS. Vale la pena notare che la topologia realizzata è versatile in quanto permette di eseguire in parallelo sia la rivelazione di segnale in ampiezza che quella in frequenza. In aggiunta, è stato sviluppato un modello analitico per stimare il minimo consumo di potenza raggiungibile per un oscillatore LC di tipo Colpitts, non differenziale e

---

basato su un singolo transistor ad effetto di campo (FET). Nel modello proposto, vengono considerati sia l'approccio di Livello 1 che l'EKV.

Infine, è fornita la caratterizzazione DC di un singolo transistor tra 300 K e 1,4 K, a partire dalle curve  $I_{DS}-V_{DS}$  fino all'estrazione del numero di portatori ( $3,5 \times 10^{16} \text{ m}^{-2}$ ) unita all'effettiva mobilità ( $0,65 \text{ m}^2/\text{Vs}$  a 300 K,  $1,2 \text{ m}^2/\text{Vs}$  al di sotto di 30 K). Il primo viene calcolato a partire dall'analisi delle oscillazioni di Shubnikov-de-Haas, mentre la seconda è estratta da una serie di misure ad effetto Hall. Inoltre, la possibilità di lavorare a temperature criogeniche estreme con l'oscillatore LC di tipo HEMT permette di studiare la presenza di salti nella frequenza di lavoro al variare della tensione di alimentazione.

Parole chiave: Risonanza di spin elettronico, ESR, spettroscopia ESR, Oscillatore LC, CMOS, HEMT, microonde, temperature criogeniche, basso consumo di potenza, basso rumore, sensore di prossimità.





# Glossary

<b>2DEG</b>	3-Dimensional Electron Gas
<b>3D</b>	3-Dimensional (space)
<b>ABS</b>	Acrylonitrile Butadiene Styrene
<b>AC</b>	Alternating Current
<b>ADC</b>	Analog to Digital Converter
<b>BDPA</b>	$\alpha,\gamma$ -bis(diphenylene)- $\beta$ -phenylallyl
<b>BPF</b>	Band Pass Filter
<b>CCCS</b>	Current Controlled Current Source
<b>CMOS</b>	Complementary Metal Oxide Semiconductor
<b>COTS</b>	Commercial Off The Shelf
<b>CTI</b>	Commission for Technology and Innovation
<b>DAC</b>	Digital to Analog Converter
<b>DAQ</b>	Digital Acquisition (board)
<b>DC</b>	Direct Current
<b>DFG</b>	German Research Foundation
<b>DLD</b>	Delay Line Discriminator
<b>DNP</b>	Dynamic Nuclear Polarization
<b>DPPH</b>	2,2-diphenyl-1-picrylhydrazyl
<b>EDA</b>	Electronic Design Automation
<b>EPR</b>	Electron Spin Resonance
<b>FET</b>	Field Effect Transistor
<b>FFT</b>	Fast Fourier Transform
<b>FM</b>	Frequency Modulation
<b>FMR</b>	Ferromagnetic Resonance
<b>FN</b>	Frequency Noise
<b>HEMT</b>	High Electron Mobility Transistor
<b>HPF</b>	High Pass Filter
<b>IC</b>	Integrated Circuit
<b>JPA</b>	Josephson Parametric Amplifier
<b>LDO</b>	Low Dropout (linear regulator)
<b>LNA</b>	Low Noise Amplifier
<b>LPF</b>	Low Pass Filter

---

<b>MOM</b>	Metal Oxide Metal
<b>MOS</b>	Metal Oxide Semiconductor
<b>MOSFET</b>	Metal Oxide Semiconductor Field Effect Transistor
<b>MR</b>	Magnetoresistance
<b>MW</b>	Microwave
<b>NMR</b>	Nuclear Magnetic resonance
<b>PCB</b>	Printed Circuit Board
<b>PFD</b>	Phase Frequency Detector
<b>PD</b>	Phase Detector
<b>PLL</b>	Phase Locked Loop
<b>PN</b>	Phase Noise
<b>RF</b>	Radio Frequency
<b>SdH</b>	Shubnikov-de-Haas
<b>SMD</b>	Surface Mount Device
<b>SMT</b>	Surface Mount Technology
<b>SNR</b>	Signal to Noise Ratio
<b>SNSF</b>	Swiss National Science Foundation
<b>SQC</b>	Superconducting Quantum Circuits
<b>TSMC</b>	Taiwan Semiconductor Manufacturing Company
<b>USB</b>	Universal Serial Bus
<b>ULTV</b>	Ultra Low Threshold Voltage
<b>VCO</b>	Voltage Controlled Oscillator
<b>YIG</b>	Yttrium Iron Garnet

# Contents

<b>List of figures</b>	<b>xvii</b>
<b>List of tables</b>	<b>xix</b>
<b>1 Introduction</b>	<b>1</b>
1.1 Electron spin resonance - basics . . . . .	1
1.2 Bloch equation . . . . .	2
1.3 LC oscillators for ESR detection . . . . .	4
1.4 Frequency and amplitude detection for an LC Colpitts oscillator . . . . .	6
1.5 Typical ESR experiments . . . . .	8
1.6 State of the art . . . . .	11
1.7 Goal of this work and thesis organization . . . . .	12
<b>2 A portable ESR scanner operating from 400 to 610 MHz</b>	<b>15</b>
2.1 Abstract . . . . .	15
2.2 Motivation . . . . .	16
2.3 Design approach . . . . .	16
2.4 Top-Level description . . . . .	17
2.5 Magnetic system . . . . .	20
2.6 Sensing oscillator . . . . .	23
2.7 Modulator . . . . .	27
2.8 Power unit . . . . .	29
2.9 Back-end system . . . . .	29
2.10 Characterization and experimental results . . . . .	31
2.11 Design variations . . . . .	33
2.12 Discussion and outlook . . . . .	34
2.13 Acknowledgement . . . . .	35
<b>3 Single-chip CMOS ESR detectors operating at 50, 92, and 146 GHz</b>	<b>37</b>
3.1 Abstract . . . . .	37
3.2 Motivation . . . . .	37
3.3 Description of the single-chip ESR detectors . . . . .	38
3.4 Electron spin resonance experiments . . . . .	42
3.5 Discussion and outlook . . . . .	47
	xv

## Contents

---

3.6	Acknowledgement . . . . .	50
<b>4</b>	<b>A single-chip ESR detector based on a single HEMT</b>	<b>51</b>
4.1	Abstract . . . . .	51
4.2	Motivation . . . . .	51
4.3	Description of the single-chip ESR detector . . . . .	52
4.4	Electron spin resonance experiments . . . . .	55
4.5	Discussion and outlook . . . . .	61
4.6	Acknowledgement . . . . .	62
4.7	Appendix. Comparison with single-chip ESR detectors based on CMOS . . . . .	62
4.8	Appendix. Comparison with other inductive approaches for high spin sensitivity on nanoliter and subnanoliter samples . . . . .	64
<b>5</b>	<b>A low power microwave HEMT LC oscillator operating down to 1.4 K</b>	<b>69</b>
5.1	Abstract . . . . .	69
5.2	Motivation . . . . .	69
5.3	Description of the realized devices and of the measurements set-up . . . . .	70
5.4	HEMT transistor characterization and parameters extraction . . . . .	73
5.5	HEMT LC Colpitts oscillator characterization . . . . .	76
5.6	Discussion and outlook . . . . .	78
5.7	Acknowledgement . . . . .	79
5.8	Appendix. Proposal for a HEMT LC Colpitts oscillator with further reduced power consumption . . . . .	79
<b>6</b>	<b>Microwave inductive proximity sensors with sub-pm resolution</b>	<b>87</b>
6.1	Abstract . . . . .	87
6.2	Motivation . . . . .	87
6.3	Description of the realized inductive proximity sensors . . . . .	89
6.4	Experimental results and characterization of the sensors . . . . .	89
6.5	Comparison with previously reported proximity sensors . . . . .	92
6.6	Discussion and outlook . . . . .	93
6.7	Acknowledgments . . . . .	94
6.8	Appendix. Computation of sensitivity and resolution . . . . .	94
<b>7</b>	<b>Other designs</b>	<b>99</b>
7.1	Single-chip CMOS ESR detectors operating at 20 GHz (fixed-freq. and VCO) . . . . .	99
7.2	Single-chip HEMT ESR detector operating at 25 GHz . . . . .	101
7.3	Single-chip CMOS ESR detector for DNP . . . . .	103
<b>8</b>	<b>Conclusions and Outlook</b>	<b>105</b>
<b>9</b>	<b>Acknowledgement</b>	<b>107</b>
	<b>Bibliography</b>	<b>109</b>

# List of Figures

1.1	LC Colpitts oscillator . . . . .	5
1.2	EPFL-LMIS1 setup for ESR experiments . . . . .	9
2.1	Picture of the portable scanner (prototype) - Front-end . . . . .	18
2.2	Top-Level block diagram of the portable scanner . . . . .	19
2.3	Representation of the generated magnetic fields and layout of the PCBs realized for the portable scanner . . . . .	20
2.4	Picture of the portable scanner (prototype) - Front-view . . . . .	21
2.5	Schematics of the portable scanner . . . . .	22
2.6	Picture of the portable scanner (prototype) - Bottom-view . . . . .	23
2.7	PLL schematic for the portable scanner . . . . .	26
2.8	Picture of the portable scanner (prototype) - Top-view . . . . .	28
2.9	Characterization of the VCO operating from 400 MHz to 610 MHz . . . . .	32
2.10	Measurements performed with the VCO operating from 400 MHz to 610 MHz . . . . .	32
2.11	Close geometry detector operating at 610 MHz . . . . .	33
3.1	Schematics and pictures of the CMOS ESR detectors . . . . .	39
3.2	Set-up and noise spectral density of the three CMOS single-chip ESR detectors . . . . .	41
3.3	ESR experiments performed with the 50 GHz CMOS single-chip detector . . . . .	43
3.4	ESR experiments performed with the 92 GHz CMOS single-chip detector . . . . .	44
3.5	ESR experiments performed with the 146 GHz CMOS single-chip detector . . . . .	45
3.6	ESR experiments performed with the 92 GHz CMOS single-chip detector at higher harmonics . . . . .	46
4.1	Schematics, picture, and key-features of the realized HEMT single-chip ESR detector . . . . .	54
4.2	ESR experiments performed with the 11 GHz HEMT single-chip detector . . . . .	56
4.3	ESR experiments performed with the 11 GHz HEMT single-chip detector with (a, c, g) the oscillation frequency detection and (b, d, h) the oscillation amplitude detection . . . . .	57
4.4	Investigation of the ESR signal amplitude as a function of the sample position within the detection coil of the 11.2 GHz HEMT single-chip detector . . . . .	60

## List of Figures

---

4.5	<b>Schematic, picture, and measurements of a single-chip ESR detector based on a differential Colpitts topology implemented using a CMOS technology (TSMC 180 nm, MS/RF)</b> . . . . .	63
5.1	<b>Schematics, pictures, and key-features of the realized HEMT structures</b> . . .	72
5.2	<b>DC characterization of the standalone HEMT transistor</b> . . . . .	73
5.3	<b>Magnetoresistance, mobility, and Shubnikov-de-Haas oscillations of the standalone HEMT transistor</b> . . . . .	74
5.4	<b>Equivalent circuit to model the geometrical magnetoresistance</b> . . . . .	76
5.5	<b>Characterization of the HEMT LC Colpitts oscillator at 1.4 K</b> . . . . .	77
5.6	<b>Schematics of HEMT LC Colpitts oscillators</b> . . . . .	79
6.1	<b>The 500 MHz inductive proximity sensor: schematic and characteristics</b> . . .	88
6.2	<b>The 10 GHz inductive proximity sensor: schematic and characteristics</b> . . . .	90
6.3	<b>Experimental set-up for DC characterization of the inductive proximity sensors</b>	91
6.4	<b>Experimental characterization of the 500 MHz and the 10 GHz proximity sensors</b> . . . . .	92
7.1	<b>Single-chip CMOS ESR detectors operating at 20 GHz (fixed frequency and VCO)</b> . . . . .	100
7.2	<b>25 GHz HEMT single-chip ESR detectors</b> . . . . .	102
7.3	<b>28 GHz CMOS ESR detector for DNP</b> . . . . .	103

# List of Tables

2.1	Technical resume table of the scanner operating from 400 MHz to 610 MHz - Magnetic system . . . . .	21
2.2	Technical resume table of the scanner operating from 400 MHz to 610 MHz - Sensor . . . . .	24
2.3	Technical resume table of the scanner operating from 400 MHz to 610 MHz - Field modulator . . . . .	27
2.4	Technical resume table of the scanner operating from 400 MHz to 610 MHz - Power unit . . . . .	29
2.5	Technical resume table of the scanner operating from 400 MHz to 610 MHz - Back-end system . . . . .	31
3.1	Key-features of the three CMOS single-chip ESR detectors . . . . .	40
5.1	Oscillator start-up condition . . . . .	83





# 1 Introduction

## 1.1 Electron spin resonance - basics

Isolated electrons intrinsically possess nonzero spin  $\underline{S}$ . The associated intrinsic angular momentum is  $L = \hbar\sqrt{S(S+1)}$ , where  $\hbar = h/2\pi$  is the so-called reduced Planck constant,  $S$  is the spin quantum number, and  $\hbar\sqrt{S(S+1)}$  is the norm of  $\underline{S}$ . Moreover, the intrinsic magnetic dipole moment is  $\underline{\mu} = \gamma\underline{L}$ , where  $\gamma$  is the gyromagnetic ratio of the spin system and results approximately equal to  $2\pi \times 28$  GHz/T for the uncoupled electron.

In the classical interpretation, a magnetic dipole moment  $\underline{\mu}$  placed in a magnetic field  $\underline{B}$  (generally drawn along  $\hat{z}$ ) experiences a torque  $\underline{\tau} = \underline{\mu} \times \underline{B} = d\underline{L}/dt$ , so that  $d\underline{\mu}/dt = \gamma\underline{\mu} \times \underline{B}$ . For a sample with a density of magnetic dipole moments  $N$  (e.g., free radicals) the macroscopic magnetization is  $\underline{M} = N \sum_i \underline{\mu}_i$ , and hence the equation of motion for  $\underline{M}$  is

$$\frac{d\underline{M}}{dt} = \gamma\underline{M} \times \underline{B} \quad (1.1)$$

In case of a static magnetic field  $\underline{B} = \underline{B}_0$ , the solution of Eq. 1.1 gives a precession motion of  $\underline{M}$  about  $\underline{B}_0$  at the so-called Larmor frequency  $\omega_0 = \gamma B_0$ . The angle  $\theta$  formed by  $\underline{M}$  and  $\underline{B}_0$  depends on the boundary conditions and it is normally zero since the two vectors are naturally aligned (whereas  $\theta$  is generally not null for  $\underline{\mu}$ ).

If we add a second magnetic field  $\underline{B}_1$  orthogonal to  $\underline{B}_0$  (i.e., lying on the  $xy$ -plane) and rotating about it at the angular frequency  $\omega$  (i.e., a circularly polarized field which is generally in the radiofrequency range),  $\underline{M}$  tilts and  $\theta$  grows toward  $\pi/2$  at the angular speed  $\omega_1 = \gamma B_1$  as  $\omega$  approaches to  $\omega_0$ . Therefore, a very small rotating magnetic field  $\underline{B}_1$  can macroscopically act on the precession motion of the magnetization  $\underline{M}$ . That is a magnetic resonance phenomenon. When it involves the intrinsic spin of the electrons, it is called Electron Spin Resonance (ESR), whereas it is named Nuclear Magnetic Resonance (NMR) when it concerns the intrinsic spin

---

The first two sections of this chapter are based on the content of Dr. G. Boero's PhD thesis, entitled "*Integrated NMR probe for magnetometry*" [1].

of the nuclei. It is worthy to note that in all the applications shown in this thesis, the rotating radiofrequency field  $B_1$  is generated through a linearly polarized magnetic field ( $B_{RF}$ ), which is composed of two counter-rotating circularly polarized fields having the same amplitude. Consequently, if  $\underline{B}_{RF} = A \cos(\omega t) \hat{x}$ ,  $B_1$  has amplitude  $A/2$  and rotates on the plane ( $xy$ ) with angular frequency  $|\omega|$ .

Such a classical interpretation is not sufficient to explain more complex dynamics (e.g., the nuclear hyperfine interaction), so a quantum mechanical description is also required. In particular, according to the Zeeman effect, the static magnetic field  $\underline{B}_0$  creates two distinct energy levels for the intrinsic magnetic dipole moment associated to the electron. Those two states are labeled according to the projection of the electron spin ( $S = \pm 1/2$ ) on  $\underline{B}_0$  and the energy of each level is

$$E_{\pm 1/2} = \pm \frac{1}{2} g \mu_B B_0 \quad (1.2)$$

where  $\mu_B$  is the Bohr magneton and  $g$  is the  $g$ -factor (approximately equal to 2 for the free electron). The electron will have the lowest energy state when its magnetic dipole moment is parallel to  $\underline{B}_0$  and, conversely, it will have the highest energy state when aligned against  $\underline{B}_0$ . For any given magnetic field, the energy gap between the two states is  $\Delta E = g \mu_B B_0$  and that is also the necessary energy required by the electron to change its state and reach the resonance condition. This is accomplished by irradiating the sample with microwaves at a suitable frequency, since the corresponding energy provided to the system is  $E = \hbar \omega$ .

In many molecules, the interaction between electrons and nuclei (with the corresponding nuclear magnetic moment) leads to spectra composed of multiple lines. Indeed, in presence of a static magnetic field  $\underline{B}_0$ , the aforementioned interaction further splits the two energy levels of the electron (hyperfine splitting), creating multiple Zeeman transitions with different energy gaps, and then multiple lines in the spectrum. For instance, the interaction of an electron ( $S = 1/2$ ) with a nucleus having spin  $I = 1/2$  (e.g., a proton) will yield four energy levels, and then two possible transitions. In general, the interaction with many nuclei may lead to very complex patterns which are, however, always centered about the main Zeeman splitting (i.e., at  $g \cong 2$ ). Remarkably, although the hyperfine splitting may generate several energy levels, many transitions are forbidden due to quantum selection rules.

## 1.2 Bloch equation

In general, given a sample containing a density of magnetic dipole moments  $N$ , the static magnetization is  $\underline{M}_0 = (\chi_0 / \mu_0) \underline{B}_0$ , where  $\chi_0 = \mu_0 N \mu^2 / 3 k_B T$  is the static magnetic susceptibility in the Curie law approximation,  $T$  is the sample temperature,  $\mu = g_J \mu_B \sqrt{J(J+1)}$  is the total magnetic moment of the spin system,  $g_J$  is the Landé  $g$ -factor, and  $J$  is the total angular momentum quantum number. If the contribution to the total magnetic moment of the orbital angular

## 1.2. Bloch equation

momentum is negligible, the total magnetic moment of the spin system under investigation can be written similarly to the case of the isolated electron as  $\mu = g\mu_B\sqrt{S(S+1)} = \gamma\hbar\sqrt{S(S+1)}$ , where  $g$ ,  $S$ , and  $\gamma = (ge/2m_e)$  are the  $g$ -factor, the spin quantum number, and the gyromagnetic ratio of the spin system, respectively. For  $g \cong 2$  and  $S = 1/2$ , we obtain  $\gamma \cong 2\pi \times 28 \text{ GHz/T}$  and  $\chi_0 \cong \mu_0 N \gamma^2 \hbar^2 / 4k_B T$  [2].

Whenever the magnetization  $\underline{M}$  of a sample placed in a static magnetic field  $\underline{B}_0$  is not equal to  $\underline{M}_0$ , the various interactions force  $\underline{M}$  to reach the equilibrium magnetization  $\underline{M}_0$  at an exponential rate described by two time constants called relaxation times. In particular,  $T_1$  is the longitudinal or spin-lattice relaxation time, whereas  $T_2$  is the transverse or spin-spin relaxation time. Usually  $T_1 \cong T_2$  in liquids whereas  $T_1 \gg T_2$  in solids.

In 1946, Felix Bloch modified Eq. 1.1 by introducing the relaxation time constants  $T_1$  and  $T_2$

$$\frac{d\underline{M}}{dt} = \gamma \underline{M} \times \underline{B} - \frac{M_x \hat{x} + M_y \hat{y}}{T_2} - \frac{M_z - M_0}{T_1} \hat{z} \quad (1.3)$$

where  $\underline{B}$  is the overall magnetic field (i.e., the sum of the static magnetic field  $\underline{B}_0 = B_0 \hat{z}$  and the rotating radiofrequency magnetic field  $\underline{B}_1 = B_1 \cos(\omega t) \hat{x}$ ). In order to express the steady state solution (i.e., at the time  $t \gg T_1, T_2$  after any variation of the external perturbation) of the Bloch equation in a simple form, one can introduce a new frame  $(x', y', z' \equiv z)$ , rotating at  $\omega$  about  $B_0 \hat{z}$ , with  $\hat{x}'$  along the direction of the rotating magnetic field  $\underline{B}_1$ , and  $\hat{y}'$  orthogonal to both  $\underline{B}_0$  and  $\underline{B}_1$ . The result is

$$\begin{cases} M_{x'} = \frac{(\omega - \omega_0) \gamma B_1 T_2^2}{1 + T_2^2 (\omega - \omega_0)^2 + \gamma^2 B_1^2 T_1 T_2} M_0 \\ M_{y'} = \frac{\gamma B_1 T_2}{1 + T_2^2 (\omega - \omega_0)^2 + \gamma^2 B_1^2 T_1 T_2} M_0 \\ M_{z'} = \frac{1 + T_2^2 (\omega - \omega_0)^2}{1 + T_2^2 (\omega - \omega_0)^2 + \gamma^2 B_1^2 T_1 T_2} M_0 \end{cases} \quad (1.4)$$

Recalling that  $M = (\chi / \mu_0) B$ , a complex susceptibility can be defined as  $\chi = \chi' - j\chi''$ , where  $\chi'$  and  $\chi''$  respectively relate  $M_{x'}$  and  $M_{y'}$  to  $2B_1$ , resulting in

$$\begin{aligned} \chi' &= -\frac{1}{2} \frac{(\omega - \omega_0) T_2^2}{1 + T_2^2 (\omega - \omega_0)^2 + \gamma^2 B_1^2 T_1 T_2} \omega_0 \chi_0 \\ \chi'' &= \frac{1}{2} \frac{T_2}{1 + T_2^2 (\omega - \omega_0)^2 + \gamma^2 B_1^2 T_1 T_2} \omega_0 \chi_0 \end{aligned} \quad (1.5)$$

where  $\gamma^2 B_1^2 T_1 T_2$  is the saturation term and must be much smaller than 1 to be negligible.

### 1.3 LC oscillators for ESR detection

The impedance of a coil filled with a material having complex susceptibility  $\chi$  is [3]

$$Z_\chi = j\omega L(1 + \eta\chi) + R = j\omega L_\chi + R_\chi \quad (1.6)$$

where  $L_\chi = L + L\eta\chi'$  and  $R_\chi = R + \omega L\eta\chi''$ .  $L$  and  $R$  are the inductance and the resistance of the coil without the sample, respectively. For  $\omega \cong \omega_0$ , the presence of the sample modifies the reactive as well as the resistive part of the coil impedance. The filling factor  $\eta$  is given by

$$\eta = \frac{\int_{V_s} |B_{u,xy}|^2 dV}{\int_V |B_u|^2 dV} = \frac{\int_{V_s} |B_{u,xy}|^2 dV}{\mu_0 L} \quad (1.7)$$

where  $B_{u,xy}$  is the field produced by a unitary current in the coil (in T/A) along the direction perpendicular to the static magnetic field  $B_0$ ,  $V_s$  is the volume occupied by the sample,  $V$  is the entire space where  $B_u$  is not zero (Ref. [4]). In general, the magnetic field produced by planar coils is highly inhomogeneous so their filling factor should be computed numerically using, e.g., the Biot-Savart law [5, 6]. However, numerical simulations performed with Comsol Multiphysics<sup>®</sup> show that for samples placed in close proximity (less than 10% of the coil diameter) to the coil surface, having a thickness smaller than the coil radius and a width smaller than the coil diameter  $d$ , the filling factor is, within an error of about  $\pm 25\%$ , given by

$$\eta \cong \frac{|B_u(0,0,0)|^2}{\mu_0 L} V_s \cong \frac{V_s}{d^3} \quad (1.8)$$

where  $B_u(0,0,0) = \frac{N}{\mu_0} d$  is the unitary field at the center of the planar coil,  $d$  is the coil diameter, and  $N$  is the number of turns. Moreover, recalling that the inductance of a circular loop having negligible thickness is  $\pi\mu_0 d/4$ , for a small sample placed at a given elevation from the coil center ( $z$ ), the filling factor is

$$\eta \cong \frac{(\frac{d}{2})^3}{2\pi(z^2 + (\frac{d}{2})^2)^3} \quad (1.9)$$

so the optimal diameter to maximize  $\eta$  is  $d = 2z$ . Since both the inductance and  $B_u^2$  are pro-

portional to  $N^2$ , such a result is independent of the number of turns.

LC oscillators are composed of a resonator (LC tank) electrically connected to an energy restoring system (one or more transistors connected to a power supply). The former sets the operating frequency whereas the latter absorbs energy from the outside in order to compensate for the energy losses of the system and therefore sustain stable oscillations, according to the Barkhausen stability criterion. If an ensemble of electron spin is placed in close proximity to the inductor of the LC tank (e.g., on the top), a natural inductive coupling arises between the two, as described by Eq. 1.6. Consequently, since the coil impedance intrinsically depends on the susceptibility of the sample under inspection, both the oscillation frequency and the oscillation amplitude are affected by the resonance condition, making LC oscillators suitable devices for ESR detection.

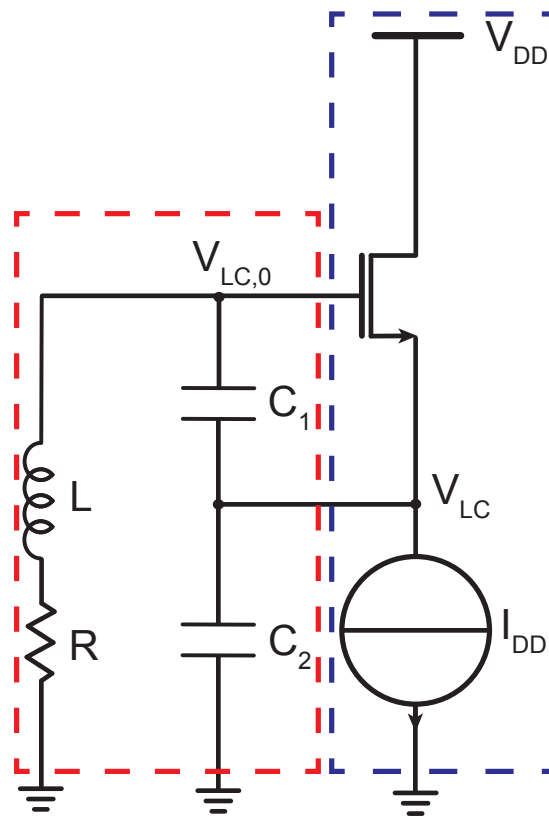


**Figure 1.1 – LC Colpitts oscillator.** The red dashed line highlights the LC resonator (i.e., the LC tank with a coil series resistance which models the dominant contribution of losses), whereas the blue dashed line highlights the energy restoring system (i.e., a single transistor connected to the power supply). When the oscillator is inductively coupled to an ensemble of electron spins,  $L$  becomes  $L_\chi$  and  $R$  becomes  $R_\chi$ .

In all the oscillators described in this thesis, the inductors are planar coils and generate the radiofrequency field  $\underline{B}_{RF}$  along their vertical axis, so particular care is taken in their positioning in order to maximize the efficiency of detection. Indeed, the plane of the rotating  $\underline{B}_1$  (which contains  $\underline{B}_{RF}$ ) must be orthogonal to  $\underline{B}_0$ , so the plane of the coil must be parallel to  $\underline{B}_0$ .

## 1.4 Frequency and amplitude detection for an LC Colpitts oscillator

The oscillation frequency of the Colpitts oscillator shown in Fig. 1.1, inductively coupled with an ensemble of electron spins, is given by [7–11]:

$$\omega_{LC\chi} \cong \frac{1}{\sqrt{L_\chi C}} \cong \frac{\omega_{LC}}{\sqrt{1 + \eta\chi'}} \quad (1.10)$$

where  $\omega_{LC} \cong 1/\sqrt{LC}$  is the unperturbed oscillation frequency and  $C \cong C_1 C_2 / (C_1 + C_2)$  is the effective capacitance. In condition of negligible saturation (i.e., for  $\gamma^2 B_1^2 T_1 T_2 \ll 1$ ) and for  $\eta\chi' \ll 1$ , the variation of the oscillator frequency is given by

$$\Delta\omega_{LC} \cong \frac{1}{2}\omega_{LC}\eta\chi' \quad (1.11)$$

Hence, at the resonance, the peak-to-peak variation of the oscillator frequency is

$$\Delta\omega_{LC,pp} \cong \frac{1}{4}\omega_{LC}^2 T_2 \eta \chi_0 \quad (1.12)$$

The oscillation amplitude at the output of the oscillator, is given by [11]:

$$V_{LC\chi} \cong \frac{5}{6} \frac{I_{DD}}{R_\chi \omega_{LC\chi}^2 C_2^2} \cong \frac{2dB_1}{\mu_0} \frac{R\omega_{LC}}{R_\chi \omega_{LC\chi}^2 C_2} \quad (1.13)$$

where  $d$  is the coil diameter. In condition of negligible saturation (i.e., for  $\gamma^2 B_1^2 T_1 T_2 \ll 1$ ) and for  $\eta\chi'' \ll 1$ , the variation of the oscillator amplitude due to the interaction with the spin ensemble is given by

$$\Delta V_{LC} \cong \frac{2dB_1}{\mu_0 C_2} \frac{L\eta\chi''}{R} \quad (1.14)$$

#### 1.4. Frequency and amplitude detection for an LC Colpitts oscillator

---

hence, at the resonance, the variation of the oscillator amplitude is

$$\Delta V_{LC,\max} \cong \frac{dB_1}{\mu_0 C_2 R} \omega_{LC} L \eta T_2 \chi_0 \quad (1.15)$$

This can be written in the following form:

$$\Delta V_{LC,\max} \cong \frac{dB_1}{\mu_0} \frac{C_1}{C_1 + C_2} Q \omega_{LC}^2 L \eta T_2 \chi_0 \quad (1.16)$$

where  $Q = \omega_{LC} L / R$  is the quality factor of the coil, which gives the intrinsic voltage gain of the resonator. The term  $C_1 / (C_1 + C_2)$  is the signal attenuation between the transistor gate node and the output node (i.e.,  $V_{LC} / V_{LC,0}$ ). Hence, the total signal gain from the coil to the output is  $Q C_1 / (C_1 + C_2)$ .

As shown in Eqs. 1.12 and 1.16, in conditions of negligible saturation, both maximizing the working frequency and the filling factor (i.e., matching the coil size with the dimensions of the sample to be inspected) are two necessary conditions to boost the ESR signals. Moreover, the oscillator frequency variation results independent of the microwave field  $B_1$  and proportional to  $\chi'$  (giving the typical shape of a "dispersion signal" to the spectrum), whereas the oscillator amplitude variation is proportional to  $B_1 \chi''$  (giving the typical shape of an "absorption signal" to the spectrum). Since  $\chi'$  and  $\chi''$  have the same denominator, minimizing the saturation term ( $\gamma^2 B_1^2 T_1 T_2 \cong 1$ ) is also crucial to maximize the ESR signals.

If we assume that the oscillator frequency noise and the oscillator amplitude noise are entirely due to the thermal noise of the coil resistance (i.e., we neglect all the other noise sources, in particular the  $1/f$  noise and the thermal noise of the transistors) we have (Ref. [12]):

$$\begin{aligned} \sqrt{S_f} &\cong \sqrt{k_B T R} (f_{LC} / V_{LC,0}) \\ \sqrt{S_V} &\cong (Q C_1 / (C_1 + C_2)) \sqrt{4 k_B T R} \end{aligned} \quad (1.17)$$

Hence, the signal-to-noise ratio for the frequency and the amplitude detection are given by

$$\begin{aligned} SNR_f &\equiv \frac{\Delta \omega_{LC,pp}}{2\pi \sqrt{S_f}} \cong \frac{1}{4} \omega_{LC} T_2 \eta \chi_0 V_{LC,0} \frac{1}{\sqrt{k_B T R}} \\ SNR_V &\equiv \frac{\Delta V_{LC,\max}}{\sqrt{S_V}} \cong \frac{dB_1 \omega_{LC}^2 L T_2 \eta \chi_0}{\mu_0} \frac{1}{\sqrt{4 k_B T R}} \end{aligned} \quad (1.18)$$

Since  $B_1$  is approximately given by

$$B_1 \cong \frac{1}{2} \frac{V_{LC,0}}{\omega_{LC} L} \frac{\mu_0}{d} \quad (1.19)$$

we obtain that  $SNR_f/SNR_V \cong 1$ . Consequently, under the assumption that the dominant noise contribution is the thermal noise of the coil resistance, the two detection methods allow to obtain the same signal-to-noise ratio (and, hence, the same spin sensitivity). The largest signal-to-noise ratio is obtained, in both detection methods, for  $B_1$  such that  $\gamma^2 B_1^2 T_1 T_2 \cong 1$ . For the oscillation frequency detection, such condition minimizes the noise ( $V_{LC,0}$  is linearly proportional to  $B_1$ ), without significantly decreasing the oscillation frequency variation. For the oscillation amplitude detection, such condition maximizes the oscillation amplitude variation, with no increase of the amplitude thermal noise which is, in first approximation, independent of  $B_1$ . The optimal conditions are significantly different in presence of  $1/f$  noise, in particular when the  $1/f$  noise increases with the oscillation amplitude. This dependence would determine an optimal condition for the frequency detection which is close to the start-up, whereas for the amplitude detection the optimal condition would be obtained for  $B_1$  values below the saturation condition  $\gamma^2 B_1^2 T_1 T_2 \cong 1$ .

The  $3\text{-}\sigma$  spin sensitivity (given in spins/Hz<sup>1/2</sup>) of an ESR detector can be defined as  $N_{\min} = 3N_S/SNR$ , where  $N_S$  is the number of spins in the sample, and  $SNR$  is the signal-to-noise ratio. For the frequency detection, the signal is given in Hz and the noise is expressed as its spectral density in Hz/Hz<sup>1/2</sup>, whereas for the amplitude detection, the signal is given in V and the noise is expressed as its spectral density in V/Hz<sup>1/2</sup>.

It is worthy to note that, in the field of oscillators, engineers normally refer to phase noise ( $PN$ ) rather than frequency noise ( $FN$ ).  $PN$  is expressed in dBc/Hz whereas  $FN$  is expressed in Hz/Hz<sup>1/2</sup>, and they are both defined at a given frequency offset ( $f_m$ ) from the carrier. However, in order to calculate the  $SNR$ , one must convert  $PN$  to  $FN$  according to the following equation.

$$FN = f_m \sqrt{10 \frac{PN}{10}} \quad (1.20)$$

## 1.5 Typical ESR experiments

According to the nature of the ESR detector, it is possible to inspect the spectrum for magnetic resonance signals in two different ways. In particular, one can fix the working frequency of the oscillator and sweep the magnitude of the static magnetic field (field sweep) or viceversa (frequency sweep). The two solutions are equivalent for several experiments and the suitable approach is normally chosen as a consequence of the system constraints. For instance, if the magnetic field is fixed (e.g., generated by a set of permanent magnets), one is forced to sweep the frequency of the oscillator by using variable capacitors (varactors) or exploiting the



## 1.5. Typical ESR experiments

intrinsic pullability of the oscillator itself (i.e., sweeping the bias supply). Conversely, if the oscillator has to work at a certain fixed frequency (e.g., for noise minimization or to reduce the saturation phenomenon), one is forced to sweep the static magnetic field. As a result, a typical ESR experiment produces a 2D-plot, where the x-axis refers to the swept variable (equivalently expressed in terms of either frequency or field, according to  $\omega = \gamma B$ ) and the y-axis refers to the magnitude of any ESR signal (either a voltage or a frequency variation according to the detection method, as explained in Sec. 1.4). The analysis of the spectrum may give useful information for spectroscopy, such as the specific position of the peaks, the number of lines, the overall shape, the intensity, and the linewidth. Moreover, if the  $g$ -factor of the sample under investigation is known (e.g., DPPH and BDPA show a single peak with  $g$ -factor approximately equal to 2), one can evaluate the working frequency of the oscillator from the position of the ESR signal ( $\omega_0 = \gamma B_0$ , where  $\gamma \cong 2\pi \times 28 \text{ GHz/T}$ ).

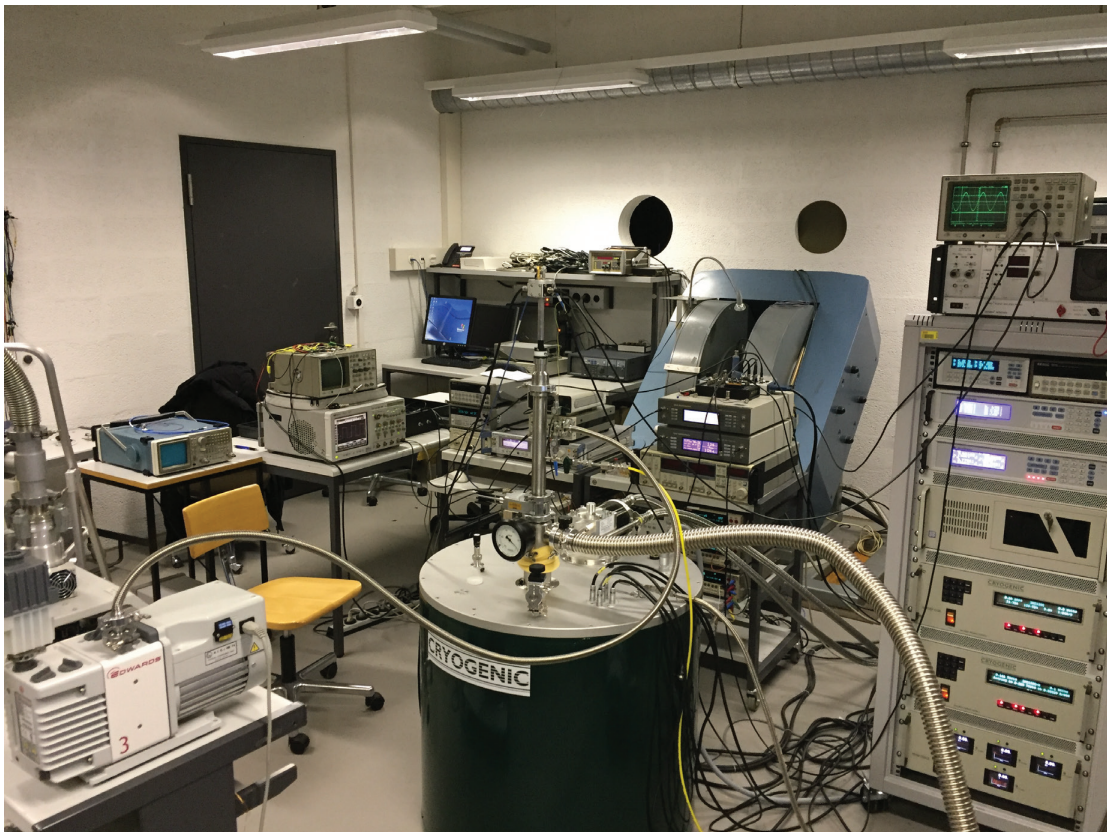


**Figure 1.2 – EPFL-LMIS1 setup for ESR experiments.** In the middle of the picture there is the programmable cryogenic magnet (0.3-300 K, 0-9.4 T) with a probe located in the insertion tube. On the right, there is a vertical rack with the temperature controller and the power unit to set the static field  $B_0$ . On the rack, there is the AC current driver to set the modulation field  $B_m$ . On the left of the picture, there is a set of pumps/turbo-pumps to vacuum the cryogenic chamber. Behind the magnet, there are four rolling tables respectively carrying (from the left) a spectrum analyzer and two oscilloscopes to monitor the output signals, a delay-line discriminator to perform the frequency-to-voltage conversion, a set of RF amplifiers, mixers and frequency dividers to handle the AC signal at the very output of the ESR detector, a reference clock in the GHz range, the DC power sources to supply the ESR detector, and a set of lock-ins to perform the synchronous detection up to the MHz range.

In order to extract the ESR signals through the presented detectors, different solutions are

adopted according to whether we use either the amplitude or the frequency detection method. Indeed, the former only requires a simple peak-detector (e.g., a diode) to monitor the voltage variation caused by the magnetic resonance condition, whereas the latter needs a suitable frequency-to-voltage converter for carrier tracking, such as a phase-locked-loop (PLL) or a delay-line-discriminator (DLD). Nevertheless, the frequency detection method is definitely more robust against both signal attenuation and radiofrequency cross-talk. Consequently, despite its higher degree of complexity, such an approach is always preferable.

In Sec. 1.4, the only noise contribution considered was the thermal noise generated by the coil resistance. However, the presence of transistors in the overall architecture leads to the introduction of additional frequency-dependent noise. That is the so-called  $1/f$  noise (a.k.a., flicker noise) and its contribution is dominant at low frequencies, where it results much larger than the previously introduced thermal noise (Sec. 1.4). In LC oscillators, the flicker noise is intrinsically up-converted to the oscillation frequency (carrier), and it decreases as the frequency offset ( $f_m$ ) from the carrier goes up. The frequency offset at which the  $1/f$  noise magnitude becomes negligible with respect to the thermal noise floor is called corner frequency ( $f_c$ ). In this context, performing ESR experiments by simply tracking the carrier of the oscillator is not convenient since the  $1/f$  noise is huge at  $f_m = 0$  (DC measurement). Instead, modulating the working point at  $f_m = f_c$  (AC measurement) would be beneficial in terms of  $SNR$  as the flicker noise is negligible there. That is the reason why in typical ESR experiments we use the so-called synchronous detection (a.k.a., lock-in detection). In particular, a modulating coil driven by an external current source (operating at frequency  $f_m$  in the kHz range) is added to the detection chain in order to create an AC magnetic field  $B_m$  parallel to  $B_0$  (field modulation). Then, in order to demodulate the signal, a lock-in amplifier must be added to the chain (Fig. 1.2), at the output of the diode (for amplitude detection) or at the output of the PLL/DLD (for frequency detection). Such a block needs a reference signal at  $f_m$  and performs the IQ demodulation of the ESR signal (from  $f_m$  to baseband), leading to two output signals (I and Q) which can be easily acquired by means of a digital acquisition board. When we perform the synchronous detection, the acquired signals are always the first derivative of the original ones (both absorption and dispersion). Additionally, the higher the amplitude of  $B_m$ , the higher the  $SNR$  but the modulation field should always be lower than the linewidth of interest (at least a factor of two) in order to neither broaden the ESR spectrum nor to reduce the spectral resolution for narrow signatures. It is worthy to note that if  $\underline{B}_m$  is not orthogonal to  $\underline{B}_1$ , the modulation field would couple some magnetic flux across the sensing coil, leading to a spurious frequency modulation of the carrier. The latter would generate a spurious signal at the output of the detection chain (a.k.a., leakage). In this context, in order for any ESR signal to be detectable, we must ensure that the leakage becomes negligible through a proper alignment of the modulation coil.

Regarding the sample handling, since all the paramagnetic substances addressed in this thesis are solid powders or crystals, they are always placed on the top of the planar coil by using a toothpick sharpened with a metallic cutter. The samples adhere to the chip surface by van der Waals forces either without any adhesive or with the help of a small drop ( $< 100$  pL) of high vacuum grease (Dow Corning). Also, in order to evaluate the expected theoretical ESR signal,

the dimensions of the samples are measured by means of an optical microscope, with an error in the estimation of the volume of less than a factor of two.

Finally, it is worthy to notice that noise always adds up in quadrature whereas deterministic signals (e.g., ESR signals) add up linearly. Hence, performing multiple sweeps (averaging) would always lead to a better  $SNR$ , as from Eq. 1.21.

$$SNR_{N,av} = \frac{\frac{1}{N} \sum_{i=1}^N s}{\frac{1}{N} \sqrt{\sum_{i=1}^N n^2}} = \frac{\frac{1}{N} N \cdot s}{\frac{1}{N} \sqrt{N \cdot n^2}} = \frac{N}{\sqrt{N}} SNR = \sqrt{N} \cdot SNR \quad (1.21)$$

Since each sweep lasts for a certain time, the overall duration of the measurement is proportional to the number of scans ( $N$ ). Then, for an infinite time any sensor would in principle produce an infinite  $SNR$ . However, all electrical systems naturally drift in time so, besides the intuitive fact that we cannot wait an infinite amount of time to get a measurement, when the required timeframe becomes too long, the frequency drift of the oscillator would naturally cancel out the useful information. Moreover, there are situations in which the chemical evolution of the sample (e.g., denaturation) needs the measurement to be sufficiently fast. That is the reason why time matters and, in this thesis, the spin sensitivity related to each system is always provided for a single scan.

## 1.6 State of the art

Methods based on the electron spin resonance (ESR) phenomenon are powerful spectroscopic tools, used in physics, chemistry, material science, biology and medicine, to investigate the structure, the dynamics, and the spatial distribution of paramagnetic species (i.e., substances with unpaired electrons) in a wide range of frequencies (typically from 100 MHz to 1 THz) and temperatures (typically from 10 mK to 1000 K) [13–15]. At frequencies above 1 GHz, the measurements are usually performed using either relatively large cavities (mL to  $\mu$ L sensitive volumes) or miniaturized conducting [7–10, 16–25] and superconducting [26–34] resonators ( $\mu$ L to sub-pL sensitive volumes). Miniaturized resonators are used in order to maximize the signal-to-noise ratio in experiments with small samples. Inductive methods based on microresonators have sensitivities at the level of  $10^7$  to  $10^{11}$  spins/Hz<sup>1/2</sup> at room temperature [4, 7, 9, 20, 24] and of  $10^2$  to  $10^6$  spins/Hz<sup>1/2</sup> at low temperature [9, 23, 28, 29, 32–34], mainly depending on the sample relaxation times, the sensitive volume of the microresonator, the operating frequency, and the adopted normalization criteria (App. 4.8). Non-inductive techniques can achieve single electron spin sensitivity [35–37] but are generally considered as less versatile than those based on the more conventional inductive approach [23, 29, 38].

Since 2008, the group of Dr. G. Boero has been working on the integration of single-chip inductive ESR detectors (Refs. [7–10]), fabricated using complementary metal oxide semiconductor

(CMOS) technologies, and operating at 8-28 GHz in the temperature range from 300 K down to 4 K. As described in Secs. 1.3-1.4, the ESR phenomenon is generally detected as a variation of the working frequency of an integrated LC oscillator, due to an effective variation of its coil impedance caused by the resonant complex susceptibility of the sample. The main advantages of the single-chip approach are:

- the low cost scalability of the final detectors
- the small size of the overall sensing system (which is important, e.g., for compact arrays of detectors in the same magnet)
- the elimination of bulky and expensive microwave connections
- the possibility to embody detectors in human cavities (e.g., for local oxymetry measurements)
- the possibility to handle frequency encoded signals (i.e., intrinsic robustness against signal attenuation and cross-talk)
- the high power efficiency thanks to the local generation of the microwave power
- the possibility of reaching sufficiently high frequency inexpensive sources which can match the largest available magnetic fields

### 1.7 Goal of this work and thesis organization

The objectives of this thesis may be briefly summarized as in the following.

- Design, implementation, and test of a complete portable security solution for ESR material inspection of suitable paramagnetic inks or ferromagnetic patterns (Chap. 2). Goal: to assess the feasibility of the project and eventually implement an autonomous ESR detector operating at 550 MHz for contactless inspection up to 3 mm.
- Test and experimental characterization of previously developed CMOS ESR sensors operating up to 146 GHz, from 300 K to 10 K (Chap. 3). Goal: to study the performance of single-chip CMOS ESR detectors and reach the highest ever reported working frequency.
- Design, implementation, test and experimental characterization of a HEMT ESR sensor operating at 11 GHz, from 300 K to 1.4 K (Chap. 4). Goals: to introduce HEMT technology in single-chip ESR detectors as a means to reach the lowest ever reported power consumption (i.e., to extend the temperature range below 4 K) and the lowest saturation condition in the GHz range.
- Characterization of a standalone HEMT transistor and of the HEMT LC Colpitts oscillator introduced in Chapter 4, from 300 K to 1.4 K and in presence of magnetic fields up to 8

## **1.7. Goal of this work and thesis organization**

---

T (Chap. 5). Goal: to model the behaviour of extremely low power HEMT LC Colpitts oscillators.

- Design, implementation, test and characterization of 550 MHz and 10 GHz pMOS oscillators for inductive proximity detection operating with sub-pm distance resolution (Chap. 6). Goals: to investigate a different application (other than ESR spectroscopy) for low noise LC oscillators and to model the achievable distance resolution when used as proximity sensors.
- Description of further implemented integrated circuits (Chap. 7).



## 2 A portable ESR scanner operating from 400 to 610 MHz

### 2.1 Abstract

In this chapter, we report on the design, fabrication, and characterization of an electron spin resonance (ESR) inductive scanner for material inspection, operating in the frequency range from 400 MHz to 610 MHz. The system is low-cost, low-power, portable, and allows for contactless detection of targets located up to 3 mm above the sensor. It is a comprehensive standing alone architecture composed of five sub-systems: the ESR sensor, the magnetic system, the field modulator, the power unit, and the back-end system. The first unit includes an integrated cross-coupled voltage-controlled-oscillator (VCO) having an off-chip resonator, composed of a sensing planar coil (6 mm in diameter) to provide the radio-frequency (RF) field ( $B_1$ ), and a discrete ultra-low noise phase-locked-loop (PLL) to perform the frequency-to-voltage conversion with a 160 kHz bandwidth. The second unit is a U-shaped magnetic circuit composed of 9 permanent magnets ( $\text{Nd}_2\text{Fe}_{14}\text{B}$ ) and two lateral L-shaped branches made of permennorm to provide the required static magnetic field ( $B_0$ ) in the sensitive volume (i.e.,  $4\times 4\times 4\text{ mm}^3$  above the sensing coil). The third unit is a 4-channel 10 kHz modulator based on a 17 mm wide planar trace located below the sensing coil to provide the modulation magnetic field ( $B_m$ ) in the sensing volume. The fourth unit is composed of a 5 W USB power interface, a discrete switching regulator (Buck converter), and a set of linear converters (LDOs) to supply the entire system. The fifth unit is composed of a pre-amplifier, a programmable digital-acquisition-board (DAQ), and a LabView control software running on a laptop. The latter manages the frequency sweep, performs the synchronous detection through an embedded lock-in, and provides the end user with a graphical interface for data-processing. The proposed scanner is intended to detect thin films (up to  $4\times 4\text{ mm}^2$ ) of paramagnetic targets through any kind of optically opaque or non-metallic interface. The oscillator thermal noise is  $0.15\text{ Hz/Hz}^{1/2}$ , which is only a factor of two above the theoretical value. The achieved spin sensitivity measured with a volume of  $\alpha,\gamma$ -bisdiphenylene- $\beta$ -phenylallyl (BDPA)/benzene complex is  $4\times 10^{15}\text{ spins/Hz}^{1/2}$  at 0 mm. An equivalent sweep range of 7.5 mT makes the scanner also suitable for ferromagnetic (FMR) detection of both isolated targets and complex patterns.

### 2.2 Motivation

Small size benchtop ESR spectrometers are commercially available products (e.g., Bruker – MicroESR, Magnettech – MS5000, Adani - Spinscan). They are general purpose solutions typically used in electrochemistry (ESR electrolytic cells), photochemistry (UV irradiation), and redox kinetic measurements (continuous and stopped-flow systems) in order to detect the formation of free radicals. Main fields of application include radiation dosimetry (alanine dosimeter readers for  $\gamma$ - and x-rays), food process-flow monitoring (e.g., fermentation quality control), car engine oil control, biological and pharmaceutical research, industrial polymer production, and cancer research. From the end user's standpoint, those spectrometers require the technicians to (1) insert any given target inside the spectrometer, (2) run the ESR inspection through the benchtop machine, and finally (3) retrieve the results of the analysis.

In this framework, the proposed standing-alone ESR detector aims at extending the versatility of the existing solutions according to the following needs.

- The ESR targets might stick/adhere to big objects which cannot be inserted in the currently available spectrometers. Consequently, in order to overcome such a limitation, the sensitive volume must be fully accessible from outside with an open ended geometry. That implies the front-end of the proposed scanner should be flat in order for the ESR targets to get inspected regardless of the object's size.
- The ESR targets might be immersed in thick, non-magnetic and optically opaque materials which may keep the sample under investigation far from the actual sensitive region. That implies the proposed sensor must be suitable for contactless ESR inspection up to a certain distance above the detector.
- On-site ESR inspections may require the proposed scanner to be portable for logistics related issues. That implies the overall system must be sufficiently light and low-power so as to be easily handled for hours without recharge. As described in Refs. [39, 40], a quasi-portable product has been already developed for nuclear magnetic resonance applications (NMR-Mouse) but portability is still an original feature in the field of ESR.

The design of the proposed ESR scanner has been supported by the Swiss Commission for Technology and Innovation (CTI) in partnership with SICPA SA (Prilly, Switzerland). The project is part of a wider industrial solution that is currently being patented. No further information can be disclosed.

### 2.3 Design approach

In order to design a detector which is robust against signal attenuation and interference, a frequency detection method is chosen (Sec. 1.4). In this context, as explained in the following, size, weight, power consumption and the architecture of the portable scanner are mainly



determined by the magnetic system.

First of all, the requirement on the open geometry leads the overall magnetic system to have very high reluctance (Sec. 2.5) so any attempt to perform a magnetic field sweep by pumping current to a suitable electromagnet would result very inefficient (i.e., high power consumption to achieve the expected magnetic field). Consequently, the proposed solution is based on a frequency sweep approach which includes (1) a single LC voltage-controlled-oscillator (VCO) (Sec. 2.6) and (2) a fixed-field magnetic system composed of suitable permanent magnets. Secondly, dealing with a magnetic system having high reluctance also means that its overall size/weight results dramatically affected by the value of the static magnetic field. Indeed, the higher the  $B_0$  value, the heavier the structure. Moreover, the static magnetic field and the working frequency of the oscillator are linked together according to the Larmor frequency (Sec. 1.1), and then the selection of the operating frequency is directly connected to the design of the magnetic system. Additionally, since the sensitive volume depends on the coil size, the sensing VCO should have a suitable central frequency in order to (1) allow for material inspection up to the required distance above the coil and (2) reduce the weight of the scanner itself. Further constraints on the magnetic system are also given by the expected field homogeneity level in the required sensitive region (Sec. 2.5).

To some extent, the adoption of an LC VCO as ESR detector leads to the need of synchronous detection for  $1/f$  noise suppression (Sec. 1.5). The latter includes a magnetic field modulator (Sec. 2.7) which has to be placed in close proximity of the sensing coil and a lock-in amplifier to perform the demodulation (Sec. 2.9). The field modulator is an intrinsic AC block and must generate the required modulation field in the entire sensitive volume without affecting the overall open geometry. That means such a block is going to be a power hungry unit and will heavily contribute to lowering the power budget for the other units. Regarding this, reducing the  $1/f$  frequency noise of the LC VCO is a necessary condition to both (1) increase the sensitivity of the scanner and (2) lower the modulation frequency for maximum performance ( $f_m$ ). The latter would in turn lead to a lower power consumption of the modulator and to the possibility of performing the lock-in detection at the level of the back-end system (i.e., using the low frequency analog-to-digital-converters (ADCs) already available within the DAQ-board).

Finally, in order not to degrade the oscillator performance, the PLL (used in this framework as frequency-to-voltage converter) has to be an ultra-low-noise subsystem in the entire operating range (Sec. 1.5). In particular, the latter must have a lock range which matches the frequency span of the VCO and its frequency-modulation (FM) bandwidth must be sufficiently wide so as not to attenuate the ESR signal at  $f_m$ .

## 2.4 Top-Level description

The proposed portable scanner is composed of five building blocks which are described in the next sections: the ESR sensor, the magnetic system, the field modulator, the power unit, and the back-end system. The first four units form the so-called front-end structure (Fig. 2.1).

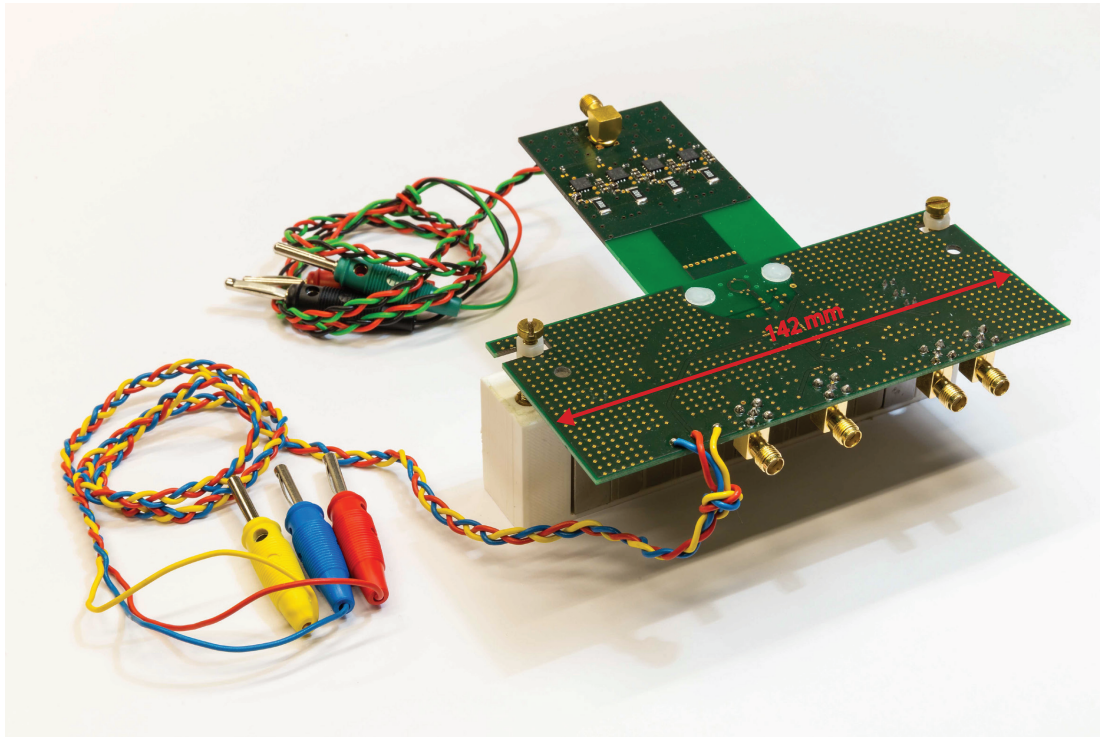
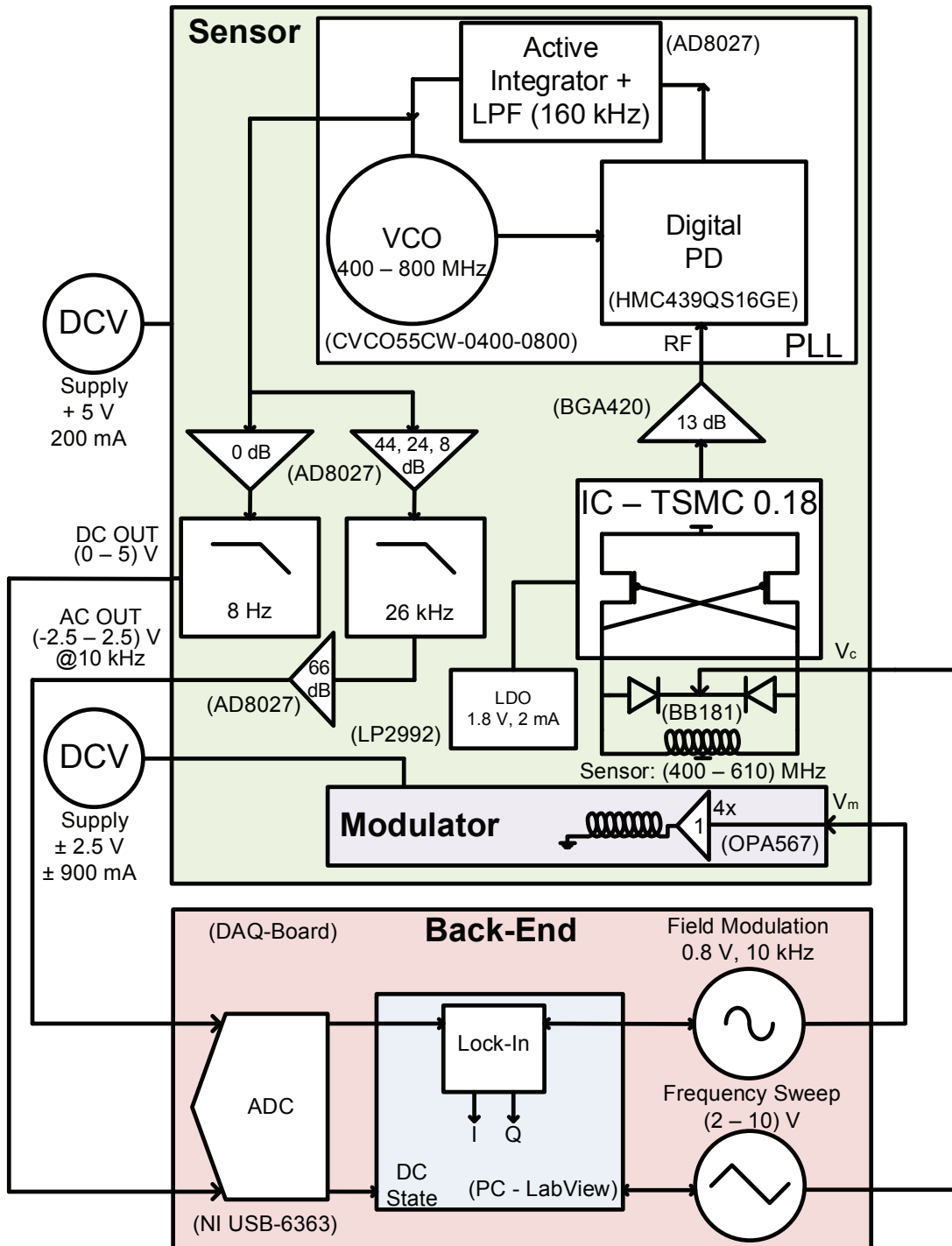


**Figure 2.1 – Picture of the portable scanner (prototype) - Front-end.** The magnetic system stands at the bottom (Fig. 2.2) and it constitutes the supporting structure for the overall front-end electronics. The ESR sensor and part of the power unit are located on the main PCB tile (142 mm wide), which is fixed to the magnetic system by means of two brass screws. The smaller rectangular PCB is the modulator and it is mechanically connected to the sensor through two nylon screws. The sensing coil is located in between the two nylon screws. The cables provide the required voltage supply to the aforementioned units, whereas both outputs and control signals are fed/extracted by means of the brass SMA connectors. See Fig. 2.8 for the top-view.

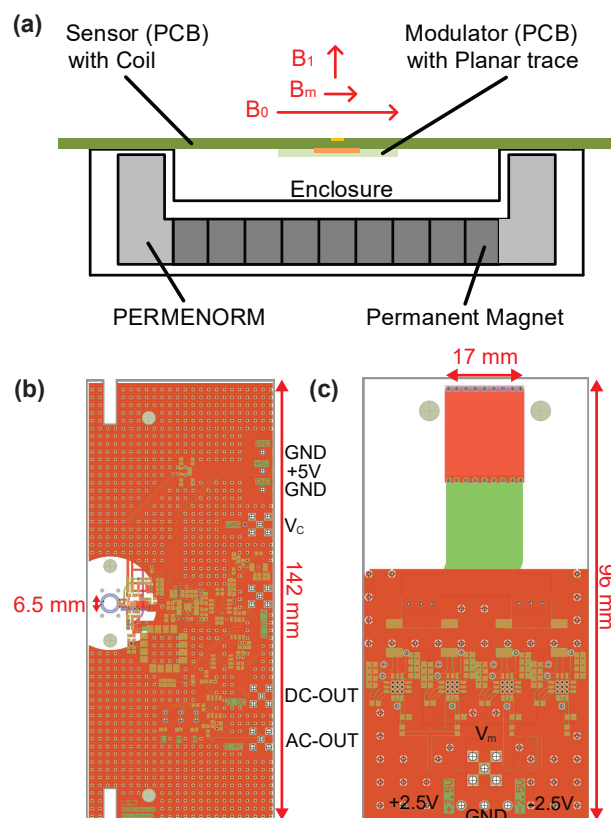
Fig. 2.2 shows a graphical representation of the main electronic units with both electrical interconnections and dynamic ranges. In particular, the ESR sensor is a printed circuit board (PCB) composed of a sensing cross-coupled voltage-controlled LC oscillator (VCO), a homemade phase-locked-loop (PLL), and some additional subsystems for both amplification and filtering. The modulator is based on a 4-channel amplifier driving the AC current into a wide microstrip whereas the back-end system is composed of a digital-acquisition-board (DAQ-board) to acquire the two outputs of the PLL and generate the control signals (i.e., the variable control voltage for the sensing VCO and the modulation signal).

Fig. 2.3a shows a graphical representation of the architecture seen in front-view with emphasis on the magnetic fields generated by the magnetic system ( $B_0$ ), the LC VCO ( $B_1$ ), and the modulator ( $B_m$ ). The orientation of the magnetic fields is the one presented in Sec. 1.1. As a matter of fact, the LC VCO generates the radio-frequency field along the axis of the coil, the modulator generates a modulating field which is parallel to the trace width (the AC current flows along the trace), and the static field closes the gap between the two expansions of the magnetic system. Finally, Fig. 2.3b,c shows the layout of the PCBs designed for the ESR sensor and the field modulator, respectively. It is worthy to note that the shape of the magnetic system and the positioning of the PCBs are such that the architecture has the expected open geometry

(i.e., the top face of the system is actually flat).



**Figure 2.2 – Top-Level block diagram of the portable scanner.** The ESR sensor, the modulator and the back-end system are electrically interconnected as shown in the diagram. For each system, all the constituting blocks are reported in terms of identification name/symbol, input/output signals, and corresponding dynamic ranges (voltage, current, or frequency). The power system is shown as composed of functional supply blocks and their corresponding power consumption (voltage and current). The magnetic system is not shown.



**Figure 2.3 – Representation of the generated magnetic fields and layout of the PCBs realized for the portable scanner.** (a) Front-end architecture (Fig. 2.1 and Fig. 2.4) seen in front-view with focus on the generated magnetic fields. The magnetic system is shown in its enclosure with the permanent magnets and the L-shaped expansions. The two PCBs correspond to the ESR sensor and the field modulator. The orange rectangle is the cross-section of the wide trace used to modulate the signal. The yellow rectangle is the front-view of the sensing oscillator. The diagram shows the open geometry of the system, the flat side of the detector, and the sensing volume above the sensor. (b) Layout of the printed circuit board (PCB) related to the ESR sensor. It is shown the diameter of the double-turn sensing coil and the signals used for the interface (Fig. 2.2). The two holes at the far ends are used for its mechanical support to the magnetic structure whereas the two holes close to the sensing coil are used to fix the modulator. (c) Layout of the printed circuit board (PCB) related to the modulator. It is shown the width of the trace and the signals used for the interface (Fig. 2.2). The two holes shown in the PCB are used for its mechanical support to the ESR sensor.

## 2.5 Magnetic system

The design of the magnetic system is carried out by means of Comsol Multiphysics<sup>®</sup>. Fig. 2.4 shows a picture of the realized structure and Tab. 2.1 summarizes the technical details. The goal is to minimize the size/weight of the overall system by ensuring a static magnetic field in the fringing field of approximately 18 mT (i.e., centered at 500 MHz) and good homogeneity level in the sensitive volume. Since the target sample is supposed to be thin (about 40  $\mu\text{m}$ ), the constraint on the vertical gradient is relaxed to a few hundreds  $\mu\text{T}/\text{mm}$ , whereas the gradient must be within 100  $\mu\text{T}$  over a surface of  $6 \times 6 \text{ mm}^2$ , up to 4 mm in elevation. These constraints on the maximum field gradients allow to measure samples having a linewidth of 100  $\mu\text{T}$  or larger without any significant broadening. Finally, the overall structure is placed into a 3D printed ABS enclosure so as to provide a fixing zone for the sensor.

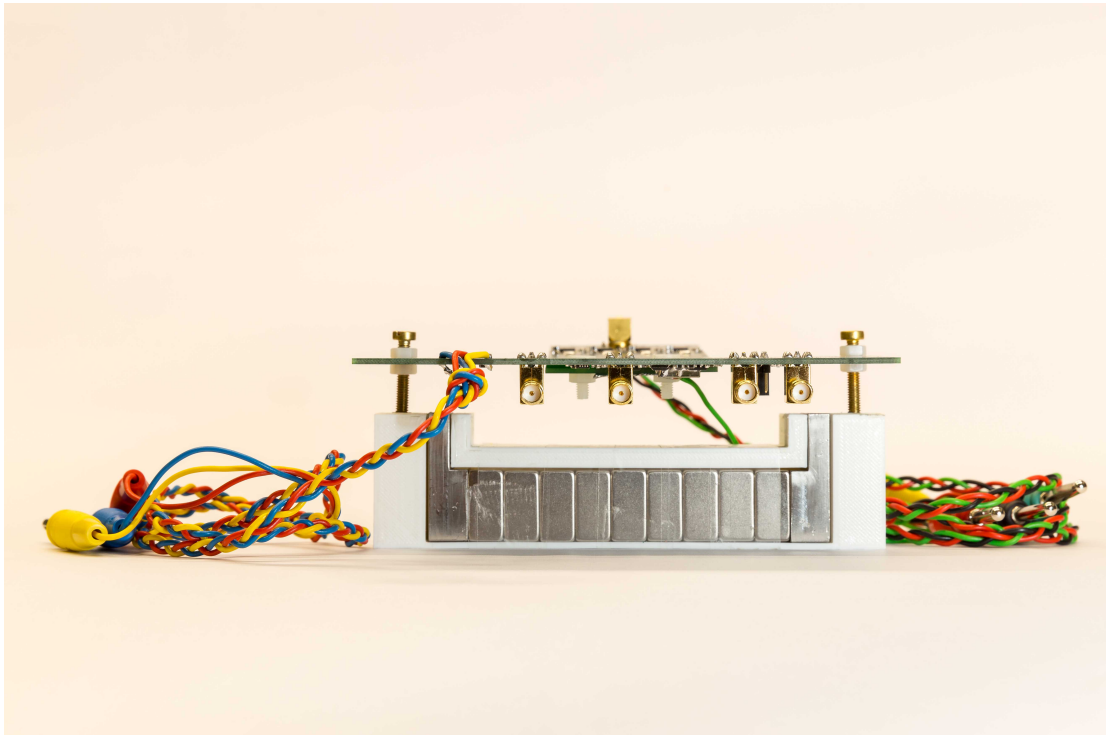


**Figure 2.4 – Picture of the portable scanner (prototype) - Front-view.** The picture of the realized prototype highlights the magnetic system in its 3D printed enclosure (the width of the PCB is equal to 142 mm). The 9 permanent magnets provide the required DC field to the equivalent magnetic circuit whereas the two L-shaped expansions provide the required shaping of the fringing field in the region of interest. The plastic nuts on the fixing brass screws allow to adjust the height of the sensing PCB according to any offset in the designed  $B_0$ .

MAGNETIC SYSTEM	
Permanent magnets (Maurer Magnetic AG)	$\text{Nd}_2\text{Fe}_{14}\text{B}$ 10×20×20 mm <sup>3</sup>
Number of permanent magnets	9 (aligned)
Residual magnetic flux density ( $B_r$ )	1.38 T
Sensitive volume above the L-shaped branches	From 0 mm to 6 mm in elevation
Vertical gradient	400 $\mu\text{T}/\text{mm}$
Surface homogeneity level	< 100 $\mu\text{T}$ over 6×6 mm <sup>2</sup>
$B_0$ @ 54 mm (elevation from ground to the sensing coil + 1 mm)	18 mT
Composition of the 2 L-shaped branches	Permenorm (soft magnetic material)
Overall weight	380 g
Overall length	112 mm
Overall height	36 mm
Thickness	20 mm
Mounting technique for the PCBs	M4 brass screws

**Table 2.1 – Technical resume table of the scanner operating from 400 MHz to 610 MHz - Magnetic system.**

## Chapter 2. A portable ESR scanner operating from 400 to 610 MHz

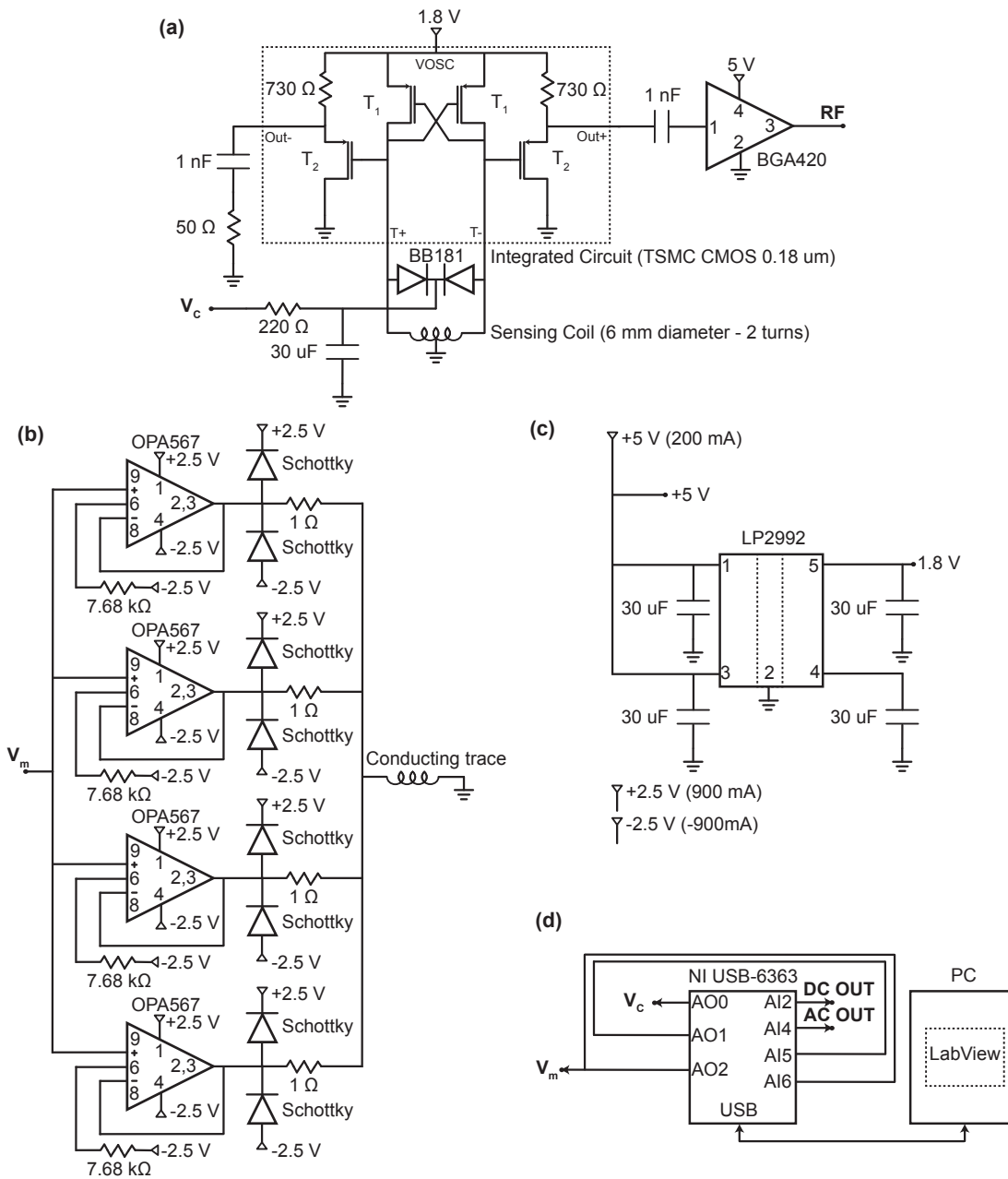


**Figure 2.5 – Schematics of the portable scanner.** (a) Schematic of the sensing oscillator and the corresponding buffer. The pMOS cross-coupled structure and the output buffer are integrated with a Si CMOS technology (TSMC 180 nm, MS/RF). The size of each transistor is reported in Tab. 2.2. The resonator is off-chip since the required coil size is large (6 mm in diameter). A 24 Hz low-pass-filter (LPF) is used to filter the control voltage of the VCO ( $V_c$ ). That is to reduce the frequency noise while still allowing for rapid sweeps (from 0.2 Hz to 2 Hz). The output amplifier (BGA420) provides further isolation for the VCO and allows to match the dynamic range of the PLL. (b) Schematic of the 4-channel field modulator. The Schottky diodes are used to protect the circuit from spikes. The 1  $\Omega$  resistors increase the stability of each amplifier at the expense of the overall power efficiency. (c) Schematic of the Power unit. The USB interface provides 5 V to the PLL and the lock-in preamplifier. A linear regulator (LP2992) provides 1.8 V to the oscillator. The voltage supply for the modulator is  $\pm 2.5$  V, and that is provided by a DC-DC converter. (d) Schematic of the back-end system. The DAQ-board is used to acquire the two outputs from the PLL and to generate both the VCO control signal ( $V_c$ ) and the modulation signal ( $V_m$ ). The other connections are used for the lock-in demodulation (embedded in LabView®).

## 2.6 Sensing oscillator

Fig. 2.6 shows a picture of the portable scanner with a focus on the ESR sensor, whereas all the technical details are summarized in Tab. 2.2. The working frequency of the sensing VCO is chosen according to the constraints on both the magnetic system (size and weight) and the need for inspection capability up to 3 mm in elevation. As mentioned in Secs. 2.3-2.5, the static magnetic field matches a working frequency of approximately 500 MHz so the VCO should be centered at that frequency. In particular, an LC resonator based on a double-turn planar coil having a diameter of 6 mm happens to be the optimal choice. Indeed, (1) the corresponding inductance is suitable for the expected working frequency and (2) the optimal diameter for contactless inspection is twice as much the required elevation distance (Eq. 1.9). Due to the size of the sensing coil, the LC resonator cannot be integrated and must be located off-chip (on the PCB). That implies that two bonding wires must be used in order to connect the integrated energy restoring system to the LC resonator. Since their parasitic inductance is significant (approximately 1 nH/mm), the inductance of the sensing coil must be large enough to make the former negligible. That is the reason why the proposed coil is based on a double-turn topology.

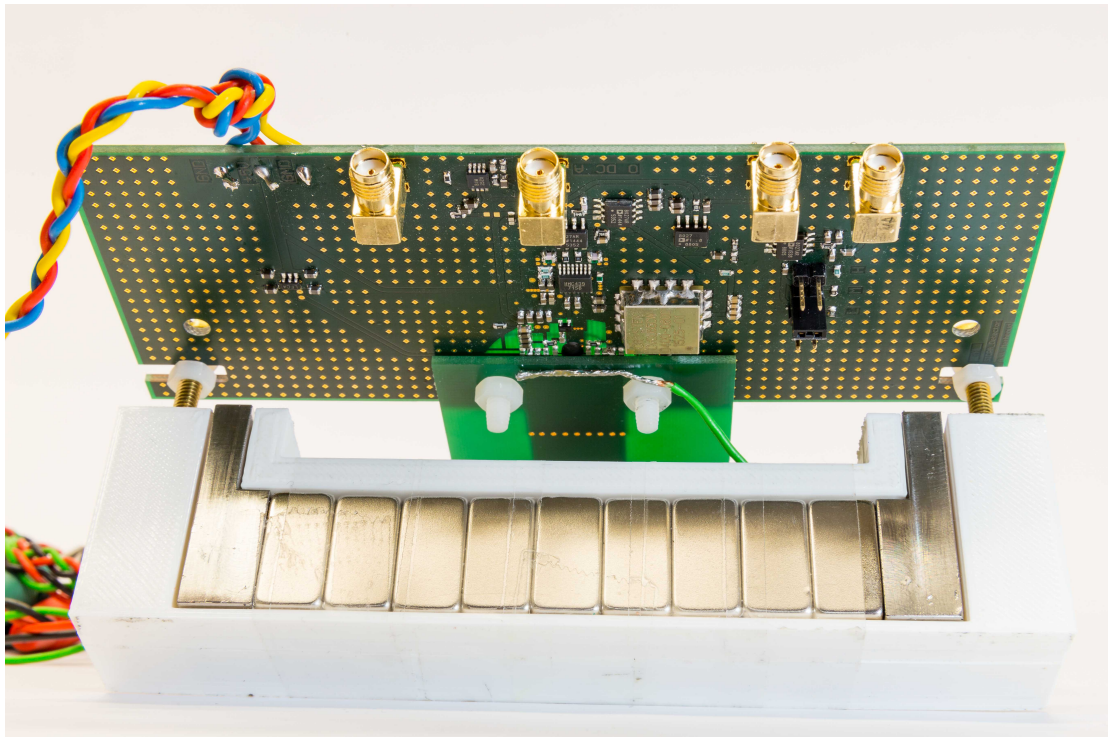


**Figure 2.6 – Picture of the portable scanner (prototype) - Bottom-view.** The picture of the realized prototype highlights the magnetic system, the tile of the ESR sensor (the width of the PCB is equal to 142 mm), and the trace of the field modulator. All the surface-mounted-devices (SMDs) are placed on the bottom layer of the PCB in order to keep the top face flat. The square component with the metal shielding is the reference oscillator for the homemade PLL. Next to it (on the left), there is the phase detector for the PLL. All the other integrated SMDs are operational amplifiers for active filtering and amplification purposes. On the right, a jumper allows to set among three different gains for the variable-gain-amplifier (VGA) of the PLL (output stage of the AC branch). On the left, the 5-pin SMD is the linear regulator to supply the board. In the picture, the modulator hides the realized integrated circuit for the VCO.

## Chapter 2. A portable ESR scanner operating from 400 to 610 MHz

ESR SENSOR	
Oscillator type	Cross-coupled (CC)
LC tank location	External (off-chip)
Tank inductance (nominal)	35 nH
AC resistance @ 500 MHz	0.5 $\Omega$
Coil geometrical description (turns, diameter, width, and spacing)	2-turn, 6 mm, 400 $\mu$ m, 200 $\mu$ m
Total tank capacitance (nominal range)	(1.3 - 4.3) pF
Capacitor type	2 in-series varactors (2 BB181)
Control voltage (range) - $V_c$	(2 - 10) V
Oscillator frequency (range)	(400 - 610) MHz
Equivalent field sweep range	7.5 mT
IC Technology	TSMC CMOS 0.18 $\mu$ m RF/MS
Cross-coupled transistors (type, fingers, total width, channel length) - $T_1$	pMOS, 12, 27 $\mu$ m, 280 nm
Output buffer transistors (type, fingers, total width, channel length) - $T_2$	pMOS, 24, 72 $\mu$ m, 180 nm
Oscillator thermal noise	0.15 Hz/Hz <sup>1/2</sup>
Oscillator corner frequency	6 kHz
Radiofrequency field ( $B_1$ ) @ 500 MHz, 0 mm	3 $\mu$ T
PLL phase margin	70 deg
PLL FM bandwidth	160 kHz
Standard AC gain (selectable)	Intermediate (90 dB)
Standard AC conversion gain	700 $\mu$ V/Hz
Noise spectral density at the AC output @ 10 kHz modulation (0.7 G @ 2.6 mm in elevation from the conducting trace)	0.5 Hz/Hz <sup>1/2</sup> (350 $\mu$ V/Hz <sup>1/2</sup> )
Overall noise at the AC output @ 10 kHz modulation (0.7 G @ 2.6 mm in elevation from the conducting trace) and typical sweep time (5 s)	6 Hz <sub>rms</sub> (4.2 mV <sub>rms</sub> )
DC conversion gain	22 nV/Hz
Power consumption	1 W (5 V, 200 mA)
DC OUT (voltage dynamic range)	(0 - 5) V
AC OUT (voltage dynamic range, frequency)	(-2.5, +2.5) V, 10 kHz
PCB (dielectric, layers, thickness, and size)	FR4, 4, 1.6 mm, 60×142 mm <sup>2</sup>

Table 2.2 – Technical resume table of the scanner operating from 400 MHz to 610 MHz - Sensor.

In order to optimize the design of the energy restoring system, an integrated solution based on a Si CMOS technology (TSMC 180 nm, MS/RF) is taken into account. As a matter of fact, the proposed integrated cross-coupled topology allows (1) to minimize parasitics coming



from the interconnections (i.e., the cross-coupled transistors are matched at layout level) and (2) to use suitable transistors in order to reduce the  $1/f$  noise (large pMOS transistors with symmetric layout and metal connections). As mentioned in Sec. 2.3, optimizing the noise performance is crucial to maximize the spin sensitivity and to relax the specifications concerning the modulator (i.e., to reduce the modulation frequency necessary to reach the thermal noise floor of the LC oscillator). Moreover, since the sensing coil diameter is in the mm range, the saturation issues related to the amplitude of  $B_1$  are not relevant for the typical bias points allowed by the technology (below 1.8 V). Consequently, it is possible to maximize the oscillation amplitude (450 mV<sub>rms</sub>) so as to reduce the frequency thermal noise (Eq. 1.18). The proposed VCO reaches a corner frequency of approximately 6 kHz and a thermal noise floor of 0.15 Hz/Hz<sup>1/2</sup>, which is only a factor of two above the theoretical limit (i.e., the expected thermal frequency noise due to the series resistance of the coil). Off-chip resonators have a quality factor which is higher than the one of integrated resonators, so the proposed topology allows to reduce the frequency thermal noise floor. Fig. 2.5a shows the schematic of the realized VCO.

As discussed in Sec. 1.5, the design of an ultra low-noise phase-locked-loop (PLL) allows to perform the frequency-to-voltage conversion without affecting the overall noise performance. A PLL is composed of a phase detector which senses the phase difference between the VCO and a reference oscillator. The signal associated to the phase difference is filtered through a suitable low-pass-filter (LPF), and that becomes the control voltage of the reference oscillator. When the PLL is locked to the VCO carrier, the frequency encoded information associated to the sensing VCO is transferred into the control voltage of the reference oscillator. In order for the PLL not to affect the noise performance of the VCO, the reference oscillator must be of much better quality (e.g., quartz oscillators) and its control signal must be low-pass filtered at the required AC bandwidth to reduce spurious signals. Particular attention is also paid at layout level since both the phase detector and the active filters are very sensitive blocks to cross-talk. The achieved noise floor of the PLL is 0.08 Hz/Hz<sup>1/2</sup> and such value has only a marginal impact on the performance of the scanner. As discussed in Ref. [41], in order to design a low noise PLL, it is necessary (1) to use a reference oscillator whose noise performance are at least ten times better than those of the VCO, (2) to use a low noise phase detector (e.g., charge pump), and (3) to reduce the FM bandwidth as much as possible. In particular, although the required FM bandwidth is about 10 kHz, the designed value is actually much larger (160 kHz) since this frequency-to-voltage converter was supposed to interface also other oscillators having corner frequencies above 100 kHz (Sec. 2.11). Reducing the FM bandwidth would allow to achieve an even lower frequency noise floor. It is worthy to note that the PLL required for this application is not conventional as there is a single carrier to track (a.k.a., RF channel) whose frequency continuously varies within the lock-range (from 400 MHz to 610 MHz) at the rate of the frequency sweep (from 0.2 Hz to 2 Hz). The latter implies that adopting a standard first-order LPF is not enough to keep tracking the carrier during the sweep, and then a second order active filter must be introduced (i.e., band-pass filter with integrator) between the charge pump and the reference oscillator (Fig. 2.7, active filter box). Its design is performed in order to preserve the stability of the PLL with a phase margin of 70

## Chapter 2. A portable ESR scanner operating from 400 to 610 MHz

deg and to ensure an FM bandwidth of 160 kHz.

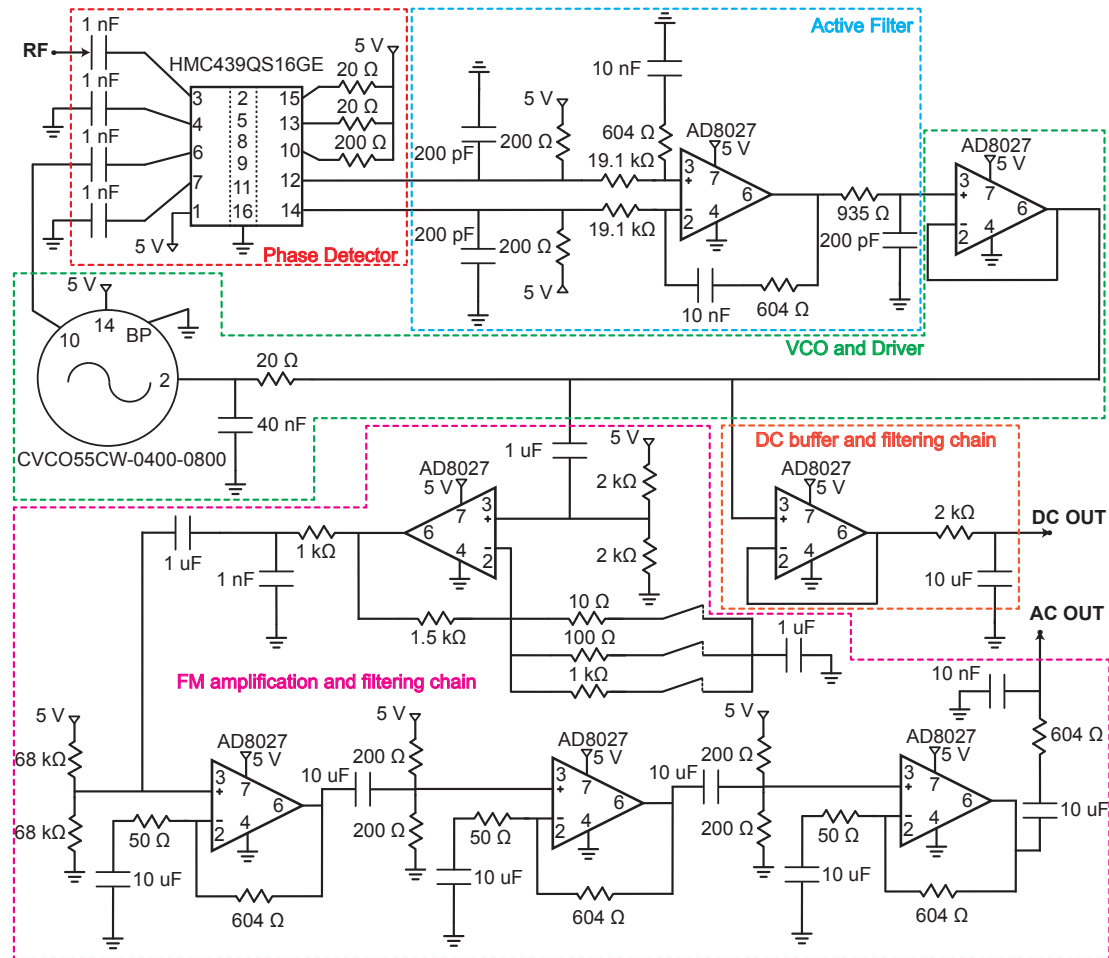


**Figure 2.7 – PLL schematic for the portable scanner.** All the main blocks are highlighted (i.e., phase detector, filters, reference VCO, and the amplification chains). The main features of the PLL are reported in Tab. 2.2. DC-OUT allows to monitor when the PLL is locked to the carrier (unsaturated voltage ranging from 0 to 5 V). AC OUT provides the modulated signal to the next stage (lock-in preamplifier) in the required bandwidth. The frequency-modulation (FM) amplification chain is a variable-gain-amplifier (VGA) and three different gains can be programmed through a mechanical jumper.

The following procedure describes the steps for the design of the active filter, whereas its final optimization is performed with Simulink®.

- The feedback capacitance and the one at the positive input of the operational amplifier must be equal and are chosen arbitrarily in order to provide reasonable values for the resistors ( $C_2 = 10 \text{ nF}$ ). Their values are subjected to optimization at the end of the design in order to improve noise performance and stability.
- The output capacitance is also chosen arbitrarily ( $C_3 = 200 \text{ pF}$ ).
- Since the phase-margin of the PLL ( $\phi$ ) has been set to 70 deg and the sensitivity of the

reference oscillator is known from its datasheet ( $K_{VCO}$ ), one can compute the three time constants of the active filter:  $T_1 = (1/\cos(\phi) - tg(\phi))/\omega_c = 187$  ns,  $T_2 = 1/(\omega_c^2 T_1) = 6$   $\mu$ s, and  $T_3 = K_V K_{VCO} \sqrt{(1 + \omega_c^2 T_2^2)/(1 + \omega_c^2 T_1^2)}/\omega_c^2 = 191$   $\mu$ s, where  $\omega_c = 2\pi f_c$ ,  $f_c$  is the FM bandwidth, and  $K_V$  is the gain of the phase detector (1 V).

- The two input resistors can be calculated as  $R_1 = T_3/C_2 = 19.1$  k $\Omega$ .
- The feedback resistor can be calculated as  $R_2 = T_2/C_2 = 600$   $\Omega$ .
- The output resistor can be calculated as  $R_3 = T_1/C_3 = 930$   $\Omega$ .

Fig. 2.7 shows the full schematic of the proposed PLL.

## 2.7 Modulator

Fig. 2.8 shows a picture of the portable scanner with a focus on the ESR sensor and the modulator. The technical details are summarized in Tab. 2.3 whereas Fig. 2.5b shows the corresponding schematic.

FIELD MODULATOR	
Number of channels	4
Width of the planar trace	17 mm
Vertical distance from the sensing coil	1.6 mm
Modulation signal (peak amplitude and frequency) - $V_m$	0.8 V, 10 kHz
Peak modulation field ( $B_m$ ) @ 2.6 mm from the conducting trace: 1.6 mm (PCB) + 1 mm in elevation	70 $\mu$ T
PCB (dielectric, layers, thickness, and size)	FR4, 4, 1.6 mm, 96 $\times$ 49 mm <sup>2</sup>
Power consumption	4.5 W ( $\pm$ 2.5 V, $\pm$ 900 mA)

**Table 2.3 – Technical resume table of the scanner operating from 400 MHz to 610 MHz - Field modulator.**

The modulator has to provide a suitable modulation field ( $\underline{B}_m$ ), which is parallel to the static magnetic field ( $\underline{B}_0$ ), within the required sensitive volume (i.e., 4 $\times$ 4 $\times$ 4 mm<sup>3</sup> above the VCO coil), and without breaking the open geometry of the scanner (Secs. 2.5-2.6). From the point of view of the power efficiency, the best housing for the modulator turns out to be below the sensing coil. As a matter of fact, the modulator has to be located as close as possible to the sensing volume without protruding outside. Moreover, the structure has to be compact so as to reduce any interference with the electronics. The best geometry results to be a rectangular metallic trace traveled by an AC current in the direction orthogonal to  $\underline{B}_0$ . However, since the specification on the maximum  $B_m$  value is approximately 50  $\mu$ T and the magnitude of

## Chapter 2. A portable ESR scanner operating from 400 to 610 MHz

---

the modulation field decays on the vertical direction above the PCB top layer, the power consumption of this unit is large (4.5 W). Furthermore, the modulator must be sufficiently far from the oscillator in order to reduce eddy currents (i.e., degradation of the VCO quality factor) so an additional distance offset must be accounted to reach the sensitive volume (approximately 2 mm).

It is worthy to note that the magnitude of the modulation field is negligible with respect to  $B_0$  so the gradient of  $B_m$  does not play a significant role. Nevertheless, if  $\underline{B}_m$  is not orthogonal to the plane of the sensing coil, the modulation field will couple some flux across the coil, leading to leakage and extra-noise (Sec. 1.5). In order to reduce such a problem, the modulation trace is made wider than the coil diameter, and then  $\underline{B}_m$  results parallel to the sensing coil in close proximity to the coil itself.

Since standard current drivers need specific heat sinks to drive the necessary power, a solution based on a 4-channel amplifier is preferred. Indeed, the heat sinks would make the structure heavier and they would also increase the overall size.

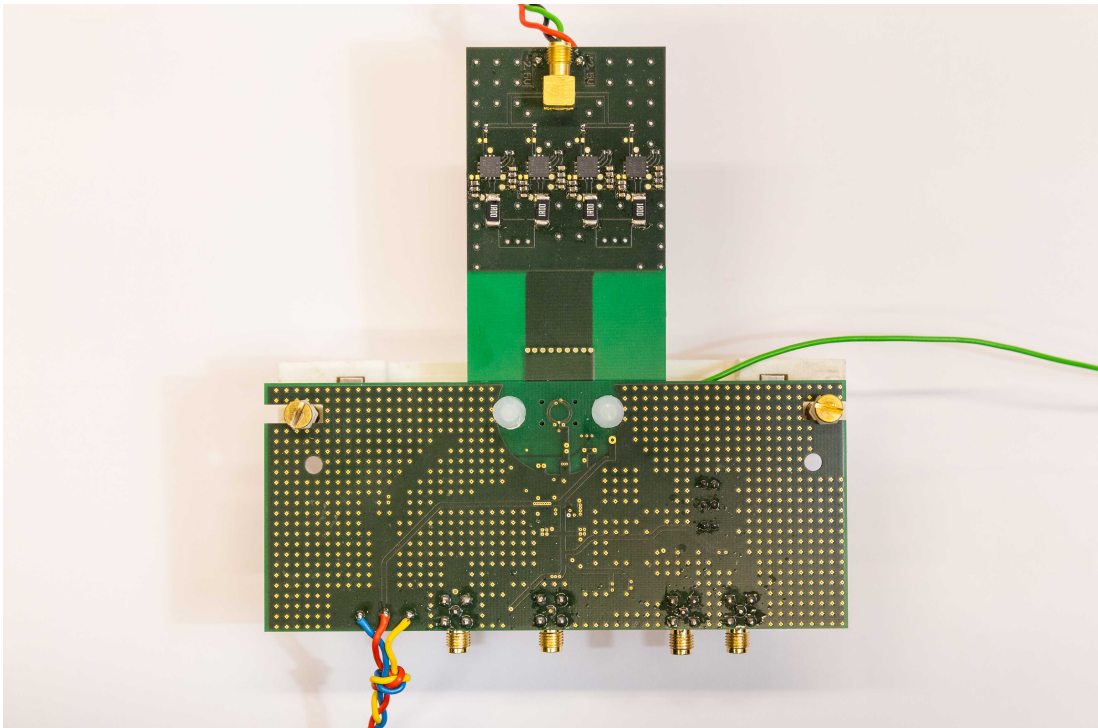


**Figure 2.8 – Picture of the portable scanner (prototype) - Top-view.** The picture of the realized prototype highlights the tile of the ESR sensor and the field modulator. The latter is fixed to the former through two flat nylon screws. The sensing coil is visible between the two screws. The trace of the modulator is much wider than the coil diameter in order to have a constant  $B_m$  in the region of interest. It is placed 1.6 mm below the sensing coil (i.e., the thickness of the PCB) in order to reduce the induced perturbations (leakage and interference). This positioning also ensures the modulator has no impact on the open geometry required for the overall architecture. The four square SMDs are the amplifiers used to drive the current into the modulation trace. They are soldered on the top layer since their height does not exceed the thickness of the PCB.

## 2.8 Power unit

The technical details of the power unit are summarized in Tab. 2.4 whereas Fig. 2.5c shows the corresponding schematic. It mainly consists of a USB power interface providing 5 V (1 A) in order to electrically drive the front-end of the portable scanner (i.e., the ESR sensor and the field modulator).

The ESR sensor needs a 5 V voltage supply for the PLL, the DC/AC amplification chains, and the lock-in preamplifier whereas the VCO needs 1.8 V. Hence, a low-dropout regulator (LDO) mounted on the ESR sensor PCB is used to supply the sensing oscillator, for an overall power consumption of the board equal to 1 W (Sec. 2.6). Conversely, the modulator needs a bipolar voltage of  $\pm 2.5$  V so a DC-DC power converter (Buck type) is used to down-convert the voltage from the USB power interface. The overall power consumption of the modulator running at full amplitude is 4.5 W (Sec. 2.7).

POWER UNIT	
Total power consumption	5.5 W
Voltage supply	5 V (200 mA), $\pm 2.5$ V ( $\pm 900$ mA)
Linear regulator	LDO @ 1.8 V (Sensor)

Table 2.4 – Technical resume table of the scanner operating from 400 MHz to 610 MHz - Power unit.

At layout level, the main concern is to avoid voltage ripple. Accordingly, a set of bypass capacitors in the range from 1 pF to 22  $\mu$ F is used for each integrated circuit, so as to have an overall bypass capacitance of approximately 66  $\mu$ F per supply pin. The low value capacitors are used in parallel to the big ones since they have much higher resonance frequency, leading to a better filtering of high frequency interference. Additionally, the metal connections are wide (800  $\mu$ m) to reduce the parasitic inductance, whereas the adoption of two ground planes (within a 4-layer PCB) allows to achieve a good reference potential for the entire electronics.

## 2.9 Back-end system

The technical details of the back-end system are summarized in Tab. 2.5 whereas Fig. 2.5d shows the corresponding connection diagram. It mainly consists of a digital acquisition board (DAQ-board) with four programmable analog-to-digital-converters (ADCs) and a laptop running the LabView<sup>®</sup> control program. The former is used to generate the control signals ( $V_c$ ,  $V_m$ ) and to acquire the two outputs from the PLL. The latter is used to perform the lock-in demodulation, to manage the user interface, and to adjust/calibrate the frequency sweep.

The frequency scan is performed in a pointwise way, as explained in the following.

- The start/stop voltage values for  $V_c$  (VCO control voltage) determine the range ( $V_{\text{range}}$ ) of the frequency sweep.

## Chapter 2. A portable ESR scanner operating from 400 to 610 MHz

---

- The step size ( $V_{\text{step}}$ ) determines the sweep resolution.
- The number of points on the graph is then  $n_p = V_{\text{range}}/V_{\text{step}}$ .
- Starting from the minimum value set for the control voltage ( $V_c$  start), the software increases  $V_c$  by  $V_{\text{step}}$  up to the maximum value ( $V_c$  stop).
- At each point, the DAQ-board acquires  $n_s$  samples at a given sampling rate ( $r$ ), and then the software computes the average in order to get the corresponding measurement point. This procedure is performed for the two outputs of the PLL (DC-OUT and AC-OUT).

The synchronous detection (modulation/demodulation) is performed as in the following.

- The DAQ-board is configured so as to generate the modulation signal ( $V_m$ ). The amplitude of  $V_m$  determines the modulation level, and the corresponding  $B_m$  must be lower than the signal linewidth in order to avoid saturation. The frequency of the modulation signal ( $f_m$ ) must be large enough to reach the thermal noise floor of the detector.
- Both  $V_m$  and its 90 deg phased shifted replica are acquired by the DAQ-board in order to have the two reference signals for the embedded lock-in amplifier (i.e.,  $V_m \sin(2\pi f_m)$  and  $V_m \cos(2\pi f_m)$ ).
- The lock-in demodulation is performed on the AC-OUT signal. Such operation is accomplished by separately multiplying AC-OUT with the two reference signals previously acquired. Each multiplication generates one of the two orthogonal outputs of the lock-in ( $X$  and  $Y$ ). The software also allows to adjust the phase so as to completely move the ESR signal on one of the two outputs.

The sampling rate ( $r$ ) must be at least ten times larger than the modulation frequency ( $f_m$ ) and the number of samples per acquisition ( $n_s$ ) must be such that the acquisition bandwidth ( $BW$ ) is both at least ten times larger than the scan rate (from 0.2 Hz to 2 Hz) and sufficiently large to describe all the required features of the ESR signal (linewidth). As a matter of fact, according to the Nyquist-Shannon theorem, the sampling frequency must be at least twice as much the bandwidth of the analog signal when using the *Sinc*-function for reconstruction, whereas a factor of ten allows to use the trivial piecewise linear reconstruction (i.e., connecting adjacent points). In this context, the lock-in integration time is  $\tau = 4n_s/r$  and the bandwidth of the acquisition system is  $BW = 1/\tau$ . Consequently, given a certain frequency noise spectral density ( $FN$ ) at  $f_m$ , the total integrated noise is  $FN\sqrt{BW}$  [Hz<sub>rms</sub>].

## 2.10. Characterization and experimental results

BACK-END SYSTEM	
DAQ board	NI USB-6363
LabView <sup>®</sup> version	2012 - Full Development System
Typical sweep time (from 400 MHz to 610 MHz)	5 s
Sampling rate ( $r$ )	123456 Sa/s
Number of samples ( $n_s$ )	223
Integration time ( $\tau$ )	7 ms
Voltage step ( $V_{\text{step}}$ ) for $V_c$	62.5 mV
Number of sweeps per measurement	1
Maximum background input voltage at the input of the DAQ board (i.e. maximum voltage offset)	1.1 V

Table 2.5 – Technical resume table of the scanner operating from 400 MHz to 610 MHz - Back-end system.

The LabView<sup>®</sup> interface allows to set all the aforementioned parameters (number of sweeps,  $V_c$  start/stop,  $V_{\text{step}}$ ,  $n_s$ ,  $r$ ,  $V_m$ , and  $f_m$ ), making the overall system versatile according to the sample under investigation. Indeed, as mentioned in Sec. 1.5, a typical ESR experiment may be optimized in many ways. For instance, one may use multiple sweeps in order to increase the SNR. However, the higher the number of sweeps, the longer the measurement time. One could perform multiple sweeps at high rate (i.e., by increasing the bandwidth of the acquisition system and then integrating more noise) or the other way around (i.e., a single slow scan, with narrow bandwidth and then lower integrated noise). Also, according to the linewidth of the spectrum under analysis, one may decide to make the sweep range narrower so as to optimize the measurement time and/or the integrated noise. Finally, the modulation amplitude and the modulation frequency must be adjusted according to the sample under investigation (i.e., the linewidth and the relaxation times, respectively).

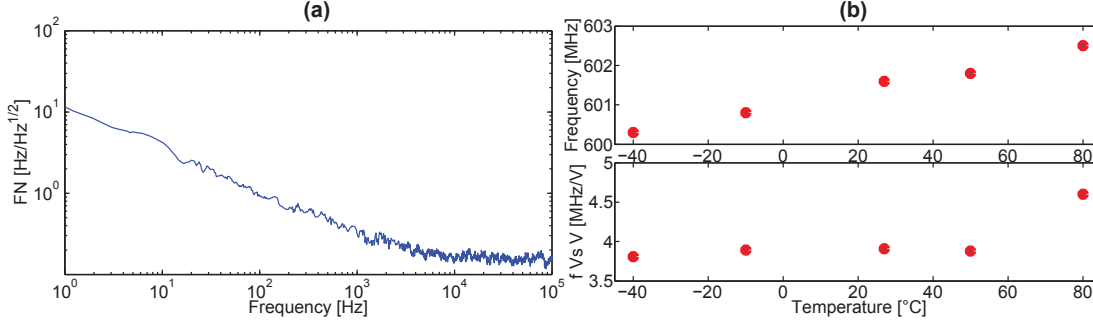
## 2.10 Characterization and experimental results

Fig. 2.9a shows the noise spectral density of the proposed VCO. The corner frequency is 6 kHz, so a frequency modulation of 10 kHz is sufficient to reach the thermal noise floor ( $0.15 \text{ Hz/Hz}^{1/2}$ ). Fig. 2.9b shows the results of a Cadence<sup>®</sup> simulation performed to investigate the stability of the operating frequency as a function of the working temperature. As a result, the frequency variation is within 3 MHz (at approximately 600 MHz) for a temperature interval ranging from  $-40 \text{ }^\circ\text{C}$  to  $+80 \text{ }^\circ\text{C}$ . Across the same range, the supply pull-in voltage (i.e., the frequency change due to a 1 V variation at the supply voltage) is within 5 MHz.

Fig. 2.10 shows the results of measurements performed with the proposed portable scanner. The experiments are performed on a  $2 \times 2 \times 0.5 \text{ mm}^3$  volume of  $1:1\alpha,\gamma$ -bis(diphenylene- $\beta$ -phenylallyl)/benzene complex (BDPA) crystals (a standard paramagnetic sample for ESR) and two types of yttrium-iron-garnet (YIG) microspheres (ferromagnetic samples for FMR) having a diameter of  $300 \text{ }\mu\text{m}$ . The latter are doped with Ga atoms in order to show FMR in

## Chapter 2. A portable ESR scanner operating from 400 to 610 MHz

the frequency range of interest ( $g \cong 2$ ). The reported ESR signals are obtained measuring the oscillation frequency variation in presence of field modulation. Hence, the signal shape is the first derivative of a dispersion signal (Secs. 1.2 and 1.5).



**Figure 2.9 – Characterization of the VCO operating from 400 MHz to 610 MHz.** (a) Noise spectral density of the standing alone VCO at 510 MHz. The corner frequency is 6 kHz and the thermal noise floor is  $0.15 \text{ Hz/Hz}^{1/2}$ . (b) Characterization of the VCO stability as a function of the ambient temperature. The two graphs show a Cadence® simulation of the frequency stability and supply pull-in voltage as a function of the temperature.

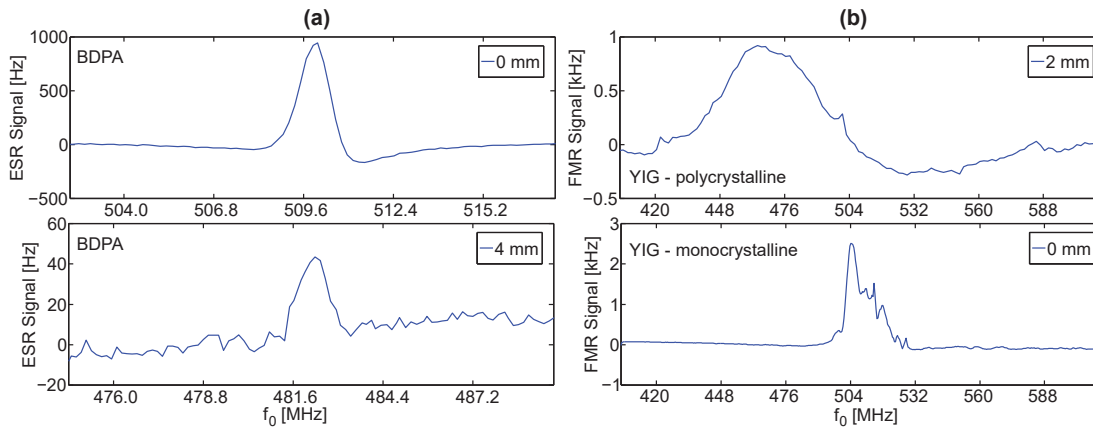


**Figure 2.10 – Measurements performed with the VCO operating from 400 MHz to 610 MHz.** (a) ESR spectra of a  $2 \times 2 \times 0.5 \text{ mm}^3$  volume of BDPA crystals at  $T = 300 \text{ K}$  with  $v_m = 10 \text{ kHz}$  (modulation frequency),  $B_m = 0.05 \text{ mT}$ , at 0 mm ( $B_1 \cong 10 \mu\text{T}$ ) and 4 mm ( $B_1 \cong 0.5 \mu\text{T}$ ) above the coil plane. For both measurements, the full frequency range is scanned but only the relevant interval is shown. (b) FMR spectra of poly/monocrystalline Ga-doped YIG spheres having a diameter of  $300 \mu\text{m}$  at  $T = 300 \text{ K}$  with  $v_m = 10 \text{ kHz}$  (modulation frequency),  $B_m = 0.08 \text{ mT}$ , at 2 mm ( $B_1 \cong 3 \mu\text{T}$ ) and 0 mm ( $B_1 \cong 15 \mu\text{T}$ ) above the coil plane. For both measurements, the full frequency range is scanned and shown.

Thanks to the large coil diameter, the  $B_1$  values are always within  $30 \mu\text{T}$  (the maximum RF current is 4 mA) so the ESR signals are not saturated (the linewidth is approximately 0.1 mT). Assuming a spin density of  $1.5 \times 10^{27} \text{ spins/m}^3$  [42], the number of spins contained in the sample is  $3 \times 10^{18}$ , and then one can estimate the spin sensitivity according to the definition given in Sec. 1.4. At 0 mm, the signal amplitude is 1100 Hz and the frequency noise spectral density is  $0.5 \text{ Hz/Hz}^{1/2}$  (i.e., the field modulation reduces the noise performance by a factor of three), so the experimentally achieved spin sensitivity results approximately  $4 \times 10^{15} \text{ spins/Hz}^{1/2}$ . At 4 mm in elevation, the filling factor decreases by twenty as expected from Eq. 1.9, and then the spin sensitivity drops by the same factor.



The proposed frequency sweep (7.5 mT) is sufficiently broad to make the scanner suitable for the aforementioned FMR experiments. Indeed, as shown in Fig. 2.10b, the polycrystalline YIG sphere has a linewidth of 3.5 mT, making it possible to visualize its full spectrum up to 2 mm above the sensing coil (i.e., the higher the elevation distance, the higher the shift in the resonance condition). Conversely, the monocrystalline YIG sphere has a non-symmetric FMR signal with a linewidth approximately equal to 1 mT. Moreover, the latter exhibits an anisotropic behavior since the shape of its spectrum depends on the orientation of the sample.

## 2.11 Design variations

In the FMR experiments shown in Fig. 2.10, the SNR is above one hundred so the system can actually tolerate a larger frequency noise for such class of measurements. Regarding this, a first modification to the proposed design is devoted to get rid of the integrated circuit in order to use commercial-off-the-shelf (COTS) components only. Indeed, the integrated energy restoring system allows to optimize the  $1/f$  noise performance of the oscillator but it requires a wire-bonding procedure and it complicates the steps for the eventual industrialization of the product (e.g., full-wafer production of chips). A suitable commercial oscillator with off-chip LC tank is the Maxim - MAX2609. It can be used in the frequency range from 550 MHz to 650 MHz, with a single-turn coil having a diameter of 6 mm, without changing the interface to the realized PLL, and with no impact on the magnetic system. As a matter of fact, the nuts used to fix the sensor tile to the magnetic structure allow to adjust its elevation distance in order to center the new frequency range. The frequency noise thermal floor results  $1.6 \text{ Hz/Hz}^{1/2}$  (i.e., ten times worse than the proposed integrated approach) with a corner frequency of 80 kHz. The latter impacts on the modulator and the overall power consumption since the modulation frequency is pushed from 10 kHz up to about 100 kHz.

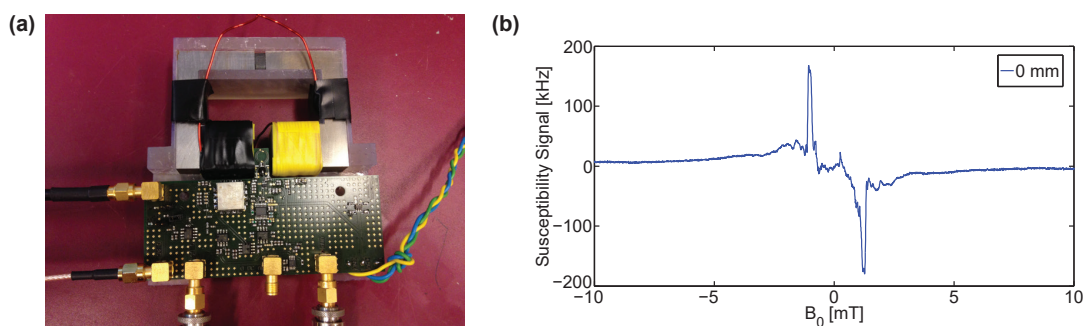


**Figure 2.11 – Close geometry detector operating at 610 MHz.** (a) Picture of the realized prototype. The magnetic system has a close geometry and the sensor PCB (142 mm wide) is modified in order for the coil to match the gap size. The structure is modular and the permanent magnet can be replaced by a piece of permenorm so as to perform zero-field measurements. A 0.75 mm thick copper wire is wound about the terminals of the two C-shaped metal branches (under the insulating yellow/black tape) in order to provide both the required modulation field ( $B_m$ ) and the field sweep capability. (b) Zero-field measurement on a 2 mm long ferromagnetic fiber placed on the trace of the sensing coil such that  $B_0$  results parallel to  $B_1$  and aligned along the axis of the fiber itself. The metal core is approximately  $30 \mu\text{m}$  thick and it is coated with glass ( $20 \mu\text{m}$ ) so as to avoid oxidation.

A second modification to the proposed scanner is shown in Fig. 2.11a. The goal is to get rid of the open geometry so as to reduce the reluctance of the magnetic circuit and increase the field homogeneity level along the three directions within the gap. The former leads to the possibility of reducing the required power consumption for an eventual field sweep and to increase the scan range for the inspection of broader signals. The latter reduces the problems of line broadening for big samples which are not thin films. Moreover, the magnetic system can be optimized in order to minimize the equivalent inductance, and then to allow for the magnetic field modulation without using a local modulation trace. As a matter of fact, the geometry shown in Fig. 2.11a is based on a  $20 \times 10 \times 5 \text{ mm}^3$  ferrite permanent magnet (HF 24/23, residual field of 365 mT) and two  $20 \times 56 \times 36 \text{ mm}^3$  C-shaped branches made of permenorm (Tab. 2.1 for technical details related to the material), leading to a  $B_0$  value of 18 mT and a homogeneity level of  $10 \text{ } \mu\text{T}/\text{mm}$  along the three directions. The gap has a volume of  $6 \times 20 \times 20 \text{ mm}^3$  and needs the PCB shape to be adjusted in order for the sensing coil to fit. A copper winding (0.75 mm thick) is added to perform both field sweep and field modulation for an overall weight of 450 g, an inductance of 13  $\mu\text{H}$ , and a DC coefficient equal to 1.5 mT/A in the gap.

Finally, the latter architecture is suitable for zero-field experiments since the ferrite block can be replaced by a piece of permenorm having the same size. In this case, it is possible to study the variation of susceptibility for suitable metal microfibers ensuring they are placed on the sensing wire, such that  $B_0$  results parallel to  $B_1$  and aligned along the axis of the fiber itself. As shown in Fig. 2.11b, a 2 mm long fiber composed of a 30  $\mu\text{m}$  thick magnetic material coated with glass leads to a peak-to-peak frequency variation of about 360 kHz within  $\pm 4 \text{ mT}$ .

### 2.12 Discussion and outlook

In this chapter, we have reported about the design, fabrication and characterization of a versatile and standing-alone ESR scanner working in the frequency range from 400 MHz to 610 MHz. Although the overall framework for the final industrial application cannot be disclosed in this thesis, all the technical details concerning the scanner are fully described.

In particular, (1) the geometry of the proposed architecture (open U-core), (2) the capability of performing ESR/FMR inspection up to 4 mm in elevation from the sensor in a few seconds, (3) the overall low power consumption (approximately 5 W), (4) the total low weight of the structure (approximately 400 g) and (5) the low frequency noise achieved by the sensing oscillator make the proposed prototype suitable to fulfill the initial requirements. Fig. 2.1 shows a picture of the standing alone ESR scanner without the back-end system.

In order to finalize the prototype, one should refine on the back-end system which is now composed of a DAQ-board and a laptop running the LabView<sup>®</sup> software for user interface. As a matter of fact, the latter should be replaced by a standard embedded computer with a small touch-screen monitor. Indeed, that would be easily embodied into the front-end electronics without dramatically affecting the total weight. Furthermore, in the realized prototype, the DAQ-board is connected to the laptop by means of a standard USB connection and that

increases the latency of the data exchange. In the final implementation, the adoption of an integrated board would contribute to reducing the measurement time.

### **2.13 Acknowledgement**

Financial support from the Swiss Commission for Technology and Innovation (CTI) is gratefully acknowledged.



# 3 Single-chip CMOS ESR detectors operating at 50, 92, and 146 GHz

## 3.1 Abstract

We report on the characterization of single-chip electron spin resonance (ESR) detectors operating at 50 GHz, 92 GHz, and 146 GHz. The core of the single-chip ESR detectors is an integrated LC oscillator, formed by a single-turn aluminum planar coil, a metal-oxide-metal capacitor, and two metal-oxide-semiconductor field effect transistors (FET) used as a negative resistance network. On the same chip, a second, nominally identical, LC oscillator together with a mixer and an output buffer are also integrated. Thanks to the slightly asymmetric capacitance of the mixer inputs, a signal at a few hundreds MHz is obtained at the output of the mixer. The latter is used for frequency down-conversion, with the aim to obtain an output signal at a frequency easily manageable off-chip. The coil diameters are 120  $\mu\text{m}$ , 70  $\mu\text{m}$ , and 45  $\mu\text{m}$  for the U-band, W-band, and the D-band oscillators, respectively. The experimental frequency noises at 100 kHz offset from the carrier are 90 Hz/Hz<sup>1/2</sup>, 300 Hz/Hz<sup>1/2</sup>, and 700 Hz/Hz<sup>1/2</sup> at 300 K, respectively. The ESR spectra are obtained by measuring the frequency variations of the single-chip oscillators as a function of the applied magnetic field. The experimental spin sensitivities, as measured with a sample of  $\alpha,\gamma$ -bisdiphenylene- $\beta$ -phenylallyl (BDPA)/benzene complex, are  $1 \times 10^8$  spins/Hz<sup>1/2</sup>,  $4 \times 10^7$  spins/Hz<sup>1/2</sup>, and  $2 \times 10^7$  spins/Hz<sup>1/2</sup> at 300 K, respectively. We also show the possibility to perform experiments up to 360 GHz by means of the higher harmonics in the microwave field produced by the integrated single-chip LC oscillators.

## 3.2 Motivation

The previously reported single-chip ESR detectors (Refs. [7–10]) operated at 8–28 GHz, in the temperature range from 300 K down to 4 K. Here, we report on the design and characterization of new ESR detectors based on the same operating principle but working at significantly

---

This chapter is a minor variation of the publication "*Single-chip electron spin resonance detectors operating at 50 GHz, 92 GHz, and 146 GHz*" [4]. The design of the integrated circuit has been carried out by G. Gualco (a former PhD student in the group of Dr. G. Boero).

higher frequencies, in particular at 50 GHz (U-band), 92 GHz (W-band), and 146 GHz (D-band). Operation at higher frequency is interesting for several reasons including a potentially better spin sensitivity (Sec. 1.4), better spectral resolution for some classes of samples, and the access to samples with large zero-field splitting which are “silent” at lower frequencies [43–47]. The possibility to work at such high frequencies is allowed by the use of the 40 nm CMOS technology, which is an advanced technology node for integrated circuits. The interesting and the problematic aspects of single-chip ESR detectors with respect to more conventional microresonator based approaches are discussed in Secs. 3.3–3.5.

### 3.3 Description of the single-chip ESR detectors

The three single-chip ESR detectors described in this work are manufactured using a standard 40 nm bulk-CMOS technology (Taiwan Semiconductor Manufacturing Company, Taiwan). The use of a 40 nm technology, instead of the 130 nm or 180 nm technologies previously adopted [8–10], is essential for the realization of oscillators operating above 100 GHz, with realistic possibilities to achieve operating frequencies above 300 GHz [48]. Each detector has a size of about  $0.6 \times 0.6 \text{ mm}^2$  (Fig. 3.1) and it is composed of two LC oscillators, a mixer, and an output buffer.

Each LC oscillator consists of two minimum-length nMOS cross-coupled transistors and an LC resonator (Fig. 3.1b). The adoption of nMOS rather than pMOS transistors is due to their higher speed [49]. No tail current transistor [49] is used in this topology and the circuit is fed by means of an external power supply. This is important to ensure reasonable headroom voltage for oscillators realized using deep sub-micrometer technologies as well as to avoid additional flicker noise up-conversion from the tail transistor [50]. The U-band and the W-band oscillators have, in parallel with the single-turn planar coil, a pair of integrated metal-oxide-metal (MOM) capacitors having nominal values of 50 fF and 15 fF, respectively. The D-band oscillator has no capacitance in parallel with the single-turn planar coil and, hence, the oscillation frequency is determined by the parasitic capacitances, mainly due to the cross-coupled MOS transistors. In Tab. 3.1, we report the key features of the realized single-chip ESR detectors, including the geometrical details, the frequency noise ( $FN$ ), and the minimum microwave magnetic field  $B_1$  at the center of the integrated single-turn planar coil. The lower limit for the value of  $B_1$  is determined by the minimum transconductance of the cross-coupled transistor pair required for stable oscillations, whereas the upper limit is given by the maximum voltage swing which can be applied across the transistors without damaging their thin gate oxide. The value of  $B_1$  is estimated by knowing the DC bias voltage of the oscillator  $V_A$ . In condition of stable oscillations [51], the oscillation amplitude is approximately given by  $V_{0A} = V_{0A+} - V_{0A-} \cong V_A$ . Hence,  $B_1 \cong (B_u V_A) / (2\omega_{LC} L)$ , where  $B_u \cong (\mu_0 / d)$ . This  $B_1$  estimation is in agreement with saturation experiments based on samples whose relaxation times are known.

### 3.3. Description of the single-chip ESR detectors

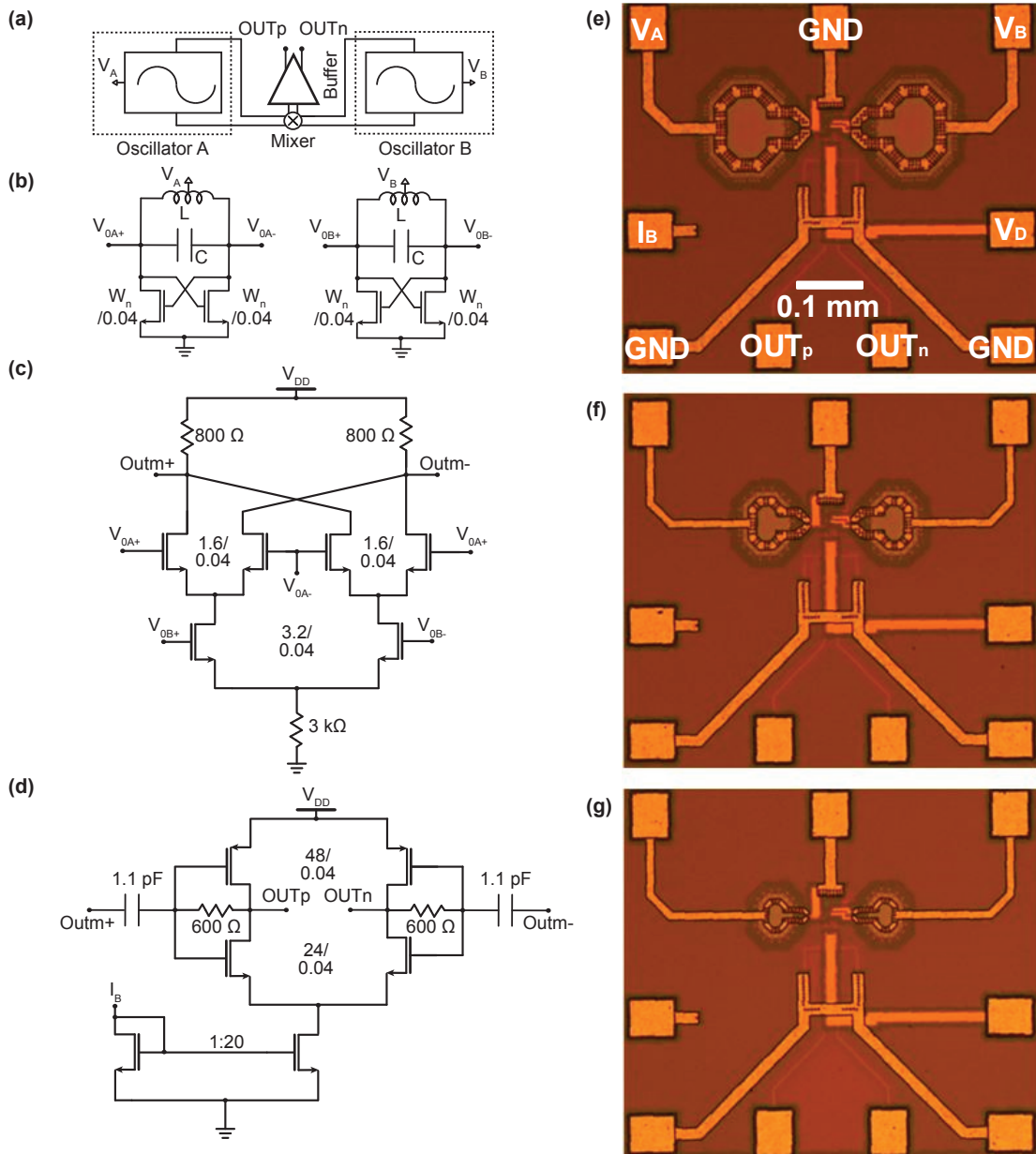


**Figure 3.1 – Schematics and pictures of the CMOS ESR detectors.** Detailed schematics of the integrated electronics in the single-chip ESR detectors: (a) block diagram, (b) LC oscillators, (c) mixer, (d) output buffer. The dimensions (width/length) of the transistors are in micrometers. The width  $W_n$  of the cross-coupled transistors of each oscillator are reported in Tab. 3.1.  $V_{DD} \cong 1.3\ \text{V}$ ,  $V_A = (0.4\ \text{V to } 1\ \text{V})$ ,  $V_B = (0.4\ \text{V to } 1\ \text{V})$ ,  $I_B \cong 10\ \mu\text{A}$ . Pictures of the single-chip ESR detectors: (e) U-band detector operating at 50 GHz ( $120\ \mu\text{m}$  diameter coil), (f) W-band detector operating at 92 GHz ( $70\ \mu\text{m}$  diameter coil), (g) D-band detector operating at 146 GHz ( $45\ \mu\text{m}$  diameter coil).

The mixer is a double-balanced Gilbert cell (Fig. 3.1c), biased through a resistor to ground since simulations revealed that is an efficient way to reduce the corresponding  $1/f$  noise. Its power consumption depends on the oscillation amplitude through the gate-source voltage of each switching transistor, and it can be minimized by reducing the oscillator voltage supply. In order to reduce the capacitive load mismatch between the two oscillators, the two lower

### Chapter 3. Single-chip CMOS ESR detectors operating at 50, 92, and 146 GHz

switches are double sized transistors with respect to the other four. The output buffer (Fig. 3.1d) is a differential class-AB amplifier whose power consumption is controlled by means of an off-chip resistor of 3.4 k $\Omega$  connected to  $V_{DD}$ . The same mixer and output buffer are used for all the detectors. The total power consumption of the mixer and the output buffer is about 130  $\mu$ W ( $V_{DD} \cong 1.3$  V,  $I_{DD} \cong 100$   $\mu$ A).

FOCUS ON THE THREE CMOS ESR DETECTORS			
	U-band	W-band	D-band
Frequency [GHz] - (Osc. A, Osc. B)	49.2 49.8	90 92	142 146
Coil diameter [ $\mu$ m]	120	70	45
Coil wire width [ $\mu$ m]	15	10	5
Approx. coil resistance at oper. frequency [ $\Omega$ ]	0.8	0.9	1.3
Approx. coil inductance [pH]	160	90	65
Approx. coil Q-factor	60	60	40
Approx. capacitance [fF] - (Osc. A, Osc. B)	65 64	35 33	20 18
MOS width [ $\mu$ m]	13.0	13.0	9.6
MOS length [nm]	40	40	40
$I_{A,min}$ [mA] $V_{A,min}$ [V] @ 300 K	1.9 0.5	2.5 0.6	2.9 0.7
$I_{A,min}$ [mA] $V_{A,min}$ [V] @ 10 K	0.6 0.4	0.8 0.5	0.9 0.5
$B_{1,min}$ [ $\mu$ T] @ 300 K	100	200	400
$B_{1,min}$ [ $\mu$ T] @ 10 K	200	400	700
$FN$ [Hz/Hz <sup>1/2</sup> ] @ 1 kHz, 300 K	900 (6)	2300 (9)	8000 (15)
$FN$ [Hz/Hz <sup>1/2</sup> ] @ 10 kHz, 300 K	300 (6)	1100 (9)	2100 (15)
$FN$ [Hz/Hz <sup>1/2</sup> ] @ 100 kHz, 300 K	90 (6)	300 (9)	700 (15)
$FN$ [Hz/Hz <sup>1/2</sup> ] @ 1 MHz, 300 K	40 (6)	110 (9)	200 (15)
$N_{min}$ [spins/Hz <sup>1/2</sup> ] @ 1 MHz, 300 K	$1 \times 10^8$ ( $3 \times 10^6$ )	$4 \times 10^7$ ( $5 \times 10^5$ )	$2 \times 10^7$ ( $2 \times 10^5$ )

**Table 3.1 – Key-features of the three CMOS single-chip ESR detectors.** Characteristics of the ESR detectors, each consisting of two LC oscillators (oscillator A and oscillator B, operating at frequencies a few percent apart), a mixer, and an output buffer. In the last two rows, both the theoretical (in parenthesis) and the experimentally measured frequency noise  $FN$  and spin sensitivity  $N_{min}$  are compared. The theoretical values of the spin sensitivity is computed using Eq.11 in Ref. [7] (i.e.,  $N_{min} = \alpha(T^{3/2}R^{1/2}B_0^{-2}B_u^{-1})$ , with  $\alpha \cong 20 \text{ m}^{-1}\text{kg}^{5/2}\text{s}^{-4}\text{K}^{-3/2}\text{A}^{-3}$ ) assuming as a noise source only the thermal noise contribution of the coil resistance  $R$  (about 0.8  $\Omega$ , 0.9  $\Omega$ , and 1.3  $\Omega$  for the 50 GHz, 92 GHz, and 146 GHz detectors, respectively). The theoretical value for of the frequency noise spectral density is computed using Eq. 1.17 (i.e.,  $(k_B TR)^{1/2}(f_{LC}/V_0)$  at the oscillation amplitudes  $V_0$  of about 0.5 V, 0.6 V, 0.7 V for the 50 GHz, 92 GHz, and 146 GHz detectors, respectively). The experimental spin sensitivity is measured with a sample of BDPA (spin density:  $1.5 \times 10^{27}$  spins/m<sup>3</sup>, relaxation times:  $T_1 \cong T_2 \cong 100$  ns) at 300 K [42, 52, 53].



### 3.3. Description of the single-chip ESR detectors

As shown in Tab. 3.1, the measured frequency noise at 100 kHz from the carrier is up to two orders of magnitude larger than the thermal noise limit due to the coil resistance (Sec. 1.4). This is mainly caused by the very large  $1/f$  frequency noise having a corner frequency above 1 MHz from the carrier. In this context, the combination of an excessively large  $B_1$  (for samples with a large  $T_1 T_2$  value) and the  $1/f$  noise are responsible for the very significant deterioration of the spin sensitivity (two to three orders of magnitude) with respect to the thermal noise limit reported in Tab. 3.1 (and discussed in Sec. 3.5). Indeed, the measured frequency noise, at least up to 1 MHz from the carrier, is dominated by the  $1/f$  noise and it is almost temperature independent from 300 K down to 10 K.

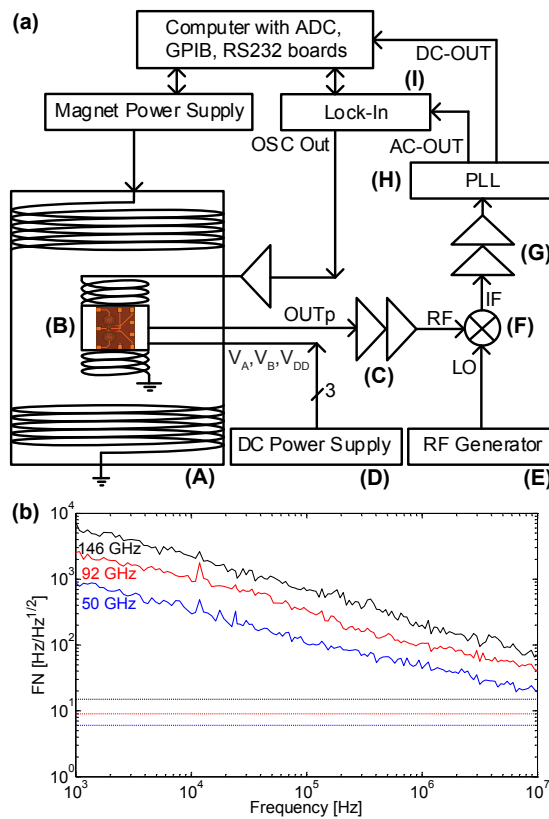


**Figure 3.2 – Set-up and noise spectral density of the three CMOS single-chip ESR detectors.** (a) Block diagram of the complete set-up: (A) Oxford Superconducting Magnet 0-17 T with variable temperature insert; (B) single-chip ESR detector (the frequency of the signal at the output of the chip OUTp corresponds to the frequency difference between the two integrated oscillators, i.e., 600 MHz for U-band detector, 2 GHz for the W-band detector, and 4 GHz for the D-band detector, as reported in Tab. 3.1); (C) RF amplification stage, composed of two HMC-C001 with 15 dB gain each; (D) DC power supply units (three Keithley 2400) for  $V_{DD}$ ,  $V_A$  and  $V_B$  (Fig. 3.1); (E) RF generator (Stanford Research Systems SG384); (F) Mixer (Mini-Circuits ZFM-2000+); (G) IF amplification stage (two Mini-Circuits ZFL-500LN, 24 dB gain each); (H) Homemade low-noise Phase-Locked-Loop (200 kHz FM bandwidth, 150-200 MHz lock range) based on a phase detector (HMC439QS16G) and a local oscillator (Crystek CVCO55CL-0150-0200); (I) Lock-in amplifier (EG&G 7260). (b) Measured frequency noise spectral density of the three single-chip ESR detectors at 300 K. The dashed lines show the coil resistance thermal noise limit at 300 K (Table 3.1).

In Fig. 3.2, we show the block diagram of the complete set-up used to perform the electron spin resonance experiments reported in this work. Field modulation with lock-in synchronous demodulation is used as in conventional continuous wave ESR spectroscopy. The field modu-

lation coil produces a maximum field modulation of about 0.2 mT at 100 kHz. The signal at the output of the chip is further frequency down-converted to a second intermediate frequency (150-200 MHz) so as to match the lock range of a homemade frequency-to-voltage converter based on a phase-locked-loop (PLL) [54, 55]. The latter produces two output signals: (1) an “AC-ESR signal” carrying the information on the frequency modulation of the integrated oscillator due to the field modulation, and (2) a “DC-ESR signal” containing the information about the frequency difference between the two integrated oscillators. The AC-ESR signal is subsequently demodulated using a lock-in amplifier whereas the DC-ESR signal is directly acquired. In some measurements with samples having very broad lines, the field modulation is not used and only the DC-ESR signal is measured. The DC-ESR signal is proportional to the real part of the susceptibility  $\chi'$  (and, hence, it has the shape of a dispersion signal). The AC-ESR signal is proportional to  $d\chi'/dB$  (and, hence, it has the shape of the first derivative of a dispersion signal, as described in Sec. 1.5).

### 3.4 Electron spin resonance experiments

Figs. 3.3-3.5 show the results of measurements performed with the three single-chip ESR detectors operating at 50, 92, and 146 GHz, respectively. We performed experiments on samples having very different characteristics, including an exchange narrowed standard system (BDPA), three hyperfine split systems having 100%, 1%, and 0.2% concentrations ( $\text{Cu}^{2+}$  in TPP,  $\text{Cu}^{2+}$  in  $\text{Ni}(\text{mnt})_2$ , and  $\text{Mn}^{2+}$  in  $\text{MgO}$ ), a zero field split system ( $\text{Cr}^{3+}$  in  $\text{Al}_2\text{O}_3$ ), and a quantum magnet with a very broad line in its paramagnetic state ( $\text{SrCu}(\text{BO}_3)_2$ ). Details of each sample are given below. This variety of samples helps in underlining both the interesting and the problematic aspects of the single-chip ESR detector approach.

In Fig. 3.3, we report the results of measurements performed using the 50 GHz single-chip oscillator. Fig. 3.3a shows the spectrum obtained with a powder sample of  $\text{MgO}$  (98% purity, Sigma Aldrich, 220361) having a volume of about  $20 \times 20 \times 10 \mu\text{m}^3$ . The spectrum mainly consists of six hyperfine lines, originating from the  $^{55}\text{Mn}^{2+}$  ion having nuclear spin  $I = 5/2$  (and electron spin  $S = 5/2$ ). The measured separation between the lines is about 8.7 mT, in agreement with previous measurements [56]. The measured width of each hyperfine line is about 0.8 mT for a  $B_1$  of about 0.2 mT. Measurements performed using an ordinary cavity at 10 GHz show that the unsaturated linewidth is about 0.2 mT, with significant saturation for  $B_1$  values above 0.05 mT (due to  $T_1 \cong 140$  ns and  $T_2 \cong 30$  ns). At the  $B_1$  as low as possible with our oscillator (i.e., about 0.2 mT), the signal is broadened by a factor of four and reduced in amplitude by a factor of three with respect to a measurement performed with a  $B_1$  below 0.05 mT. Additionally, in order to reduce as much as possible the  $B_1$  value, the oscillator is operated at its minimum bias voltage, a condition which increases its frequency noise by about a factor of four (i.e., from  $300 \text{ Hz/Hz}^{1/2}$  to  $1200 \text{ Hz/Hz}^{1/2}$  at 10 kHz from the carrier). The six hyperfine lines are likely to be caused only by ( $m_s = -1/2$ ,  $m_s = 1/2$ ) transitions. All the other transitions are not observed due to their strongly anisotropic character [57], which makes them invisible for a sample in powder form. Assuming an  $\text{Mn}^{2+}$  concentration of about 0.2%

### 3.4. Electron spin resonance experiments

(as estimated for a nominally identical sample in Ref. [58]) and a density of about  $3600 \text{ kg/m}^3$  (as for an MgO crystal, probably an overestimation with respect to the effective grain density), the number of  $\text{Mn}^{2+}$  spins contained in the sample is about  $4 \times 10^{11}$ . Since the signal amplitude is about 50 kHz and the noise level is about  $1200 \text{ Hz/Hz}^{1/2}$ , the spin sensitivity (as defined in Sec. 1.4) is about  $3 \times 10^{10} \text{ spins/Hz}^{1/2}$  for this sample. In order to cross-check whether the obtained value is coherent with the measurements performed on other samples, we can compute a normalized spin sensitivity for an  $S = 1/2$  spin system having a single unsaturated line of 0.1 mT measured with optimal field modulation, and that gives a normalized spin sensitivity of about  $5 \times 10^7 \text{ spins/Hz}^{1/2}$ . A large broader signal is also clearly visible close to the third hyperfine line starting from lower fields, as also reported in Ref. [58] and attributed to unknown additional paramagnetic impurities in the MgO sample. In our case, we also observe an additional broad signal between the fourth and fifth line, and further smaller lines probably caused by other impurities. As further discussed in Sec. 3.5, this experiment on the Mn:MgO sample helps in underlining a severe limitation of the single-chip ESR detectors reported in this chapter: for samples having a product  $T_1 T_2$  larger than  $10^{-15} \text{ s}^2$ , the large minimum  $B_1$  (i.e., about 0.2 mT) causes line broadening, a very significant deterioration of the signal-to-noise ratio, and, in turn, a reduction of the spin sensitivity.

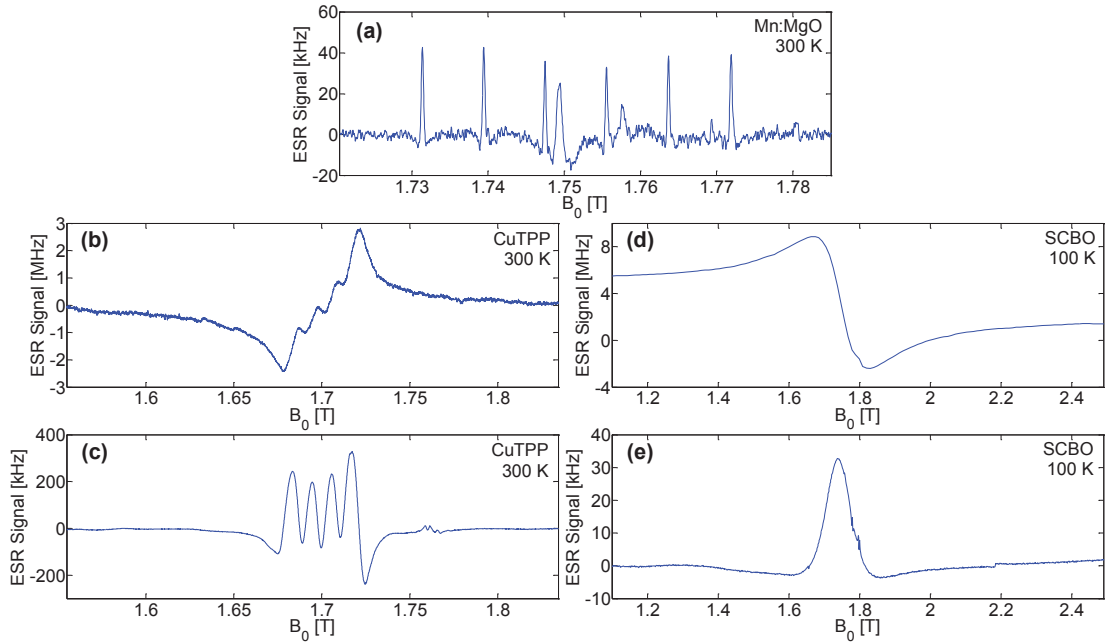


**Figure 3.3 – ESR experiments performed with the 50 GHz CMOS single-chip detector.** Experimental conditions notations: T is the sample temperature,  $B_1$  is the amplitude of the microwave magnetic field,  $B_m$  is the amplitude of the modulation magnetic field,  $\nu_m$  is the frequency of the magnetic field modulation,  $t_s$  is the time interval of the magnetic field sweep, and  $\Delta f$  is the equivalent noise bandwidth of the lock-in. (a) AC ESR spectrum of a  $20 \times 20 \times 20 \text{ }\mu\text{m}^3$  sample of Mn:MgO (see text) with  $\nu_m = 9.8 \text{ kHz}$ ,  $B_m = 0.2 \text{ mT}$ ,  $B_1 \cong 0.2 \text{ mT}$ ,  $\Delta f = 2.5 \text{ Hz}$ ,  $T = 300 \text{ K}$ ,  $t_s = 5 \text{ min}$ . (b-c) ESR spectra performed on a  $60 \times 60 \times 60 \text{ }\mu\text{m}^3$  sample of CuTPP (see text) at  $T = 300 \text{ K}$ , (b) DC signal, (c) AC signal with  $\nu_m = 9.8 \text{ kHz}$ ,  $B_m = 0.9 \text{ mT}$ ,  $B_1 \cong 0.2 \text{ mT}$ ,  $\Delta f = 2.5 \text{ Hz}$ ,  $t_s = 11 \text{ min}$ . (d-e) ESR spectra of a  $100 \times 100 \times 20 \text{ }\mu\text{m}^3$  sample of SCBO (see text) at  $T = 100 \text{ K}$ , (d) DC signal, (e) AC signal with  $\nu_m = 9.8 \text{ kHz}$ ,  $B_m = 0.15 \text{ mT}$ ,  $B_1 \cong 0.2 \text{ mT}$ ,  $\Delta f = 0.25 \text{ Hz}$ ,  $t_s = 28 \text{ min}$ .

### Chapter 3. Single-chip CMOS ESR detectors operating at 50, 92, and 146 GHz

In Fig. 3.3b,c, we report experiments with a single crystal of 5,10,15,20-Tetraphenyl-21H,23H-porphine  $\text{Cu}^{2+}$  (CuTPP, Aldrich, 252182) having a volume of  $60 \times 60 \times 60 \mu\text{m}^3$ . The spectrum consists of four hyperfine lines (the  $^{63,65}\text{Cu}$  nuclei have spin  $I = 3/2$ ) each having a width of about 10 mT and a separation from the others of about 16 mT. Due to the limited maximum field modulation available in our set-up (about 0.2 mT), the AC-ESR signal (Fig. 3.3c) is about one order of magnitude smaller than the DC-ESR signal (Fig. 3.3b). CuTPP has a density of about  $1400 \text{ kg/m}^3$  and a molecular weight of 676, so that the spin density is about  $1.2 \times 10^{27} \text{ spins/m}^3$  and the number of  $\text{Cu}^{2+}$  spins contained in the sample happens to be about  $2.7 \times 10^{14}$ . Since the signal amplitude is about 300 kHz and the noise is about  $100 \text{ Hz/Hz}^{1/2}$ , the spin sensitivity for this sample is about  $3 \times 10^{11} \text{ spins/Hz}^{1/2}$ . The normalized spin sensitivity (considering four hyperfine lines for an unsaturated 0.1 mT line of a  $S = 1/2$  system measured with optimal field modulation) is about  $2 \times 10^7 \text{ spins/Hz}^{1/2}$ , a coherent value with respect to the one computed on the Mn:MgO sample.

In Fig. 3.3d,e, we report the results obtained on a  $100 \times 90 \times 20 \mu\text{m}^3$  single crystal of  $\text{SrCu}(\text{BO}_3)_2$  (SCBO), a widely investigated quantum magnet (Refs. [59, 60]), which we measured in its paramagnetic state at 100 K. The spectrum consists of a single broad line (about 170 mT). As for the CuTPP sample, the sub-optimal field modulation amplitude determines an AC-ESR signal (about 30 kHz, as shown in Fig. 3.3e) much smaller than the DC-ESR signal (about 10 MHz, as shown in Fig. 3.3d). Despite the larger noise in the DC-ESR signal (about  $940 \text{ Hz}_{\text{rms}}$  with respect to about  $130 \text{ Hz}_{\text{rms}}$ ) the signal-to-noise ratio results larger for the DC-ESR signal.

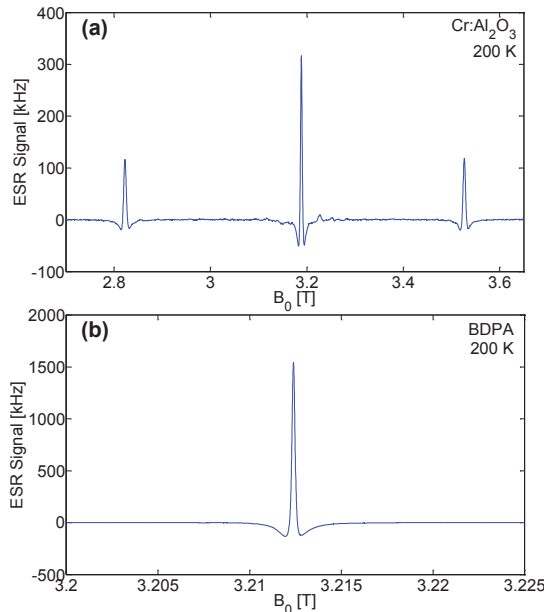


**Figure 3.4 – ESR experiments performed with the 92 GHz CMOS single-chip detector.** (a) AC ESR spectrum of a  $50 \times 50 \times 40 \mu\text{m}^3$  sample of ruby (see text) with  $\nu_m = 9.8 \text{ kHz}$ ,  $B_m = 0.15 \text{ mT}$ ,  $B_1 \cong 0.3 \text{ mT}$ ,  $\Delta f = 0.25 \text{ Hz}$ ,  $t_s = 18 \text{ min}$ ,  $T = 200 \text{ K}$ . (b) AC ESR spectrum of a  $3 \times 3 \times 3 \mu\text{m}^3$  of BDPA (see text) with  $\nu_m = 98 \text{ kHz}$ ,  $B_m = 0.12 \text{ mT}$ ,  $B_1 \cong 0.25 \text{ mT}$ ,  $\Delta f = 0.25 \text{ Hz}$ ,  $t_s = 4.5 \text{ min}$ ,  $T = 200 \text{ K}$ . The notations are defined in Fig. 3.3.

Fig. 3.4a shows the results of a measurement performed using the 92 GHz single-chip oscillator

### 3.4. Electron spin resonance experiments

on a single crystal of 1%  $\text{Cr}^{3+}:\text{Al}_2\text{O}_3$  (Ruby G10, Saphirwerk Industrieprodukt AG, Switzerland) having a volume of about  $50 \times 50 \times 40 \mu\text{m}^3$ . Only the three high field lines are shown. In Fig. 3.4b, we report the results obtained with a single crystal of BDPA (1:1  $\alpha,\gamma$ -bisdiphenylene- $\beta$ -phenylallyl/benzene complex, Sigma Aldrich 152560) having a volume of about  $3 \times 3 \times 3 \mu\text{m}^3$ . Due to the excessive  $B_1$  (about 0.25 mT) and the sub-optimal field modulation amplitude, the signal amplitude is significantly reduced (1.5 MHz instead of 13 MHz) and the linewidth is broadened (0.4 mT instead of 0.1 mT). Assuming a spin density of about  $1.5 \times 10^{27}$  spins/ $\text{m}^3$  [42], the total number of spins contained in the sample is about  $4 \times 10^{10}$ . Since the signal amplitude is about 1.5 MHz and the frequency noise spectral density is about  $300 \text{ Hz}/\text{Hz}^{1/2}$ , the experimentally achieved spin sensitivity, according to the definition given in Sec. 1.4, is about  $3 \times 10^7$  spins/ $\text{Hz}^{1/2}$ . Tab. 3.1 shows the obtained spin sensitivities measured with a BDPA sample using the three single-chip ESR detectors. The large difference (about two orders of magnitude) between the experimentally achieved spin sensitivity and the thermal noise limit (given in parenthesis) is discussed in Sec. 3.5.

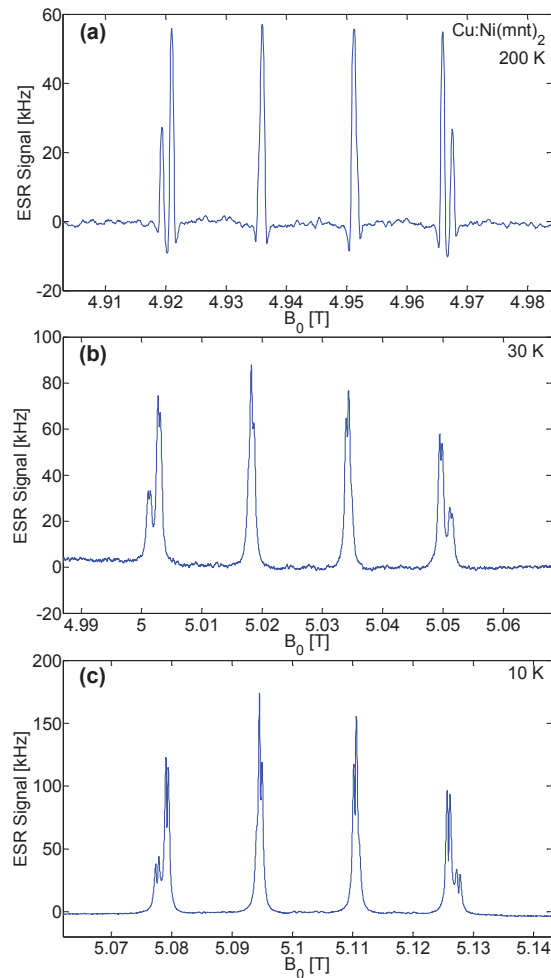


**Figure 3.5 – ESR experiments performed with the 146 GHz CMOS single-chip detector.** (a-c) AC ESR spectra of a  $40 \times 40 \times 5 \mu\text{m}^3$  sample of 1%  $\text{Cu}(\text{II})(\text{mnt})_2$  in  $\text{Ni}(\text{mnt})_2$  with  $\nu_m = 98 \text{ kHz}$ ,  $B_m = 0.15 \text{ mT}$ ,  $B_1 \cong 0.6 \text{ mT}$ ,  $\Delta f = 0.25 \text{ Hz}$ ,  $t_s = 16 \text{ min}$  at (a) 200 K, (b) 30 K, (c) 10 K. The notations are defined in Fig. 3.3.

### Chapter 3. Single-chip CMOS ESR detectors operating at 50, 92, and 146 GHz

In Fig. 3.5, we report the results of measurements performed using the 146 GHz single-chip oscillator on a single crystal of  $\text{Cu}^{2+}$ -doped tetramethylammonium-bis(maleonitriledithiolate) nickel with a Cu concentration of 1% (1%  $\text{Cu}(\text{mnt})_2$  in  $\text{Ni}(\text{mnt})_2$ ) and a volume of  $40 \times 40 \times 5 \mu\text{m}^3$ . All spectra show the hyperfine splitting produced by the Cu nuclei ( $^{63}\text{Cu}$  and  $^{65}\text{Cu}$ ), both having spin  $I = 3/2$ . The measured spectra have shapes which are temperature dependent, with more resolved lines at low temperature. Both at room temperature and at 200 K, the shape of the signal is, with good approximation, the first derivative of a dispersion curve (as expected from Sec. 1.5 and Refs. [7, 9]), whereas at low temperature it is no more the case. The reason for this behaviour is unclear. The shift of the resonance towards higher fields at low temperatures is due to the shift towards higher frequency of the oscillator (about 4.5 GHz from 300 K to 10 K). Assuming a spin density of  $1.7 \times 10^{25}$  spins/ $\text{m}^3$  (as obtained from data in Ref. [61]), the measured spin sensitivity for this sample is about  $1.8 \times 10^9$  spins/ $\text{Hz}^{1/2}$ . The normalized spin sensitivity considering eight hyperfine lines with 0.1 mT width measured with optimal field modulation is about  $4 \times 10^6$  spins/ $\text{Hz}^{1/2}$ .

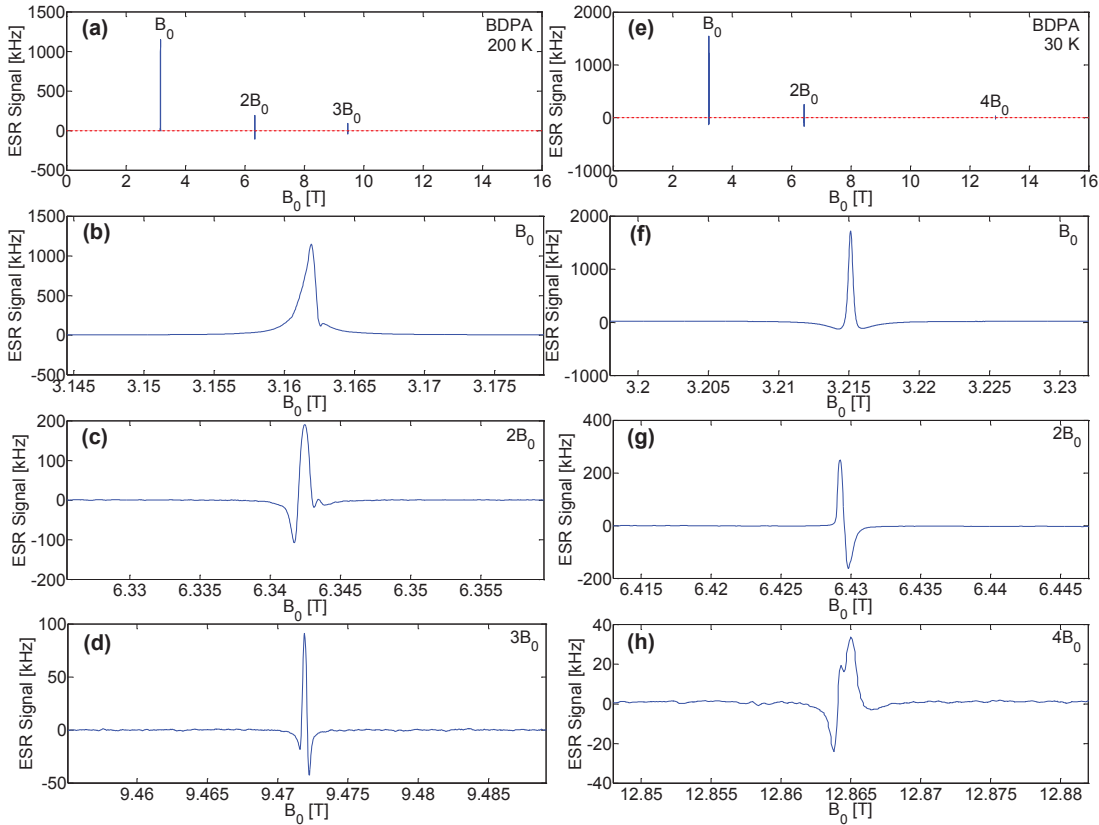


**Figure 3.6 – ESR experiments performed with the 92 GHz CMOS single-chip detector at higher harmonics.** Left side (a-d): AC ESR spectra with a  $6 \times 6 \times 5 \mu\text{m}^3$  sample of BDPA with  $\nu_m = 98$  kHz,  $B_m = 0.12$  mT,  $B_1 \cong 0.2$  mT,  $\Delta f = 0.25$  Hz,  $t_s = 3$  min,  $T = 200$  K. (a) All measurements. Narrow field sweeps about (b)  $B_0 = (\omega_{LC}/\gamma)$ , (c)  $B_0 = 2(\omega_{LC}/\gamma)$ , (d)  $B_0 = 3(\omega_{LC}/\gamma)$ . Right side (g-h): AC ESR spectra of a  $3 \times 3 \times 3 \mu\text{m}^3$  sample of BDPA with  $\nu_m = 98$  kHz,  $B_m = 0.12$  mT,  $B_1 \cong 0.2$  mT,  $\Delta f = 0.25$  Hz,  $t_s = 1$  min,  $T = 30$  K. (e) All measurements. Narrow field sweeps about (f)  $B_0 = (\omega_{LC}/\gamma)$ , (g)  $B_0 = 2(\omega_{LC}/\gamma)$ , (h)  $B_0 = 4(\omega_{LC}/\gamma)$ . The notations are defined in Fig. 3.3. Note: signals at  $B_0 = 4(\omega_{LC}/\gamma)$  at 200 K and at  $B_0 = 3(\omega_{LC}/\gamma)$  at 30 K were also observed but not reported in the graphs above because accidentally measured with a much faster magnetic field sweep rate which reduced their signal amplitude and distorted their shape.

Finally, in Fig. 3.6, we show the possibility to perform experiments at higher harmonics of the fundamental frequency of the oscillator. In particular, Fig. 3.6 shows ESR spectra obtained with BDPA samples of about  $6 \times 6 \times 5 \text{ } \mu\text{m}^3$  and  $3 \times 3 \times 3 \text{ } \mu\text{m}^3$ . Fig. 3.6a-h shows the results of experiments performed at magnetic fields from 2 T to 13 T and resonances are observed at about 3.2, 6.4, 9.5, and 12.9 T. The observed resonant fields correspond to frequencies of about 90, 180, 270, and 360 GHz, which are the fundamental and the second, third, and fourth harmonics of the integrated oscillator. This indicates that the single-chip ESR detectors are capable to perform ESR experiments at least up to the fourth harmonic of the fundamental frequency. Qualitatively, we can explain this behavior by the presence of higher harmonics in the oscillator currents and, hence, in the microwave magnetic field acting on the sample. The signal amplitude significantly decreases at higher harmonics and both the signal shape and its width are dependent on the observed harmonic. The smaller sample is sufficiently small to avoid any transition to the strong coupling regime [10], whereas the larger one is in strong coupling (at the first harmonic but not at the third one). We have attempted to model the experimental results assuming that the sample can be represented by an RLC resonator inductively coupled to the LC tank of the integrated oscillator (Ref. [10]). Performing the simulation of the overall circuit using an electronic circuit simulator (in our case Cadence<sup>®</sup>), we obtain that the variation of the fundamental frequency  $\Delta f_{LC}$  is different from zero not only when  $B_0 \cong (\omega_{LC}/\gamma)$  but also when  $B_0 \cong n(\omega_{LC}/\gamma)$ , where  $n$  is an integer number larger than 1. Indeed, simulations predict the observed results with an accuracy well within one order of magnitude for both amplitude and width, whereas the main limitation to the accuracy is presumably standing in the modeling of the harmonic content for the transistors currents at frequencies close to the cut-off. Moreover, the reduced sensitivity at higher harmonics (about an order of magnitude for the third harmonic) severely limits their applicability for high frequency spectroscopy studies of practical interest. Nevertheless, for samples having a sufficiently large signal-to-noise ratio, the possibility to perform multiple-frequency ESR experiments up to 400 GHz with a single-chip detector having a large scale production cost of a few dollars or less is certainly attractive. To some extent, CMOS [48, 62] or other integrated circuit technologies [63] currently achieving fundamental oscillation frequencies of 300 to 500 GHz, would allow for multiple-frequency ESR experiments up to the THz range.

### 3.5 Discussion and outlook

In this chapter, we have reported about the design and the performance of three single-chip ESR detectors operating at 50 GHz, 92 GHz, and 146 GHz, i.e., at significantly higher working frequencies with respect to previous designs (which operated up to 28 GHz [7–10]). As shown in Ref. [7], assuming that the frequency noise is only given by the thermal noise of the coil resistance  $R$ , the theoretical spin sensitivity results  $N_{\min} = \alpha (T^{3/2} R^{1/2} B_0^{-2} B_u^{-1}) \propto f_{LC}^{-2} d$ , with  $\alpha \cong 20 \text{ m}^{-1} \text{ kg}^{5/2} \text{ s}^{-4} \text{ K}^{-3/2} \text{ A}^{-3}$ . Hence, the theoretical spin sensitivity is  $4 \times 10^7$  spins/Hz<sup>1/2</sup> for the 21 GHz detector reported in Ref. [9] and  $2 \times 10^5$  spins/Hz<sup>1/2</sup> for the 146 GHz detector reported in this work. This expected theoretical improvement of two orders of magnitude

would be due to both the higher operating frequency (146 GHz instead of 21 GHz) and the smaller coil diameter (45  $\mu\text{m}$  instead of 185  $\mu\text{m}$ ). However, the 21 GHz detector achieved an experimental spin sensitivity of  $5 \times 10^8$  spins/Hz<sup>1/2</sup> whereas the one operating at 146 GHz achieves a spin sensitivity of  $2 \times 10^7$  spins/Hz<sup>1/2</sup>. To some extent, the higher working frequency (together with the smaller coil diameter) improves the experimental spin sensitivity only by about one order of magnitude, i.e., one order of magnitude less than expected. In fact, due to the smaller coil diameter (and, hence, due to a smaller sensitive volume), the 146 GHz detector has an experimental concentration sensitivity which is about one order of magnitude worse than the one of the 21 GHz detector.

In Tab. 3.1, we reported the experimental and the theoretical values of both spin sensitivity and frequency noise spectral density for each of the three single-chip ESR detectors. As a result, for all of them the measured spin sensitivity is about two orders of magnitude worse than the one expected if only the thermal noise of the coil resistance were considered. This sensitivity degradation is essentially due to two phenomena: (1) the presence of  $1/f$  noise in the frequency noise spectral density up to frequencies as large as 1 MHz from the carrier, and (2) the large minimum  $B_1$  (ranging from 0.2 to 0.7 mT) which causes significant saturation for samples having  $T_1 T_2$  larger than  $10^{-16}$  s<sup>2</sup>.

Field modulation at frequencies above 1 MHz would help at improving the sensitivity. However, that is not easily implementable (with amplitude above 0.1 mT) especially at low temperatures, due to heat dissipation issues and  $T_1$ -related limitations. In this context, the reduction of the  $1/f$  frequency noise is a key issue for many industrially relevant applications of integrated microwave oscillators [64–67], including ESR. Consequently, it is likely that the spin sensitivity of our application will be positively affected by the overall advances on the  $1/f$  noise related topics coming from the scientific community.

The amplitude of the microwave field  $B_1$  depends on the oscillator bias voltage  $V_A$ , the coil diameter  $d$ , and the coil inductance  $L$  (where  $B_1 \propto V_A/Ld$ , as from Sec. 3.3). In order to have stable oscillations, a minimum bias voltage  $V_A$  is required and, as experimentally observed, that is only weakly dependent on the coil size. Additionally, the presence of parasitic capacitances limits the maximum value of the coil inductance (and coil diameter) that can be used. Consequently, the overall effect is that operations at higher frequencies intrinsically determine a larger minimum  $B_1$ , and hence a more pronounced saturation for samples having large values of  $T_1 T_2$ . In principle, the saturation issue can be solved by rotating the planar coil axis with respect to the  $B_0$  field direction (usually at 90° for maximum sensitivity). However, that would reduce the sensitivity and, consequently, it is a valid approach for samples having large signal-to-noise ratio only. A possible way out for such saturation issue is the use of high electron mobility transistors (HEMT) instead of silicon MOS transistors as active elements for the LC oscillator. Indeed, the larger electron mobility (more than one order of magnitude at room temperature and more than two orders of magnitude at low temperature) should allow for lower minimum microwave currents to sustain stable oscillations and, in turn, for a lower minimum  $B_1$ . Regarding this, preliminary calculations indicate that HEMT based LC oscillators should lead to  $B_1$  fields of about ten times lower magnitude at room temperature (i.e., about 0.01 mT) and more than one hundred times at cryogenic temperatures. Another



possible solution to the excessive  $B_1$  would be to use the integrated LC oscillator as the local microwave source for a second co-integrated LC resonator connected to an amplitude detector (i.e., an integrated version of the conventional ESR spectrometer). With this approach, the  $B_1$  amplitude could be reduced to any arbitrarily low value using an integrated variable attenuator. Furthermore, this approach would also allow for the implementation of pulsed mode single-chip ESR detectors, where the  $B_1$  field could be pulsed using an integrated switch and the free induction decay (a.k.a., echo signal) could be amplified and downconverted using an integrated microwave amplifier, a mixer, and an IF amplifier (an architecture already demonstrated for NMR spectroscopy at frequencies below 1 GHz [68]). However, compared to the frequency detection, the amplitude detection would require more complex integrated circuitry and might not necessarily lead to better spin sensitivities above 10 GHz.

In general, as shown in Refs. [7, 17], the amplitude detection and the frequency detection methods should achieve the same spin sensitivity when considering the thermal noise generated by the coil resistance as the only noise contribution. In practice, the experimental spin sensitivity of the frequency detection method is affected by the additional flicker noise coming from the transistors and the minimum possible  $B_1$ , whereas the amplitude detection method is affected by both the effective amplitude noise of the oscillator and the effective noise figure of the signal amplification/downconversion chain.

In this framework, miniaturized resonators, operated in the amplitude detection mode and combined with low noise external microwave sources [16–23, 26–32], can work more easily with optimal amplitudes of  $B_1$ , and then they can potentially achieve a better spin sensitivity for samples having large  $T_1 T_2$  values. Regarding this, single-chip ESR detectors [7–10] also contain a miniaturized LC resonator (as described in Sec. 3.3) but, in contrast to conventional miniaturized resonators operated with external microwave sources, they also include both the microwave source and the most critical part of the detection electronics in a small chip of less than 1 mm<sup>2</sup>. Those characteristics make them better suited for operations at very high frequencies since the source, the resonator, and the detector are all integrated within a distance of less than 1 mm, de-facto eliminating all concerns about signal-to-noise ratio degradation through the connections. Moreover, the small size associated to the detectors would make them suitable for their implementation in arrays devoted to simultaneous spectroscopy of several samples located in the same magnet. Finally, the operation at frequencies above 100 GHz, as demonstrated in this chapter, is also an important step towards the use of arrays of single-chip LC oscillators as a low cost alternative to gyrotrons sources in dynamic nuclear polarization (DNP) set-ups. Indeed, integrated LC oscillators operating at 300 GHz and 570 GHz have been already reported [48] and operations in the THz range might be possible in the near future. Consequently, the single-chip microwave oscillator approach will be suitable for measurements up to the largest magnetic fields currently available.

### **3.6 Acknowledgement**

Financial support from the Swiss National Science Foundation (SNSF) and the German Research Foundation (DFG) are gratefully acknowledged.

# 4 A single-chip ESR detector based on a single HEMT

## 4.1 Abstract

We report on the design and characterization of a single-chip ESR detector operating with a microwave magnetic field and a power consumption orders of magnitude lower compared to previous designs. These significant improvements are mainly due to the use of a high electron mobility transistor (HEMT) technology instead of a complementary metal-oxide-semiconductor (CMOS) technology. The realized single-chip ESR detector, which operates at 11.2 GHz, consists of an LC Colpitts oscillator realized with a single high-electron mobility transistor and a co-integrated single-turn planar coil having a diameter of 440  $\mu\text{m}$ . The realized detector operates from 300 K down to 1.4 K, at least. Its minimum microwave magnetic field is 0.4  $\mu\text{T}$  at 300 K and 0.06  $\mu\text{T}$  at 1.4 K, whereas its power consumption is 90  $\mu\text{W}$  at 300 K and 4  $\mu\text{W}$  at 1.4 K, respectively. The experimental spin sensitivity on a sensitive volume of about 30 nL, as measured with a single crystal of  $\alpha,\gamma$ -bis(diphenylene)- $\beta$ -phenylallyl (BDPA)/benzene complex, is of  $8 \times 10^{10}$  spins/Hz<sup>1/2</sup> at 300 K and  $2 \times 10^9$  spins/Hz<sup>1/2</sup> at 10 K, respectively. In a volume of about 100 pL, located in proximity to the coil wire, the spin sensitivity improves by two orders of magnitude.

## 4.2 Motivation

Two major problems of the previously reported single-chip ESR detectors (Refs. [4, 7–10]) were the large minimum microwave magnetic field (0.1–0.7 mT) and the large power consumption (0.5–200 mW), severely limiting their use for the investigation of samples having long relaxation times (Sec. 1.4) and for operations at low temperatures. Here, we report on the design and characterization of single-chip ESR detectors operating with microwave magnetic fields down to 0.4  $\mu\text{T}$  (at 300 K) and 0.06  $\mu\text{T}$  (at 1.4 K), and power consumptions down to 90  $\mu\text{W}$  (at 300 K) and 4  $\mu\text{W}$  (at 1.4 K), i.e., orders of magnitude lower compared to previous designs

---

This chapter is a minor variation of the publication "A single chip electron spin resonance detector based on a single high electron mobility transistor" [2].

[4, 7–10]. These significant improvements are mainly due to (1) the use of an InGaAs high electron mobility transistor (HEMT) technology instead of a Si CMOS technology [69], and (2) the drastic simplification of the integrated electronics to a single transistor with a few passive components instead of any other more complex circuitry. Reducing the microwave field amplitude and the power consumption allows to extend the use of the single-chip ESR detector approach to samples having much longer relaxation times (up to  $T_1 T_2$  products as large as  $10^{-10} \text{ s}^2$  at 300 K and  $10^{-8} \text{ s}^2$  below 30 K) and to lower temperatures (down to 1.4 K with ordinary  $^4\text{He}$  variable temperature inserts and, probably, even below with high cooling power  $^3\text{He}$  probes and  $^3\text{He}$ - $^4\text{He}$  dilution refrigerators).

### 4.3 Description of the single-chip ESR detector

The single-chip ESR detector described in this work is manufactured using a high electron mobility transistor (HEMT) technology (D007IH mHEMT, OMMIC, France). The transistor channel consists of a two dimensional electron gas (2DEG) in  $\text{In}_{0.7}\text{Ga}_{0.3}\text{As}$  and the gate length is 70 nm. The key properties of transistors and low noise amplifiers operating up to 220 GHz realized with the technology used in this work have been investigated in Refs. [70, 71], in the temperature range from 300 K down to 20 K. In this work, we report on the design and characterization of a single-chip integrated ESR detector based on an 11 GHz oscillator operating in the temperature range from 300 K down to 1.4 K, at least.

Fig. 4.1a shows the detailed schematic of the single-chip ESR detector. The integrated detector is a Colpitts LC oscillator [11, 65, 72], consisting of a single HEMT transistor, a single-turn planar coil inductor, a resistor, and two capacitors. In particular, the resonator is connected to a common drain amplifier in order to achieve a low output impedance without loading the LC resonator. The DC bias of the transistor is obtained connecting the source to ground through an integrated  $500 \Omega$  resistor (acting as current generator thanks to the much lower drain-source impedance of the transistor) and connecting the gate to ground (the coil inductor has a DC impedance of about  $0.6 \Omega$  and no DC current flows through it). The positive feedback from the transistor source through the two resonator capacitors creates an equivalent negative resistance which compensates for the losses in the resonator, and then leads to stable oscillations (Sec. 1.3). It is worthy to note that the calculations proposed in Sec. 1.4 still hold true since  $R_b \gg (\omega_{LC} C_2)^{-1}$ . Moreover, in the HEMT technology used in this work, the availability of on-chip connections to ground using metalized holes from the front-side to the back-side of the chip (commonly called vias) allows to avoid the use of wire-bonding for the connections to ground, which makes it feasible to integrate simple non-differential topologies with relatively low parasitic capacitances, inductances, and resistances. The oscillator frequency varies from 11.2 GHz to 11.4 GHz, depending on the temperature and the DC bias voltage  $V_{DD}$ . The overall size of the integrated Colpitts LC oscillator is  $0.8 \times 0.5 \text{ mm}^2$  (Fig. 4.1c). The chip is glued with a conductive epoxy (Epo-Tek, H20E-FC) on a standard FR4 printed circuit board and electrically connected by wedge-wedge Au wire bonding ( $20 \mu\text{m}$  wire diameter).

In Fig. 4.1b, we show the block diagram of the complete set-up used to perform the ESR

### 4.3. Description of the single-chip ESR detector

experiments reported in this work. Since the integrated common drain amplifier is not saturated, it is possible to measure both the oscillator amplitude and the oscillator frequency at the same time. For this purpose, the output signal from the integrated oscillator is amplified and, subsequently, processed by two separated electronic chains. The frequency detection branch consists of a frequency divider, a mixer, and a delay-line-discriminator used as a frequency-to-voltage converter. The amplitude detection branch consists of a microwave diode detector. Field modulation with lock-in synchronous demodulation is used, as in conventional continuous-wave ESR spectroscopy (Sec. 1.5), for both the oscillator frequency and the oscillator amplitude detection.

In Fig. 4.1d, we report the key features of the realized single-chip ESR detectors, including the geometrical and the electrical details of the integrated coil, the minimum power consumption required for stable oscillation (hence, the corresponding minimum microwave magnetic field  $B_1$ ), and the spin sensitivity.  $B_1$  and  $N_{\min}$  values are given for samples placed in the geometric center of the coil as well as in close proximity to the internal side of the coil wire. The value of  $B_1$  is estimated from the value of the microwave current in the coil obtained from electronic circuit simulations performed using ADS<sup>®</sup> (Advanced Design System, Keysight). Taking into consideration that the simulations accurately predict the oscillation frequency, the oscillation amplitude, and the DC power consumption (both current and voltage), we estimate that the computed value of  $B_1$  is accurate within a factor of two. The spin sensitivity (given in spins/Hz<sup>1/2</sup>) is computed from the experimental results obtained with a sample of BDPA as  $N_{\min} = (3N_S/SNR)$ , where  $N_S$  is the number of spins in the sample and  $SNR$  is the signal-to-noise ratio (Sec. 1.5). The signal, expressed as its peak-to-peak value, is given in Hz and the noise is expressed as its spectral density in Hz/Hz<sup>1/2</sup> (App. 4.8).

In Fig. 4.1e, we report the experimentally measured frequency noise at 300 K, 100 K, and 1.4 K. The measured noise floor (i.e., the noise at frequencies above the  $1/f$  noise corner frequency) corresponds, within a factor of two, to the thermal frequency noise originating from the coil resistance given by  $(k_B TR)^{1/2}(f_{LC}/V_{LC,0})$ , where  $V_{LC,0}$  is the oscillation amplitude and  $R$  is the coil resistance at the operating frequency [12] (Fig. 4.1a). The experimentally measured thermal noise and  $1/f$  noise have an opposite dependence on the oscillator amplitude, in agreement with the model reported in Ref. [73]. In particular, the thermal noise is minimized by maximizing the oscillation amplitude, whereas the lowest  $1/f$  noise is obtained close to the minimum oscillation amplitude (i.e., close to the start-up condition for the oscillator). Since at the largest field modulation frequency possible with our set-up (about 150 kHz) the  $1/f$  noise is still dominant, the noise is minimized at the minimum bias voltage. A detailed discussion on the achieved spin sensitivity is reported in Sec. 4.4 and in App. 4.8.

## Chapter 4. A single-chip ESR detector based on a single HEMT

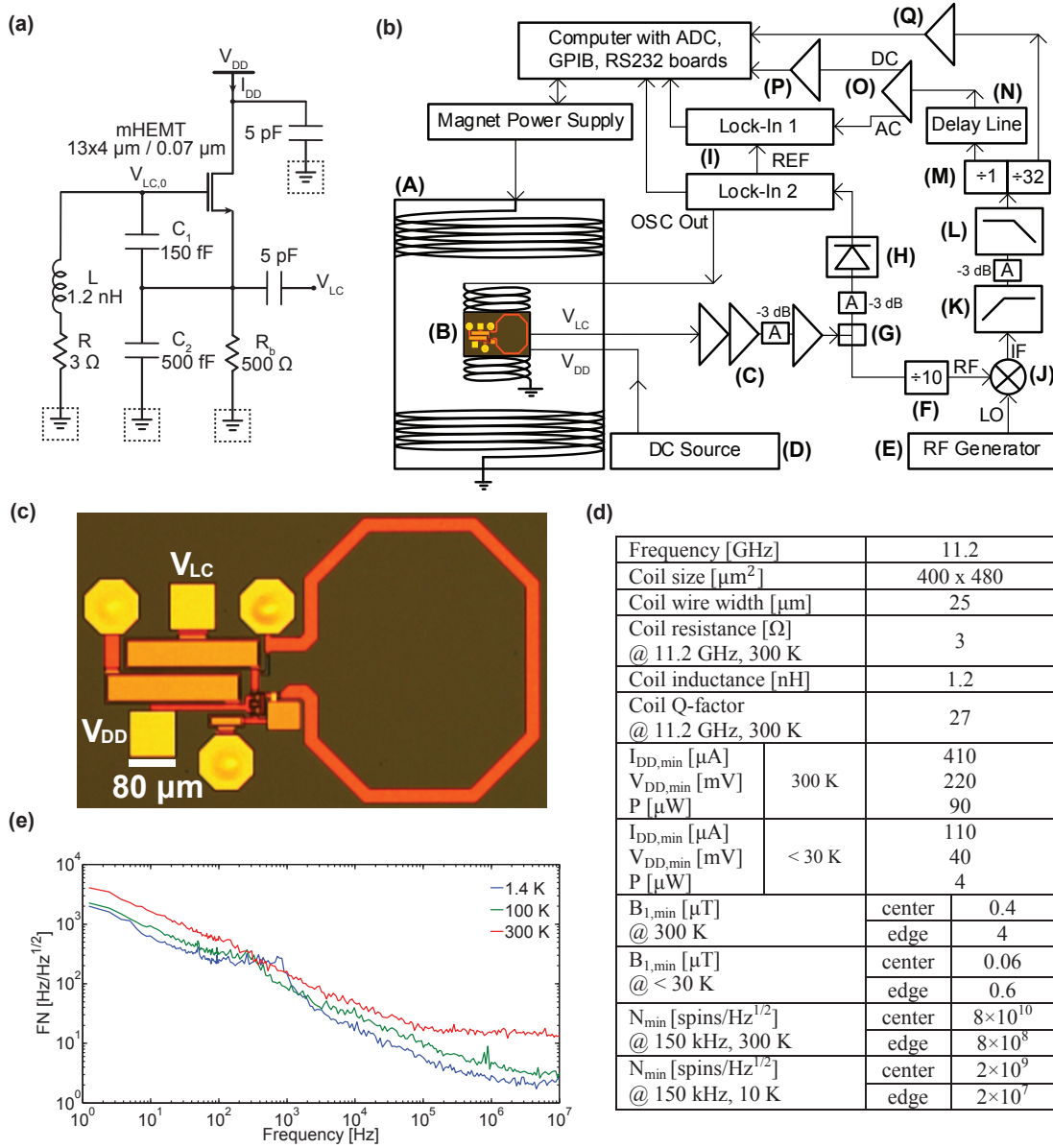


**Figure 4.1 – Schematics, picture, and key-features of the realized HEMT single-chip ESR detector.** (a) Detailed schematic of the detector (LC Colpitts oscillator). It consists of a single HEMT transistor, an inductor (having inductance  $L$  and series resistance  $R$ ), two capacitors ( $C_1$  and  $C_2$ ), and a bias resistor ( $R_b$ ). The transistor has a gate width of  $52 \mu\text{m}$  (four fingers, each having a width of  $13 \mu\text{m}$ ) and a gate length of  $0.07 \mu\text{m}$ . The oscillator is powered with a DC source ( $V_{DD}$ , current:  $I_{DD}$ ). (b) Block diagram of the complete spectrometer: (A) Superconducting magnet with variable temperature insert (1.4 K to 300 K, 0 to 9.4 T, Cryogenic Ltd) and resistive field modulation coil; (B) Single-chip ESR detector; (C) RF amplification stage composed of three RF amplifiers (Analog Devices, HMC-C001) and a 3 dB attenuator; (D) DC power supply (Keithley 2400); (E) RF generator (R&S, SMR-20); (F) Frequency divider (Analog Devices, HMC-C040); (G) Power splitter (ZX10-2-126); (H) Diode detector (Macom 2086-6000-13); (I) Lock-in amplifiers (EG&G 7265); (J) Mixer (Mini-Circuits ZFM-2000+); (K) 100 MHz high-pass filter (Crystek CHPFL-0100); (L) 300 MHz low-pass filter (Crystek CLPFL-0300); (M) Frequency divider (Valon Technology 3010); (N) Homemade delay-line-discriminator [41, 74] (200 MHz central frequency, 1 MHz detection range, 5 MHz FM bandwidth); (O) Amplifier (Stanford Research Systems SR560); (P) Amplifier (EG&G 5113); (Q) Amplifier (NF 5305). (c) Picture of the single-chip ESR detector. Coil size:  $400 \mu\text{m} \times 480 \mu\text{m}$ . The yellow squares ( $80 \mu\text{m} \times 80 \mu\text{m}$ ) are the bonding pads. The yellow hexagons ( $100 \mu\text{m}$  in diameter) are metallized holes, commonly called vias. The vias connect the electronics on the front side of the chip to a  $3.5 \mu\text{m}$  thick layer of Au acting as ground plane on the back side of the chip. The thickness of the chip is  $100 \mu\text{m}$ . The overall size of the oscillator is  $0.8 \text{ mm} \times 0.5 \text{ mm}$ . (d) Key-features of the single-chip ESR detector. In the last two rows, it is reported the spin sensitivity  $N_{\text{min}}$  measured with a sample of BDPA ( $1.5 \times 10^{27}$  spins/ $\text{m}^3$ ,  $T_1 \cong T_2 \cong 100 \text{ ns}$ ) [42, 52, 53]. (e) Measured frequency noise spectral density of the detector at 300 K, 100 K, and 1.4 K at the minimum bias (i.e., minimum  $B_1$ ), which also corresponds to the condition of minimum noise.

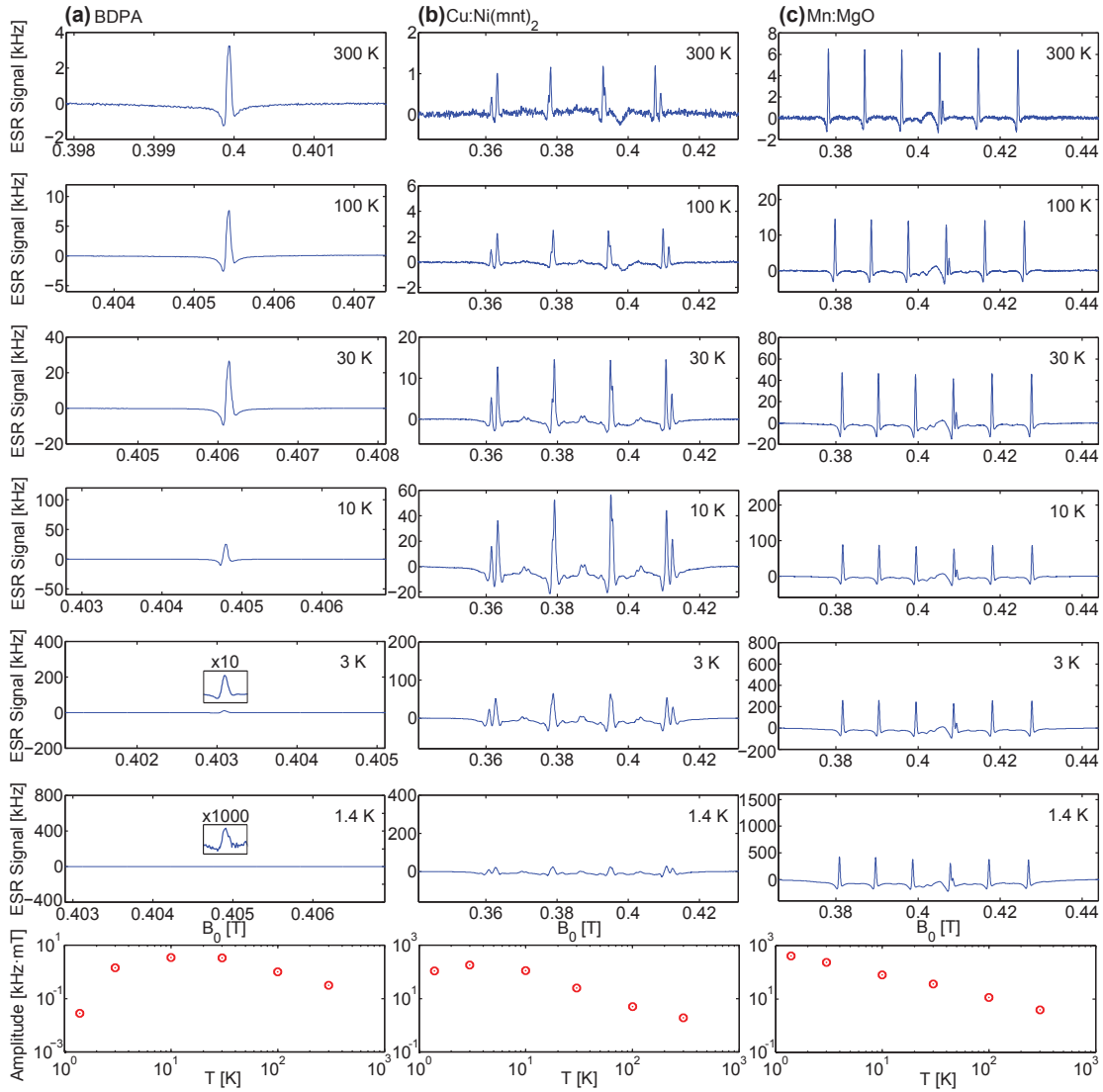
## 4.4 Electron spin resonance experiments

Fig. 4.2 shows the results of measurements performed with the single-chip ESR detector at temperatures from 300 K down to 1.4 K. We performed experiments on three samples having different characteristics, an exchange narrowed standard system (a single crystal of BDPA) and two hyperfine split systems (a single crystal of 5% Cu<sup>2+</sup> in Ni(mnt)<sub>2</sub> and a powder of 0.2% Mn<sup>2+</sup> in MgO). The reported ESR signals are obtained measuring the oscillation frequency variation in presence of field modulation. Hence, the signal shape is the first derivative of a dispersion signal (Secs. 1.2-1.5).

In Fig. 4.2a, we show the results obtained on a single crystal of BDPA (1:1 $\alpha,\gamma$ -bisdiphenylene- $\beta$ -phenylallyl/benzene complex, Sigma Aldrich 152560) having a volume of about 30 $\times$ 30 $\times$ 5  $\mu\text{m}^3$ . Thanks to the low  $B_1$  value (0.4  $\mu\text{T}$  at 300 K and 0.06  $\mu\text{T}$  at temperatures below 30 K), the signal is neither saturated nor broadened (the linewidth is 0.1 mT) and its amplitude approximately grows as  $1/T$  down to 30 K (i.e., it follows the Curie law). Below 10 K the signal amplitude decreases, probably due to a decrease in the susceptibility caused by the proximity with the antiferromagnetic transition [75–78]. In this context, assuming a spin density of  $1.5 \times 10^{27}$  spins/m<sup>3</sup> [42], the number of spins contained in the sample is  $7 \times 10^{12}$ , and then we can estimate the spin sensitivity according to the definition given in Sec. 4.3. At 300 K, the signal amplitude is 4.5 kHz (with a slightly suboptimal field modulation amplitude) and the frequency noise spectral density is 17 Hz/Hz<sup>1/2</sup>, so the experimentally achieved spin sensitivity results  $8 \times 10^{10}$  spins/Hz<sup>1/2</sup>. At 10 K, the signal is 38 kHz, the noise is 4 Hz/Hz<sup>1/2</sup>, and then the spin sensitivity results  $2 \times 10^9$  spins/Hz<sup>1/2</sup>. Remarkably, optimal field modulation amplitude improves the spin sensitivity by a factor of two, with a spectral resolution degraded by the same factor (Sec. 1.5).

In Fig. 4.2b, we report the results of measurements performed on a single crystal of Cu<sup>2+</sup>-doped tetramethylammonium-bis(maleonitriledithiolate) nickel with a Cu concentration of 5% (5% Cu in Ni(mnt)<sub>2</sub>) and a volume of 150 $\times$ 150 $\times$ 50  $\mu\text{m}^3$ . All spectra show the hyperfine splitting produced by the Cu nuclei (<sup>63</sup>Cu and <sup>65</sup>Cu), both having spin  $I = 3/2$ . The spectrum contains four main lines (split in two by the two Cu isotopes) with a linewidth of 0.8 mT. Additional spectral features are visible at low temperatures (Fig. 4.3c,d), which might have the same origin as those studied in Refs. [79, 80]. Also for this sample, thanks to the low  $B_1$  value, the signal is neither saturated nor broadened and increases approximately as  $1/T$  down to 10 K. Below 3 K the signal amplitude slightly decreases due to saturation (i.e.,  $\gamma^2 B_1^2 T_1 T_2 \cong 1$  at the minimum  $B_1$  of about 0.06  $\mu\text{T}$ , as determined by measurements at  $B_1 > 0.06 \mu\text{T}$ ). Assuming a spin density of  $9 \times 10^{25}$  spins/m<sup>3</sup> (as obtained from data in Ref. [61]), the number of spins contained in the sample is about  $1 \times 10^{14}$ . Consequently, at 300 K, the signal amplitude is 1.5 kHz, the noise is 17 Hz/Hz<sup>1/2</sup>, and the measured spin sensitivity for this sample is  $4 \times 10^{12}$  spins/Hz<sup>1/2</sup>. At 3 K, the signal is 100 kHz, the noise is 4 Hz/Hz<sup>1/2</sup>, and the spin sensitivity results  $1 \times 10^{10}$  spins/Hz<sup>1/2</sup>. Similarly to the previous sample, optimal field modulation amplitude improves the spin sensitivity by sixteen times, with a spectral resolution degraded by a factor of two (Sec. 1.5).

## Chapter 4. A single-chip ESR detector based on a single HEMT



**Figure 4.2 – ESR experiments performed with the 11 GHz HEMT single-chip detector.** The range of the ordinates (i.e. the ESR signal) is scaled as  $1/T$ , where  $T$  is the sample temperature (this visualization helps to underline the temperature range where the Curie law dependence of the signal amplitude is verified). Experimental conditions notations:  $B_1$  is the amplitude of the microwave magnetic field,  $B_m$  is the amplitude of the modulation magnetic field,  $\nu_m$  is the frequency of the magnetic field sweep,  $t_s$  is the time interval of the magnetic field sweep, and  $\Delta f$  is the equivalent noise bandwidth of the lock-in. (a) ESR spectra of a  $30 \times 30 \times 5 \mu\text{m}^3$  single crystal of BDPA from  $T = 300 \text{ K}$  to  $1.4 \text{ K}$  with  $\nu_m = 153 \text{ kHz}$ ,  $B_m = 0.05 \text{ mT}$ ,  $B_1 \cong 0.4 \mu\text{T}$  at  $300 \text{ K}$ ,  $B_1 \cong 0.06 \mu\text{T}$  below  $30 \text{ K}$ ,  $\Delta f = 2.5 \text{ Hz}$ ,  $t_s \cong 2 \text{ min}$ . (b) ESR spectra of a  $150 \times 150 \times 50 \mu\text{m}^3$  single crystal of  $5\% \text{ Cu}^{2+}$  in  $\text{Ni}(\text{mnt})_2$  from  $T = 300 \text{ K}$  to  $1.4 \text{ K}$ , with  $\nu_m = 153 \text{ kHz}$ ,  $B_m \cong 0.05 \text{ mT}$ ,  $B_1 \cong 0.4 \mu\text{T}$  at  $300 \text{ K}$ ,  $B_1 \cong 0.06 \mu\text{T}$  below  $30 \text{ K}$ ,  $\Delta f = 0.25 \text{ Hz}$ ,  $t_s \cong 3 \text{ min}$ . (c) ESR spectra of a  $400 \times 400 \times 150 \mu\text{m}^3$  powder sample of  $0.2\% \text{ Mn}^{2+}$  in  $\text{MgO}$  from  $T = 300 \text{ K}$  to  $1.4 \text{ K}$  with  $\nu_m = 153 \text{ kHz}$ ,  $B_m \cong 0.05 \text{ mT}$ ,  $B_1 \cong 0.4 \mu\text{T}$  at  $300 \text{ K}$ ,  $B_1 \cong 0.06 \mu\text{T}$  below  $30 \text{ K}$ ,  $\Delta f = 2.5 \text{ Hz}$ ,  $t_s \cong 6 \text{ min}$ . At the bottom of each column, it is shown the product of the signal amplitude times the linewidth as a function of the temperature. The noise level at the modulation frequency of  $153 \text{ kHz}$  is  $17 \text{ Hz}/\text{Hz}^{1/2}$  at  $300 \text{ K}$ ,  $8 \text{ Hz}/\text{Hz}^{1/2}$  at  $100 \text{ K}$ , and  $4 \text{ Hz}/\text{Hz}^{1/2}$  at temperatures below  $30 \text{ K}$ .



#### 4.4. Electron spin resonance experiments

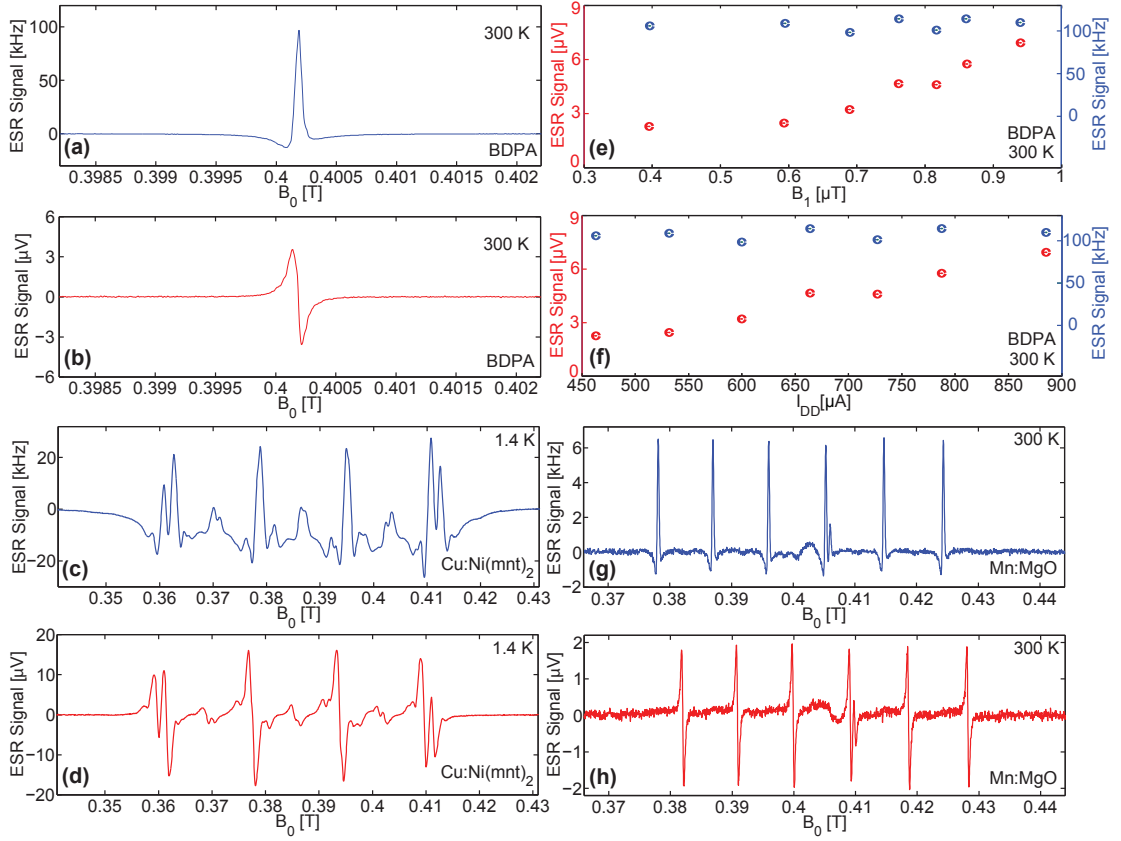


**Figure 4.3** – ESR experiments performed with the 11 GHz HEMT single-chip detector with (a, c, g) the oscillation frequency detection and (b, d, h) the oscillation amplitude detection. The oscillation amplitude is computed dividing the measured signal at the output of the lock-in amplifier by the overall gain from the oscillator to the lock-in amplifier (110 dB), which also includes the losses between the oscillator and the first stage amplifier (4 dB). Experimental conditions notations: see caption of Fig. 4.2. (a, b, e, f) Measurements performed on a  $40 \times 40 \times 30 \mu\text{m}^3$  single crystal of BDPA at  $T = 300 \text{ K}$  with  $\nu_m = 153 \text{ kHz}$ ,  $B_m \cong 0.06 \text{ mT}$ ,  $\Delta f = 2.5 \text{ Hz}$ ,  $t_s \cong 2 \text{ min}$ . (a, b) ESR spectra at  $B_1 \cong 0.95 \mu\text{T}$  obtained by measuring the oscillation frequency and the oscillation amplitude, respectively. (e, f) Peak-to-peak ESR signal obtained by measuring the oscillation frequency and the oscillation amplitude as a function of  $B_1$  and  $I_{DD}$ , respectively. (c, d) ESR spectra (oscillation frequency and amplitude) on a  $150 \times 150 \times 50 \mu\text{m}^3$  single crystal of 5% Cu:Ni(mnt)<sub>2</sub> at  $T = 1.4 \text{ K}$  with  $\nu_m = 153 \text{ kHz}$ ,  $B_m \cong 0.05 \text{ mT}$ ,  $B_1 \cong 0.6 \mu\text{T}$ ,  $\Delta f = 2.5 \text{ Hz}$ ,  $t_s \cong 3 \text{ min}$ . The two measurements are performed with the same  $B_1$  (i.e., at the same DC bias current  $I_{DD}$ ). (g, h) ESR spectra (oscillation frequency and amplitude) on a  $400 \times 400 \times 150 \mu\text{m}^3$  powder sample of 0.2% Mn:MgO at  $T = 300 \text{ K}$  with  $\nu_m = 153 \text{ kHz}$ ,  $B_m \cong 0.05 \text{ mT}$ ,  $B_1 \cong 0.4 \mu\text{T}$  and  $0.85 \mu\text{T}$  respectively,  $\Delta f = 2.5 \text{ Hz}$ ,  $t_s \cong 2 \text{ min}$ . In order to maximize the SNR, the two measurements are performed with different values of  $B_1$  (i.e., with different values of  $I_{DD}$ ). Since the oscillator frequency is dependent on  $I_{DD}$ , the two spectra are shifted by 3.8 mT, corresponding to a frequency shift of 106 MHz.

Fig. 4.2c shows the spectra obtained with a powder sample of Mn:MgO (98% purity, Sigma Aldrich, 220361) having a volume of about  $400 \times 400 \times 150 \mu\text{m}^3$ . The spectrum mainly consists of six hyperfine lines, originating from the  $^{55}\text{Mn}^{2+}$  ion having nuclear spin  $I = 5/2$  (and electron spin  $S = 5/2$ ). The measured separation between the lines is 8.7 mT, in agreement with previous measurements [56], whereas the measured width of each hyperfine line is 0.4 mT. Remarkably, the six hyperfine lines are likely to be caused only by ( $m_s = -1/2$ ,  $m_s = 1/2$ ) transitions since all the other ones are not observed due to their strongly anisotropic character [57], which makes them invisible for a sample in powder form. Assuming a  $\text{Mn}^{2+}$  concentration of about 0.2% (as estimated for a nominally identical sample in Ref. [58]) and a density

of about  $3600 \text{ kg/m}^3$  (as for a MgO crystal, probably an overestimation with respect to the effective grain density), the density of  $\text{Mn}^{2+}$  spins is about  $1 \times 10^{26} / \text{m}^3$  and the number of spins contained in the sample is about  $2 \times 10^{15}$ . So, at 300 K, the signal amplitude is 7 kHz, the noise is  $17 \text{ Hz/Hz}^{1/2}$ , and the spin sensitivity is  $1 \times 10^{13} \text{ spins/Hz}^{1/2}$ . At 1.4 K, the signal amplitude is 590 kHz, the noise is  $4 \text{ Hz/Hz}^{1/2}$ , and the spin sensitivity is  $3 \times 10^{10} \text{ spins/Hz}^{1/2}$ . Again, optimal field modulation amplitude improves the spin sensitivity by eight times, with a degradation of the spectral resolution by a factor of two (Sec. 1.5). Additionally, a large broader signal is also clearly visible close to the third hyperfine line starting from lower fields, as similarly reported in Ref. [58] and attributed to unknown additional paramagnetic impurities in the MgO sample. In our case, we also observe an additional signal between the fourth and fifth line.

The results of these measurements on BDPA,  $\text{Cu:Ni}(\text{mnt})_2$ , and  $\text{Mn:MgO}$  underline the essential advantage of the HEMT sensor proposed in this chapter with respect to the other reported CMOS sensors. In fact, the previously reported CMOS sensors [4, 7–10] had much larger  $B_1$  values (in the range from 0.1 mT to 0.8 mT), causing both line broadening and signal reduction, leading to a very significant deterioration of the spin sensitivity. In particular, the excessive  $B_1$  was severely limiting the use of those sensors on samples having a product  $T_1 T_2$  smaller than  $10^{-15} \text{ s}^2$  (i.e., relaxation times shorter than 30 ns for  $T_1 \cong T_2$ ). Regarding this, in order to more directly compare CMOS and HEMT sensors, in App. 4.7 we show measurements performed with a CMOS sensor having similar oscillator topology and operating frequency. The main result of such a comparison is that the HEMT based detector has a much lower minimum  $B_1$ , allowing for the investigation of samples having larger  $T_1 T_2$  products.

Contrary to previous designs [4, 7–10], in this work the integrated oscillator output is directly connected to the output pads, without saturated electronics co-integrated on the same chip (such as saturated mixers and frequency dividers). This allows the simultaneous measurement of the oscillation frequency and the oscillation amplitude for the integrated oscillator, giving access to both the real and the imaginary part of the complex susceptibility  $\chi = \chi' - j\chi''$  (Secs. 1.2-1.4).

In Fig. 4.3a,b, there are reported the ESR spectra of a single crystal of BDPA at 300 K, obtained by measuring the oscillator frequency (Fig. 4.3a) and the oscillator amplitude (Fig. 4.3b). The BDPA sample has a volume of  $40 \times 40 \times 30 \text{ } \mu\text{m}^3$  and it is placed in the center of the oscillator coil. Both measurements are performed with magnetic field modulation. Hence, the shape of the oscillator frequency variation corresponds to the first derivative of  $\chi'$  (i.e., to the first derivative of a dispersion signal, as described in Sec. 1.5) whereas the shape of the oscillator amplitude variation corresponds to the first derivative of  $\chi''$  (i.e., to the first derivative of an absorption signal, as from Sec. 1.5). In Fig. 4.3e,f, there are reported the peak-to-peak variations of the oscillation frequency (in blue) and of the oscillation amplitude (in red) as a function of the microwave field  $B_1$  (and the DC bias current  $I_{DD}$ ). As expected (Secs. 1.2-1.4), at low microwave field (i.e., for  $\gamma^2 B_1^2 T_1 T_2 \ll 1$ ), the frequency variation is independent of  $B_1$  whereas the oscillator amplitude variation has an approximately linear dependence on it, except for the lowest values of  $B_1$  where the transistor exhibits a larger gain. The measured oscillator frequency variation is the maximum possible whereas the maximum oscillator amplitude variation obtained at the largest  $B_1$  of  $1 \text{ } \mu\text{T}$  is about thirty times smaller than the expected

value measurable with an optimal  $B_1$  of about 60  $\mu\text{T}$ . This clearly underlines a major difference between the frequency and the amplitude measurements. Unfortunately, with the present oscillator design, the DC bias current  $I_{DD}$  cannot be increased above 1 mA (i.e., the  $B_1$  value cannot be increased above 1  $\mu\text{T}$ ) since the oscillator exhibits much larger noise and the ESR spectra are significantly distorted. This behavior is probably due to the instauration of a chaotic regime, as previously observed in other Colpitts oscillators [81]. For the oscillator frequency detection, the largest SNR (and, hence, the best spin sensitivity) is obtained close to the minimum bias (i.e., for  $I_{DD} \cong 0.5$  mA and  $B_1 \cong 0.4$   $\mu\text{T}$ ) whereas, for the oscillator amplitude detection, the largest SNR is close to the maximum bias (i.e., for  $I_{DD} \cong 1$  mA and  $B_1 \cong 1$   $\mu\text{T}$ ). In these measurements, the frequency detection allows to achieve an SNR which is about eight times larger than the one obtained with the amplitude detection.

In Fig. 4.3, we also report the results of experiments performed with 5% Cu:Ni(mnt)<sub>2</sub> single crystal at 1.4 K (Fig. 4.3c,d) and a 0.2% Mn:MgO powder sample at 300 K (Fig. 4.3g,h). In each of these four experiments, we have used different values of  $B_1$  in order to obtain the maximum SNR.

For the BDPA sample, the frequency detection allows to achieve an SNR which is about eight times larger than the one obtained with the amplitude detection. For the Cu:Ni(mnt)<sub>2</sub> and the Mn:MgO, the frequency detection has an SNR which is about two times larger than the one obtained with the amplitude detection. As discussed in Sec. 1.4, if the noise were dominated by the thermal noise of the coil series resistance, we would expect to obtain the same SNR for both the frequency and the amplitude detection, for all values of  $B_1$ . Instead, the observed differences are due to the presence of the  $1/f$  noise, in combination with the relaxation properties of the investigated samples. Remarkably, the larger difference in SNR measured with the BDPA sample can be explained by its smaller  $T_1 T_2$  product with respect to the other two samples.

In Fig. 4.4, we report the results of measurements and simulations performed to show that the spin sensitivity of the realized single-chip ESR detector is strongly dependent on the sample position with respect to the single-turn planar coil of the integrated LC oscillator. A single crystal of BDPA, having a volume of about  $10 \times 10 \times 5 \mu\text{m}^3$ , is firstly placed at the center of the coil (Fig. 4.4a) and later in contact with the internal side of the coil wire (Fig. 4.4b). As the number of spins in the sample is about  $7 \times 10^{11}$  whereas the signal amplitude is respectively 620 Hz at the center of the coil and 64 kHz at the edge of the coil wire, the experimentally obtained enhancement of the oscillator frequency variation is about 100, in agreement with the simulation shown in Fig. 4.4c. Since the noise is  $17 \text{ Hz/Hz}^{1/2}$ , the room temperature spin sensitivity for this sample of BDPA results  $6 \times 10^{10} \text{ spins/Hz}^{1/2}$  in the center of the coil and such a value is coherent with the one obtained from the measurement shown in Fig. 4.2 (within 30%).

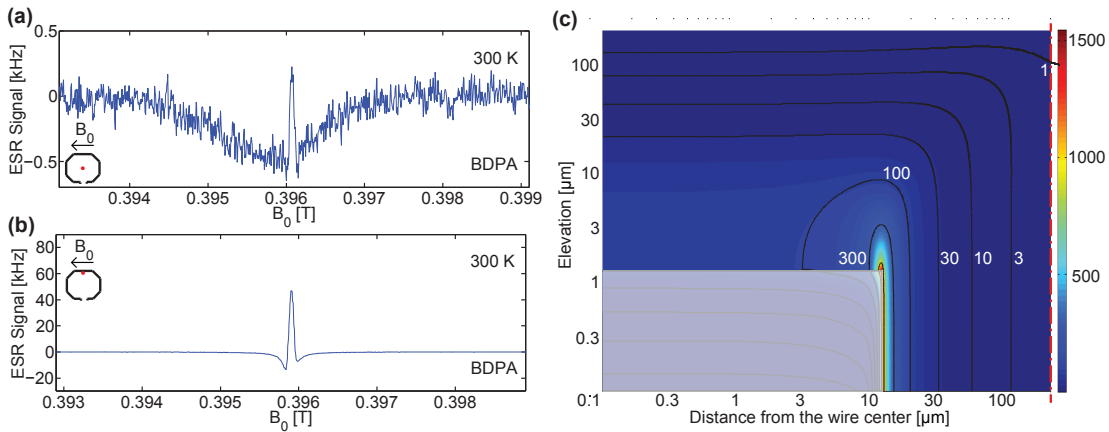


**Figure 4.4 – Investigation of the ESR signal amplitude as a function of the sample position within the detection coil of the 11.2 GHz HEMT single-chip detector.** Experimental conditions notations: see caption of Fig. 4.2. (a,b) ESR spectra of a  $10 \times 10 \times 5 \mu\text{m}^3$  single crystal of BDPA (placed in the center of the coil and at the inner edge of the coil wire, respectively) at  $T = 300 \text{ K}$ ,  $\nu_m = 153 \text{ kHz}$ ,  $B_m \cong 0.05 \text{ mT}$ ,  $B_1 \cong 0.4 \mu\text{T}$  and  $4 \mu\text{T}$  respectively,  $\Delta f = 2.5 \text{ Hz}$ ,  $t_s \cong 3 \text{ min}$ . (c) Comsol Multiphysics® simulation of the ESR signal enhancement (i.e., the ratio of the filling factor in an arbitrary point and its value in the coil center) shown as an intensity graph. The origin of the two axes is in the center of the coil wire cross-section. Both axes are in logarithmic scale. The red vertical dashed line crosses the coil plane in the center of the coil. The light purple area is the wire cross-section.

Remarkably, the small difference is mainly due to the difficulties in precisely estimating the volume of the two BDPA samples. Conversely, the spin sensitivity in the most sensitive region (i.e., a volume of about 100 pL all along the internal side of the coil wire) is  $6 \times 10^8 \text{ spins/Hz}^{1/2}$ . The broad signal (about 10 mT) visible in Fig. 4.4a is a background signal of unclear origin. In Fig. 4.4c, we report the results of microwave Comsol Multiphysics® simulations obtained by modeling the oscillator coil with a circular coil of 440  $\mu\text{m}$  in diameter placed at a distance of 100  $\mu\text{m}$  from an infinitely thick ground plane (to mimic the ground plane on the backside of the chip). In this context, the assumption of circular coil and cylindrical symmetry for the structure under analysis allows for short computation time (about 40 s) with a sufficiently fine mesh. The microwave simulation (instead of a simple DC simulation) is required to model the effect of the ground plane on the magnetic field distribution and its value. Moreover, it allows to properly compute the non-uniform current density in the coil wire and, hence, the magnetic field close to it. As a result, the presence of the ground plane reduces the inductance of the coil (by 15%) and increases its effective resistance (by 5%). Hence, the oscillator frequency and losses are only marginally affected by the presence of the ground plane. However, the latter reduces the filling factor (and, hence, the spin sensitivity) by a factor of 2.4 in the center of the coil whereas its effect is negligible in close proximity to the coil wire. Fig. 4.4c shows, as an intensity graph, the value of the ESR signal enhancement computed as the ratio of the filling factor (Sec. 1.3) in any arbitrary point of the space over the filling factor in the coil center. In this figure, we have used a logarithmic scale to show the distance from the center of the coil wire to better visualize the large enhancement close to the coil wire edge. As shown by the Comsol Multiphysics® simulations reported in Fig. 4.4c, for samples having dimensions in the order of  $(10 \mu\text{m})^3$  placed in proximity to the coil wire edge, the signal enhancement is about 100, in agreement with the experimental results reported in Fig. 4.4a. For an even smaller

sample having a volume in the order of  $(1 \mu\text{m})^3$  the expected enhancement is about 2000, leading to a spin sensitivity of  $3 \times 10^7$  spins/Hz<sup>1/2</sup> at 300 K and  $1 \times 10^6$  spins/Hz<sup>1/2</sup> at 10 K (i.e., the spin sensitivity is improved by three orders of magnitude with respect to the coil center). It is worthy to note that, at such small distances from the coil wire edge,  $B_1$  is 10-40 times larger than at the center. However, these  $B_1$  values are still sufficiently low to avoid the saturation of a BDPA sample (and of any other sample having  $T_1 T_2 < 10^{-13}$  s<sup>2</sup> at 300 K and  $T_1 T_2 < 10^{-11}$  s<sup>2</sup> at 10 K).

Finally, for all the samples investigated in this work, the measured ESR signals (for both frequency and amplitude detection) are always in agreement with the theoretical values computed through the equations given in Sec. 1.4, with a maximum deviation of a factor of three (mainly due to the difficulties in precisely evaluating the sample volume, the spin density, and the relaxation times).

## 4.5 Discussion and outlook

In this chapter, we have reported about the design and the performance of an 11 GHz single-chip ESR detector realized using a HEMT technology. The main advantages with respect to the previous designs realized using CMOS technologies [4, 7–10] are the drastically reduced minimum microwave magnetic field and power consumption. These features allow the use of the HEMT oscillator with samples having much larger  $T_1 T_2$  products and to operate at lower temperatures. Such improved key characteristics are mainly due to the much larger electron mobility of InGaAs HEMT transistors with respect to Si CMOS transistors.

The previously reported CMOS detectors were based on coils having diameters ranging from 45  $\mu\text{m}$  to 200  $\mu\text{m}$  and operated at frequencies from 8 GHz to 146 GHz. Due to the larger diameter of the integrated coil (i.e., the larger sensitive volume) and the lower working frequency, the spin sensitivity for samples having small  $T_1 T_2$  products obtained with the HEMT ESR detector reported here is up to three orders of magnitude worse than the best results we reported on CMOS detectors [4, 9]. However, the availability of a very low minimum  $B_1$  allows the HEMT based detector to benefit from the geometrical signal enhancement (2-3 orders of magnitude for small samples) with no signal degradation due to saturation. Moreover, the HEMT approach proposed here can be certainly extended to higher frequencies and smaller coil diameters. Preliminary simulations show that the same HEMT technology used in this work should allow for the design of oscillators operating at 40 GHz, with single-turn coil diameter of 150  $\mu\text{m}$ , minimum  $B_1$  values below 1  $\mu\text{T}$ , and a minimum power consumption below 10  $\mu\text{W}$  at low temperatures. The combined increase of the operating frequency, the reduction of the sensitive volume, the reduced negative effect of the ground plane, together with an expected increase of the noise by about a factor of three, should result in a spin sensitivity improved by more than two orders of magnitude with respect to the present oscillator. This should realistically allow to achieve a spin sensitivity on a sample of BDPA of about  $10^8$  spins/Hz<sup>1/2</sup> at 300 K and about  $10^6$  spins/Hz<sup>1/2</sup> at 10 K on a sensitive volume of about 1 nL. Obviously, the larger minimum  $B_1$  will slightly restrict the class of samples which can be measured without

significant saturation.

Oscillators realized with technologies having larger electron mobility, shorter gate length, or different topology, might have lower minimum  $B_1$ , thus allowing for spectroscopy on a larger class of samples. Nevertheless, for samples having a  $T_1 T_2$  product still too large to be measured with the minimum available  $B_1$ , the design of a pulsed mode single-chip ESR detector would be a possible valid alternative to overcome this limitation. Indeed, HEMT technologies are particularly well suited for such an approach thanks to the possibility of designing ultra-low noise amplifiers, both at room temperature and at cryogenic temperatures. Finally, the HEMT approach has already shown a maximum oscillation frequency as large as 1.3 THz [82], clearly indicating that these technologies represent a valid alternative to CMOS for the realization of single-chip ESR detectors operating at frequencies corresponding to the largest magnetic fields currently available.

### 4.6 Acknowledgement

Financial support from the Swiss National Science Foundation (SNSF) is gratefully acknowledged (grant 200020-175939).

### 4.7 Appendix. Comparison with single-chip ESR detectors based on CMOS

In this appendix, we show measurements performed with a single-chip ESR detector based on a Colpitts oscillator realized using a Si CMOS technology (TSMC 180 nm, MS/RF). These results are reported to experimentally underline the differences between using a HEMT rather than a CMOS technology. The comparison is fair and useful, without pretending to be very accurate since the oscillator topologies, the operating frequencies, the coils, and the transistor lengths are similar but definitely not identical.

Fig. 4.5c shows the ESR spectra obtained with a powder sample of 0.2% Mn:MgO using the CMOS detector described in Fig. 4.5a,b. The ESR signal amplitude increases by less than a factor of three reducing the temperature from 300 K to 1.4 K, and that is in clear contrast with the results obtained through the HEMT detector (Fig. 4.2c). In fact, the latter increases by two orders of magnitude as the temperature drops from 300 K to 1.4 K, as expected from the Curie law in condition of negligible saturation. Fig. 4.5e shows a direct comparison between the measurements performed with the two sensors whereas the main differences between the two detectors are reported in Fig. 4.5d. In particular, although the CMOS sensor has a better spin sensitivity when measured with a BDPA sample, it exhibits worse performance when saturation becomes significant, as in the case of the Mn:MgO at low temperatures. Indeed, at low temperatures, the HEMT and the CMOS detectors have a minimum  $B_1$  of about 0.06  $\mu\text{T}$  and 30  $\mu\text{T}$ , respectively. In this context, such large difference (a factor of 500) is due to the lower minimum microwave current in the coil (a factor of 100), to the larger coil diameter (a factor of two), and to the use of a single-turn instead of double-turn coil (a factor of two).

## 4.7. Appendix. Comparison with single-chip ESR detectors based on CMOS

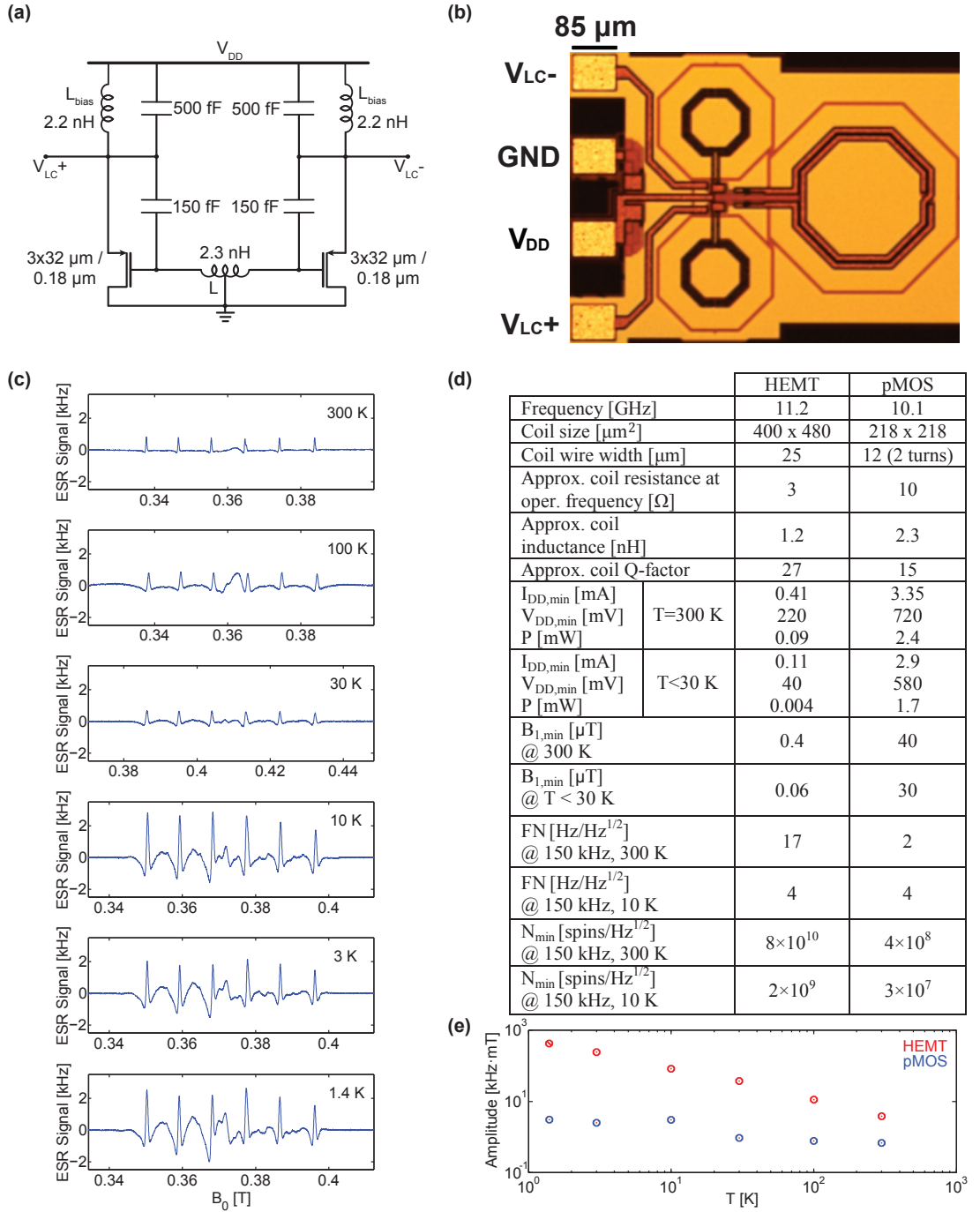


**Figure 4.5 – Schematic, picture, and measurements of a single-chip ESR detector based on a differential Colpitts topology implemented using a CMOS technology (TSMC 180 nm, MS/RF).** (a) Detailed schematic of the integrated LC Colpitts oscillator. The excitation/detection coil is indicated by  $L$ . The bias inductors are indicated by  $L_{bias}$ . (b) Picture of the CMOS single-chip ESR detector. The excitation/detection coil is the larger one on the right side (diameter: 218  $\mu\text{m}$ ), whereas the other two coils are the bias inductors. The yellow rectangles (65  $\mu\text{m}$   $\times$  85  $\mu\text{m}$ ) are the bonding pads. The overall size of the oscillator is about (0.85 mm  $\times$  0.63 mm). (c) ESR spectra of a 200 $\times$ 200 $\times$ 100  $\mu\text{m}^3$  powder sample of 0.2% Mn:MgO from  $T = 300$  K to 1.4 K with  $\nu_m = 153$  kHz,  $B_m \cong 0.05$  mT,  $B_1 \cong 40$   $\mu\text{T}$  at 300 K,  $B_1 \cong 30$   $\mu\text{T}$  below 30 K,  $\Delta f = 2.5$  Hz,  $t_s \cong 6$  min. (d) Key-features of the CMOS and HEMT single-chip ESR detectors. In the last four rows, there are reported the measured frequency noise  $FN$  and spin sensitivity  $N_{min}$ . The spin sensitivity is measured with a sample of BDPA ( $1.5 \times 10^{27}$  spins/ $\text{m}^3$ ,  $T_1 \cong T_2 \cong 100$  ns) [42, 52, 53]. (e) Measurement results obtained with a sample of 0.2% Mn:MgO using the CMOS and the HEMT detectors. For both detectors, the product of the frequency variation times the linewidth is plotted as a function of the temperature.

The lower minimum microwave current in the coil results from the smaller oscillation start-up current, which is in turn mainly due to both the larger transconductance and the smaller drain-to-source resistance of the HEMT transistor. Both these characteristics are caused by the larger electron mobility, the larger effective carrier density, and the shorter gate length of the HEMT with respect to the CMOS transistor.

In CMOS technologies, it is possible to design oscillators based on both n-type (nMOS) and p-type (pMOS) transistors. Oscillators based on nMOS transistors show higher operating frequency and lower power consumption, whereas those based on pMOS transistors have a lower corner frequency for the  $1/f$  noise. Preliminary simulations show that the use of an nMOS transistor with a gate length of 65 nm (instead of a pMOS transistor with a gate length of 180 nm) should reduce the minimum  $B_1$  by one order of magnitude. Nevertheless, the lower carrier mobility of Si MOSFETs (lower than  $0.1 \text{ m}^2/\text{Vs}$  at 300 K, lower than  $1 \text{ m}^2/\text{Vs}$  at low temperatures [69, 83]) than 2DEG HEMTs is the key parameter which makes HEMT technologies more suitable to build oscillators with low start-up power consumption and low minimum  $B_1$ . In particular, the electron mobility of 2DEGs in InGaAs (as the one used in this work) is about  $1 \text{ m}^2/\text{Vs}$  at 300 K and about  $6 \text{ m}^2/\text{Vs}$  below 50 K [69, 84], whereas mobilities as large as  $3000 \text{ m}^2/\text{Vs}$  at low temperatures have been reported for other HEMT technologies [69]. Hence, 2DEGs could allow to further reduce both power consumption and  $B_1$  values for the next generation of HEMT ESR detectors.

### 4.8 Appendix. Comparison with other inductive approaches for high spin sensitivity on nanoliter and subnanoliter samples

In the following, we compare the single-chip ESR detector approach [4, 7–10] to those based on conducting or superconducting microresonators with external microwave sources and amplifiers [16–21, 23–34].

As discussed in Sec. 1.4, the spin sensitivity of an ESR detector can be defined as  $N_{\min} = (3N_S/SNR)$ , where  $N_S$  is the number of spins in the sample and  $SNR$  is the signal-to-noise ratio. In case of frequency detection, the signal is given in Hz and the noise is expressed as its spectral density in  $\text{Hz}/\text{Hz}^{1/2}$ . In case of amplitude detection, the signal is given in V and the noise is expressed as its spectral density in  $\text{V}/\text{Hz}^{1/2}$ . In both cases, the spin sensitivity is given in  $\text{spins}/\text{Hz}^{1/2}$ . The presence of the factor of three in the definition of the spin sensitivity makes the value  $N_{\min}$  a more realistic estimation for the spin sensitivity itself. Indeed, if the peak-to-peak signal amplitude is equal to the root-mean-square value of the noise (i.e., the spectral density multiplied by the bandwidth), the signal is not clearly discernable from the noise. This definition, which we used throughout this work and all our previous works, is widely accepted [38], sometimes with the omission of the factor three. The spin sensitivity, as computed from the equation above, depends not only on the spectrometer performance but also on the sample used for its experimental determination. In particular, it depends on the sample properties such as the relaxation times ( $T_1$ ,  $T_2$ ,  $T_2^*$ ), the magnetic moment of the involved spin system, and the number of spectral lines with their degeneracy. For this reason,



#### 4.8. Appendix. Comparison with other inductive approaches for high spin sensitivity on nanoliter and subnanoliter samples

---

the sample used to characterize the spin sensitivity is usually specified. In order to compare the performance of spectrometers characterized with different samples or to extrapolate their performance with other (existing or hypothetical) samples, several normalization criteria have been used so far. These include, e.g., normalizations performed by dividing the effective spin sensitivity (as defined above) by the measured linewidth [44], by the number of lines in the spectrum [14, 29], and by the ratio between the sample linewidth and the excitation bandwidth [29]. All these normalization criteria have a physical background but should be used with care to avoid misunderstandings. In particular, in our opinion, it is preferable to underline the effective spin sensitivity (specifying the sample employed and its key properties) rather than the normalized one, obtained upon the application of one or a series of normalization criteria. The best normalized spin sensitivity obtained to date with an inductive approach has been reported in Ref. [33]. In this work, the authors estimated a normalized experimental spin sensitivity of  $65 \text{ spins/Hz}^{1/2}$  on an effective sensitive volume of about 0.2 pL. These measurements are performed at 12 mK and 7 GHz, at a relatively low magnetic field of about 5 mT, on a sample of isotopically enriched  $^{28}\text{Si}$  with implanted Bi donors ( $T_1 \cong 19 \text{ ms}$ ,  $T_2 \cong 1.7 \text{ ms}$ ). In these pulsed experiments, a planar superconducting Al resonator having a size of about  $1 \text{ mm}^2$  is used. It consists of an interdigitated capacitor in parallel with a wire inductor having a length of  $100 \text{ }\mu\text{m}$  and a width of  $0.5 \text{ }\mu\text{m}$ . The 100 nm thick Al layer is directly deposited over the Si chip. The Bi donors are mainly contained into a thin layer of 100 nm at the surface of the Si chip, with a density of  $8 \times 10^{22} \text{ spins/m}^3$ . The Bi: $^{28}\text{Si}$  shows resonance lines at low magnetic fields, a necessary condition to operate with an Al superconducting resonator. In order to maximize the signal-to-noise ratio, the authors used a magnetically shielded Josephson parametric amplifier (JPA) also cooled down to 12 mK as an ultra-low noise first amplification stage, followed by a low noise amplifier cooled down to 4 K. The Al resonator is placed inside a Cu box and coupled with the external electronics using two (transmit and receive) antennas. The Bi donors under the resonator are about  $10^{10}$ , those just under the wire inductor are about  $4 \times 10^5$ , whereas those that are considered as responsible of the measured signal are about 200. This estimation of the number of spins contributing to the measured signal (which allows to compute the spin sensitivity from the measured signal-to-noise ratio) is obtained from (1) a careful analysis of the signal contributions from regions outside of the most sensitive volume of the resonator and (2) the application of a series of two normalization criteria. The analysis of the signal contributions takes into consideration both the highly non-uniform  $B_1$  generated by the resonator and the Purcell effect (which reduces  $T_1$  in the region of maximum sensitivity from 1600 s to about 19 ms). The normalization, which determines a reduction of the number of involved spins of three orders of magnitude (from  $4 \times 10^5$  to about 200) is based on the idea that only one out of the nine transitions of the Bi donor is actually excited and that, due to the high Q-factor of the superconducting resonator, the excitation bandwidth (about 20 kHz) is only 1% of the resonance line (about 2 MHz). With a hypothetical sample having a single resonance line narrower than the resonator linewidth and optimal relaxation times, the experimentally measured spin sensitivity would be effectively close to the normalized one. In this sense, the normalization is a valid concept, but it has to be taken with care. To clarify this point, let's consider a thought experiment in which 100 Bi donors are implanted in the

most sensitive part of the resonator. If the spin sensitivity is effectively of  $100 \text{ spins/Hz}^{1/2}$  for the Bi:<sup>28</sup>Si sample, it should be possible to see a signal from those 100 spins with an SNR of about 1 in a measuring time of about 1 s. In reality, an SNR of 1 is achievable only after 11 days, showing that the effective spin sensitivity on a Bi:<sup>28</sup>Si sample is of  $10^5 \text{ spins/Hz}^{1/2}$  rather than  $100 \text{ spins/Hz}^{1/2}$ . In a previous experiment [29], the same authors reported a normalized spin sensitivity of  $1700 \text{ spins/Hz}^{1/2}$  with a wire inductor having a length of  $700 \mu\text{m}$  and a width of  $5 \mu\text{m}$ . Scaling down the area of the inductor wire by two orders of magnitude improved the spin sensitivity by an order of magnitude. As for the previous experiment, the declared spin sensitivity is obtained after the same normalization (from an effective spin sensitivity of  $10^7 \text{ spins/Hz}^{1/2}$  to a normalized spin sensitivity of  $1700 \text{ spins/Hz}^{1/2}$ ).

A very similar approach has been reported in Ref. [32]. The pulsed experiments reported in this work are performed at 20 mK, in a magnetic field of 180 mT, at a frequency of 5 GHz, on a  $2 \mu\text{m}$  thick sample of phosphorous donors in isotropically purified silicon (P:<sup>28</sup>Si) having  $T_2^* \cong 2 \mu\text{s}$ ,  $T_2 \cong 1.1 \text{ ms}$ , and  $T_1 \cong 3 \text{ s}$  (also affected by the Purcell effect [31, 32]). In this case, the authors used a planar Nb superconducting resonator consisting of an inductive wire and an interdigitated capacitor. The resonator is coupled with the external electronics using a coplanar transmission line placed nearby the resonator. The inductive wire has a length of  $100 \mu\text{m}$  and a width of  $2 \mu\text{m}$ . From the reported spin concentration ( $5 \times 10^{21} / \text{m}^3$ ) and the number of spins considered as responsible for the detected signal ( $1.5 \times 10^5$ ) the effective detection volume would be about 0.03 pL. Also in these experiments, the use of a JPA as a first stage amplifier is essential to improve the spin sensitivity. In particular, a spin sensitivity of  $1.5 \times 10^4$  spins in a single shot with a 0.1 Hz repetition rate is reported (i.e.,  $5 \times 10^4 \text{ spins/Hz}^{1/2}$ ). Also in this case, the authors had to carefully estimate the effective sensitive volume of the resonator because the P:<sup>28</sup>Si sample was also extending under the entire resonator having a size much larger than the effective sensitive volume. Since the authors have not used normalizations, the reported spin sensitivity ( $5 \times 10^4 \text{ spins/Hz}^{1/2}$ ) is the effective value actually achieved on the specific sample at the given conditions.

These approaches based on the use of superconducting resonators, superconductor based amplifiers, very small sensitive volumes, and extremely low temperatures are very interesting for fundamental studies as well as for future quantum information applications [85]. However, the small sensitive volume together with the constraints on the operating temperature and the magnetic field reduce their versatility.

An alternative (more versatile) approach for high spin sensitivity inductive experiments on small samples has been described by the group of Blank in several works over the last ten years [20–23]. In Ref. [23], it is reported a spin sensitivity of  $7 \times 10^3 \text{ spins/Hz}^{1/2}$  obtained with a surface loop-gap microresonator coupled with a transmission line to the external electronics. The microresonator, consisting of a Cu layer structured over a dielectric substrate, has a diameter of about 1 mm with its most sensitive volume of about 0.2 pL. Also in this case, the most sensitive volume is a very small fraction of the resonator, thus requiring a careful evaluation of the effective sensitivity volume in order to correctly estimate the number of spins contributing to the measured signal ( $2 \times 10^6$  spins in the 0.2 pL volume with a spin density of  $10^{22} / \text{m}^3$ ). The experiments were performed on a sample of P:<sup>28</sup>Si at 10 K ( $T_1 \cong 1 \text{ ms}$ ,  $T_2 \cong 260 \mu\text{s}$ ,  $T_2^* \cong 0.8$

#### 4.8. Appendix. Comparison with other inductive approaches for high spin sensitivity on nanoliter and subnanoliter samples

---

$\mu\text{s}$ ) in a magnetic field of 1.2 T at 34 GHz. The same group has reported results obtained with surface loop resonators operating from 10 GHz to 100 GHz with most sensitive volumes from 0.1 nL down to less than 0.1 pL and operating temperatures from 300 K down to 10 K [20]. This approach, being based on non-superconducting materials, is more versatile and the obtained best effective (i.e., not normalized) spin sensitivity at 10 K is almost an order of magnitude better than the one obtained with the superconducting resonators described above, operating at 20 mK and characterized on a similar sample (with different relaxation times).

All these previous works indicate that, at low temperatures, the inductive approach has the potential to reach the single spin sensitivity in a measuring time shorter than 1 hour on samples having optimal relaxation times. However, that is likely possible only through resonators with sensitive volumes in the order of 1 pL or even smaller. This clearly underlines the existing trade-off between spin sensitivity and spin concentration sensitivity.

The best effective spin sensitivity reported up to now for the single-chip ESR detector approach described in this work (and in our previous works [4, 7–9]) is of about  $10^6$  spins/Hz<sup>1/2</sup> with a sensitive volume of about 2 nL [9]. Such a spin sensitivity was achieved at 10 K with a sample of DPPH having relaxation times  $T_1 \cong T_2 \cong 60$  ns. Hence, the effective spin sensitivity is about two orders of magnitude worse than the best result described above [23, 32, 33]. However, since the sensitive volume is about four orders of magnitude larger, the spin concentration sensitivity is two orders of magnitude better with the single-chip detector. This comparison further remarks the compromise between spin sensitivity and sensitive volume (and then the spin concentration sensitivity). In other words, the optimal detector is the one having its sensitive volume matched to the volume of the sample under investigation. As discussed in Sec. 4.4, a single-turn planar coil has a region with two to three orders of magnitude enhanced spin sensitivity all along the coil wire. By locally reducing the width of the coil wire, an even more localized sensitivity volume could be obtained, further improving the spin sensitivity with a negligible deterioration of the quality factor of the coil (and, hence, of the noise). In all single-chip ESR detectors realized so far, the on-chip integrated resonator consisted of a lumped inductor (a planar coil of 440–45  $\mu\text{m}$  in diameter) and lumped capacitors. An improved spin sensitivity could also be obtained using a different approach for the realization of the integrated resonator. Indeed, integrated circuit technologies are also well suited to investigate the adoption of resonators consisting of distributed structures (such as those used in Refs. [29, 32, 33]) as alternatives to the lumped LC resonators used so far. Similarly to the non-integrated approaches described above, the scaling down of the sensitive volume would improve the spin sensitivity, under the assumption that the resulting  $B_1$  is sufficiently low to avoid saturation. Despite the very significant improvements demonstrated in this work, the possible saturation still due to an excessive  $B_1$  is the major drawback of our approach based on a continuous wave excitation. Nevertheless, the single-chip integrated method is, in principle, not intrinsically limited to the continuous wave excitation with a minimum  $B_1$  determined by the oscillator start-up condition. As a matter of fact, the single-chip integrated approach can also be used to develop an integrated pulsed detector (consisting of an oscillator, variable attenuators, switches, a separate resonator, low noise amplifiers, and mixers) or an integrated continuous wave detector (consisting of an oscillator, variable attenuators, a separated res-

onator, low noise amplifiers, and mixers). The latter two, having the oscillator physically separated from the sensing resonator, would solve the  $B_1$  issue existing in the current approach but would require the design of a significantly more complex electronics, characterized by the difficult optimization of parameters in order to obtain low power consumption, low noise, broad tunability of  $B_1$ , and wide operating temperature range.

Regardless of the specific integrated electronics, single-chip ESR detectors [4, 7–10] include the microwave source, the miniaturized resonator, and the most critical part of the detection electronics in a small chip having an area of  $1 \text{ mm}^2$  or less, in contrast to conventional miniaturized resonators which are operated with external microwave sources and amplifiers. That makes single-chip ESR detectors better suited for operations at very high frequencies since the source, the resonator, and the detector are within a distance of less than 1 mm, de-facto eliminating all concerns about signal-to-noise ratio degradation across the connections. The availability of small detectors would also enable their implementation in a arrays of sensors for simultaneous spectroscopy of several samples inside the same magnet.

# 5 A low power microwave HEMT LC oscillator operating down to 1.4 K

## 5.1 Abstract

We report on the design and characterization of a low power HEMT LC Colpitts oscillator operating at 11 GHz whose minimum power consumption is 90  $\mu\text{W}$  at 300 K and 4  $\mu\text{W}$  at 1.4 K. The fully integrated oscillator is based on a single HEMT transistor having a gate length of 70 nm and realized using a 2DEG in  $\text{In}_{0.7}\text{Ga}_{0.3}\text{As}$ . The power consumption of the realized oscillator is the lowest reported in the literature so far for an LC oscillator operating in the same frequency range. In order to investigate the behavior of the oscillator, we also performed a detailed characterization of a standalone HEMT transistor from 1.4 to 300 K in the presence of a static magnetic field from 0 to 8 T. The carrier mobility, which is about 0.65  $\text{m}^2/\text{Vs}$  at 300 K and 1.2  $\text{m}^2/\text{Vs}$  below 30 K, is extracted from geometrical magnetoresistance experiments. The carrier density, which is about  $3.5 \times 10^{16} \text{ m}^{-2}$ , is extracted from the Shubnikov-de-Haas (SdH) oscillations observed at 1.4 K. From the extracted values of the transistor parameters, we estimate and compare the minimum power necessary to start-up the oscillations for two different Colpitts topologies.

## 5.2 Motivation

High electron mobility transistors (HEMT) based on two dimensional electron gases (2DEG) in III-V heterostructures have superior charge carrier mobility compared to silicon based complementary metal-oxide-semiconductor (CMOS) technologies. Their large mobility makes them particularly attractive for a variety of low noise and high power radio frequency, microwave, and terahertz applications [70, 87–89]. HEMTs are currently widely used also for cryogenic applications, and considered as promising candidates for the cold read-out electronics of future quantum computers [90–97]. At temperatures of about 1.5 K and above, the cooling power of  $^4\text{He}$  based cooling systems can exceed 100 mW [98]. At temperature below 1.5 K,

---

This chapter is a minor variation of the publication "A Low Power Microwave HEMT LC Oscillator Operating Down to 1.4 K" [86].

the effective cooling power available with  $^3\text{He}$  and  $^3\text{He}^4\text{He}$  dilution refrigerators is typically below 1 mW [99]. Hence, for applications at temperatures in the order of 1 K and below, the electronics has to be designed considering the power consumption as a critical constraint.

In this chapter, we investigate microwave LC oscillators based on HEMTs, with the goal of using them for low temperature studies and applications. In particular, we report on the design and characterization of an ultra-low power HEMT based LC Colpitts oscillator [11, 65, 72], operating at 11 GHz and in the temperature range from 1.4 K to 300 K, at least. The achieved power consumption is of 90  $\mu\text{W}$  at 300 K and 4  $\mu\text{W}$  at 1.4 K.

In the design of integrated CMOS and HEMT microwave oscillators, the main effort is usually focused on the improvement of phase noise, output power, and tuning range [100–103]. Recently, motivated by their use in room temperature applications where power consumption is important (such as RF identification), several low power CMOS and HEMT designs have been reported [104–113]. For instance, a HEMT oscillator operating at 4.7 GHz has achieved power consumption of 2.7 mW [113] whereas CMOS oscillators have achieved power consumptions of 280  $\mu\text{W}$  at 40 GHz [104] and, very recently, of 130  $\mu\text{W}$  at 57.4 GHz [107]. In this context, a very limited literature exists on microwave oscillators operating at liquid helium temperature (i.e., 4.2 K) and below [114–117]. Moreover, the lowest reported power consumption is of about 7 mW [117]. Hence, the HEMT oscillator reported in this work achieves a room temperature power consumption which is slightly better than the state-of-the-art, and a significantly lower power consumption at cryogenic temperatures.

Reducing power consumption in LC oscillators is of crucial importance, e.g., for their application as single-chip electron spin resonance (ESR) spectroscopy detectors at low temperatures [2, 4, 7–10]. Exploring the behavior of microwave LC oscillators at cryogenic conditions is also interesting for studies on phase noise of both thermal and non-thermal origin [49, 65]. Particularly interesting would be the operation in the condition  $\hbar\omega > k_B T$ , which should result in a dramatic reduction of phase noise of thermal origin (power spectral density), well beyond the linear dependence on  $T$  in the condition  $\hbar\omega < k_B T$  [118, 119], where  $k_B$  is the Boltzmann constant,  $T$  is the temperature,  $\hbar$  is the reduced Planck constant, and  $\omega$  is the oscillation angular frequency. Also, the study of the zero-point quantum noise [118, 120–123], which in this case should be likely present in the form of oscillator phase noise, would be experimentally accessible.

### 5.3 Description of the realized devices and of the measurements set-up

In this work, we designed and investigated the behavior of a standalone HEMT transistor and of a microwave LC Colpitts oscillator based on a single HEMT transistor. In particular, we performed their characterization in the temperature range from 1.4 to 300 K and in the magnetic field range from 0 to 8 T. Both devices were manufactured using a HEMT technology having a minimum gate length of 70 nm (D007IH mHEMT, OMMIC, France). The transistor channels consist of a 2DEG in  $\text{In}_{0.7}\text{Ga}_{0.3}\text{As}$ . In Refs. [70, 71], transistors and low noise mi-

### 5.3. Description of the realized devices and of the measurements set-up

---

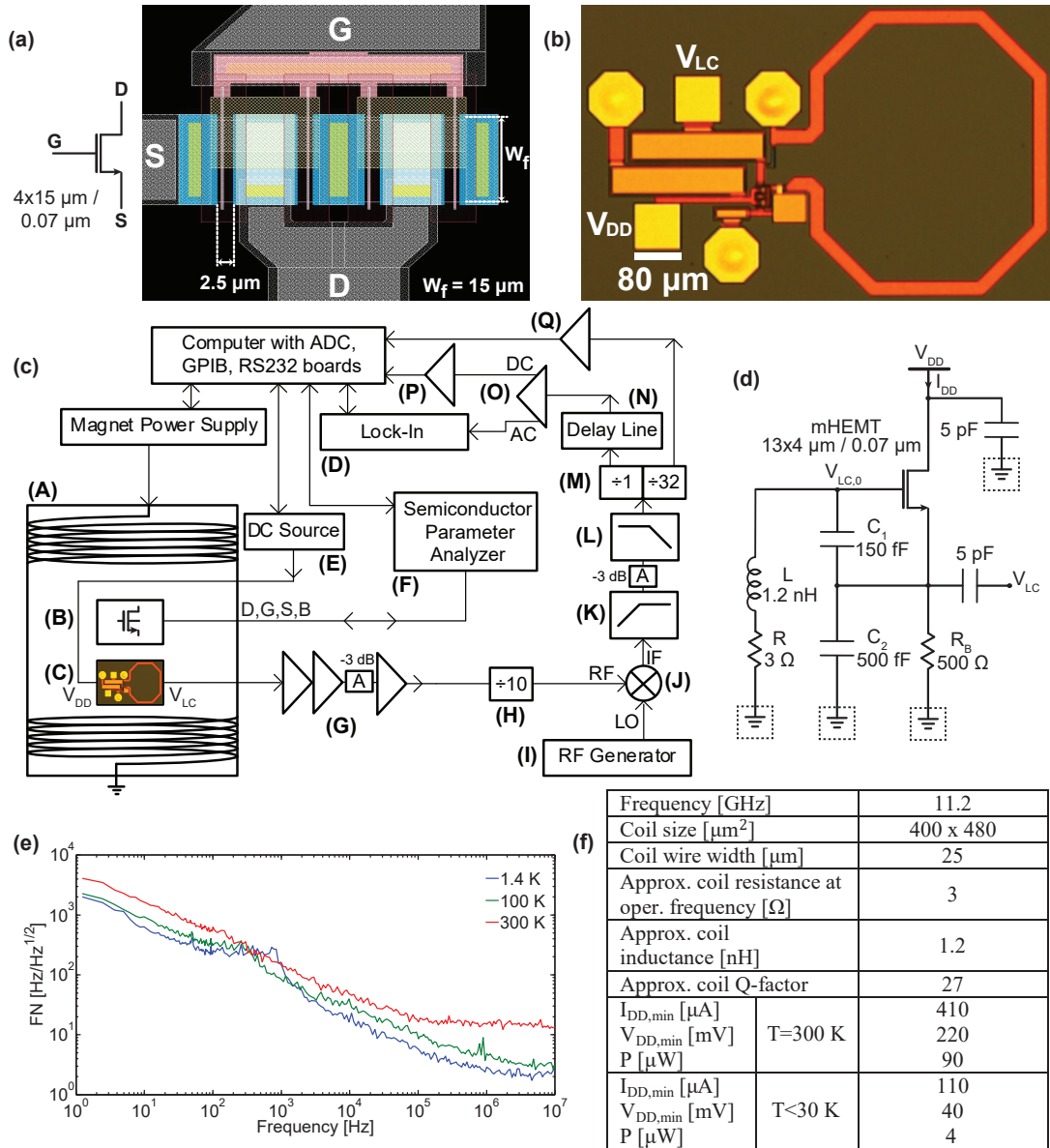
microwave amplifiers fabricated with the same technology are characterized in the temperature range from 20 to 300 K. In this work, we extend the investigation to microwave oscillators, enlarging the temperature range and adding a strong magnetic field as a means to extract useful information concerning the properties of transistors.

Fig. 5.1a shows the layout of the standalone HEMT transistor, which consists of four fingers having a width of 15  $\mu\text{m}$ , a drain-source distance of 2.5  $\mu\text{m}$ , and a gate length of 70 nm. The properties of this standalone HEMT transistor as a function of the temperature (1.4 to 300 K) and of the magnetic field (0 to 8 T) are investigated in Sec. 5.4.

Fig. 5.1b,d,f shows a picture of the realized HEMT LC Colpitts oscillator, its detailed schematics, and its key features, including both the geometrical and the electrical details of the integrated coil, as well as the minimum power consumption required for stable oscillations. As shown in Fig. 5.1d, the oscillator consists of a single HEMT transistor, a single-turn planar coil inductor, a resistor, and two capacitors. It is the same oscillator described in the previous chapter and used for single-chip cryogenic ESR. From the topology perspective, the realized common-drain Colpitts topology achieves low output impedance without loading the LC resonator and the capacitors  $C_1$  and  $C_2$  not only provide the positive feedback to the amplifier but also form the resonator together with the inductor. The latter is connected to ground by means of metalized holes (vias) which connect the top-side to the bottom-side of the chip. These vias are useful to avoid the adoption of bonding wires for ground connections, hence allowing for the implementation of non-differential topologies with low parasitics. Since the source-drain on-resistance of the HEMT transistor and the DC resistance from gate to ground are very low, the 500  $\Omega$  resistor determines the DC operating point of the oscillator and acts as a current source. The operating frequency of the oscillator depends on the bias voltage  $V_{DD}$  and on the temperature, with an overall range from 11.2 GHz to 11.4 GHz. The integrated Colpitts LC oscillator has a size of 0.8 $\times$ 0.5 mm<sup>2</sup> (Fig. 5.1b). A conductive epoxy (Epo-Tek, H20E-FC) is used to glue the chip to a standard FR4 printed circuit board and Au wires having a diameter of 20  $\mu\text{m}$  are used for wedge-wedge bonding of the chip to the board.

Fig. 5.1c shows the block diagram of the set-up used to characterize the standalone HEMT transistor and the HEMT LC Colpitts oscillator. The standalone transistor is connected to a semiconductor parameter analyzer in Kelvin 4-wires configuration. The signal at the output of the oscillator is down-converted to 200 MHz so as to match the central frequency of a homemade delay-line-discriminator (DLD) [41, 74] which performs the frequency-to-voltage conversion. The voltage noise spectral density at the output of the DLD is measured using a lock-in amplifier. The frequency noise spectral density (Fig. 5.1e) is computed from the measured voltage noise spectral density and the frequency-to-voltage conversion factor of the DLD. The amplifiers shown in the block diagram are used to match the dynamic range of both the frequency dividers and the analog-to-digital-converters of the acquisition board. The filters are used to improve the spectral purity of the signals.

## Chapter 5. A low power microwave HEMT LC oscillator operating down to 1.4 K



**Figure 5.1 – Schematics, pictures, and key-features of the realized HEMT structures.** (a) Symbol and layout of the standalone HEMT transistor. The finger width  $W_f$  is 15  $\mu\text{m}$ , the source-drain distance is 2.5  $\mu\text{m}$ , and the gate length is 70 nm. (b) Picture of the HEMT LC Colpitts oscillator. Coil size: 400  $\mu\text{m} \times 480 \mu\text{m}$ . The yellow squares (80  $\mu\text{m} \times 80 \mu\text{m}$ ) are the bonding pads. The yellow hexagons (100  $\mu\text{m}$  in diameter) are metallized holes, commonly called vias. The vias connect the integrated electronics on the front side of the chip to a 3.5  $\mu\text{m}$  thick layer of Au acting as ground plane on the back side. The thickness of the chip is 100  $\mu\text{m}$ . The overall size of the oscillator is 0.8 mm  $\times$  0.5 mm. (c) Block diagram of the set-up for the characterization of the standalone transistor and the LC oscillator: (A) Superconducting magnet with variable temperature insert (1.4 to 300 K, 0 to 9.4 T, Cryogenic Ltd); (B) Standalone HEMT transistor; (C) HEMT LC Colpitts oscillator; (D) Lock-in amplifier (EG&G 7265 up to 250 kHz, Stanford Research Systems SR844 up to 10 MHz); (E) DC power supply (Keithley 2400); (F) Semiconductor parameter analyzer (HP 4156A); (G) RF amplification stage composed of three RF amplifiers (Analog Devices, HMC-C001) and a 3 dB attenuator; (H) Frequency divider (Analog Devices, HMC-C040); (I) RF generator (R&S, SMR-20); (J) Mixer (Mini-Circuits ZFM-2000+); (K) 100 MHz high-pass filter (Crystek CHPFL-0100); (L) 300 MHz low-pass filter (Crystek CLPFL-0300); (M) Frequency divider (Valon Technology 3010); (N) Homemade DLD [41, 74] (200 MHz central frequency, 1 MHz detection range, 5 MHz FM bandwidth); (O) Amplifier (Stanford Research Systems SR560); (P) Amplifier (EG&G 5113); (Q) Amplifier (NF 5305). (d) Schematic of the HEMT LC Colpitts oscillator. It consists of a single HEMT transistor, an inductor, two capacitors, and a bias resistor. The transistor has a gate width of 52  $\mu\text{m}$  (four fingers, each having a width of 13  $\mu\text{m}$ ) and a gate length of 0.07  $\mu\text{m}$ . The oscillator is powered through a DC source (voltage:  $V_{DD}$ , current:  $I_{DD}$ ). (e) Measured frequency noise spectral density of the HEMT LC Colpitts oscillator at 1.4 K, 100 K, and 300 K at the minimum noise, which also corresponds to the condition of minimum noise. (f) Key-features of the HEMT LC Colpitts oscillator.



## 5.4. HEMT transistor characterization and parameters extraction

Finally, the divide-by-32 divider is used to get a lower frequency signal which can be measured by the frequency counter embedded in the multifunction data-acquisition-board.

In Fig. 5.1e, we report the experimentally measured frequency noise at 1.4 K, 100 K, and 300 K. The measured noise floor (i.e., the noise at frequencies above the  $1/f$  noise corner frequency) corresponds, within a factor of two, to the thermal frequency noise originating from the coil resistance given by  $(k_B TR)^{1/2}(f_{LC}/V_{LC,0})$ , where  $V_{LC,0}$  is the oscillation amplitude and  $R$  is the coil resistance at the operating frequency [12].

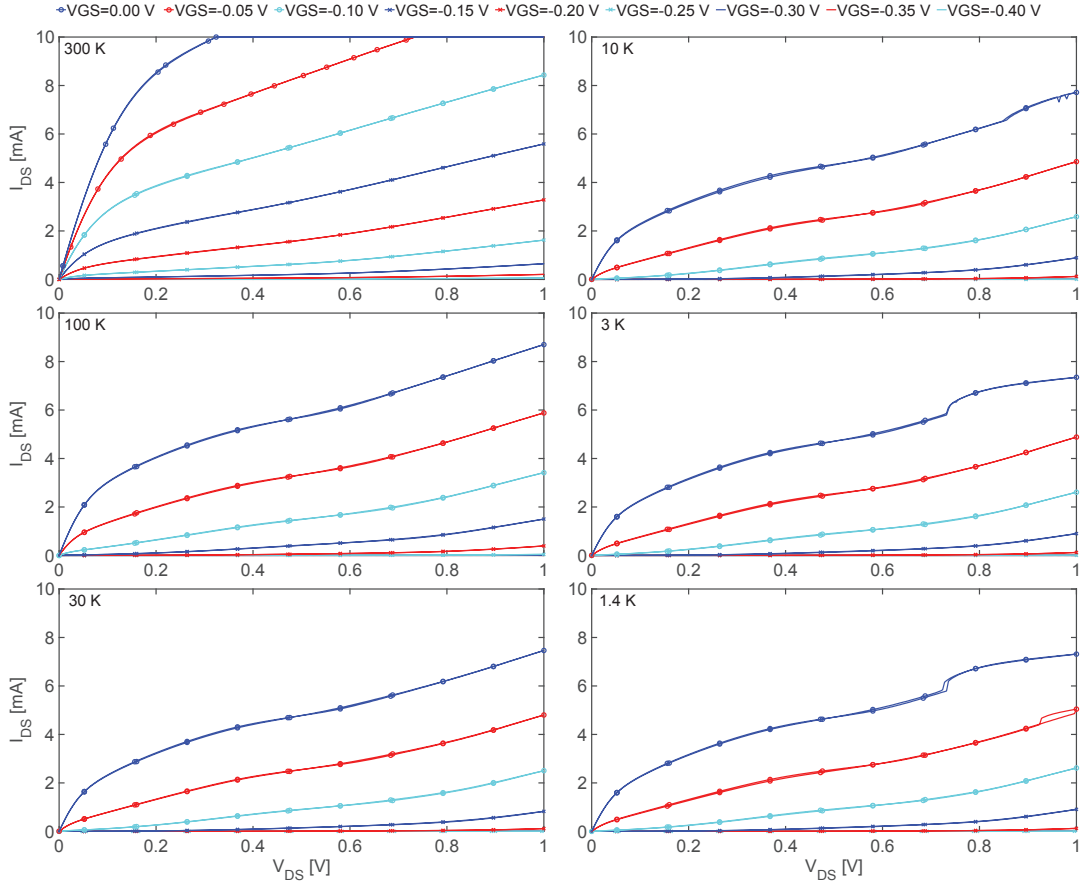


**Figure 5.2 – DC characterization of the standalone HEMT transistor.** The DC drain-source current  $I_{DS}$  is shown as a function of the drain-source voltage  $V_{DS}$  for different gate-source voltages  $V_{GS}$ , from 1.4 to 300 K. The transistor is composed of 4 fingers (each having a width of  $15\ \mu\text{m}$  for a total width of  $60\ \mu\text{m}$ ). It has a source-drain distance of  $2.5\ \mu\text{m}$  and a gate length of  $70\ \text{nm}$  (Fig. 5.1a).

## 5.4 HEMT transistor characterization and parameters extraction

In this section, we report the characterization of the standing alone HEMT transistor shown in Fig. 5.1a ( $15\ \mu\text{m}$  finger width, 4 fingers,  $60\ \mu\text{m}$  total width,  $2.5\ \mu\text{m}$  source-drain distance,  $70\ \text{nm}$  gate length) in the temperature range from 1.4 to 300 K. A static magnetic field from 0 to 8 T is used to measure its geometrical magnetoresistance and its Shubnikov-de-Haas (SdH) resistance oscillations. The former allows to extract the effective drain-source mobility

whereas the latter leads to the extraction of the charge carriers density. As shown below, the values of these parameters extracted from magnetoresistance measurements are in good agreement with those obtained from the DC characterization of the transistor at zero magnetic field.

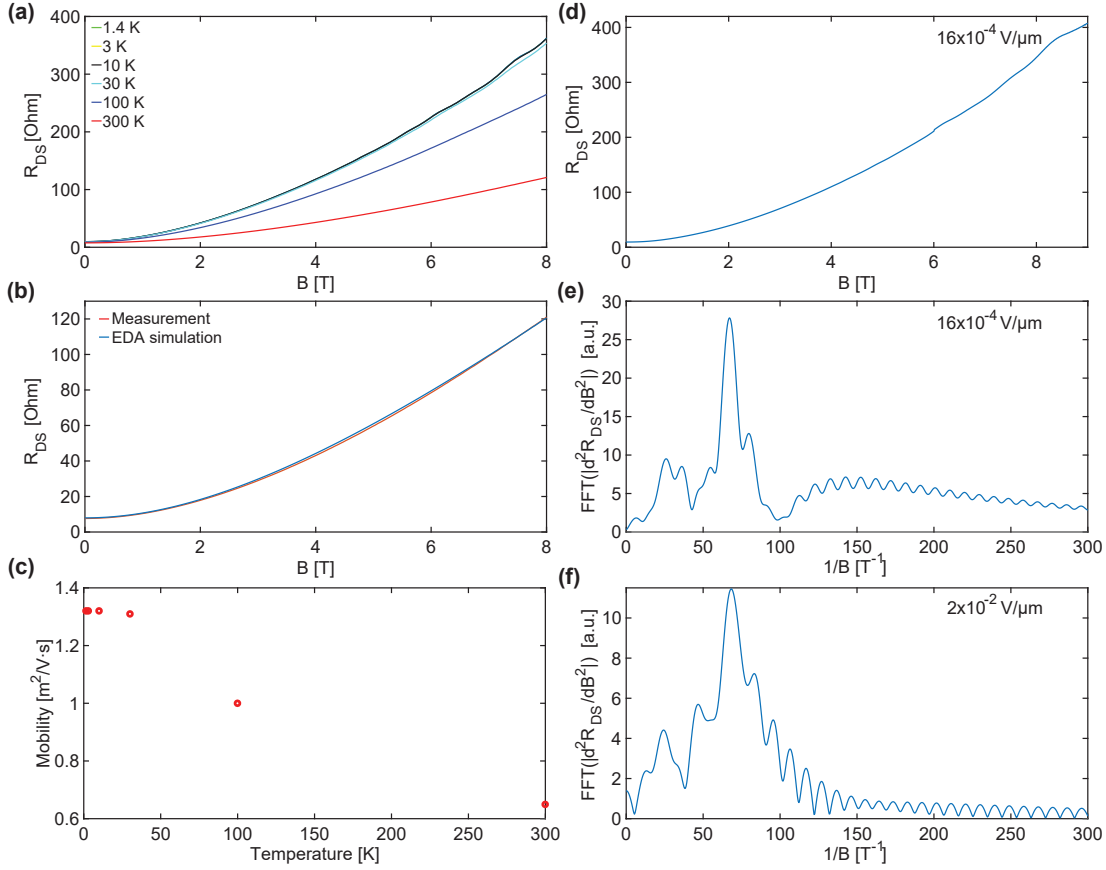


**Figure 5.3 – Magnetoresistance, mobility, and Shubnikov-de-Haas oscillations of the standalone HEMT transistor.** (a) Source-drain resistance  $R_{DS}$  as a function of the applied static magnetic field (from 0 to 8 T, orthogonal to the 2DEG) from 1.4 to 300 K. The curves from 1.4 to 30 K overlap. The transistor is biased with  $V_{GS} = 0.2$  V and  $V_{DS} = 50$  mV. (b) Comparison between the measured and the EDA simulated  $R_{DS}$  as a function of the applied static magnetic field (see details of the EDA simulation in the text). (c) Extracted effective carrier mobility as a function of the temperature. The magnitude of the carrier mobility has no significant variation from 1.4 to 30 K, and decreases by a factor of two from 30 to 300 K. (d) Source-drain resistance  $R_{DS}$  as a function of the magnetic field for  $V_{GS} = 0.2$  V and  $V_{DS} = 4$  mV (i.e., electric field of  $16 \times 10^{-4}$  V/ $\mu\text{m}$ ). Small Shubnikov-de-Haas oscillations are visible above 5 T. (e) FFT of  $d^2 R_{DS} / dB^2$  plotted as a function of  $1/B$ . The source-drain resistance  $R_{DS}$  is the one plotted in (d). The main periodicity of the Shubnikov-de-Haas oscillations is at  $70 \text{ T}^{-1}$ . (f) FFT of  $d^2 R_{DS} / dB^2$  plotted as a function of  $1/B$ . The source-drain resistance  $R_{DS}$  is measured at  $V_{DS} = 50$  mV (i.e., electric field of  $2 \times 10^{-2}$  V/ $\mu\text{m}$ ). The periodicity is the same as in (e) but with a much smaller amplitude, presumably due to the larger electric field applied.

Fig. 5.2 shows the DC characterization ( $I_{DS}$ - $V_{DS}$  curves for different  $V_{GS}$  values) from 1.4 to 300 K of the HEMT transistor shown in Fig. 5.1a.  $V_{DS}$  is swept from 0 to 1 V whereas  $V_{GS}$  spans from -0.4 to 0 V. For a given bias condition ( $V_{GS}$  and  $V_{DS}$ ), the drain current  $I_{DS}$  is almost constant from 1.4 to 30 K, and increases from 30 to 300 K. The kink effect with hysteresis [124] is visible below 10 K.

#### 5.4. HEMT transistor characterization and parameters extraction

According to the level 1 Shichman-Hodges model [125–127], we extract the threshold voltage  $V_{th}$ , the intrinsic  $\beta$ , and the channel length modulation factor  $\lambda$  from the DC characterization shown in Fig. 5.2. In order to extract  $V_{th}$ , we plot the  $I_{DS}$ - $V_{GS}$  curves from the data shown in the  $I_{DS}$ - $V_{DS}$  characterization, and we identify the tangent line with the maximum slope for  $V_{DS} = 10$  mV. The latter intercepts the  $V_{GS}$  axis at the point which corresponds to the threshold voltage  $V_{th}$  [128]. The value of  $\beta$  is directly extracted from the source-drain resistance  $R_{DS} = V_{DS}/I_{DS}$  when the transistor is polarized in the triode region ( $V_{DS} \ll V_{GS} - V_{th}$ ), i.e.,  $\beta = 1/(R_{DS}(V_{GS} - V_{th}))$ . The channel length modulation factor is extracted in deep saturation ( $V_{DS} \gg V_{GS} - V_{th}$ ) and can be written as  $\lambda = 2\Delta I_{DS}/(\Delta V_{DS}\beta(V_{GS} - V_{th})^2)$ . From the experimental data, we obtain  $V_{th} = -0.22$  V at 300 K and  $V_{th} = -0.07$  V at 1.4 K. A similar behavior has been already reported in the literature for both CMOS and HEMT transistors at low temperature [129–131]. The extracted value of  $\beta$  is  $0.28$  A/V<sup>2</sup> at 300 K and  $0.47$  A/V<sup>2</sup> at 1.4 K.  $\lambda$  is approximately  $10$  V<sup>-1</sup> at 300 K and  $2$  V<sup>-1</sup> at 1.4 K.

Fig. 5.3a shows the measured HEMT transistor source-drain resistance  $R_{DS}$  as a function of the static magnetic field  $B$  applied in the direction orthogonal to the 2DEG plane. If the magnetic field is applied parallel to the 2DEG plane, a much smaller change of  $R_{DS}$  is measured (approximately 2.5% from 0 to 8 T) and this indicates that the observed resistance variation is due to the geometrical magnetoresistance (i.e., the Hall effect). The measurement of the geometrical magnetoresistance is widely used as a method for the extraction of the charge carrier mobility [132–134]. In order to model the device and extract the carrier mobility, we used the equivalent circuit described by Popovic et al. [135] and shown in Fig. 5.4. Such a model, which can be implemented in any electronic-design-automation (EDA) simulator, consists of a network of identical magnetic field dependent resistors and current-controlled-current-sources (CCCS). The extracted mobility value is  $0.65$  m<sup>2</sup>/Vs at 300 K and  $1.2$  m<sup>2</sup>/Vs at 1.4 K. This result is coherent with the extracted  $\beta$ , which also increases by a factor of two at low temperature.

The drain-source resistance  $R_{DS}$  is approximately  $8$   $\Omega$  at zero field, regardless of the temperature (Fig. 5.3a). Since the conductivity is defined as  $\sigma = en\mu$  (where  $e$  is the elementary charge,  $n$  is the density of carriers, and  $\mu$  is the mobility) and the resistance is  $R_{DS} = L_{SD}/W\sigma$  (where  $L_{SD} = 2.5$   $\mu\text{m}$  and  $W = 60$   $\mu\text{m}$  are the transistor source-drain distance and width, respectively), we estimate a density of carriers of about  $5 \times 10^{16}$  m<sup>-2</sup>. In order to cross check such a result, we measured the periodicity of the SdH oscillations [132, 136]. In our case, the SdH oscillations are the oscillations of  $R_{DS}$  as a function of the applied magnetic field, which we measured at 1.4 K. As shown in Fig. 5.3d,e,f, we observe SdH oscillations for magnetic field values above 5 T, at 1.4 K, and for  $V_{DS}$  values of 50 mV (i.e., electric field of  $2 \times 10^{-2}$  V/ $\mu\text{m}$ ) and 4 mV (i.e., electric field of  $16 \times 10^{-4}$  V/ $\mu\text{m}$ ). The periodicity is more evident at the lowest electric field. Performing the Fast-Fourier-Transform (FFT) of  $d^2R_{DS}/dB^2$ , plotted as a function of  $1/B$ , allows to extract the oscillation frequency. As shown in Fig. 5.3e,f, there is a main frequency component at about  $70$  T<sup>-1</sup>. According to Ref. [136], we compute the density of carriers as  $n \cong \frac{2e/h}{\Delta(1/B)} \cong 3.5 \times 10^{16}$  m<sup>-2</sup>, where  $h$  is the Planck constant and  $\Delta(1/B)$  is the periodicity of the SdH oscillations. This value for the density of carriers is in good agreement with the one estimated above, obtained from measurements of the resistance (i.e.,  $5 \times 10^{16}$  m<sup>-2</sup>). However, the SdH oscillations reported in this work are significantly smaller than those reported in

previous publications [136–140]. This might be due to the larger electric fields applied to the HEMT transistor with respect to those usually reported in the literature. Accordingly, Refs. [137–139] show that the SdH oscillations get reduced when the applied electric field increases. In our measurements, the minimum practically applicable electric field is approximately  $10^{-3}$  V/ $\mu$ m. Indeed, in our experimental set-up, at lower  $V_{DS}$  (i.e., at lower electric fields) the magnetoresistance measurements are too noisy to allow for the extraction of the charge carrier density.

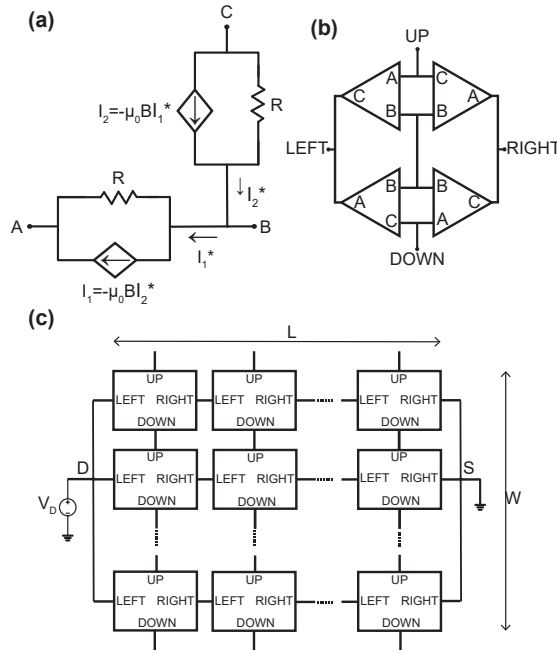


**Figure 5.4 – Equivalent circuit to model the geometrical magnetoresistance.** The equivalent circuit is described by Popovic et al. [135] and it is composed of a modular architecture based on three building parts: (a) magnetoresistance unit cells (MRs), (b) magnetoresistance blocks, and the overall (c) device channel model. First, for each MR, the value for the two resistances is chosen according to both the geometry and the device resistance without magnetic field as  $R = R_{DS} \frac{W}{L} N$ , where  $W$  is the channel width for each finger,  $L$  is the channel length, and  $N$  is the number of fingers. In our case, the resistance of the transistor at zero magnetic field is  $8 \Omega$  and the number of fingers is 4, hence  $R = 192 \Omega$ . The CCCSs are defined as  $I_1 = -\mu_0 B I_2^*$  and  $I_2 = -\mu_0 B I_1^*$ . Four MRs are connected together to form a block. Hence, a lattice of blocks is structured in order to model the real device. The ratio between the number of rows and columns is  $W/L = 6$  whereas the number of columns has to be sufficiently large (20 in our case) for the simulation to converge to a value with a small error. Finally, the lattice is replicated four times (i.e., 9600 MR units) in order to take into account the number of fingers. In the EDA simulation, the mobility is adjusted in order for  $R$  to match the experimental curve.

## 5.5 HEMT LC Colpitts oscillator characterization

In this section, we report the results of measurements performed on the LC Colpitts oscillator shown in Fig. 5.1d. In particular, we investigated the start-up condition as a function of temperature and the oscillation frequency as a function of the supply voltage.

The HEMT LC Colpitts oscillator shows a minimum (i.e., start-up) power consumption of 90  $\mu$ W at 300 K ( $V_{DD} = 220$  mV,  $I_{DD} = 400 \mu$ A) and 4  $\mu$ W below 30 K ( $V_{DD} = 40$  mV,  $I_{DD} = 110 \mu$ A). This is, at the best of our knowledge, the lowest power consumption reported to date for an LC

## 5.5. HEMT LC Colpitts oscillator characterization

oscillator working in the same frequency range.

As reported above, the realized oscillator shows a lower power consumption at cryogenic temperature than at 300 K. This is presumably due to the following reasons. The decrease of the threshold voltage from -0.22 to -0.07 V allows to reduce  $V_{DD}$  so as to obtain the same overdrive voltage  $V_{GS} - V_{th}$ . Also, the decrease of the coil resistance results in a lower  $g_m^{\min}$  (and, hence, in a lower minimum  $V_{DD}$ ), whereas the increase of  $\beta$  results in a larger  $g_m$  (Sec. 5.8).

It is worthy to note that the topology of the LC oscillator reported here (Fig. 5.1d) is optimized for low parasitics and area occupation. Indeed, only a few components are required and the bias point of the oscillator is set through a single voltage supply  $V_{DD}$  (i.e., no extra pads are needed). However, as discussed in Sec. 5.8, this architecture is not optimized for low power consumption. As a matter of fact, the bias resistance  $R_B$  is large with respect to  $R_{DS}$  and  $R$  so the majority of the power provided by the generator is dissipated across  $R_B$ , which has the only aim to producing a suitable  $V_{GS}$  bias. Additionally, since the threshold voltage of the transistor varies as a function of the temperature, it would be beneficial to optimize  $V_{GS}$  independently (e.g., by adjusting the gate voltage) whereas in the proposed architecture it results intrinsically defined by  $V_{DD}$ . As discussed in Sec. 5.8 (and shown in Fig. 5.6b), a slightly more complex topology, where  $R_B$  is replaced by an inductor  $L_B$  and the gate-source voltage  $V_{GS}$  is freely adjustable, should allow to obtain a further significant reduction of the start-up power consumption.

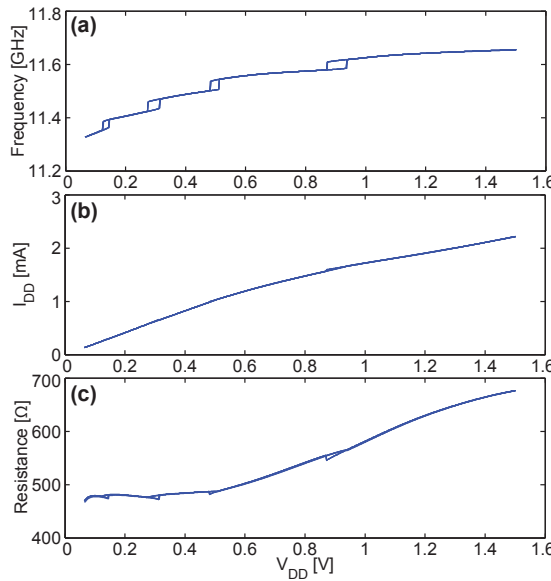


**Figure 5.5 – Characterization of the HEMT LC Colpitts oscillator at 1.4 K.** Plots of (a) working frequency, (b) bias current and (c) resistance of the oscillator as a function of its bias voltage. The latter is swept up and down for ten times from 65 mV to 1.5 V. Jumps and hysteresis phenomena are clearly visible and reproducible for both the frequency and the resistance. The frequency jumps are approximately equal to 35 MHz for all transitions.

Fig. 5.5 reports measurements of the operating frequency, the DC current  $I_{DD}$ , and the resistance  $R_{DD}$  as a function of the bias voltage  $V_{DD}$  at 1.4 K. The bias voltage is swept up

and down from 65 mV (i.e., close to the start-up condition of 40 mV) to 1.5 V for ten times. As shown in Fig. 5.5a,b,c, the oscillation frequency (as well as the current and the resistance) shows discontinuities as a function of the bias voltage. The corresponding frequency jumps are of approximately 35 MHz. The position of the transitions and their amplitude change as a function of both the applied magnetic field and the temperature. Moreover, the density of transitions increases close to the start-up bias point. Transitions get smoother above 30 K and disappear above 70 K. In contrast to CMOS based oscillators [141], no random telegraph signals (RTS) are present. We also observed that it is possible to induce frequency jumps at fixed bias voltage  $V_{DD}$  by changing the applied magnetic field (both parallel and orthogonal to the 2DEG). We performed the previous characterization on four nominally identical oscillators, obtaining similar (although not identical) results. For a bias  $V_{DD}$  ranging from 65 mV to 1.5 V, the number of sharp transitions changes from three to five and their amplitude from 20 MHz to 200 MHz. As for the CMOS oscillators reported in [141], the physical origin of the measured frequency jumps is still unclear to us.

### 5.6 Discussion and outlook

In this chapter, we have reported about the design and characterization of a low power HEMT LC Colpitts oscillator operating at 11 GHz. In particular, we investigated the minimum power consumption to sustain stable oscillations and the frequency noise in the temperature range from 1.4 to 300 K. The realized oscillator shows the lowest power consumption reported in the literature for an LC oscillator working in this frequency range. We have also reported on the results of simulations which indicate that the power consumption can be further reduced by using a slightly different topology. In such a context, a reduced power consumption is of crucial importance for measurements at low temperatures. As a matter of fact, below 1 K, the limited effective cooling power of  $^3\text{He}$  and  $^3\text{He}^4\text{He}$  dilution refrigerator systems demands for devices operating in the  $\mu\text{W}$  range and below, especially when the power has to be dissipated in a very small volume (e.g., in the channel of a HEMT transistor suitable to operate at microwave frequencies above 10 GHz). It is of particular interest the possibility of reaching the condition  $\hbar\omega > k_B T$ , where we expect to observe the reduction of the thermal noise and, possibly, also a quantum behavior related to the energy quantization of the oscillator coupled with the non linear behavior of the transistor. Indeed, LC resonators operating in the condition  $\hbar\omega > k_B T$  are, in principle, possible candidates to show a macroscopic quantum behavior but, due to their linear behavior, the energy (frequency) quantization is not observable [142]. In contrast, the LC oscillators described in this work show a relatively strong dependence of the oscillator frequency on the applied bias voltage, which makes them highly anharmonic. This condition might be sufficient to observe interesting unexplored phenomena, which might include their behavior as artificial atoms, as reported before for superconducting quantum circuits (SQC) based on Josephson junctions [142, 143].

## 5.7 Acknowledgement

Financial support from the Swiss National Science Foundation (SNSF) is gratefully acknowledged (grant 200020-175939).

## 5.8 Appendix. Proposal for a HEMT LC Colpitts oscillator with further reduced power consumption

The HEMT LC oscillator topology sketched in Fig. 5.1a and described in Sec. 5.4 has a limited versatility since the DC gate voltage is tied to ground and the DC source voltage is intrinsically determined by the voltage drop across  $R_B$ . As a consequence,  $V_{GS}$  cannot be independently adjusted with respect to  $V_{DS}$ .

Fig. 5.6b shows an improved topology which would allow to (1) decouple  $V_{GS}$  from  $V_{DD}$  and (2) avoid the power dissipated across the bias resistor  $R_B$ . In this more versatile topology,  $V_{GS}$  can be independently adjusted with respect to  $V_{DS}$  and the series resistance of the bias inductor  $R_{LB}$  is much smaller than the bias resistor  $R_B$  used in the topology shown in Fig. 5.6a. As a consequence, we expect that this topology should allow to reduce the oscillator power consumption at the start-up (i.e., the minimum power consumption required by the LC Colpitts oscillator to produce stable oscillations).

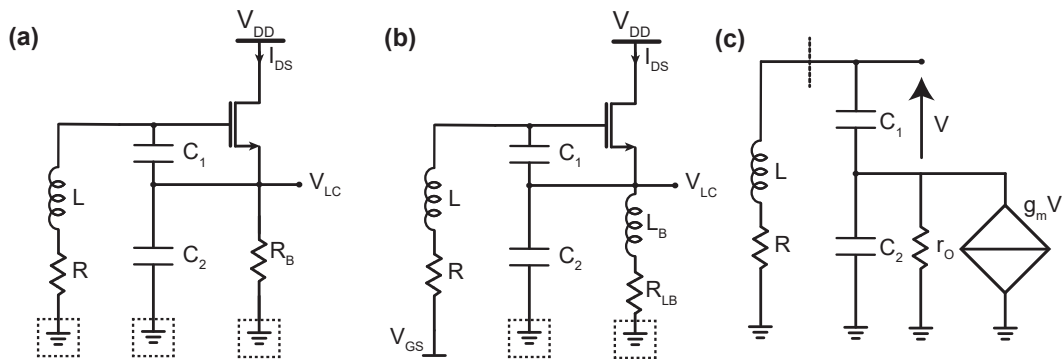


**Figure 5.6 – Schematics of HEMT LC Colpitts oscillators.** (a) Schematic of the HEMT LC Colpitts oscillator designed and characterized in this chapter. It consists of a single HEMT transistor, a tank inductor (inductance  $L$ , series resistance  $R$ ), two tank capacitors ( $C_1$  and  $C_2$ ), and a bias resistor ( $R_B$ ). The value of the components used in simulations at 300 K and 1.4 K are:  $L = 1.15$  nH,  $R = 3 \Omega$  at 300 K ( $1 \Omega$  at 1.4 K),  $C_1 = 150$  fF,  $C_2 = 500$  fF, and  $R_B = 500 \Omega$  ( $350 \Omega$  at 1.4 K). (b) Schematic of the low power optimized HEMT LC Colpitts oscillator. It consists of a single HEMT transistor, a tank inductor (inductance  $L$ , series resistance  $R$ ), two tank capacitors ( $C_1$  and  $C_2$ ) and a bias inductor (inductance  $L_B$ , series resistance  $R_{LB}$ ). The value of the components used in simulations at 300 K and 1.4 K are:  $L = 1.15$  nH,  $R = 3 \Omega$  ( $1 \Omega$  at 1.4 K),  $C_1 = 150$  fF,  $C_2 = 500$  fF,  $L_B = 15$  nH, and  $R_{LB} = 3 \Omega$  ( $1 \Omega$  at 1.4 K). The oscillator is powered with a DC source (voltage:  $V_{DD}$ , current:  $I_{DS}$ ). (c) Detailed schematic of the AC small-signal model related to the low power optimized HEMT LC Colpitts oscillator sketched in (b). The HEMT transistor is modeled by a voltage-controlled-current-source and an  $r_o$  resistor.

In this topology, the bias inductance  $L_B$  is chosen sufficiently large such that  $\omega_{LC} L_B \gg 1/\omega_{LC} C_2$ . Hence, the oscillator frequency is, also for this topology, given by  $\omega_{LC} = 1/\sqrt{LC}$ ,

where  $C = C_1 C_2 / (C_1 + C_2)$  is the effective capacitance. In order to compute the start-up condition for this oscillator, we can use the small-signal AC model shown in Fig. 5.6c, which is valid regardless of (1) the type of FET transistor (MOSFET or HEMT) and (2) its polarization (triode or saturation). The transistor is modeled by its transconductance ( $g_m = \partial I_{DS} / \partial V_{GS}$ ) and its output resistance ( $r_O = \partial V_{DS} / \partial I_{DS}$ ). Stable oscillations are obtained when the negative resistance created by the transistor compensates for the overall losses in the system. In order to analyze the circuit, we separate the tank inductor from the energy restoring system at the level of the dashed line (Fig. 5.6c). Since the reactance of the compensation system only affects the operating frequency, we can consider the resistive part of the overall impedance, only. The condition required for the total resistance to be zero (i.e., for the compensation of the losses) is

$$R = -g_m \frac{C_2}{C_1} \frac{r_O^2}{\omega_{LC}^2 r_O^2 C_2^2 + 1} + \frac{r_O}{1 + \omega_{LC}^2 r_O^2 C_2^2}. \quad (5.1)$$

Consequently, the minimum transconductance for stable oscillations is

$$g_m^{\min} = \left( R + \frac{r_O}{1 + \omega_{LC}^2 r_O^2 C_2^2} \right) \frac{C_1}{C_2} \frac{1 + \omega_{LC}^2 r_O^2 C_2^2}{r_O^2}. \quad (5.2)$$

According to a level 1 model, the transistor is characterized by three parameters ( $V_{th}$ ,  $\beta$ ,  $\lambda$ ), and its transconductance in triode and saturation regions is

$$g_m^{\text{tri}} = \frac{2I_{DS}}{2(V_{GS} - V_{th}) - V_{DS}}, \quad g_m^{\text{sat}} = \frac{2I_{DS}}{V_{GS} - V_{th}}. \quad (5.3)$$

Indeed, according to the bias point, we have the following equations.

$$\text{Triode} \begin{cases} I_{DS} = \frac{1}{2} \beta V_{DS} (2(V_{GS} - V_{th}) - V_{DS}) (1 + \lambda V_{DS}) \\ V_{DS} \leq V_{GS} - V_{th} \\ V_{GS} > V_{th} \end{cases} \rightarrow \begin{cases} g_m = \frac{2I_{DS}}{2(V_{GS} - V_{th}) - V_{DS}} \\ r_O = \frac{\partial I_{DS}}{\partial V_{DS}} \end{cases} \quad (5.4)$$

$$\text{Saturation} \begin{cases} I_{DS} = \frac{1}{2} \beta (V_{GS} - V_{th})^2 (1 + \lambda V_{DS}) \\ V_{DS} \geq V_{GS} - V_{th} \\ V_{GS} > V_{th} \end{cases} \rightarrow \begin{cases} g_m = \frac{2I_{DS}}{V_{GS} - V_{th}} \\ r_O = \frac{2}{\beta (V_{GS} - V_{th})^2 \lambda} \end{cases} \quad (5.5)$$



### 5.8. Appendix. Proposal for a HEMT LC Colpitts oscillator with further reduced power consumption

The minimum drain-source current is  $I_{DS}^{\min} = \min(I_{DS}^{\text{tri}}(g_m = g_m^{\min}), I_{DS}^{\text{sat}}(g_m = g_m^{\min}))$  whereas the minimum drain-source voltage is  $V_{DS}^{\min} = \min(V_{DS}^{\text{tri}}(I_{DS} = I_{DS}^{\min}), V_{DS}^{\text{sat}}(I_{DS} = I_{DS}^{\min}))$ . Hence, the minimum power at the start-up is  $P_{\text{start-up}}^{\min} = V_{DS}^{\min} I_{DS}^{\min}$ .

The amplitude of the corresponding steady-state oscillation can be computed according to the Fourier series expansion. In particular, we can consider the time-varying signal at the gate as defined by  $v_{GS}(t) = V_m \cos(\omega_{LC} t) + V_{GS}$ , and then we may solve the following system focusing on the first two Fourier coefficients (i.e., DC bias and fundamental tone) so as to extract  $V_m$  (distorsion is not taken into account so the coefficients related to the harmonics are not calculated).

$$\begin{cases} I_0 = I_{DS}^{\min} = \frac{\omega_{LC}}{\pi} \int_0^{T/2} I_{DS}^{\text{tri,sat}}(v_{GS}(t)) dt \\ I_1 = \frac{2\omega_{LC}}{\pi} \int_0^{T/2} I_{DS}^{\text{tri,sat}}(v_{GS}(t)) \cos(\omega_{LC} t) dt \end{cases} \quad (5.6)$$

Hence, the overall minimum power consumption for an LC Colpitts oscillator running in steady-state regime is  $P_{\text{tot}}^{\min} = V_{DS}^{\min} \sqrt{(I_{DS}^{\min})^2 + (I_1^{\text{rms}})^2}$ .

Numerical computations, based on the previous equations implemented in Mathematica<sup>®</sup>, reveal that the minimum power consumption is weakly dependent on  $r_0$ , which can be assumed to be  $\infty$  (i.e.,  $\lambda = 0$ ). Moreover, since the gate-source voltage  $V_{GS}$  is adjustable, we can consider the overdrive voltage ( $V_{GS} - V_{th}$ ) as a single variable. The numerical computations also show that the optimal bias for minimum power consumption is at the transition between saturation and the quadratic region, where  $V_{DS} \cong (V_{GS} - V_{th})$  and  $I_{DS} \cong (\beta/2)(V_{GS} - V_{th})^2$ . By introducing these assumptions, we obtain the following simplified equations

$$\begin{cases} I_{DS}^{\min} \cong \frac{(g_m^{\min})^2}{2\beta} \\ V_{DS}^{\min} \cong V_{GS}^{\min} - V_{th} = \frac{g_m^{\min}}{\beta} \\ g_m^{\min} \cong RC_1 C_2 \omega_{LC}^2 \end{cases} \quad (5.7)$$

$$\begin{cases} I_{DS} = \frac{1}{2}\beta(V_{GS} - V_{th})^2 \\ V_{DS} \geq V_{GS} - V_{th} \\ V_{GS} > V_{th} \end{cases} \rightarrow \begin{cases} g_m = \frac{2I_{DS}}{V_{GS} - V_{th}} \\ r_0 = \infty \end{cases} \rightarrow \begin{cases} g_m^{\min} = \sqrt{2I_{DS}^{\min}\beta} \\ V_{DS}^{\min} = V_{GS}^{\min} - V_{th} = \frac{g_m^{\min}}{\beta} \\ g_m^{\min} = RC_1 C_2 \omega_{LC}^2 \end{cases} \quad (5.8)$$

Hence, for weak oscillation amplitudes, we end up with

$$\left\{ \begin{array}{l} V_m^{\min} = \frac{\sqrt{2}}{\beta} \sqrt{2\beta I_{DS}^{\min} - (g_m^{\min})^2} \\ I_1^{\min} = V_m^{\min} g_m^{\min} \\ I_{DS}^{\min} = \frac{(g_m^{\min})^2}{2\beta} \end{array} \right. \rightarrow I_{tot}^{rms} = \sqrt{(I_{DS}^{\min})^2 + \left(\frac{\sqrt{2}}{2} I_1^{\min}\right)^2} \rightarrow P_{tot}^{\min} = V_{DS}^{\min} I_{tot}^{rms} \quad (5.9)$$

If we consider  $I_1$  to be negligible with respect to  $I_{DS}$  (a reasonable assumption for low amplitude oscillations), the minimum power consumption for an LC Colpitts oscillator having the topology shown in Fig. 5.6b results

$$P^{\min} = \frac{(g_m^{\min})^3}{2\beta^2} = \frac{(RC_1 C_2 \omega_{LC}^2)^3}{2\beta^2} = \frac{(R(C_1 + C_2)/L)^3}{2\beta^2}. \quad (5.10)$$

As intuitively expected, the power consumption is reduced for a smaller coil resistance  $R$  and for a larger  $\beta$ . From the previous equation, the use of a transistor with a larger width (and hence with a larger  $\beta$ ) would allow to achieve a lower power consumption. However, a larger transistor would have larger parasitic capacitances, de-facto limiting the maximum achievable oscillation frequency.

For an oscillator based on the topology optimized for power consumption (Fig. 5.6b) and having the same parameters as those reported in this work (Fig. 5.6a) (i.e.,  $L = 1.15$  nH,  $R = 3$   $\Omega$ ,  $C_1 = 150$  fF,  $C_2 = 500$  fF,  $\beta = 0.28$  A/V<sup>2</sup>,  $\omega_{LC} = 2\pi \times 11$  GHz), the theoretical minimum power consumption expected from Eq. 5.10 would be of about 50 nW. It is important to note that a moderate error in the estimation of the parameters in Eq. 5.10 would result in a very large variation of the power consumption. For example, the combined effect of a two times larger  $R$  with a two times smaller  $\beta$  would result in a minimum power consumption increase by a factor of 32, resulting in a power consumption of about 2  $\mu$ W.

In order to test the validity of the simple analytical result given by Eq. 5.10 for the oscillator topology in Fig. 5.6b, we performed simulations with different transistor models. The results of these simulations are reported in Tab. 5.1, which also includes simulations and experimental results obtained with the oscillator topology shown in Fig. 5.6a (i.e., the one designed, experimentally characterized, and reported in this work). The simulated results are obtained, respectively, using a level 1 model [126, 127], a level 1 model with parasitics, and the foundry model. The level 1 parameters are extracted from the standalone HEMT transistor experimental characterization reported in Sec. 5.3 whereas the transistor parasitics are obtained from the foundry model. The approximate values for the capacitances between the transistor terminals ( $C_{gs}$ ,  $C_{ds}$ ,  $C_{gd}$ ) are of 15 fF, the capacitances terminals to ground ( $C_d$ ,  $C_s$ ) are of 25 fF, the series resistances of the terminals ( $R_g$ ,  $R_s$ ,  $R_d$ ) are of 3 to 5  $\Omega$ , and the series inductances of the terminals ( $L_g$ ,  $L_d$ ,  $L_s$ ) are of 3 to 5 pH.

## 5.8. Appendix. Proposal for a HEMT LC Colpitts oscillator with further reduced power consumption

The topology in Fig. 5.6a has a start-up up condition where the minimum supply voltage  $V_{DD}^{\min}$  is approximately given by  $V_{th}$  and the minimum current  $I_{DS}^{\min}$  is approximately given by  $V_{DD}^{\min}/R_B \cong V_{th}/R_B$ . Hence, the minimum power consumption is  $P^{\min} = V_{DD}^{\min} I_{DS}^{\min} \cong V_{th}^2/R_B$ . For this topology, an accurate transistor modeling is not critical for the determination of the power consumption. Hence, it is not surprising that the simulations performed using a level 1 model for the transistor can predict quite accurately the minimum power consumption required for stable oscillations. As shown in Tab. 5.1, for this oscillator topology, the experimentally obtained minimum power consumption is in agreement, within a factor of two, with the simulations performed using the level 1 model.

ELECTRICAL PARAMETER	MODEL	Fig.5(a)	Fig.5(b)
$V_{DD}^{\min}$ [mV] @300 K	experimental	220	-
	foundry	255	34
	level 1	188	7
	level 1 with parasitics	191	19
$I_{DS}^{\min}$ [ $\mu$ A] @300 K	experimental	410	-
	foundry	420	450
	level 1	500	6
	level 1 with parasitics	450	94
$P^{\min}$ [ $\mu$ W] @300 K	experimental	90	-
	foundry	107	16
	level 1	94	0.05
	level 1 with parasitics	85	2
$V_{DD}^{\min}$ [mV] @1.4 K	experimental	40	-
	level 1	51	2
	level 1 with parasitics	57	6
$I_{DS}^{\min}$ [ $\mu$ A] @1.4 K	experimental	110	-
	level 1	130	2
	level 1 with parasitics	150	20
$P^{\min}$ [ $\mu$ W] @1.4 K	experimental	4	-
	level 1	7	0.004
	level 1 with parasitics	8	0.120

**Table 5.1 – Oscillator start-up condition.** Experimental and simulated start-up conditions for the two LC Colpitts topologies shown in Fig. 5.6, both implemented using a HEMT technology (D0071H mHEMT 70 nm, OMMIC, France). The simulations are performed using the level 1 model of the HEMT transistor, with the parameter values extracted from the standalone HEMT transistor characterization reported in Sec. 5.4 and the foundry model supplied by OMMIC. Simulations are performed using Quite Universal Circuit Simulator (QUCS<sup>®</sup>) for the level 1 model and Advanced Design System (ADS<sup>®</sup>) for the foundry model. The values for the level 1 parameters at 300 K are:  $V_{th} = -220$  mV,  $K_P = 3.4 \times 10^{-3}$  A/V<sup>2</sup>,  $W = 52$   $\mu$ m,  $L = 0.07$   $\mu$ m,  $\lambda = 10$  V<sup>-1</sup>,  $\gamma = 0$ . The values at 1.4 K are:  $V_{th} = -70$  mV,  $K_P = 6.5 \times 10^{-3}$  A/V<sup>2</sup>,  $W = 52$   $\mu$ m,  $L = 0.07$   $\mu$ m,  $\lambda = 2$  V<sup>-1</sup>,  $\gamma = 0$ .  $K_P$  is obtained from the extracted value of  $\beta$  as  $K_P = \beta(L/W)$ .

For the topology sketched in Fig. 5.6b, the minimum power consumption obtained from level 1 simulations is in agreement, within a few percent, with the analytical expression given by Eq.

5.10. However, this only means that Eq. 5.10 is properly derived from the basic equations of the level 1 model. In contrast, if we use the model given by the foundry, the power consumption at 300 K is two orders of magnitude larger than what expected from the level 1 model without parasitics. If the parasitics described above are introduced in the level 1 model, the agreement improves significantly but the difference in power consumption is still of about one order of magnitude. The causes of this still large discrepancy are unclear. Despite the relatively poor modeling agreement, both simulations and the intuitive arguments related to the biasing freedom indicate that the oscillator topology shown in Fig. 5.6b should achieve a significantly lower power consumption with respect to the one of Fig. 5.6a. In the near future, we plan to implement and experimentally characterize this oscillator topology, with the aim of obtaining a power consumption below 1  $\mu$ W at low temperature and as a means to give more robust guidelines for the modeling of ultra-low power HEMT oscillators (especially for deep cryogenic applications).

Since the overdrive voltage has to be small for low power consumption, if the adopted transistor were a MOSFET we could introduce the EKV model [144] to describe its behaviour with a single equation (in the saturation regime) regardless of the inversion level (i.e., strong, moderate, or weak inversion). The EKV model is more accurate out of the strong inversion region but it has never been investigated for HEMTs. However, since the characteristic DC curves have a similar shape, we have attempted to describe both transistors with the same equations. The drain-source current described by the EKV model is

$$I_{DS} = \frac{2}{k} \beta V_t^2 \ln^2 \left( 1 + e^{\frac{k(V_{GS} - V_{th})}{2V_t}} \right) \quad (5.11)$$

where  $V_t = \frac{k_B T}{q}$ ,  $k_B$  is the Boltzmann constant,  $T$  is the working temperature,  $q$  is the elementary electric charge, and  $k$  is an intrinsic parameter which ranges from 1.2 to 1.4 for MOSFETs. Consequently, recalling that  $g_m = \partial I_{DS} / \partial V_{GS}$ , we end up with

$$g_m = \frac{k I_{DS}}{V_t} \frac{2}{1 + \sqrt{1 + 2 \frac{I_{DS} k}{\beta V_t^2}}} \quad (5.12)$$

When  $\beta$  is large (e.g.,  $\mu_0$  is large),  $g_m \cong k I_{DS} / V_t$ . Recalling that  $g_m^{\min} = RC_1 C_2 \omega_{LC}^2$ , the minimum drain-source current results

$$I_{DS}^{\min} = RC_1 C_2 \omega_{LC}^2 V_t \frac{1}{k} \quad (5.13)$$

### 5.8. Appendix. Proposal for a HEMT LC Colpitts oscillator with further reduced power consumption

---

In order for the transistor to operate in saturation region, we must ensure that  $V_{DS} \geq V_{DS}^{\min} \cong 4V_t$ . Hence the minimum power consumption is  $P_{\text{tot}}^{\min} = I_{DS}^{\min} V_{DS}^{\min}$ . For the 11 GHz oscillator under analysis, the calculated minimum power consumption at room temperature is about 6  $\mu\text{W}$ , which is coherent to the simulations based on the complete HEMT model within a factor of three. It is worthy to note that for large values of  $\beta$ , the power consumption is proportional to  $T^2$ . Such a result has triggered the curiosity to investigate whether the EKV model could be applied to HEMTs, and that is a theoretical study which might be accomplished in the future.



# 6 Microwave inductive proximity sensors with sub-pm resolution

## 6.1 Abstract

Inductive proximity sensors are low cost and versatile detectors achieving resolutions in the nm and sub-nm range. Their typical working frequency ranges from tens of kHz to a few MHz and the operation at higher frequencies is considered as a possible route for the improvement of the performance. Here, we report on the design of two microwave inductive proximity sensors based on LC oscillators operating at 500 MHz and 10 GHz, respectively. Both detectors are based on a frequency-encoded architecture, leading to an intrinsic robustness against both interference and signal attenuation. The 500 MHz oscillator is composed of an off-chip resonator with a planar coil having a diameter of 6.4 mm and a CMOS integrated cross-coupled transistor pair. It achieves a frequency noise floor of  $0.15 \text{ Hz/Hz}^{1/2}$  (above the  $1/f$  corner frequency of 6 kHz), which leads to a distance resolution of  $0.5 \text{ pm/Hz}^{1/2}$  at 110  $\mu\text{m}$  from the coil. The integrated noise in the 1 mHz to 1 kHz bandwidth corresponds to a distance resolution of  $130 \text{ pm}_{\text{rms}}$ . The 10 GHz oscillator is a fully integrated CMOS differential Colpitts with a planar coil having a diameter of 270  $\mu\text{m}$ . It achieves a frequency noise floor of  $2 \text{ Hz/Hz}^{1/2}$  (above the  $1/f$  corner frequency of 10 kHz) which leads to a distance resolution of  $0.3 \text{ pm/Hz}^{1/2}$  at 70  $\mu\text{m}$  from the coil. The integrated noise in the 1 mHz to 1 kHz bandwidth corresponds to a distance resolution of  $100 \text{ pm}_{\text{rms}}$ .

## 6.2 Motivation

Position and displacement sensors with nanometer and sub-nanometer resolution are required in many industrial and research areas [146–149]. For several of these applications, inductive and capacitive sensors show sufficiently good performance, specifically in terms of resolution, accuracy, bandwidth, long term stability, temperature cross-sensitivity, power consumption, size, and cost. Additionally, both inductive and capacitive proximity sensors

---

This chapter is a minor variation of the publication "*Microwave inductive proximity sensors with sub-pm/Hz<sup>1/2</sup> resolution*" [145].

## Chapter 6. Microwave inductive proximity sensors with sub-pm resolution

are absolute detectors and they do not require the medium between the sensing element and the target plate to be optically transparent. These characteristics make such detectors more versatile than optical interferometers. Since unwanted magnetic permeability variations are, in general, less common than electric permittivity variations, the inductive sensors are more suitable than the capacitive ones for operations in harsh environments [146, 147, 149]. Displacement detectors based on magnetic sensors (mainly Hall devices and giant or anisotropic magnetoresistors) are also competitive in terms of distance resolution, power consumption, and size, but require the target to be ferromagnetic [148].

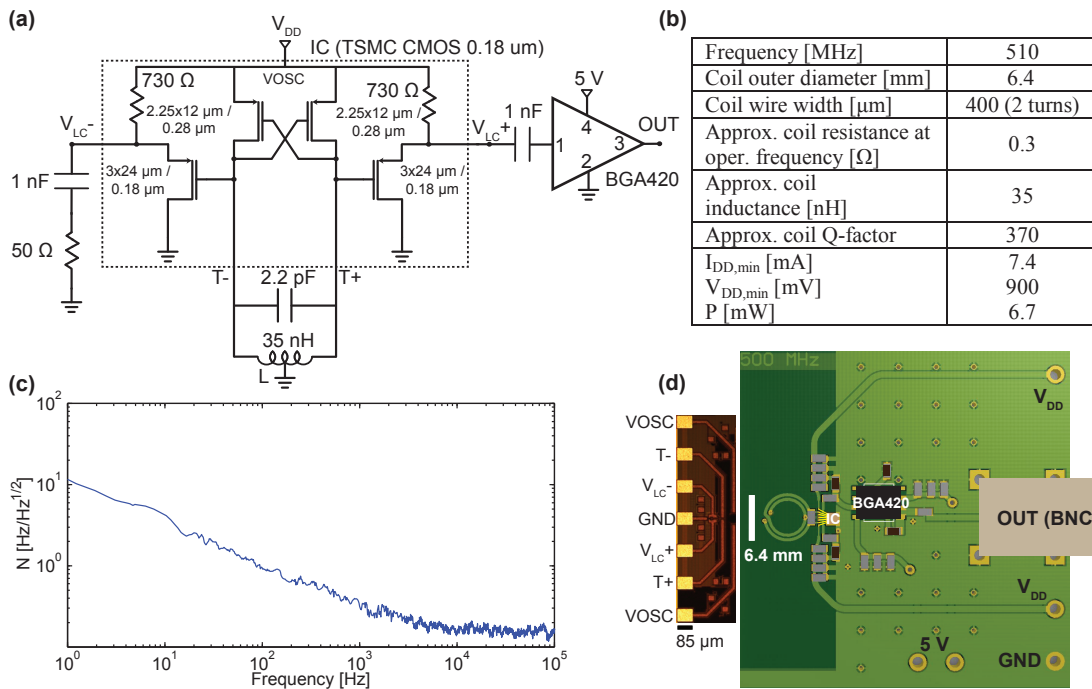


**Figure 6.1 – The 500 MHz inductive proximity sensor: schematic and characteristics.** (a) Detailed schematic of the LC cross-coupled oscillator. The integrated part is realized with a Si CMOS technology (TSMC 180 nm, MS/RF). The sensing coil is indicated by  $L$ . The dashed rectangle identifies the integrated energy restoring system (i.e., a cross-coupled pair of transistors) and the output buffer. The LC resonator is off-chip. The Infineon BGA420 is a fixed-gain 50 Ω-matched amplifier. (b) Key-features of the detector. (c) Measured frequency noise spectral density. (d) Picture of the detector. All the surface-mounted-devices (SMD) on the printed-circuit-board (PCB) are bypass capacitors (grey) and bias resistors (dark brown) for the BGA420 amplifier.

Inductive proximity sensors are typically operated at frequencies below 10 MHz, with only a few exceptions up to about 100 MHz [149–151]. Nevertheless, the operation at higher frequencies is considered as a promising approach to achieve better performance (Refs. [147, 149, 152–154]). Microwave LC oscillators are widely used as local oscillators in microwave circuits [41, 49, 74] but also as sensors (and bio-sensors) for magnetic beads counting [155–158], dielectric spectroscopy [159, 160], electron spin resonance (ESR) spectroscopy [2, 4, 7–9], and accelerometers [161, 162]. Here, we report on the design and characterization of two inductive proximity sensors based on partially and fully integrated microwave LC oscillators operating at 500 MHz and 10 GHz, i.e., at significantly higher frequencies than those previously reported in



the literature. The interesting and problematic aspects related to the operation at microwave frequencies are also discussed.

### 6.3 Description of the realized inductive proximity sensors

The two inductive proximity sensors described in this chapter are based on the LC oscillators operating at 500 MHz and 10 GHz which have been already presented in Chap. 2 and Sec. 4.7 as ESR detectors. In particular, their good frequency noise performance with respect to the theoretical limits triggered the curiosity to use the two oscillators as proximity sensors, too. The former is a cross-coupled LC oscillator with an off-chip LC resonator located on a printed circuit board (PCB) (Fig. 6.1a,d), whose inductor is a planar double-turn coil having an outer diameter of 6.4 mm. The latter is a fully integrated LC differential Colpitts oscillator (Fig. 6.2a,d), whose inductor is a planar double-turn coil with an outer diameter of 270  $\mu\text{m}$ . Both systems are based on a silicon CMOS technology (TSMC 180 nm, MS/RF) and the integrated transistors are relatively large in size and p-type in order to reduce their  $1/f$  noise. Also, both oscillators operate with a power consumption below 10 mW.

The working principle of the proposed inductive proximity sensors is based on the change of impedance of the LC resonator when the target metal plate approaches the sensing coil (Sec. 6.8). The eddy-currents in the target plate, produced by the microwave magnetic field generated by the oscillator inductor, create a counter magnetic field which leads to a reduction of the effective inductance (and to an increase of the effective resistance) of the oscillator inductor. The former leads the oscillation frequency to rise whereas the latter produces a reduction of the oscillation amplitude. As for the ESR sensors, the information associated to the frequency variation is intrinsically more robust, being significantly less affected by signal amplitude attenuation and interference. Hence, the proposed interface tracks the frequency variation of the two oscillators so as to perform the proximity detection. It is worthy to note that since both attenuation and interference become less critical with such approach, the sensing probe can be eventually placed relatively far apart from the processing unit.

In the realized prototypes, the frequency-to-voltage conversion is performed by a delay-line-discriminator (DLD) whose central frequency is 200 MHz. As shown in Fig. 6.3b, in order to match the DLD central frequency and improve the signal spectral purity, the signal at the output of the detector is amplified, mixed with an external reference, filtered, and shaped through a divide-by-1 frequency divider (a divide-by-32 unit is also used for direct frequency measurement by means of a frequency counter).

### 6.4 Experimental results and characterization of the sensors

The two proposed proximity sensors are characterized as follows. The PCB holding the detector is fixed in a vice. A metal target is mounted on a micrometric positioning stage and approached to the sensor starting from a large distance (Fig. 6.3a). As mentioned in the previous section and further discussed in Sec. 6.8, the frequency of the oscillator increases as the metal plate

## Chapter 6. Microwave inductive proximity sensors with sub-pm resolution

gets closer to the detection coil (Fig. 6.4a,b). Remarkably, the integrated coil of the 10 GHz detector has a much lower quality factor than the 500 MHz system (Figs. 6.1b and 6.2b), so the losses introduced by the metal target at distances below 70  $\mu\text{m}$  are large enough to switch the oscillator off.

The sensitivity of the proximity sensors at a distance  $d$  reported in Fig. 6.4 is computed as the oscillator frequency variation for a small distance variation (i.e.,  $S_d = \partial f / \partial d|_d$ ). Moreover, as shown in Figs. 6.1c and 6.2c, both LC oscillators have a frequency noise spectral density which is affected by  $1/f$  noise up to a few kHz from the carrier. Their noise floor is, within a factor of three, determined by the thermal noise of the series resistance of the inductor (Sec. 6.8). In Fig. 6.4, we also report the experimentally measured distance resolution. The 1- $\sigma$  distance resolution (i.e., the minimum detectable variation of distance between the coil and the conducting plate) is computed as  $d_{\min,d} = (N/S_d)$ , where  $N$  is the frequency noise spectral density. The integrated distance resolution is computed as  $d_{\min,\text{int},d} = (N_{\text{int}}/S_d)$ , where  $N_{\text{int}}$  is the noise integrated over the 0.1 mHz to 1 kHz bandwidth (Sec. 6.8).

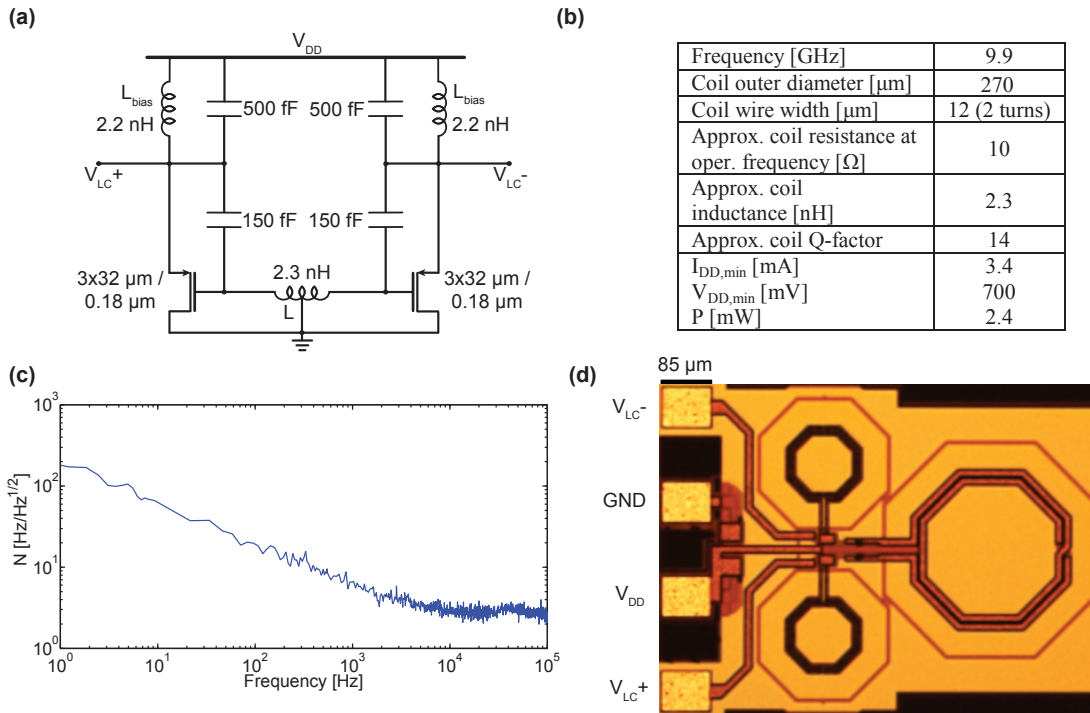


**Figure 6.2 – The 10 GHz inductive proximity sensor: schematic and characteristics.** (a) Detailed schematic.  $L$  is the sensing coil. (b) Key-features of the detector. (c) Measured frequency noise spectral density. (d) Picture of the detector. The sensing coil is the large one (outer diameter: 270  $\mu\text{m}$ ). The other two are the bias inductors. The yellow rectangles (65  $\mu\text{m} \times 85 \mu\text{m}$ ) are the bonding pads. The overall size is about 0.85  $\times$  0.63 mm $^2$ .

The 500 MHz oscillator achieves a frequency noise floor of 0.15 Hz/Hz $^{1/2}$  (above the  $1/f$  corner frequency of 6 kHz) which leads to a distance resolution of 0.5 pm/Hz $^{1/2}$  at 110  $\mu\text{m}$  from the coil. The integrated noise in the 1 mHz to 1 kHz bandwidth (i.e., in the  $1/f$  noise region) corresponds to a distance resolution of 130 pm $_{\text{rms}}$ . At a distance equal to the coil

## 6.4. Experimental results and characterization of the sensors

radius (i.e., at 3 mm), the 500 MHz sensor achieves a resolution of about  $20 \text{ pm/Hz}^{1/2}$  and an integrated resolution of about  $8 \text{ nm}_{\text{rms}}$ . At a distance equal to the coil diameter (i.e., at 6 mm), the 500 MHz sensor achieves a resolution of about  $200 \text{ pm/Hz}^{1/2}$  and an integrated resolution of about  $50 \text{ nm}_{\text{rms}}$ .

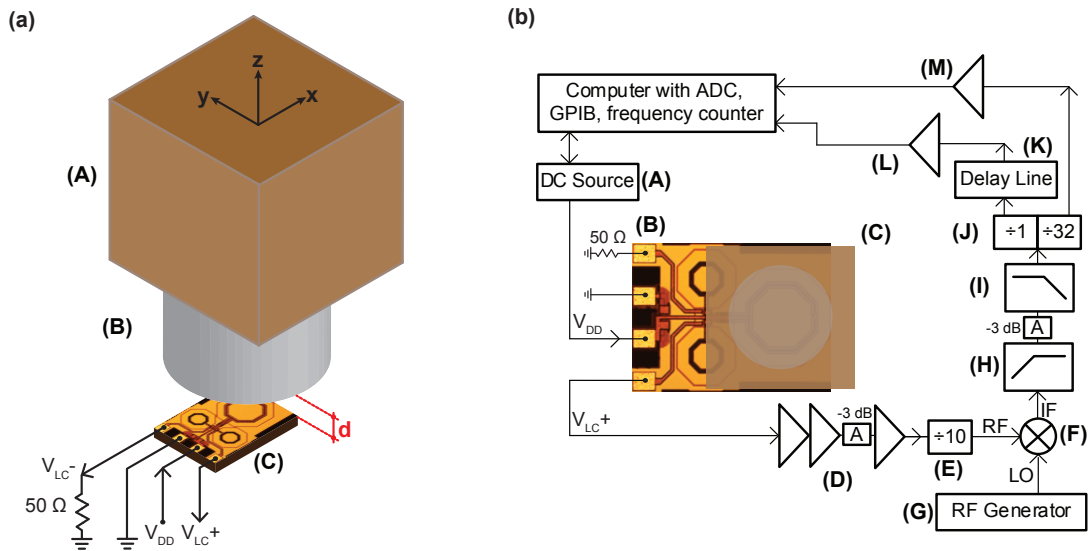


**Figure 6.3 – Experimental set-up for DC characterization of the inductive proximity sensors.** (a) Measurement set-up: (A) Three-axis micropositioning stage (OWIS); (B) Metal target (for the 500 MHz sensor: an aluminum square plate of 50 mm side and 10 mm thickness, for the 10 GHz sensor: a copper cylinder with 1 mm diameter and 5 mm length); (C) Proximity sensor (the 10 GHz detector is shown). (b) Block diagram of the measurement chain: (A) DC power supply (Keithley 2400); (B) Proximity sensor operating at 10 GHz; (C) OWIS micropositioning stage; (D) RF amplification stage composed of 3 RF amplifiers (Analog Devices, HMC-C001) and a 3 dB attenuator (these amplifiers are removed from the detection chain for the 500 MHz sensor); (E) Frequency divider (Analog Devices, HMC-C040) (removed for the 500 MHz sensor); (F) Mixer (Mini-Circuits ZFM-2000+); (G) RF generator (R&S, SMR-20); (H) 100 MHz high-pass filter (Crystek CHPFL-0100); (I) 300 MHz low-pass filter (Crystek CLPFL-0300); (J) Frequency divider (Valon Technology 3010); (K) Homemade delay-line-discriminator [41, 74] (200 MHz central frequency, 1 MHz detection range, 5 MHz FM bandwidth); (L) Amplifier (Stanford Research Systems SR560); (M) Amplifier (NF 5305).

The 10 GHz oscillator achieves a frequency noise floor of  $2 \text{ Hz/Hz}^{1/2}$  (above the  $1/f$  corner frequency of 10 kHz) which leads to a distance resolution of  $0.3 \text{ pm/Hz}^{1/2}$  at  $70 \text{ }\mu\text{m}$  from the coil. The integrated noise in the 1 mHz to 1 kHz bandwidth (i.e., in the  $1/f$  noise region) corresponds to a distance resolution of  $100 \text{ pm}_{\text{rms}}$ . At a distance equal to the coil diameter (i.e., at 0.2 mm), the 10 GHz sensor achieves a resolution of about  $8 \text{ pm/Hz}^{1/2}$  and an integrated resolution of about  $3 \text{ nm}_{\text{rms}}$ .

The obtained sensitivity values are, within a factor of three and without any fitting parameter, in agreement with the values computed from Eq. 6.1 in Sec. 6.8. The observed discrepancies are probably due to (1) the capacitive effects not included in the model and (2) the slightly nonparallel arrangement of the sensing coil with respect to the target metal plate.

## Chapter 6. Microwave inductive proximity sensors with sub-pm resolution

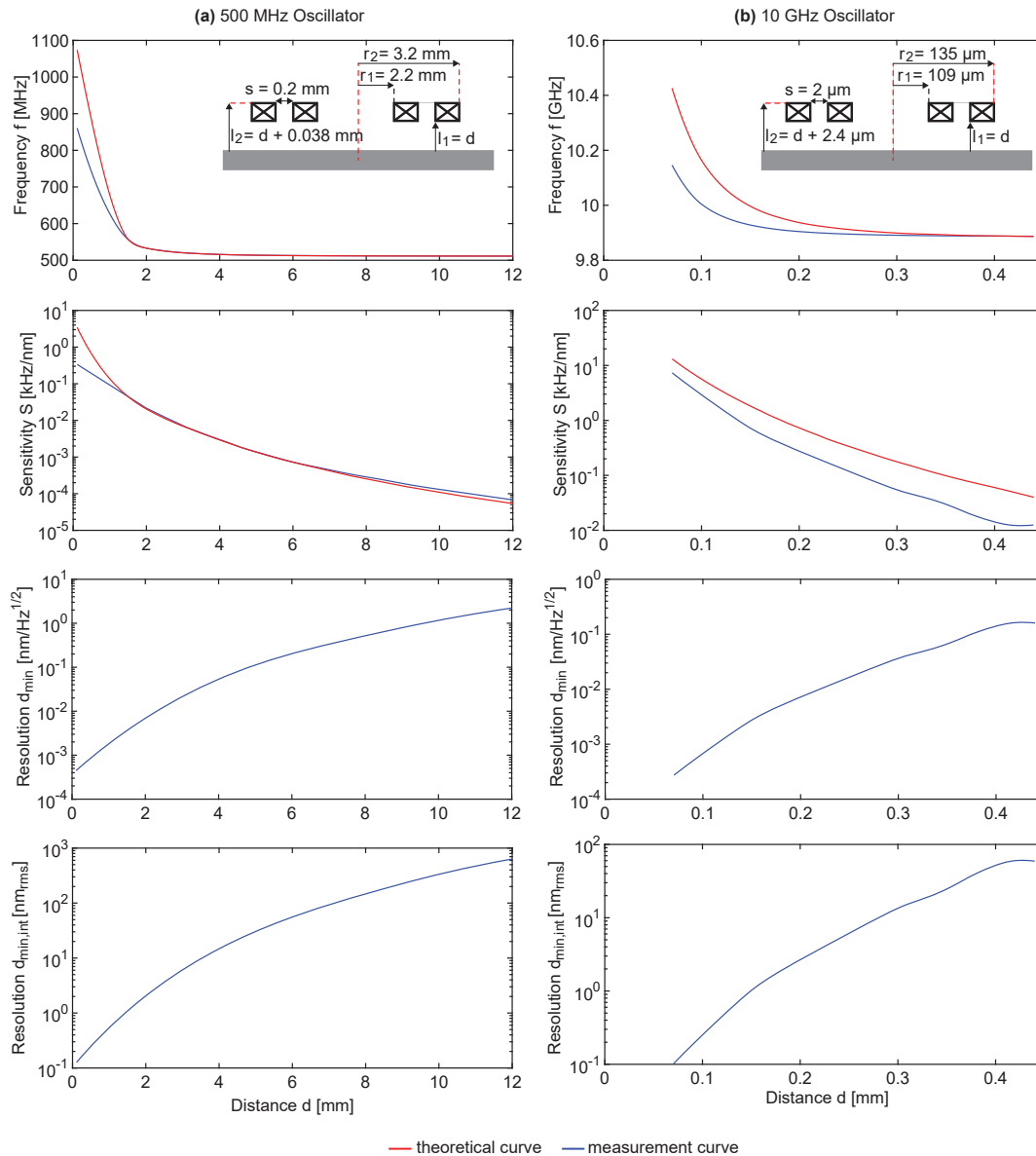


**Figure 6.4 – Experimental characterization of the 500 MHz and the 10 GHz proximity sensors.** Plots of the frequency variation, sensitivity, and distance resolution as functions of the distance between the metal plate and the sensing coil for (a) the 500 MHz and (b) the 10 GHz proximity sensors. The distance resolution is given as noise spectral density above the  $1/f$  corner frequency (in nm/Hz $^{1/2}$ ) and as integrated noise over the 1 mHz to 1 kHz bandwidth (in nm $_{\text{rms}}$ ). The theoretical curves for the sensitivity are obtained from Eq. 6.1 in Sec. 6.8 using Mathematica $^{\text{®}}$ . The geometrical parameters of the two coils are also shown.

### 6.5 Comparison with previously reported proximity sensors

In the following, we briefly compare the distance resolution achieved by the inductive proximity sensors described so far with those previously reported. High resolution commercially available inductive proximity sensors (such those proposed by Balluff, Eaton, Lion Precision, Microdetectors, Micro-Epsilon, Kaman, Keyence, Omron, and Pepperl+Fuchs), achieve in-

egrated resolutions down to about  $1 \text{ nm}_{\text{rms}}$  with a bandwidth of about 1 kHz at distances of about  $100 \text{ }\mu\text{m}$ , with resolutions above the  $1/f$  noise corner frequency down to about  $100 \text{ pm}/\text{Hz}^{1/2}$ . The Precision Lion ECL202-U3 achieves an integrated resolution of  $15 \text{ nm}_{\text{rms}}$  in a bandwidth of 1 kHz at  $50 \text{ }\mu\text{m}$ . The coil diameter is presumably slightly smaller than the diameter of the sensor front face (i.e., 3 mm). In the review paper of Fleming [146], the Kaman SMU9000-15N, which has a coil diameter of 3.6 mm, has a resolution of  $20 \text{ pm}/\text{Hz}^{1/2}$  above 20 Hz and the integrated resolution is  $5 \text{ nm}_{\text{rms}}$  over a 1 kHz bandwidth (the sensor-to-target distance is not specified but it is presumably equal to  $100 \text{ }\mu\text{m}$  according to the values reported in the manual of the sensor). The Micro-Epsilon DT3701-U1-A-C3 achieves a resolution of  $1.3 \text{ nm}_{\text{rms}}$  in a bandwidth of 1 kHz at  $100 \text{ }\mu\text{m}$  (from the reported integrated resolutions, with 10 Hz and 1 kHz bandwidths, a resolution of about  $40 \text{ pm}/\text{Hz}^{1/2}$  at 1 kHz and  $100 \text{ }\mu\text{m}$  is expected). The coil diameter is presumably slightly smaller than 4 mm.

The best resolution reported to date in non-commercially available sensors is probably the one of Chaturvedi et al. [149]. They developed a 126 MHz sensor based on a 8 mm diameter coil, consisting of four  $35 \text{ }\mu\text{m}$  thick turns with a  $200 \text{ }\mu\text{m}$  pitch. The sensor achieves, at a distance of about  $100 \text{ }\mu\text{m}$ , a noise floor of  $13 \text{ pm}/\text{Hz}^{1/2}$  and an integrated resolution of  $600 \text{ pm}_{\text{rms}}$  in a 2 kHz bandwidth (the integration extrema are not specified, but the reported integrated resolution value corresponds to a white noise of spectral density equal to the noise floor, indicating a negligible contribution from the  $1/f$  noise). At the same distance, the resolution in the noise floor of our 500 MHz sensor is more than one order of magnitude better. We can also tentatively compare the integrated resolutions. Considering an integration bandwidth of 1 mHz to 2 kHz (i.e., entirely in the  $1/f$  noise for our sensor), the integrated resolution of the 500 MHz sensor is about  $150 \text{ pm}_{\text{rms}}$  (i.e., about four times better than the one reported in Ref. [149]). Our 10 GHz sensor has a resolution and an integrated resolution which are slightly better (i.e.,  $0.3 \text{ pm}/\text{Hz}^{1/2}$  and  $100 \text{ pm}_{\text{rms}}$ , respectively) but, due to the much smaller coil size, the distance resolution at distances larger than  $200 \text{ }\mu\text{m}$  is much worse.

## 6.6 Discussion and outlook

In this work, we have focused our investigation on the distance resolution for two microwave sensors based on LC oscillators, operating at frequencies which are up to two orders of magnitude larger than those of previously reported inductive proximity sensors. The experimentally achieved distance resolutions are better than the best values reported in the literature and the two realized sensors have an operating frequency as well as a coil diameter differing by more than one order of magnitude (approximately a factor of twenty for both parameters). The achieved resolution at  $100 \text{ }\mu\text{m}$  is only slightly better for the 10 GHz sensor with respect to the 500 MHz sensor. Despite the fact that the distance resolution is not significantly improved at higher frequency (as also expected theoretically and discussed in Sec. 6.8), the obtained larger sensitivity reduces the requirements on the input equivalent frequency noise of the electronics necessary to perform the frequency-to-voltage conversion. As an example, for the sensors reported in this chapter, the frequency-to-voltage conversion is performed with a

delay-line-discriminator (or a phase-locked-loop) having an equivalent input frequency noise lower than  $0.1 \text{ Hz/Hz}^{1/2}$ . Since the noise of the LC oscillators is larger (Figs. 6.1c and 6.2c), the achieved distance resolution is not significantly influenced by the noise of the frequency-to-voltage converter.

A lower frequency noise, which would be achievable with an oscillator operating at lower frequency, would demand for a more performing frequency-to-voltage conversion, which is more difficult to obtain, especially when FM bandwidths larger than 100 kHz are desired. Additionally, as pointed out in Refs. [149, 163], operation at higher frequency allows for a strongly reduced penetration depth of the microwave field, which significantly reduces the dependence on both the target conductivity and the temperature cross-sensitivity.

A practical problematic aspect of operating at higher frequency with an inductive sensor based on an LC oscillator is the effect of parasitic capacitances. Indeed, the positive feedback electronics has a non-negligible capacitance which makes hardly possible, for example, to have a 10 GHz sensor with a coil larger than 1 mm. As a consequence and in very general terms, sensors operating at higher frequency achieve better sensitivities at short distances but are less sensitive at larger distances due to their reduced coil size (as practically shown with the two sensors reported in this work).

It is important to notice that the distance resolution is only one of the several important key-features of an inductive proximity sensor. Among them, the linked features of temperature cross-sensitivity, accuracy, and long term stability are essential in many applications. The work reported in Refs. [149, 164, 165] are particularly interesting for the strategies adopted to reduce the temperature cross-sensitivity and the  $1/f$  noise. As a matter of fact, the latter will be investigated also in the case of microwave proximity sensors based on measurements of the frequency variation for an LC microwave oscillator.

### 6.7 Acknowledgments

Financial support from the Swiss National Science Foundation (SNSF) is gratefully acknowledged (grant 200020-175939).

### 6.8 Appendix. Computation of sensitivity and resolution

The modeling of the electromagnetic interaction between a circular coil carrying a sinusoidal current and a conducting plate has been already investigated in details [163, 166–177]). The work of Dodd and Deeds [167] is considered as the cornerstone in the modeling of eddy currents related problems. The common aim of these works is to find a closed form expression for the impedance of the coil which takes into consideration the eddy currents produced into the conducting plate. The approach is based on the computation of the vector potential from the Maxwell equations, which is simplified by the cylindrical symmetry of the problem. Some of these papers only discuss the case of a single-turn coil having undefined thickness and wire width (i.e., a single-turn elementary coil) [163, 166, 168, 169, 171–174, 177]. Others also

## 6.8. Appendix. Computation of sensitivity and resolution

discuss the more general and realistic case of a multi-turn coil having defined thickness and width [167, 170, 175].

The elementary single-turn results can be tentatively extended also to a multi-turn coil. To some extent, for a small number of turns  $n$ , all having approximately the same radius, we can assume a dependence as  $n^2$  for the inductance, which is justified by the linear dependence of both the vector potential and the integration path on the number of turns. The elementary approach gives slightly simpler equations for the computation of the inductance. However, it requires the introduction of two different values for the coil radius as arguments of the Bessel functions in order to avoid an overestimation of the inductance (which is physically equivalent to consider that the single-turn coil wire is actually not elementary).

In this work, we have computed the inductance values (and their variations) using an approach which explicitly considers the number of turns and the actual dimensions of the coil winding. The expression obtained by Dodd and Deeds [167] for the inductance  $L_d$  of a coil having rectangular cross section, placed at a distance  $d$  from a semi-infinite homogeneous conducting non-ferromagnetic plate, can be written as the sum of the inductance of the coil  $L_0$  when the conducting plate is very far (i.e.,  $d = l_1 \rightarrow \infty$ ) and an interaction term

$$\begin{aligned} L_d &= \frac{\pi\mu_0 n^2}{(l_2-l_1)^2(r_2-r_1)^2} \int_0^\infty \frac{1}{\alpha^5} I^2(r_1, r_2) \left( 2(l_2-l_1) + \frac{1}{\alpha} (2e^{-\alpha(l_2-l_1)} - 2 + \Delta_M) \right) d\alpha \\ \Delta_M &= (e^{-2\alpha l_2} + e^{-2\alpha l_1} - 2e^{-\alpha(l_2+l_1)}) \left( \frac{\alpha-\alpha_1}{\alpha+\alpha_1} \right) \\ L_0 &= \frac{\pi\mu_0 n^2}{(l_2-l_1)^2(r_2-r_1)^2} \int_0^\infty \frac{1}{\alpha^5} I^2(r_1, r_2) \left( 2(l_2-l_1) + \frac{1}{\alpha} (2e^{-\alpha(l_2-l_1)} - 2) \right) d\alpha \end{aligned} \quad (6.1)$$

where  $n$  is the number of turns in the coil,  $\alpha_1 = (\alpha^2 + j\omega\mu_0\sigma)^{1/2}$ ,  $\sigma$  is the conductivity of the metal plate,  $r_1$  is the coil inner radius,  $r_2$  is the coil outer radius,  $(r_1 - r_2)$  is the coil width,  $l_1 = d$  is the distance between the bottom of the coil and the metal plate;  $(l_1 - l_2)$  is the coil thickness,  $\omega = 2\pi f$  is the angular frequency of the current circulating in the coil,  $\delta = (2/\omega\mu_0\sigma)^{1/2}$  is the skin depth,  $I(r_1, r_2) = \int_{\alpha r_1}^{\alpha r_2} x J_1(x) dx$ , and  $J_1$  is the Bessel function of the first kind and order 1.

The geometrical parameters for the two realized inductive proximity sensors are shown in Fig. 6.4.

Assuming the coil has a very small thickness with respect to the distance from the conducting plate, the previous equation can be simplified as [175]

$$\begin{aligned} L_d &= \frac{\pi\mu_0 n^2}{(r_2-r_1)^2} \int_0^\infty \frac{1}{\alpha^4} I^2(r_1, r_2) (e^{-2\alpha d}) \left( \frac{\alpha-\alpha_1}{\alpha+\alpha_1} \right) d\alpha \\ L_0 &= \frac{\pi\mu_0 n^2}{(r_2-r_1)^2} \int_0^\infty \frac{1}{\alpha^4} I^2(r_1, r_2) d\alpha \end{aligned} \quad (6.2)$$

The air inductance (i.e.,  $L_0$ ) obtained with this equation is in good agreement (within 10%) with

## Chapter 6. Microwave inductive proximity sensors with sub-pm resolution

---

the simple expressions given in Ref. [178] as well as with numerical simulations performed with Comsol Multiphysics<sup>®</sup>, at least for coils having dimensions similar to the ones reported in this work.

Let us now consider, as for the sensors reported in this chapter, that the coil inductance variation is measured as the oscillation frequency variation of an LC oscillator. Since the oscillator frequency variation due to the variation of the coil resistance is negligible, the oscillator frequency variation is

$$\Delta f_d \cong f_0 \left( \frac{L_0}{L_d} \right)^{1/2} \left( 1 - \left( 1 - \frac{\Delta L_d}{L_d} \right)^{-1/2} \right) \cong f_0 \left( \frac{L_0}{L_d} \right)^{1/2} \frac{1}{2} \frac{\Delta L_d}{L_d} \quad (6.3)$$

where  $\Delta L_d = (L_d - L_{d+\Delta d})$  is the inductance variation when the coil is moved from a distance  $d$  to a distance  $d + \Delta d$ , and  $f_0$  is the oscillator frequency when the conducting plate is very far from the coil. Hence, the distance sensitivity of the sensor (in Hz/m) at the distance  $d$  can be defined as

$$S_d = \Delta f_d / \Delta d = \partial f / \partial d \big|_d \quad (6.4)$$

From the previous equations it can be shown that, for ordinary metals at high frequency, the sensitivity is independent of both the metal plate conductivity and the number of turns of the coil. Moreover, it is linearly proportional to the operating frequency and, for a fixed ratio between distance and coil radius, it is inversely proportional to the coil radius itself. Numerical simulations show that an approximate expression for the sensitivity, valid for  $d > (1/10)r$ , is

$$S_d \cong 100 \frac{f_d}{r} e^{-8\sqrt[3]{d/r}} \quad (6.5)$$

where  $r \cong (r_1 + r_2)/2$ .

Concerning the noise contribution, an LC oscillator has a frequency noise dominated by (1) the thermal noise of the coil resistance and (2) the up-conversion of the  $1/f$  noise originating from the feedback circuit. The frequency noise spectral density  $N$  (in Hz/Hz<sup>1/2</sup>) and the integrated frequency noise  $N_{\text{int}}$  (in Hz<sub>rms</sub>) can be written as

$$N = (F(f^2/V^2)2k_B T R(1 + f_{mc}/f_m))^{1/2} \quad (6.6)$$

$$N_{\text{int}} = \left( \int_{f_{m1}}^{f_{m2}} N^2 df_m \right)^{1/2}$$



## 6.8. Appendix. Computation of sensitivity and resolution

---

where  $(f^2/V^2)2k_B TR$  is the power spectral density (Sec. 1.4) of the thermal frequency noise due to the coil resistance  $R$ ,  $V$  is the oscillation amplitude,  $f$  is the oscillation frequency,  $T$  is the coil temperature,  $F$  is a factor to take into account the noise contribution of the feedback circuitry,  $f_m$  is the frequency offset from the carrier, and  $f_{mc}$  is the  $1/f$  corner frequency (i.e., the offset frequency at which the thermal noise  $F(f^2/V^2)2k_B TR$  is equal to the  $1/f$  noise). The distance resolution (i.e., the minimum detectable distance variation at a distance  $d$ ) can be defined as  $d_{\min,d} = (N/S_d)$  (in  $\text{m}/\text{Hz}^{1/2}$ ) and  $d_{\min,d,\text{int}} = (N_{\text{int}}/S_d)$  (in  $\text{m}_{\text{rms}}$ ). It is important to note that since both the sensitivity and the thermal noise spectral density linearly increase with the working frequency, the distance resolution at a frequency offset from the carrier above the  $1/f$  corner frequency is, in principle, independent of the working frequency for a given coil size and at a given distance. Moreover, the  $1/f$  noise has also the tendency to increase for oscillators operating at higher frequencies. This seems to indicate that, despite the increase in sensitivity, operation at higher frequencies does not improve the achievable distance resolution. However, this conclusion is valid only whether the noise is effectively dominated by the intrinsic noise sources of the oscillator (as it is approximately the case for the two proximity sensors described in this chapter).



## 7 Other designs

### 7.1 Single-chip CMOS ESR detectors operating at 20 GHz (fixed-freq. and VCO)

Fig. 7.1 shows both schematics and pictures of the two realized systems. They are based on a Si CMOS technology (TSMC 180 nm, MS/RF) and they are integrated on the same chip. The goal for this design was to maximize the working frequency by still retaining good performance in terms of both saturation (i.e., low  $B_1$ ) and frequency noise (Sec. 1.4).

In order to minimize the  $1/f$  noise (both its magnitude and the corner frequency), all the oscillators are based on p-type transistors having non-minimal area, for an operating frequency approximately equal to 20 GHz. The only difference between the two systems stands in the overall capacitance of the LC tank. In particular, one system is composed of two cross-coupled oscillators having two fixed-value series capacitors (86 fF) leading to a fixed-frequency architecture, whereas the second system is composed of two voltage-controlled-(cross-coupled) oscillators (VCOs) having two tunable capacitors (a.k.a., varactors). Indeed, the latter allow the oscillators to change their operating frequency (18-22 GHz) according to the applied control voltage ( $V_{\text{VAR,A,B}}$ ). In order to avoid any direct driving of  $50\ \Omega$  loads in the GHz range, the two oscillators are mixed together, and then a simple source follower provides driving capabilities at low-frequency, according to the working principle already discussed in Sec. 3.3. Since the detection chain is not linear (mainly due to the mixer and to the relatively high oscillation amplitude), the two proposed systems are not optimized for amplitude detection (Sec. 1.4). For the fixed-frequency detector, the start-up current of each oscillator at room temperature is approximately 1.5 mA (0.7 V), leading to a minimum  $B_1$  of about  $20\ \mu\text{T}$ . The output signal has a power of about -22 dBm and its frequency is 320 MHz. Conversely, the VCO has a start-up current of 2.5 mA (0.8 V), a minimum  $B_1$  of about  $40\ \mu\text{T}$ , and an output signal ranging from 80 MHz to 2 GHz at -23 dBm and -25 dBm, respectively. For normal operation, a series resistance of  $1\ \text{k}\Omega$  is generally inserted between the oscillator and the voltage supply. In fact, that is useful to reduce any injection of spurious signals from both the power supply and the modulation coil (i.e., the leakage introduced in Sec. 1.5).

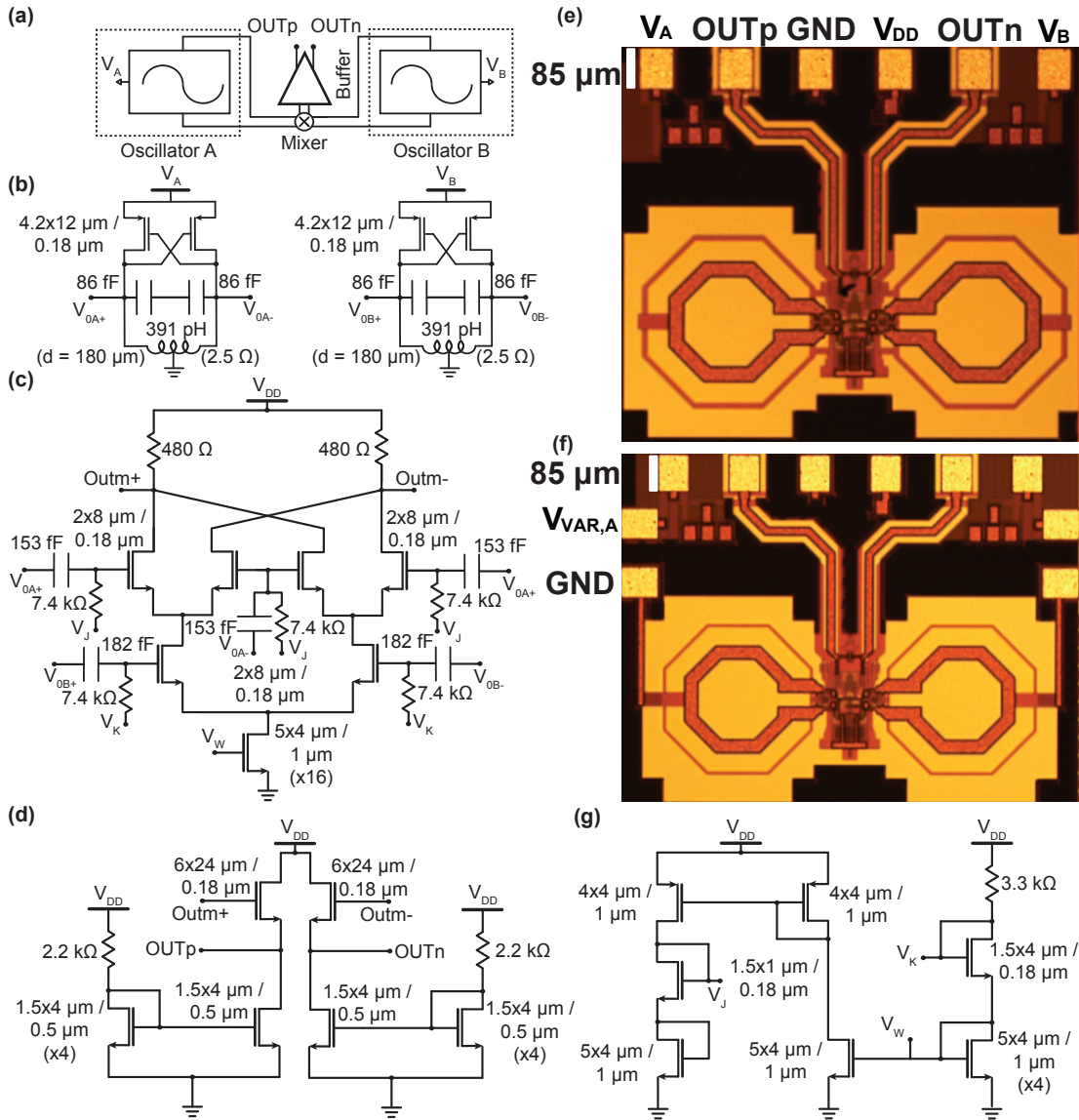


**Figure 7.1 – Single-chip CMOS ESR detectors operating at 20 GHz (fixed frequency and VCO).** (a) Block diagram of the fixed-frequency detector. (b) Schematics of the fixed-frequency cross-coupled oscillators. The VCOs are based on two series-connected varactors instead of the two capacitors shown in the picture. (c) Four-quadrant multiplier (Gilbert cell). (d) Output buffer (source follower) to drive 50  $\Omega$  loads. (e) Picture of the fixed-frequency detector. (f) Picture of the VCO-based detector. The regular pads are located in the same position as for the fixed-frequency system. Additionally, the two VCOs have specific control pins ( $V_{VAR,A,B}$ ) and dedicated GND connections. (g) Integrated supply unit.

Considering that the power consumption of the mixer and the buffer is about 9 mW (1.8 V, 5 mA), the overall power dissipated by both detectors happens to be about 15 mW, making it impossible for them to operate at deep cryogenic temperatures. At 100 kHz, the frequency noise is about 30 Hz/Hz<sup>1/2</sup> and 50 Hz/Hz<sup>1/2</sup> for the fixed-frequency system and the VCO-based system, respectively. The minimum reachable working temperature is 2.3 K, with an overall power consumption of 7 mW for both oscillators and almost no change in noise performance.

## 7.2. Single-chip HEMT ESR detector operating at 25 GHz

At 100 K, the fixed-frequency oscillator reaches its best noise performance with approximately  $20 \text{ Hz/Hz}^{1/2}$  at 100 kHz. It is worthy to note that the corner frequency ranges between 100 kHz and 150 kHz according to the operating point, and that is a value much larger than expected from simulations (maybe due to the presence of n-type transistors in both the mixer and in the output buffer). Finally, the measured spin sensitivity for a BDPA sample is in the order of  $10^8 \text{ spin/Hz}^{1/2}$ .

A VCO-based detector is also suitable for experiments based on the frequency sweep rather than the usual field sweep (Sec. 1.5). That allows to optimize the working point of each oscillator according to the requirements, such as the output frequency ( $\Delta f = f_{\text{osc1}} - f_{\text{osc2}}$ ) or the saturation level. Additionally, one could apply pulsed sequences to the sensing VCO so as to reach the resonance condition and then get out for a sufficiently long time, in order to study the shape of the ESR signal within the relaxation time (experimental approach to be checked for real validity in the future). However, the presence of a control voltage across the LC resonator makes this system more sensitive to noise as any spurious on  $V_{\text{VAR,A,B}}$  would directly affect the working frequency.

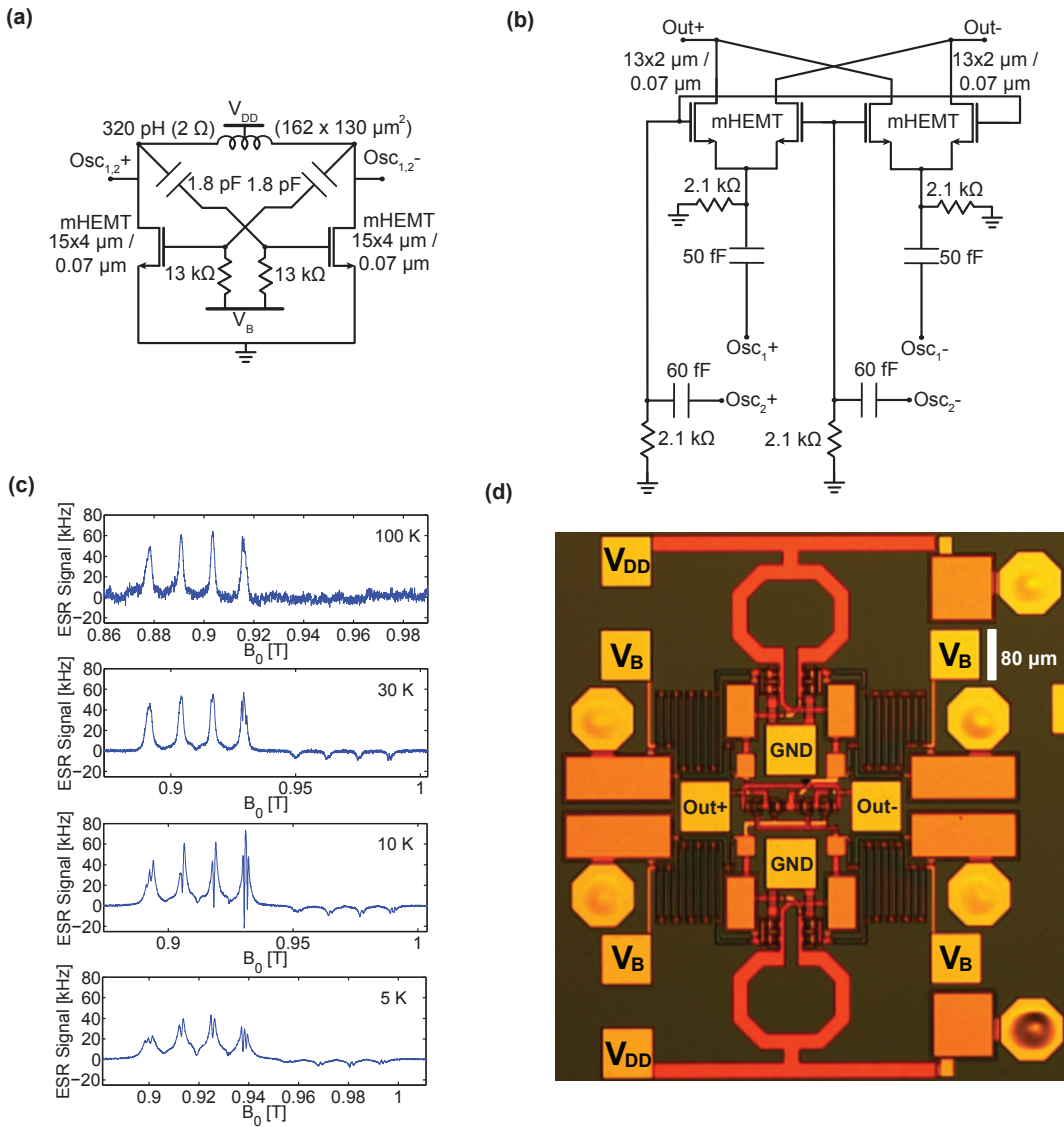
## 7.2 Single-chip HEMT ESR detector operating at 25 GHz

Fig. 7.2 shows the schematics of the realized detector, a set of measurements performed on a  $200 \times 130 \times 30 \text{ }\mu\text{m}^3$  single crystal of 5%  $\text{Cu}^{2+}$  in  $\text{Ni}(\text{mnt})_2$  from  $T = 100 \text{ K}$  to  $5 \text{ K}$ , and a picture of the overall system. The sensor is based on a HEMT technology (D007IH mHEMT 70 nm, OMMIC, France) and the goal for this design was to maximize the working frequency (Sec. 1.4).

The proposed architecture is composed of two cross-coupled oscillators and a passive mixer so as to down-convert the signal, and then drive a  $50 \text{ }\Omega$  load (Secs. 3.3 and 7.1). Although the HEMT technology shows good performance in terms of mobility, noise figure, and  $f_t$  (Refs. [70, 71]), it suffers from many constraints at layout level, such as the presence of only two metal layers, the high sheet resistance of the inner metal layer, the relatively high minimum required trace spacing, and the impossibility to match transistors. Consequently, designing those complex structures which are common in CMOS technologies results impossible. In this design, the adoption of a passive mixer rather than a more complex Gilbert cell allows to reduce parasitics and simplify the layout, whereas the introduction of two bias resistors at the gate of the cross-coupled oscillators allows to adjust the gate voltage. In fact, the threshold voltage is negative (about  $-0.24 \text{ V}$  at room temperature) and the DC gate voltage should never be positive for safe operation (i.e., it must not be tied to  $V_{DD}$  as for usual CMOS designs). Nevertheless, the constraints on the trace routing impose to use many pads (and bonding wires) for the same nets, leading to extra parasitics and further sensitive points for noise injection.

At room temperature, the start-up condition is  $V_B = -0.3 \text{ V}$  and  $V_{DD} = 0.24 \text{ V}$  (1.4 mA), leading to an overall power consumption of about  $670 \text{ }\mu\text{W}$ , an output power of  $-31 \text{ dBm}$ , and an output frequency of  $630 \text{ MHz}$ . In this condition, the simulated  $B_1$  is about  $15 \text{ }\mu\text{T}$ , which is

almost ten times smaller than the BDPA linewidth.



**Figure 7.2 – 25 GHz HEMT single-chip ESR detectors.** (a) Schematic of the cross-coupled oscillator. (b) Schematic of the passive mixer. (c) ESR spectra of a 200x130x30 μm<sup>3</sup> single crystal of 5% Cu<sup>2+</sup> in Ni(mnt)<sub>2</sub> from T = 100 K to 5 K, with  $\nu_m = 153$  kHz,  $B_m \cong 0.05$  mT,  $B_1$  sufficiently large to saturate the measurement,  $\Delta f = 0.25$  Hz (equivalent noise bandwidth of the lock-in),  $t_s \cong 3$  min (overall measurement time). The sample size is big enough to be also detected by the reference oscillator, leading to the mirrored image spectrum shown at higher magnetic fields. (d) Picture of the overall system (i.e., two oscillators connected to the passive mixer). The yellow hexagons (100 μm in diameter) are metallized holes, commonly called vias. The vias connect the electronics on the front side of the chip to a 3.5 μm thick layer of Au acting as ground plane on the backside of the chip. The thickness of the chip is 100 μm.

However, the measured frequency noise at 100 kHz is about 1-2 kHz/Hz<sup>1/2</sup>, and this noise level is not suitable for normal ESR operation. A possible explanation for such a high noise could be the malfunction of the passive mixer since it requires high oscillation amplitudes to work properly. As a matter of fact, increasing the bias voltage up to 0.9 V (5.62 mA) leads

to lower noise levels (in the order of  $500 \text{ Hz/Hz}^{1/2}$  at 100 kHz) but to much higher  $B_1$  values (for  $V_B = -0.1 \text{ V}$ ). In fact, the ESR experiment shown in Fig. 7.2c, points out that the working frequency of the oscillator is approximately 25 GHz, and the  $B_1$  level is big enough to saturate the measurements at different temperatures (i.e., the spectra do not follow the Curie law described in Sec. 1.2). Moreover, due to the high power consumption (about 10 mW), the minimum achievable cryogenic temperature is 5 K, where the frequency noise drops down to  $30 \text{ Hz/Hz}^{1/2}$  at 100 kHz.

### 7.3 Single-chip CMOS ESR detector for DNP

Fig. 7.3 shows the picture of the realized system. It is based on a Si CMOS technology (TSMC 180 nm, MS/RF) and the goal for this design was to implement a suitable ESR detector for dynamic nuclear polarization (DNP) experiments. The latter results from transferring the spin polarization from electrons to nuclei. In particular, a regular ESR detector (i.e., similar to the one shown in Fig. 7.1) is used to excite the unpaired electrons of a certain paramagnetic sample by sweeping the magnetic field until the ESR condition is achieved. Then, a suitable integrated transceiver for nuclear magnetic resonance (NMR) pulsed experiments can be used to inspect the polarization transfer from the electrons to the nuclei [68].

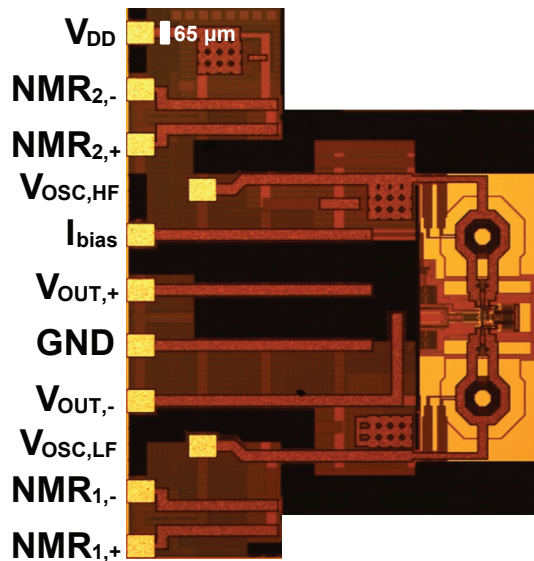


**Figure 7.3 – 28 GHz CMOS ESR detector for DNP.** Picture of the overall system. The corresponding chip contains several systems, whereas in the picture it is only shown the design under analysis. The connections to the pads are long in order to leave enough space for the placement of microcapillaries containing suitable samples in liquid solution.

From the electrical standpoint, the integrated system is a fixed-frequency single-chip ESR detector nominally operating at 28 GHz whose architecture is identical to the one shown in Fig. 7.1a,c,d,g. The main difference stands in the proposed oscillators which are now based on two pairs of n-type transistors ( $22.8 \mu\text{m}/180 \text{ nm}$ , 12 fingers) in order to maximize the

working frequency thanks to their relatively higher mobility (Sec. 1.4). Also, the LC resonator is composed of a 200 pH single-turn planar coil (90  $\mu\text{m}$  in diameter, 30  $\mu\text{m}$  in width,  $Q$ -factor approximately equal to 27) and two series-connected capacitors of 180 fF. Moreover, each planar coil contains an inner multi-layer NMR coil composed of ten turns in metal-3, ten turns in metal-4, ten turns in metal-5, and six turns in metal-6 (130 nH, 216  $\Omega$  DC resistance). The one placed on the sensing oscillator is intended to be connected to the NMR transceiver, whereas the other one should be just connected to a 50  $\Omega$  load in order to ensure the same impedance matching.

In this context, the presence of the NMR coils dramatically affects both the inductance of the LC tank and its intrinsic quality factor. Since the circuit simulator did not allow for post-layout simulation, it was impossible to accurately predict the real operating frequency and the start-up current. Consequently, it was also expected to have an output signal in the GHz range as a consequence of the unpredictable operating points associated to the two oscillators. So, in order to make the system more robust, the output buffer's current mirror (Fig. 7.1d) has no integrated resistance and the reference current can be supplied/adjusted from outside according to the actual output signal (through the  $I_{\text{bias}}$  pin shown in Fig. 7.3).

As a result, the oscillators do not start-up at room temperature whereas they begin to work properly at 77 K. In particular, when  $I_{\text{bias}} = 100 \mu\text{A}$ , the oscillators are fed with 3.1 mA and the voltage supply must be set to  $V_{DD} = 1.8 \text{ V}$ . In these conditions, the output signal has a frequency of 1.7 GHz and the system pullability is approximately 4 MHz/100  $\mu\text{A}$ . Up to now, no DNP experiments have been yet carried out due to lack of time.



## 8 Conclusions and Outlook

In this thesis, we have investigated the application of the ESR detection principle introduced by the group of Dr. G. Boero in the frequency range from 400 MHz to 360 GHz. In this framework, the main achievements reported in this work are (1) the realization of the first portable standalone scanner for contactless material inspection of paramagnetic thin films, (2) the ESR experiments performed at the highest reported frequency for a single-chip detector, (3) the improvement of the single-chip ESR detectors so as to obtain an experimental spin sensitivity up to two orders of magnitude better than that of commercially available spectrometers, and (4) the realization of the first HEMT based detectors to overcome the limitations of previously developed CMOS architectures (i.e., low power consumption and low levels of microwave magnetic fields in order to extend the cryogenic temperature range and reduce saturation related issues). Moreover, the realized 10 GHz CMOS oscillator achieves the best distance resolution currently reported in the literature when used as an inductive proximity sensor, whereas the realized 11 GHz HEMT oscillator achieves the record minimum power consumption with respect to the other reported LC oscillators working in the same frequency range. The levels of low power consumption reached with the proposed HEMT architecture clearly highlight the possibility of improving current performance by using more advanced technology nodes. Additionally, according to the proposed analytical model, the expected achievable minimum power consumption, which could be reached by rearranging the Colpitts topology (without changing the process technology), is even lower than what has been reported in this thesis. Consequently, future designs based on HEMT technologies should also lead to even lower levels of radiofrequency magnetic fields, with a more extended number of measurable samples. Furthermore, the overall spin sensitivity of the HEMT detectors can be improved by orders of magnitude by shrinking the sensing coil, and, hence, by both increasing the working frequency and maximizing the filling factor in the nL scale. As a matter of fact, the intrinsic cut-off frequency of the proposed HEMT technology is already in the order of hundreds of GHz whereas it can be further enlarged through the adoption of commercially available In/Al based heterostructures. The aforementioned improvements would also contribute to matching the  $\hbar\omega \gg k_B T$  condition at much higher frequencies, leading to the chance of better investigating quantum related phenomena by reducing the number of equivalent photons coupled with the

LC tank.

On the other hand, the availability of advanced CMOS technologies (e.g., 28 nm) based on ultra-low-threshold-voltage (ULTV) transistors would allow to fabricate ESR detectors working at frequencies above 200 GHz, with the possibility of keeping acceptable values of microwave magnetic fields and then of reducing saturation related issues. Moreover, CMOS technologies are intrinsically more versatile than HEMT technologies since they allow for transistor matching at finger level, the use of several metal layers for connections, and they hold less restrictive constraints for layout clearance (i.e., less parasitics and higher integration density). Consequently, CMOS processes may enable future designers to use complex topologies in order to attain advanced integrated ESR single-chip architectures (e.g., pulsed ESR approaches with an embedded generator and a sensing resonator operating in the microwave range). The operation at frequencies above 100 GHz is also an important step towards the use of arrays of single-chip LC oscillators as a low cost alternative to gyrotrons sources in dynamic nuclear polarization (DNP) set-ups. In this thesis, it has been realized a single-chip CMOS ESR detector operating at 28 GHz for DNP purposes but it has not yet been tested in combination with the NMR counterpart (transceiver). Hence, that is definitely a topic which is going to be investigated in the near future.

Finally, although no details concerning the developed scanner for industrial applications can be disclosed, the realized ESR sensor matches the expected requirements since (1) its geometrical size is optimized for the expected sensitive volume and (2) both weight and power consumption are reasonable for a low-cost portable solution. Nevertheless, further efforts should be sustained in order to (1) reduce the impact of the modulation field on the overall noise performance (e.g., by shielding the most sensitive components) and (2) complete the embodiment of the architecture inside a unique enclosure.

## 9 Acknowledgement

After five years at EPFL, I really wish to express my sincere gratitude to many people. It has been an exciting chapter of my life, surrounded by new friends, wonderful colleagues, helpful technicians, and amazing mentors.

First of all, Giovanni. Of all the people I've ever met, he is the one who best embodies the genuine concept of scientist in everything he says, thinks or does. His enthusiastic approach, his attitude to problem solving, and his deep knowledge in so many areas made his presence essential for the success on every challenge encountered in this journey. He has supported me in all the activities without looking at the time, the day of the week, neither lunch nor dinner. He was simply always available. I will never forget our exciting discussions on transistors, oscillators, and experiments... but also about politics, classical music, life... and God! He also taught me that ethics at work and passion in what we do repay us much more than a (further) publication on a scientific journal, and that's why, even in periods of hard work (i.e., every day), smiles and jokes were never missing.

Second, I would like to thank Gabriele for his introduction to the world of integrated circuits, for the "(non-)well-known"  $k_B T/C$  noise, and, above all, for being my first new friend "made in Switzerland". He finished the doctoral program a few years ago but whenever he passes by to visit us it is always a joy!

Thank you Nergiz for your hard work, help, and support! You joined the group only a few months ago but your contribution has been essential in all our activities, especially for the journal papers! Moreover, thank you and Mohammad for sharing your food, for making the office such a friendly environment, for introducing me to both Turkish and Persian culture, and also for tolerating me constantly mispronouncing your names. Thank you Enrica and Marco for being so nice teammates. We spent years "sharing" (i.e., stealing from each other) oscilloscopes, generators, power supplies, PCBs, schematics, connectors, magnets... and the usual mess under the microscope!

I also wish to thank the R&D group of SICPA, in particular Lorenzo, Oscar, Anissa and Joëlle for their great collaboration in the CTI project. Their industrial application triggered my curiosity to ESR, and then the will to start my PhD!

A warm thank you goes to Jürgen for hosting me in his laboratory (LMIS1), for managing

## Chapter 9. Acknowledgement

---

both the team and the facility with care, for sharing his experience/knowledge in academics, for adding some German precision to a group of Italians, and for tolerating Valentin and me singing along our Christmas outings.

A special thank you for all the lab members... for these exciting years at the EPFL. Thank you Samuel for sharing one semester of exercises in the course of physics and, together with Lorenz, for your efforts in trying to understand my funny primitive German. Thank you Ya, Henry, Jack, Su, Zongming, Xiaosheng, Qiyuan, Yinben, Zhiwei and Jiley for the good time spent together, for our chats, and for recalling me your Chinese names so many times. Thank you Thomas for NOT caring about soccer when France won the world cup whereas Italy did not even qualify. Thank you Matthieu for your support with the 3D printer, your "experience" in pubs and beer in Lausanne, and for making me feel like a loser when I "only" run 10 km and I think of you running for 10 hours. Thank you Chris for your kindness and your "English" English in our group meetings. Thank you Jongmoon for leaving the office always late, and then for making me feel never alone. Thank you Yuliya for the only gift I have received when I passed my candidacy exam. Thank you Henry and Jack for sharing your experience from TSMC. Thank you Jonas for our daily jogging back to Lausanne... those two years I trained as never before and I also learned French with shortness of breath. Thank you Mario for adding a little Latin spirit to the group and for the parties at your place (although I hate Game of Thrones). A huge thank you to the group of Prof. Enz (in particular to Alessandro, Farzan and Arnout) for the access to the 28 nm TSMC technology and thank you Tom for sharing your experience in so many fields.

A special acknowledgment also goes to Mingee in the good memory of the nights spent monitoring the experiments at 10 K after every "standard working day". Thank you for sharing your expertise... and the risk!

Merci Séverine pour avoir géré mes factures pendant toutes ces années et surtout pour tes gâteaux d'anniversaire fantastiques!!! Merci Giancarlo pour toutes les puces que je t'ai fait bonder. Tu as été toujours extrêmement rapide et j'ai gagné beaucoup de temps grâce à toi. Merci également à André pour les wire-bonding faits dans le passé. Merci Patrick (PAM) pour ton aide pendant l'installation de l'aimant cryogénique à 0.3K et pour le remplissage hebdomadaire avec l'azote liquide. Merci Matthieu de m'avoir présenté à la fonderie HEMT OMMIC à Paris. Merci Lénaïc pour la caractérisation du capteur de proximité!

Grazie alla mia famiglia per tutto ciò che ha fatto anche in questi anni. Grazie per il nostro appuntamento skype del mercoledì sera che mi riporta sempre a casa col pensiero. Grazie per le cene ritardate del venerdì sera... e per quelle anticipate della Domenica. Grazie per le telefonate a Mario e a Zacchia e grazie per la valigia sempre pronta che ho trovato ad ogni (ri)partenza. Grazie per tutto il supporto logistico e morale che anche questa volta mi ha permesso di giungere alla meta. Per quanto vi ringrazi, non lo farò mai abbastanza!

...Sabrina, futura moglie e mamma, sei il mio amore! :) Grazie per essere come sei. Per altri cinque anni ti ho fatto aspettare il mio ritorno, ma questa è davvero la mia ultima tesi!

# Bibliography

- [1] G. Boero. *Integrated NMR probe for magnetometry*. Hartung-Gorre, Series in Microsystems (Vol. 9), 2000.
- [2] A.V. Matheoud, N. Sahin, and G. Boero. A single chip electron spin resonance detector based on a single high electron mobility transistor. *J. Magn. Reson.*, 294:59–70, 2018.
- [3] C.P. Slichter. *Principles of magnetic resonance, third enlarged and updated ed.* Springer, Berlin etc., 1996.
- [4] A.V. Matheoud, G. Gualco, M. Jeong, I. Zivkovic, J. Brugger, H.M. Rønnow, J. Anders, and G. Boero. Single-chip spin resonance detectors operating at 50 ghz, 92 ghz, and 146 ghz. *J. Magn. Reson.*, 278:113–121, 2017.
- [5] J.D. Jackson. *Classical electrodynamics, Third ed.* Wiley, New York etc., 1999.
- [6] D.J. Griffiths. *Introduction to electrodynamics, 4th ed.* Pearson, Boston, 2014.
- [7] T. Yalcin and G. Boero. Single-chip detector for electron spin resonance spectroscopy. *Rev. Sci. Instrum.*, 79:094105, 2008.
- [8] J. Anders, A. Angerhofer, and G. Boero. K-band single-chip electron spin resonance detector. *J. Magn. Reson.*, 217:19–26, 2012.
- [9] G. Gualco, J. Anders, A. Sienkiewicz, S. Alberti, L. Forro, and G. Boero. Cryogenic single-chip electron spin resonance detector. *J. Magn. Reson.*, 247:96–103, 2014.
- [10] G. Boero, G. Gualco, R. Lisowski, J. Anders, D. Suter, and J. Brugger. Room temperature strong coupling between a microwave oscillator and an ensemble of electron spins. *J. Magn. Reson.*, 231:133–140, 2013.
- [11] Q.T. Huang. Exact calculation of oscillation amplitude and predicting power consumption for cmos colpitts oscillators. In *Proceedings of IEEE International Symposium on Circuits and Systems*, pages 1401–1404. ISCAS, 1997.
- [12] J. Anders, M. Ortmanns, and G. Boero. Noise in frequency-sensitive esr detectors. In *Proceeding Volumes, 45*, pages 451–456. IFAC, 2012.

## Bibliography

---

- [13] A. Schweiger and G. Jeschke. *Principles of pulse electron paramagnetic resonance*. Oxford University Press, Oxford, 2005.
- [14] J.A. Weil and J.R. Bolton. *Electron paramagnetic resonance elementary theory and practical applications, 2nd ed.* Wiley-Interscience, Hoboken, N.J., 2007.
- [15] C.P. Poole. *Electron spin resonance a comprehensive treatise on experimental techniques, 2nd ed.* Wiley, New York, 1983.
- [16] R. Narkowicz, H. Ogata, E. Reijerse, and D. Suter. A cryogenic receiver for epr. *J. Magn. Reson.*, 237:79–84, 2013.
- [17] G. Boero, M. Bouterfas, C. Massin, F. Vincent, P.A. Besse, R.S. Popovic, and A. Schweiger. Electron-spin resonance probe based on a 100  $\mu$  m planar microcoil. *Rev. Sci. Instrum.*, 74:4794–4798, 2003.
- [18] R. Narkowicz, D. Suter, and I. Niemeyer. Scaling of sensitivity and efficiency in planar microresonators for electron spin resonance. *Rev. Sci. Instrum.*, 79:084702, 2008.
- [19] R. Narkowicz, D. Suter, and R. Stonies. Planar microresonators for epr experiments. *J. Magn. Reson.*, 175:275–284, 2005.
- [20] Y. Twig, E. Dikarov, and A. Blank. Ultra miniature resonators for electron spin resonance: sensitivity analysis, design and construction methods, and potential applications. *Mol. Phys.*, 111:2674–2682, 2013.
- [21] Y. Twig, E. Dikarov, W.D. Hutchison, and A. Blank. Note: High sensitivity pulsed electron spin resonance spectroscopy with induction detection. *Rev. Sci. Instrum.*, 82:076105, 2011.
- [22] Y. Twig, E. Dikarov, and A. Blank. Cryogenic electron spin resonance microimaging probe. *J. Magn. Reson.*, 218:22–29, 2012.
- [23] Y. Artzi, Y. Twig, and A. Blank. Induction-detection electron spin resonance with spin sensitivity of a few tens of spins. *Appl. Phys. Lett.*, 106:084104, 2015.
- [24] Y. Twig, A. Sorkin, D. Cristea, A. Feintuch, and A. Blank. Surface loop-gap resonators for electron spin resonance at w-band. *Rev. Sci. Instrum.*, 88:123901, 2017.
- [25] A. Blank, E. Dikarov, R. Shklyar, and Y. Twig. Induction-detection electron spin resonance with sensitivity of 1000 spins: En route to scalable quantum computations. *Phys. Lett. A*, 377:1937–1942, 2013.
- [26] O.W.B. Benningshof, H.R. Mohebbi, I.A.J. Taminiau, G.X. Miao, and D.G. Cory. Superconducting microstrip resonator for pulsed esr of thin films. *J. Magn. Reson.*, 230:84–87, 2013.

- [27] H. Malissa, D.I. Schuster, A.M. Tyryshkin, A.A. Houck, and S.A. Lyon. Superconducting coplanar waveguide resonators for low temperature pulsed electron spin resonance spectroscopy. *Rev. Sci. Instrum.*, 84:025116, 2013.
- [28] A.J. Sigillito, H. Malissa, A.M. Tyryshkin, H. Riemann, N.V. Abrosimov, P. Becker, H.-J. Pohl, M.L. Thewalt, K.M. Itoh, and J.J. Morton. Fast, low-power manipulation of spin ensembles in superconducting microresonators. *Appl. Phys. Lett.*, 104:222407, 2014.
- [29] A. Bienfait, J.J. Pla, Y. Kubo, M. Stern, X. Zhou, C.C. Lo, C.D. Weis, T. Schenkel, M.L.W. Thewalt, D. Vion, D. Esteve, B. Julsgaard, K. Molmer, J.J.L. Morton, and P. Bertet. Reaching the quantum limit of sensitivity in electron spin resonance. *Nat. Nanotechnol.*, 11:253–257, 2016.
- [30] P. Haikka, Y. Kubo, A. Bienfait, P. Bertet, and K. Mølmer. Proposal for detection of a single electron spin in a microwave resonator. *Phys. Rev. A*, 95:022306, 2017.
- [31] A. Bienfait, J.J. Pla, Y. Kubo, X. Zhou, M. Stern, C.C. Lo, C.D. Weis, T. Schenkel, D. Vion, D. Esteve, J.J.L. Morton, and P. Bertet. Controlling spin relaxation with a cavity. *Nature*, 531:74–77, 2016.
- [32] C. Eichler, A.J. Sigillito, S.A. Lyon, and J.R. Petta. Electron spin resonance at the level of 10000 spins using low impedance superconducting resonators. *Phys. Rev. Lett.*, 118:037701, 2017.
- [33] S. Probst, A. Bienfait, P. Campagne-Ibarcq, J.J. Pla, B. Albanese, J.F. Da Silva Barbosa, T. Schenkel, D. Vion, D. Esteve, K. Mølmer, J.J.L. Morton, R. Heeres, and P. Bertet. Inductive-detection electron-spin resonance spectroscopy with 65 spins/ hz sensitivity. *Appl. Phys. Lett.*, 111:202604, 2017.
- [34] A.T. Asfaw, A.J. Sigillito, A.M. Tyryshkin, T. Schenkel, and S.A. Lyon. Multi-frequency spin manipulation using rapidly tunable superconducting coplanar waveguide microresonators. *Appl. Phys. Lett.*, 111:032601, 2017.
- [35] D. Rugar, R. Budakian, H. Mamin, and B. Chui. Single spin detection by magnetic resonance force microscopy. *Nature*, 430:329–332, 2004.
- [36] M.S. Grinolds, M. Warner, K. De Greve, Y. Dovzhenko, L. Thiel, R.L. Walsworth, S. Hong, P. Maletinsky, and A. Yacoby. Subnanometre resolution in three-dimensional magnetic resonance imaging of individual dark spins. *Nat. Nano.*, 9:279–284, 2014.
- [37] S. Baumann, W. Paul, T. Choi, C.P. Lutz, A. Ardavan, and A.J. Heinrich. Electron paramagnetic resonance of individual atoms on a surface. *Science*, 350:417–420, 2015.
- [38] A. Blank, Y. Twig, and Y. Ishay. Recent trends in high spin sensitivity magnetic resonance. *J. Magn. Reson.*, 280:20–29, 2017.

## Bibliography

---

- [39] B. Blümich, P. Blümli, G. Eidmann, A. Guthausen, R. Haken, U. Schmitz, K. Saito, and G. Zimmer. The nmr-mouse: construction, excitation, and applications. *Magn. Reson. Imag.*, 16:479–484, 1998.
- [40] G. Eidmann, R. Savelsberg, P. Blümer, and B. Blümich. The nmr mouse, a mobile universal surface explorer. *J. Magn. Reson., Series A*, 122:104–109, 1996.
- [41] R.E. Best. *Phase-locked loops design, simulation, and applications, 5th ed.* McGraw-Hill, New York, 2003.
- [42] N. Azuma, T. Ozawa, and J. Yamauchi. Molecular and crystal structures of complexes of stable free radical bdpa with benzene and acetone. *Bulletin of the Chem. Society of Japan*, 67:31–38, 1994.
- [43] E.J. Reijerse. High-frequency epr instrumentation. *Appl. Magn. Reson.*, 37:795–818, 2010.
- [44] K.L. Nagy, D. Quintavalle, T. Feher, and A. Janossy. Multipurpose high-frequency esr spectrometer for condensed matter research. *Appl. Magn. Reson.*, 40:47–63, 2011.
- [45] C. Caspers, P.F. da Silva, M. Soundararajan, M.A. Haider, and J.-P. Ansermet. Field and frequency modulated sub-thz electron spin resonance spectrometer. *APL Photonics*, 1:026101, 2016.
- [46] M. Bennati and T.F. Prisner. New developments in high field electron paramagnetic resonance with applications in structural biology. *Reports on Progress in Physics*, 68:411, 2005.
- [47] G.W. Morley, L.-C. Brunel, and J. van Tol. A multifrequency high-field pulsed electron paramagnetic resonance/electron-nuclear double resonance spectrometer. *Rev. Sci. Instrum.*, 79:064703, 2008.
- [48] B. Razavi. A 300-ghz fundamental oscillator in 65-nm cmos technology. *IEEE J. Solid-St. Circ.*, 46:894–903, 2011.
- [49] B. Razavi. *RF microelectronics, 2nd, international ed.* Pearson Education International, Upper Saddle River, NJ, 2012.
- [50] S. Levantino, C. Samori, A. Bonfanti, S.L.J. Gierkink, A.L. Lacaita, and V. Bocuzzi. Frequency dependence on bias current in 5 ghz cmos vcocs: impact on tuning range and flicker noise upconversion. *IEEE J. Solid-St. Circ.*, 37:1003–1011, 2002.
- [51] P. Kinget. Amplitude detection inside cmos lc oscillators. *IEEE Int. Symp. Circ. S*, pages 5147–5150, 2006.
- [52] J.P. Goldsborough, M. Mandel, and G.E. Pake. Influence of exchange interaction on paramagnetic relaxation times. *Phys. Rev. Lett.*, 4:13–15, 1960.



- [53] D.G. Mitchell, R.W. Quine, M. Tseitlin, R.T. Weber, V. Meyer, A. Avery, S.S. Eaton, and G.R. Eaton. Electron spin relaxation and heterogeneity of the 1:1  $\alpha,\gamma$ -bis(diphenylene- $\beta$ -phenylallyl (bdpa)/benzene complex. *The J. of Phys. Chemistry B*, 115:7986–7990, 2011.
- [54] F.M. Gardner. *Phaselock techniques, 3rd ed.* Wiley, Hoboken, N.J., 2005.
- [55] R.E. Best. *Phase-locked loops design, simulation, and applications, 5th ed.* McGraw-Hill, New York, 2003.
- [56] J.S. Thorp and A.R. Skinner. The dependence of epr linewidth on concentration in mn/mgo single crystals. *J. Magn. Magn. Mater.*, 69:34–42, 1987.
- [57] T. Phan, P. Zhang, H. Tran, and S. Yu. Electron spin resonance study of mn-doped metal oxides annealed at different temperatures. *J. of the Korean Physical Society*, 57:1270–1276, 2010.
- [58] E. Ohmichi, Y. Tokuda, R. Tabuse, D. Tsubokura, T. Okamoto, and H. Ohta. Multi-frequency force-detected electron spin resonance in the millimeter-wave region up to 150 ghz. *Rev. Sci. Instrum.*, 87:073904, 2016.
- [59] S. Haravifard, D. Graf, A.E. Feiguin, C.D. Batista, J.C. Lang, D.M. Silevitch, G. Srajer, B.D. Gaulin, H.A. Dabkowska, and T.F. Rosenbaum. Crystallization of spin superlattices with pressure and field in the layered magnet  $\text{SrCu}_2(\text{BO}_3)_2$ . *Nat. Commun.*, 7, 2016.
- [60] M.E. Zayed, C. Rüegg, T. Strässle, U. Stühr, B. Roessli, M. Ay, J. Mesot, P. Link, E. Pomjakushina, M. Stingaciu, K. Conder, and H.M. Rønnow. Correlated decay of triplet excitations in the shastry-sutherland compound  $\text{SrCu}_2(\text{BO}_3)_2$ . *Phys. Rev. Lett.*, 113:067201, 2014.
- [61] P. Kuppusamy and P.T. Manoharan. Exchange interactions in bis(tetramethylammonium) bis(maleonitriledithiolato)cuprate(ii),  $[\text{nme}_4]_2[\text{Cu}(\text{mnt})_2]$  - a quasi-1-d weak-exchange system. *Inorg. Chem.*, 24:3053–3057, 1985.
- [62] W. Steyaert and P. Reynaert. A 0.54 thz signal generator in 40 nm bulk cmos with 22 ghz tuning range and integrated planar antenna. *IEEE J. Solid-St. Circ.*, 49:1617–1626, 2014.
- [63] M. Seo, M. Urteaga, J. Hacker, A. Young, Z. Griffith, R. Jain, V. Pierson, P. Rowell, A. Skalare, and A. Peralta. Inp hbt ic technology for terahertz frequencies: Fundamental oscillators up to 0.57 thz. *IEEE J. Solid-St. Circ.*, 46:2203–2214, 2011.
- [64] A. Hajimiri and T.H. Lee. *The design of low noise oscillators, 2nd ed.* Kluwer Academic Publisher, Boston, 2000.
- [65] A. Hajimiri and T.H. Lee. A general theory of phase noise in electrical oscillators. *IEEE J. Solid-St. Circ.*, 33:179–194, 1998.

## Bibliography

---

- [66] T.H. Lee and A. Hajimiri. Oscillator phase noise: a tutorial. *IEEE J. Solid-St. Circ.*, 35:326–336, 2000.
- [67] M. Shahmohammadi, M. Babaie, and R.B. Staszewski. A 1/f noise upconversion reduction technique for voltage-biased rf cmos oscillators. *IEEE J. Solid-St. Circ.*, 51:2610–2624, 2016.
- [68] M. Grisi, G. Gualco, and G. Boero. A broadband single-chip transceiver for multi-nuclear nmr probes. *Rev. Sci. Instrum.*, 86, 2015.
- [69] J.A. del Alamo. Nanometre-scale electronics with iii-v compound semiconductors. *Nature*, 479:317–323, 2011.
- [70] A.H. Akgiray, S. Weinreb, R. Leblanc, M. Renvoise, R. Frijlink, P. Lai, and S. Sarkozy. Noise measurements of discrete hemt transistors and application to wideband very low-noise amplifiers. *IEEE T. Microw. Theory*, 61:3285–3297, 2013.
- [71] C.C. Chiong, H.M. Chen, J.C. Kao, H. Wang, and M.T. Chen. 180-220 ghz mmic amplifier using 70-nm gaas mhemt technology. *IEEE International Symposium on Radio-Frequency Integration Technology*, 2016.
- [72] P. Andreani, X. Wang, L. Vandi, and A. Fard. A study of phase noise in colpitts and lc-tank cmos oscillators. *IEEE J. Solid-St. Circ.*, 40:1107–1118, 2005.
- [73] W. Loh, S. Yegnanarayanan, R.J. Ram, and P.W. Juodawlkis. Unified theory of oscillator phase noise ii: Flicker noise. *IEEE T. Microw. Theory*, 61:4130–4144, 2013.
- [74] E.M. Gardner. *Phaselock techniques, 3rd ed.* Wiley, Hoboken, N.J., 2005.
- [75] R.S. Rhodes, J.H. Burgess, and A.S. Edelstein. Exchange-ordering and observation of forbidden spin resonance transitions in crystalline organic radicals. *Phys. Rev. Lett.*, 6:462, 1961.
- [76] M. Inoue and M. Kubo. Magnetic susceptibilities of alternating linear ising antiferromagnets and 2 coupled ising chains. *J. Magn. Reson.*, 4:175, 1971.
- [77] W. Duffy, J.F. Dubach, P.A. Pianetta, and J.F. Deck. Antiferromagnetic linear chains in crystalline free-radical bdpa. *J. Chem. Phys.*, 56:2555, 1972.
- [78] J. Yamauchi. Linear antiferromagnetic interaction in organic free radicals. *Bulletin of the Chem. Society of Japan*, 44:2301, 1971.
- [79] J. Stach, R. Kirmse, and W. Dietzsch. Single-crystal epr study of (normal-bu<sub>4</sub>n)[cu/ni(mnt)(et<sub>2</sub>dtp)]. *Inorg. Nucl. Chem. Lett.*, 14:143–147, 1978.
- [80] R. Kirmse, J. Stach, W. Dietzsch, and E. Hoyer. <sup>533</sup> hyperfine interactions in single-crystal esr-spectra of (n-bu<sub>4</sub>n)<sub>2</sub>[<sup>63</sup>cu(mnt)<sub>2</sub>]. *Inorg. Chim. Acta*, 26:53–55, 1978.

- [81] M.P. Kennedy. Chaos in the colpitts oscillator. *IEEE Transactions on Circuits and Systems I-Fundamental Theory and Applications*, 41:771–774, 1994.
- [82] T. Takahashi, Y. Kawano, K. Makiyama, S. Shiba, M. Sato, Y. Nakasha, and N. Hara. Maximum frequency of oscillation of 1.3 thz obtained by using an extended drain-side recess structure in 75-nm-gate inalas/ingaas high-electron-mobility transistors. *Appl. Phys. Express*, 10, 2017.
- [83] G. Ghibaudo and F. Balestra. Low temperature characterization of silicon cmos devices. *Microelectron. Reliab.*, 37:1353–1366, 1997.
- [84] T. Matsuoka, E. Kobayashi, K. Taniguchi, C. Hamaguchi, and S. Sasa. Temperature-dependence of electron-mobility in ingaas/inalas heterostructures. *Jpn. J. Appl. Phys. 1*, 29:2017–2025, 1990.
- [85] J.J.L. Morton and P. Bertet. Storing quantum information in spins and high-sensitivity esr. *J. Magn. Reson.*, 287:128–139, 2018.
- [86] A.V. Matheoud, N. Sahin Solmaz, and G. Boero. A low power microwave hemt lc oscillator operating down to 1.4 k. *IEEE Trans. on Microwave Theory and Techniques (submitted in December, 2018)*.
- [87] J.A. Del Alamo. Nanometre-scale electronics with iii-v compound semiconductors. *Nature*, 479:317, 2011.
- [88] T. Takahashi, Y. Kawano, K. Makiyama, S. Shiba, M. Sato, Y. Nakasha, and N. Hara. Maximum frequency of oscillation of 1.3 thz obtained by using an extended drain-side recess structure in 75-nm-gate inalas/ingaas high-electron-mobility transistors. *App. Physics Express*, 10:024102, 2017.
- [89] J. Ajayan, D. Nirmal, T. Ravichandran, P. Mohankumar, P. Prajoon, L. Arivazhagan, and C.K. Sarkar. Inp high electron mobility transistors for submillimetre wave and terahertz frequency applications: A review. *AEU-Intern. J. of Electr. and Comm.*, 2018.
- [90] J. Schlee, G. Alestig, J. Halonen, A. Malmros, B. Nilsson, P.A. Nilsson, J.P. Starski, N. Wadefalk, H. Zirath, and J. Grahn. Ultralow-power cryogenic inp hemt with minimum noise temperature of 1 k at 6 ghz. *IEEE Elect. Dev. Lett.*, 33:664–666, 2012.
- [91] S. Montazeri, W.-T. Wong, A.H. Coskun, and J.C. Bardin. Ultra-low-power cryogenic sigel low-noise amplifiers: Theory and demonstration. *IEEE Trans. on Microwave Theory and Tech.*, 64:178–187, 2016.
- [92] J.M. Hornibrook, J.I. Colless, I.D.C. Lamb, S.J. Pauka, H. Lu, A.C. Gossard, J.D. Watson, G.C. Gardner, S. Fallahi, and M.J. Manfra. Cryogenic control architecture for large-scale quantum computing. *Phys. Rev. App.*, 3:024010, 2015.

## Bibliography

---

- [93] N. Oukhanski, M. Grajcar, E. Ilichev, and H.-G. Meyer. Low noise, low power consumption high electron mobility transistors amplifier, for temperatures below 1 k. *Rev. of scient. instr.*, 74:1145–1146, 2003.
- [94] A.M. Korolev, V.I. Shnyrkov, and V.M. Shulga. Note: Ultra-high frequency ultra-low dc power consumption hemt amplifier for quantum measurements in millikelvin temperature range. *Rev. of Scientific Instruments*, 82:016101, 2011.
- [95] A.M. Korolev, V.M. Shulga, I.A. Gritsenko, and G.A. Sheshin. Phemt as a circuit element for high impedance nanopower amplifiers for ultra-low temperatures application. *Cryogenics*, 67:31–35, 2015.
- [96] L.A. Tracy, D.R. Luhman, S.M. Carr, N.C. Bishop, G.A. Ten Eyck, T. Pluym, J.R. Wendt, M.P. Lilly, and M.S. Carroll. Single shot spin readout using a cryogenic high-electron-mobility transistor amplifier at sub-kelvin temperatures. *App. Physics Letters*, 108:063101, 2016.
- [97] I.T. Vink, T. Nooitgedagt, R.N. Schouten, L.M.K. Vandersypen, and W. Wegscheider. Cryogenic amplifier for fast real-time detection of single-electron tunneling. *App. Physics Letters*, 91:123512, 2007.
- [98] C. Wang, T. Hanrahan, and M. Johnson. High capacity closed-cycle 1 k cryocooler. *Cryogenics*, 95:64–68, 2018.
- [99] S. Krinner, S. Storz, P. Kurpiers, P. Magnard, J. Heinsoo, R. Keller, J. Luetolf, C. Eichler, and A. Wallraff. Engineering cryogenic setups for 100-qubit scale superconducting circuit systems. *arXiv preprint arXiv:1806.07862*, 2018.
- [100] O. Momeni and E. Afshari. High power terahertz and millimeter-wave oscillator design: A systematic approach. *IEEE J. of Solid-State Circuits*, 46:583–597, 2011.
- [101] Y. Nakasha, S. Masuda, K. Makiyama, T. Ohki, M. Kanamura, N. Okamoto, T. Tajima, T. Seino, H. Shigematsu, and K. Imanishi. E-band 85-mw oscillator and 1.3-w amplifier ics using 0.12  $\mu\text{m}$  gan hemts for millimeter-wave transceivers. In *Compound Semiconductor Integrated Circuit Symposium (CSICS)*, pages 1–4. IEEE, 2010.
- [102] Y. Kwon and D. Pavlidis. Large signal analysis and experimental characteristics of monolithic inp-based w-band hemt oscillators. In *Microwave Conf.*, volume 1, pages 161–166. IEEE, 1991.
- [103] V.S. Kaper, V. Tilak, H. Kim, A.V. Vertiatchikh, R.M. Thompson, T.R. Prunty, L.F. Eastman, and J.R. Shealy. High-power monolithic AlGaIn/GaN HEMT oscillator. *IEEE J. of Solid-State Circuits*, 38:1457–1461, 2003.
- [104] P. Burasa, N.G. Constantin, and K. Wu. Low-power injection-locked zero-if self-oscillating mixer for high gbit/s data-rate battery-free active  $\mu\text{rfid}$  tag at millimeter-wave frequencies in 65-nm cmos. *IEEE Trans. on Microwave Theory and Techniques*, 64:1055–1065, 2016.

- [105] S.-L. Jang and Y.-C. Lin. Low-power three-path inductor class-c vco without any dynamic bias circuit. *Electr. Lett.*, 53:1186–1188, 2017.
- [106] W.-S. Feng, C. Yeh, C.-M. Tsao, H.-H. Li, P. Chatterjee, and C.-H. Chen. Low power design for rf circuits. In *Cross Strait Quad-Regional Radio Science and Wireless Technology Conference (CSQRWC)*, volume 1, pages 657–660, 2011.
- [107] M. Motoyoshi, S. Kameda, and N. Suematsu. 57 ghz 130  $\mu$ w cmos millimeter-wave oscillator for ultra low power sensor node. In *11th Global Symposium on Millimeter Waves (GSMM)*, pages 1–4, 2018.
- [108] S.-L. Jang and C.-F. Lee. A low voltage and power lc vco implemented with dynamic threshold voltage mosfets. *IEEE microwave and wireless comp. lett.*, 17:376–378, 2007.
- [109] D. Fathi and A.G. Nejad. Ultra-low power, low phase noise 10 ghz lc vco in the subthreshold regime. *Circuits and Systems*, 4:350, 2013.
- [110] F. Yu. A low-voltage and low-power 3-ghz cmos lc vco for s-band wireless applications. *Wireless personal comm.*, 78:905–914, 2014.
- [111] B. Li, Y. Zhai, B. Yang, T. Salter, M. Peckerar, and N. Goldsman. Ultra low power phase detector and phase-locked loop designs and their application as a receiver. *Microelectronics J.*, 42:358–364, 2011.
- [112] W. Xiushan, W. Zhigong, L. Zhiqun, X. Jun, and L. Qing. Design and realization of an ultra-low-power low-phase-noise cmos lc-vco. *J. of Semiconductors*, 31:085007, 2010.
- [113] S.-L. Jang, Y.-J. Su, K.J. Lin, and B.-J. Wang. An 4.7 ghz low-power cross-coupled gan hemt oscillator. *Microwave and Optical Techn. Lett.*, 60:2442–2447, 2018.
- [114] A. Hollmann, D. Jirovec, M. Kucharski, D. Kissinger, G. Fischer, and L.R. Schreiber. 30 ghz-voltage controlled oscillator operating at 4 k. *arXiv preprint arXiv:1804.09522*, 2018.
- [115] R. Kojouharov, I. Angelov, E. Kollberg, Z. Ivanov, Y.F. Chen, T. Claeson, and L.G. Yohansson. An x-band hemt microwave oscillator stabilized with a superconducting resonator. *Superconductor Science and Technology*, 10:71, 1997.
- [116] E. Vollmer and P. Gutmann. X-band gaas mesfet oscillator for cryogenic application at 4.2 k. *Electronics Lett.*, 27:2210–2211, 1991.
- [117] B. Patra, R.M. Incandela, J.P.G. Van Dijk, H.A.R. Homulle, L. Song, M. Shahmohammadi, R.B. Staszewski, A. Vladimirescu, M. Babaie, and F. Sebastiano. Cryo-cmos circuits and systems for quantum computing applications. *IEEE J. of Solid-State Circuits*, 53:309–321, 2018.
- [118] V.J. Urick, K.J. Williams, and J.D. McKinney. *Fundamentals of microwave photonics*, volume 1. John Wiley & Sons, 2015.

## Bibliography

---

- [119] H. Nyquist. Thermal agitation of electric charge in conductors. *Phys. Rev.*, 32:110–113, 1928.
- [120] A.A. Clerk, M.H. Devoret, S.M. Girvin, F. Marquardt, and R.J. Schoelkopf. Introduction to quantum noise, measurement, and amplification. *Rev. of Modern Physics*, 82:1155, 2010.
- [121] A.R. Kerr. Suggestions for revised definitions of noise quantities, including quantum effects. *IEEE Trans. on Microwave Theory and Tech.*, 47:325–329, 1999.
- [122] M.A. Castellanos-Beltran, K.D. Irwin, G.C. Hilton, L.R. Vale, and K.W. Lehnert. Amplification and squeezing of quantum noise with a tunable josephson metamaterial. *Nature Physics*, 4:929, 2008.
- [123] L.B. Kish, G.A. Niklasson, and C.G. Granqvist. Zero-point term and quantum effects in the johnson noise of resistors: a critical appraisal. *J. of Statistical Mechanics: Theory and Experiment*, 2016:054006, 2016.
- [124] P. Altuntas, N. Defrance, M. Lesecq, A. Agboton, R. Ouhachi, E. Okada, C. Gaquiere, J.-C. De Jaeger, E. Frayssinet, and Y. Cordier. On the correlation between kink effect and effective mobility in inaln/gan hemts. In *European Microwave Integrated Circuit Conference (EuMIC), 9th*, pages 88–91. IEEE, 2014.
- [125] H. Shichman and D.A. Hodges. Modeling and simulation of insulated-gate field-effect transistor switching circuits. *IEEE J. of Solid-State Circuits*, 3:285–289, 1968.
- [126] K.R. Laker and W.M.C. Sansen. *Design of analog integrated circuits and systems*. McGraw-Hill New York, 1994.
- [127] P. Antognetti and G. Massobrio. *Semiconductor device modeling with SPICE*. McGraw-Hill, Inc., 1990.
- [128] A. Ortiz-Conde, F.J.G. Sánchez, J.J. Liou, A. Cerdeira, M. Estrada, and Y. Yue. A review of recent mosfet threshold voltage extraction methods. *Microelectronics Reliability*, 42:583–596, 2002.
- [129] R.M. Incandela, L. Song, H. Homulle, E. Charbon, A. Vladimirescu, and F. Sebastian. Characterization and compact modeling of nanometer cmos transistors at deep-cryogenic temperatures. *IEEE J. of the Electr. Dev. Society*, 2018.
- [130] C.H. Lin, W.K. Wang, P.C. Lin, C.K. Lin, Y.J. Chang, and Y.J. Chan. Transient pulsed analysis on gan hemts at cryogenic temperatures. *IEEE Electr. Dev. Letters*, 26:710–712, 2005.
- [131] S.H. Hong, G.B. Choi, R.H. Baek, H.S. Kang, S.W. Jung, and Y.H. Jeong. Low-temperature performance of nanoscale mosfet for deep-space rf applications. *IEEE Electr. Dev. Lett.*, 29:775–777, 2008.

- [132] C.-S Chang, H.R. Fetterman, and C.R. Viswanathan. The characterization of high electron mobility transistors using shubnikov–de haas oscillations and geometrical magnetoresistance measurements. *J. of App. Physics*, 66:928–936, 1989.
- [133] R.S. Popovic. *Hall effect devices - Magnetic sensors and characterization of semiconductors*. Adam-Hilger, 1991.
- [134] T.R. Jervis and E.F. Johnson. Geometrical magnetoresistance and hall mobility in gunn effect devices. *Solid-State Electr.*, 13:181–189, 1970.
- [135] P.D. Dimitropoulos, P.M. Drljaca, R.S. Popovic, and P. Chatzinikolaou. Horizontal hall devices: A lumped-circuit model for eda simulators. *Sens. and Act. A: Physical*, 145:161–175, 2008.
- [136] M.K. Mishra, R.K. Sharma, R. Manchanda, R.K. Bag, O.P. Thakur, and R. Muralidharan. Comprehensive magnetotransport characterization of two dimensional electron gas in algan/gan high electron mobility transistor structures leading to the assessment of interface roughness. *AIP Advances*, 4:097124, 2014.
- [137] M.C. Arikan, A. Straw, and N. Balkan. Warm electron energy loss in gainas/alinas high electron mobility transistor structures. *J. of App. Physics*, 74:6261–6265, 1993.
- [138] Z. Tan, C. Tan, L. Ma, G.T. Liu, L. Lu, and C.L. Yang. Shubnikov-de haas oscillations of a single layer graphene under dc current bias. *Physical Rev. B*, 84:115429, 2011.
- [139] E. Tiras, O. Celik, S. Mutlu, S. Ardali, S.B. Lisesivdin, and E. Ozbay. Temperature dependent energy relaxation time in algan/aln/gan heterostructures. *Superlattices and Microstruct.*, 51:733–744, 2012.
- [140] J.P. Campbell, K.P. Cheung, L.C. Yu, J.S. Suehle, A. Oates, and K. Sheng. Geometric magnetoresistance mobility extraction in highly scaled transistors. *IEEE Elec. Dev. Lett.*, 32:75–77, 2011.
- [141] G. Gualco, M. Grisi, and G. Boero. Frequency jumps in single chip microwave lc oscillators. *App. Phys. Lett.*, 105:242102, 2014.
- [142] U. Vool and M. Devoret. Introduction to quantum electromagnetic circuits. *Intern. J. of Circ. Theory and Applications*, 45:897–934, 2017.
- [143] X. Gu, A.F. Kockum, A. Miranowicz, Y.X. Liu, and F. Nori. Microwave photonics with superconducting quantum circuits. *Physics Reports*, 718-719:1–102, 2017.
- [144] C.C. Enz and E.A. Vittoz. *Charge-based MOS transistor modeling: the EKV model for low-power and RF IC design*. John Wiley & Sons, 2006.
- [145] A.V. Matheoud, N. Sahin, L. Frehner, and G. Boero. Microwave inductive proximity sensors with sub-pm/ $\sqrt{\text{hz}}$  resolution. *Sens. and Act. A: Physical (submitted in September, 2018)*.

## Bibliography

---

- [146] A.J. Fleming. A review of nanometer resolution position sensors: operation and performance. *Sens. and Act. A: Physical*, 190:106–126, 2013.
- [147] S. Nihtianov. Measuring in the subnanometer range - capacitive and eddy current nanodisplacement sensors. *IEEE Ind. Elec. Mag.*, pages 6–15, 2014.
- [148] B. George, Z. Tan, and S. Nihtianov. Advances in capacitive, eddy current, and magnetic displacement sensors and corresponding interfaces. *IEEE Trans. Ind. Elec.*, 64:9595–9607, 2017.
- [149] V. Chaturvedi, J.G. Vogel, K.A.A. Makinwa, and S. Nihtianov. A 19.8-mw eddy-current displacement sensor interface with sub-nanometer resolution. *J. Solid-State Circ.*, 53:2273–2283, 2018.
- [150] P. Kejik, C. Kluser, R. Bischofberger, and R.S. Popovic. A low-cost inductive proximity sensor for industrial applications. *Sens. and Act. A: Physical*, 110:93–97, 2004.
- [151] M.R. Nabavi, M.A.P. Pertijs, and S. Nihtianov. An interface for eddy-current displacement sensors with 15-bit resolution and 20 mhz excitation. *IEEE J. of Solid-State Circ.*, 48:2868–2881, 2013.
- [152] V. Chaturvedi, M.R. Nabavi, J.G. Vogel, and S. Nihtianov. Demodulation techniques for self-oscillating eddy-current displacement sensor interfaces: a review. *IEEE Sens. J.*, 17:2617–2624, 2017.
- [153] M.R. Nabavi. *Low-power high-performance integrated interface for eddy-current displacement sensors*. Ph.D. dissertation, Delft Univ. Technol., Dept. Microelectron., The Netherlands, 2011.
- [154] A. Fekri, M. Nabavi, N. Radeljic-Jakic, Z.-Y. Chang, M. Pertijs, and S. Nihtianov. An eddy-current displacement-to-digital converter based on a ratio-metric delta-sigma adc. In *40th Eur. Solid State Circuits Conf.*, pages 403–406. ESSCIRC, 2014.
- [155] H. Wang, S. Kosai, C. Sideris, and A. Hajimiri. An ultrasensitive cmos magnetic biosensor array with correlated double counting noise suppression. In *MTT-S Int. Microwave Symp.*, pages 616–619. IEEE, 2010.
- [156] H. Wang, Y. Chen, A. Hassibi, A. Scherer, and A. Hajimiri. A frequency-shift cmos magnetic biosensor array with single-bead sensitivity and no external magnet. In *International Solid-State Circ. Conf. - Digest of Technical Papers*, pages 616–619. IEEE, 2009.
- [157] H. Wang, A. Mahdavi, D.A. Tirrell, and A. Hajimiri. A magnetic cell-based sensor. *Lab on a Chip*, 12:4465–4471, 2012.
- [158] C. Sideris and A. Hajimiri. Design and implementation of an integrated magnetic spectrometer for multiplexed biosensing. *IEEE trans. on biom. circ. and sys.*, 7:773–784, 2013.



- [159] T. Mitsunaka, D. Sato, N. Ashida, A. Saito, K. Iizuka, T. Suzuki, Y. Ogawa, and M. Fujishima. Cmos biosensor ic focusing on dielectric relaxations of biological water with 120 and 60 ghz oscillator arrays. *IEEE J. of Solid-State Circ.*, 51:2534–2544, 2016.
- [160] J.-C. Chien and A.M. Niknejad. Oscillator-based reactance sensors with injection locking for high-throughput flow cytometry using microwave dielectric spectroscopy. *J. Solid-State Circuits*, 51:457–472, 2016.
- [161] Y. Chiu, H.-C. Hong, and P.-C. Wu. Development and characterization of a cmos-mems accelerometer with differential lc-tank oscillators. *J. of microelectromechanical sys.*, 22:1285–1295, 2013.
- [162] Y. Chiu, H.-C. Hong, and C.-M. Chang. Three-axis cmos mems inductive accelerometer with novel z-axis sensing scheme. In *Solid-State Sens., Act, and Microsys. (TRANSDUCERS), 19th Int. Conf.*, pages 410–413. IEEE, 2017.
- [163] D.H.S. Cheng. The reflected impedance of a circular coil in the proximity of a semi-infinite medium. *IEEE Transactions on Instrumentation and Measurement*, 14:107–116, 1965.
- [164] H. Wang and Z. Feng. Ultrastable and highly sensitive eddy current displacement sensor using self temperature compensation. *Sens. and Act. A: Physical*, 203:362–368, 2013.
- [165] H. Wang, C.-C. Weng, and A. Hajimiri. Phase noise and fundamental sensitivity of oscillator-based reactance sensors. *IEEE Trans. Microw. Theory Tech.*, 61:2215–2229, 2013.
- [166] J. Vine. Impedance of a coil placed near to a conducting sheet. *Int. J. of Elec.*, 16:569–577, 1964.
- [167] C.V. Dodd and W.E. Deeds. Analytical solutions to eddy-current probe-coil problems. *J. of App. Phys.*, 39:2829–2838, 1968.
- [168] A.J.M. Zaman, S.A. Long, and C.G. Gardner. The impedance of a single-turn coil near a conducting half space. *J. Nondestructive Eval.*, 1:183–189, 1980.
- [169] D. Schieber. Operation of eddy current probe coil. *J. of the Franklin Inst.*, 310:271–280, 1980.
- [170] M.W. Coffey. Theory for coil impedance of a conducting half space: analytic results for eddy current analysis. *J. Appl. Phys.*, 89:2473–2481, 2001.
- [171] P.A. Passeraub, P.A. Besse, and R.S. Popovic. Scaling down an inductive proximity sensor. *Sens. and Act. A*, 52:114–118, 1996.
- [172] H. Sutcliffe. Principles of eddy-current distance gauges. In *Proceedings of Inst. Elec. Eng.*, pages 479–484. IEE, 1977.

## Bibliography

---

- [173] J.R. Wait and K.P. Spies. Low-frequency impedance of a circular loop over a conducting ground. *Elec. Letters*, 9:346–348, 1973.
- [174] S.K. Burke. A perturbation method for calculating coil impedance in eddy-current testing. *J. of Physics D: App. Physics*, 18:1745, 1985.
- [175] R.J. Ditchburn, S.K. Burke, and M. Posada. Eddy-current nondestructive inspection with thin spiral coils: long cracks in steel. *J. of Nondestructive Eval.*, 22:63–77, 2003.
- [176] T.P. Theodoulidis and E.E. Kriezis. *Eddy current canonical problems (with applications to nondestructive evaluation)*. Tech Science Press, 2006.
- [177] U. Tröltzsch, F. Wendler, and O. Kanoun. Simplified analytical inductance model for a single turn eddy current sensor. *Sens. and Act. A: Physical*, 191:11–21, 2013.
- [178] S.S. Mohan, M. del Mar Hershenson, S.P. Boyd, and T.H. Lee. Simple accurate expressions for planar spiral inductances. *IEEE J. of Solid-State Circ.*, 34:1419–1424, 1999.

# Curriculum Vitae



## Personal information

Name / Surname **Alessandro Valentino Matheoud**  
E-mail ale.val.mthd@gmail.com  
Nationality Italian  
Date and Place of birth 14/02/1988 – Ivrea (To) – Italy

## Work experience

Dates October 2012 – January 2013  
Occupation or position held Resident Engineer at Robert Bosch, ETAS GmbH headquarter (Stuttgart - Germany)  
Main activities and responsibilities Commercial supporter and technical reference for both HW equipment and SW applications designed for rapid prototyping in automotive. Main working activities held at Fiat Industrial, Magneti Marelli, Audi, Ferrari, Maserati, and Mercedes.

Dates February 2013 – June 2013  
Occupation or position held Developer Engineer at Autostrade Tech S.p.A. headquarter (Florence - Italy)  
Main activities and responsibilities Analyst and designer of electrical, electronics and telecommunication systems for tolling and monitoring solutions. Main activities devoted to the implementation of innovative architectures in foreign markets, such as the free-flow-multilane structures in France, Poland and Chile.

Dates August 2013 – September 2018  
Occupation or position held Electronic Engineer and Scientific Assistant at the École Polytechnique Fédérale de Lausanne (EPFL), Microsystems Laboratory (Lausanne - Switzerland) – Partnership with SICPA HOLDING SA headquarter (Prilly - Switzerland)  
Main activities and responsibilities No information can be disclosed.

Dates Since August 2018  
Occupation or position held RF – Antenna Engineer at ViaSat Antenna Systems SA (Lausanne - Switzerland)  
Main activities and responsibilities No information can be disclosed.

## Education and training

Dates September 2007 – July 2010  
Title of qualification awarded Bachelor of Science in Telecommunication Engineering (Laurea in Ingegneria delle Telecomunicazioni)  
Name and type of organisation providing education and training Politecnico di Torino (Italy)  
Thesis Underwater Radio Frequency Transmission for Diver to Diver Communication – Internship at the Istituto Superiore Mario Boella (ISMB) research center  
Grade in national classification 110/110 cum Laude (GPA 29.76/30.00)

Date	September 2010 – November 2012
Title of qualification awarded	<u>Master of Science in Electronic Engineering (Laurea Magistrale in Ingegneria Elettronica)</u>
Name and type of organisation providing education and training	Politecnico di Torino, Politecnico di Milano (Italy) – Double degree program
Thesis	UHF Radio Frequency Modules for Ground-Satellite Communication – Internship at the Space Avionic Center of the Polytechnic of Turin
Grade in national classification	110/110 cum Laude (GPA 30.00/30.00)
Date	January 2011 – December 2012
Title of qualification awarded	<u>Master of Science in Electrical and Computer Engineering</u>
Name and type of organisation providing education and training	University of Illinois at Chicago (U.S.A.)
Thesis	UHF Radio Frequency Modules for Ground-Satellite Communication
Grade in national classification	Summa cum Laude (GPA 4.00/4.00)
Date	September 2010 – December 2012
Title of qualification awarded	<u>Alta Scuola Politecnica Diploma</u> , special joint degree program of Politecnico di Torino and Politecnico di Milano for excellence in multidisciplinary innovation, marketing and business strategy. Master of Business Administration (MBA). The minimum student's GPA to be admitted was 27.00/30.00.
Date	February 2015 – October 2018
Title of qualification awarded	<u>PhD Candidate in Microsystems and Microelectronics</u>
Name and type of organisation providing education and training	École Polytechnique Fédérale de Lausanne (EPFL), Microsystems Laboratory LMIS1 (Lausanne - Switzerland)
Thesis	Electron-Spin-Resonance (ESR) detectors from 400 MHz to 360 GHz

### **Additional information**

FELLOWSHIPS: UIC University Fellowship, the most distinguished doctoral award conferred by the Graduate College of the University of Illinois at Chicago.

QUALIFICATION: Achievement of the *Abilitazione all'Esercizio della Professione di Ingegnere* after passing the Italian State Examination in 2013. Affiliation to the *Ordine degli Ingegneri – Sezione A (Dottori Magistrali) – Settore dell'Informazione*.

### PUBLICATIONS:

- Matheoud A.V., Gualco G., Jeong M., Zivkovic I., Brugger J., Ronnow H.M., Anders J. and Boero G., *Single-chip electron spin resonance detectors operating at 50 GHz, 92 GHz, and 146 GHz*, Journal of Magnetic Resonance, vol. 278, p. 113-121, 2017.
- Chavarria M., Matheoud A.V., Marmillod P. and Boero G., *High sensitivity field asymmetric ion mobility spectrometer*, Review of Scientific Instruments, vol. 88, p. 035115-1 - 035115-13, 2017.
- Matheoud A.V., Sahin Solmaz N. and Boero G., *A single-chip electron spin resonance detector based on a single high electron mobility transistor*, Journal of Magnetic Resonance, vol. 294, p. 59-70, 2018.
- Matheoud A.V., Sahin Solmaz N., Frehner L. and Boero G., *Microwave inductive proximity sensors with sub-pm/√Hz resolution*, submitted to Sensors & Actuators: A. Physical.
- Matheoud A.V., Sahin Solmaz N. and Boero G., *A low power microwave HEMT LC oscillator operating down to 1.4 K*, submitted to IEEE Transactions on Microwave Theory and Techniques.



